A Determination of the Mass and Width of the W Boson at LEP2

Juan Pablo Palacios
Wolfson College, Oxford
DELPHI Experiment, CERN

A thesis submitted for the degree of Doctor of Philosophy
at the University of Oxford

Hilary Term, 2001

To Marco, Alicia and Gabriela

A Determination of the Mass and Width of the **W** Boson at LEP2

Juan Pablo Palacios
Wolfson College, Oxford
DELPHI Experiment, CERN

submitted for the degree of Doctor of Philosophy
at the University of Oxford

Hilary Term, 2001

ABSTRACT

During 1998 and 1999 LEP produced electron-positron collisions at centre of mass energies ranging between 189 and 202 GeV. An integrated luminosity of 372 pb^{-1} was collected by the DELPHI experiment during this period. From these data, samples of events with $\mathrm{e}\overline{\nu}_{\mathrm{e}}\mathrm{q}\bar{\mathrm{q}}'$, $\mu\overline{\nu}_{\mu}\mathrm{q}\bar{\mathrm{q}}'$ and $\tau\overline{\nu}_{\tau}\mathrm{q}\bar{\mathrm{q}}'$ final states were selected. These were analysed to obtain values for the mass and width of the W boson using the method of invariant mass direct reconstruction. Combining the results obtained for both running periods and the three $\mathrm{l}\overline{\nu}_{\mathrm{l}}\mathrm{q}\bar{\mathrm{q}}'$ channels, the following values are obtained:

$$\mathrm{M_W} = 80.308 \pm 0.113\ (stat) \pm 0.038\ (syst)\ \mathrm{GeV}$$

$$\Gamma_{\mathrm{W}} = 1.857 \pm 0.298\ (stat) \pm 0.155\ (syst)\ \mathrm{GeV}$$

Preface

In 1998 the LEP accelerator produced e^+e^- collisions at a centre of mass energy of 189 GeV, delivering more than twice the integrated luminosity of 1997. This, combined with a higher cross section for $\mathrm{W^+W^-}$ production, set the stage for a marked increase in the sensitivity in the determination of $\mathrm{M_W}$. In 1999 LEP operated at four centre of mass energy points: 192, 196, 200, and 202 GeV, again delivering considerably more luminosity than in the previous year. This thesis is concerned with the analysis of the data selected during these two running periods, and with the determination of the LEP beam energy, a crucial quantity in the determination of $\mathrm{M_W}$.

Events selected in the $\mathrm{e\overline{\nu}_e q\bar{q}'}$, $\mu\overline{\nu}_\mu \mathrm{q\bar{q}'}$ and $\tau\overline{\nu}_\tau \mathrm{q\bar{q}'}$ $\mathrm{W^+W^-}$ decay channels have been used to measure the mass and width of the W boson. For this purpose, a new unbinned maximum likelihood method has been developed, tested, and implemented by the author. The performance and statistical sensitivity of the method has been tested using a series of re-sampling methods and Monte Carlo experiments. The main systematic uncertainties associated to the measurement of $\mathrm{M_W}$ and Γ_W with this method have been fully evaluated as a part of this analysis. A systematic uncertainty unique to the non-parametric maximum likelihood method presented here, that due to the limited statistics of reference simulation samples, has been evaluated empirically using a technique developed by the author. A two-dimensional binned maximum likelihood has been developed as a cross check.

The author was heavily involved with the LEP Spectrometer Project. Software for the analysis of scans of the integrated bending field of the dipole magnet was developed by the author and used to analyse the dependence of the integrated bending field on temperature and transverse position. Algorithms for the interpretation of local magnetic readings in terms of total bending fields were obtained from the analysis of field maps. These allow for the precise determination of the bending field of the spectrometer magnet during LEP operations and is one of the key ingredients in the determination of the beam energy with the spectrometer. The accuracy to which the integrated bending can be inferred was measured and shown to be a well within the required accuracy.

The reader is referred to the acknowledgements section for details regarding the contributions from other members of the DELPHI collaboration and the CERN SL division.

Chapter One gives a summary of the Standard Model of Particle Physics with emphasis on Electroweak theory and the W boson. The importance of the measurement of $\mathrm{M_W}$ is presented here.

Chapter Two provides background information on the LEP accelerator. Particular attention is paid to the beam energy calibration. The LEP spectrometer is described in detail, particularly regarding the analysis of its dipole magnet. Preliminary results with the spectrometer are given in the final sections.

Chapter Three is a description of the DELPHI detector and its constituent sub-detectors. Overviews of the online and offline processing are also provided.

Chapter Four treats the selection of the data used for this thesis. It consists of brief summaries on track and run selection, a description of the Iterative Discriminant Analysis method and its application to the selection of $\mathrm{l\overline{\nu}_l q\bar{q}'}$ events. It concludes with some comments on the treatment of the selected events.

Chapter Five contains a detailed general description of the maximum likelihood method employed in this thesis, statistical tests that can be applied to gauge its sensitivity and consistency, and the application of the method to the measurements given here.

Chapter Six is dedicated to the study of the main systematic uncertainties in the measurement of $\mathrm{M_W}$ and Γ_W. The sources of uncertainty and the methods applied to measure them are described, and the results from the study quoted. The correlations between the sources of uncertainty are discussed.

Chapter Seven contains the $\mathrm{M_W}$ and Γ_W results, their interpretation in terms of higher order electroweak corrections, the Higgs mass, and the internal consistency of the standard model in its relation between the two parameters. Finally, conclusions are given.

Appendix A sketches the proof to the equivalent number of reweighted events approximation.

Appendix B gives details of `PUFITC+`, the kinematic fit package used in the $\mathrm{M_W}$ and Γ_W analyses.

Acknowledgements

I am very grateful to my supervisor Pete Renton for his input and guidance concerning all the aspects of this thesis, and for his supervision during my three and a half years of graduate study.

The W mass analysis was developed in close collaboration with Chris Parkes. His input to it proved invaluable. I am also grateful for the role he played in supporting my work in DELPHI.

My work within the LEP Energy Working Group was closely guided by Guy Wilkinson. I am grateful for his input in the analysis of the LEP Spectrometer mapping campaign data and in the development and refinement of the magnet model.

I would like to thank Chris Parkes, Pete Renton and Guy Wilkinson for reading various drafts of this manuscript.

I am grateful to the following people for specific contributions to the work presented in this thesis.

Chapter One In the preparation of this chapter I have made extensive use of the books by Pete Renton [1], Halzen & Martin [2], the proceedings of the RAL summer school [3], and the theses of Chris Parkes [4] and Jim Libby [5]. Figures 1.2 to 1.8 have been produced from code supplied by Chris Parkes.

Chapter Two In this chapter Figures 2.1 to 2.11, 2.21 and 2.22 were obtained from the CERN SL division, the LEP Energy Working Group, and from the LEP spectrometer project.

Chapter Three The figures in this chapter were taken from the DELPHI web pages. The DELPHI sub-detector specification tables 3.1, 3.2 and are based upon those in the thesis of Jim Libby.

Chapter Four The track selection section is based on work and information from Chris Parkes. The description of the electron identification algorithms make extensive use of [6]. The section on muon identification is inspired by [7] and benefited from discussions with Guy Wilkinson. The event selection was developed by Daniel Jeans for the W^+W^- cross section measurement and is used here with minor modifications. The standard W^+W^- analysis code was developed alongside other members of the W team.

Chapter Five Figure 5.3 was obtained from the thesis of Jim Libby. The technical input of Fabio Cossutti, Martijn Mulders, Niels Kjær, Jim Libby and Chris Parkes were invaluable in the implementation of the methods presented in this chapter.

Chapter Six The evaluation of the systematic errors due to electron energy and muon momentum resolution use the results of studies performed by Ahmimed Ouraou and Guy Wilkinson respectively. The combination of errors was performed using modified versions of software provided by Chris Parkes.

Chapter Seven The fitted Higgs Boson masses presented in Equations 7.3 to 7.5 were provided by Pete Renton.

I am grateful for the financial assistance of PPARC during the first three years of my graduate studies. I extend my gratitude to the University of Liverpool, and Themis Bowcock in particular, for the financial assistance during the final months of my D.Phil, and for their patience.

This document is produced from a template provided by John Holt.

This thesis benefited, directly or indirectly, from many discussions with Jim Libby, Jonas Rademacker, Barbara Raeven, Daniel Jeans, Geoff Morton, Sofia Andringa and Isabel Marthinsen.

Many thanks to John Holt for his patience and enthusiasm as MUB expert and ski instructor.

I am very grateful to Dave Charlton and Tony Weidberg for reading this manuscript in such detail and examining the work presented in it.

Finally, thanks to Patricia for making these times so special.

Juan Pablo Palacios
24th April 2001

Contents

List of Figures

List of Tables

Chapter 1

The Standard Model and the W Boson

1.1 Introduction

In this chapter the most important components of the standard model (SM) of particle physics are outlined. It is assumed that the reader is familiar with the SM and its constituents and so emphasis is made on the aspects related to the W boson and on its importance within the model. After a brief review of the salient features of the SM there follows a section on the physics of $W^{\pm}$ production and decays, concentrating on W-pair production in $e^{+}e^{-}$ collisions, followed by a description of the importance of the measurement of $\mathrm{M_W}$ and Γ_{W}.

1.2 The Standard Model of Particle Physics

The standard model of particle physics [1, 2, 3] describes the properties of fundamental particles, and their interactions through three forces. The fundamental constituents of the model are a set of spin-$\frac{1}{2}$ fermions, a set of spin-1 bosons, and a scalar boson. The vector bosons act as force carriers and so mediate the interactions between the fermions. The gauge boson is a consequence of the mechanism by which the constituents of the model acquire a mass. It is a relativistic quantum field theory whose interactions are described by a set of *renormalisable* gauge theories, namely Quantum Chromodynamics (QCD, the theory of Strong interactions), the Weak Force, and Quantum Electrodynamics (QED). Together, these form the SM gauge group $SU(3)_C \otimes SU(2)_L \otimes U(1)_Y$. The SM does not require its constituents to be massive, in fact, the mass generation is introduced in a gauge-invariant way via the Higgs Mechanism of spontaneous symmetry breaking. Despite being of great importance in the large scales of our universe, the force of Gravity has negligible effect in the interactions between fundamental particles. It does not form a part of the SM, and although its absence has no effect on experimentally measurable quantities in high energy physics, it is one of the reasons why the SM is far from being a final theory. In the following sections the constituents of the SM will be introduced, followed by a discussion of the $U(1)_Y$ and $SU(2)_L$ gauge groups and the Higgs mechanism. The theory of strong interactions is of little relevance to the work presented here and so the gauge group $SU(3)_C$ will not be discussed any further.

1.2.1 Fundamental Constituents of the Standard Model

Fermions

There are two distinct types of spin-$\frac{1}{2}$ fermions in the SM: *quarks* and *leptons*. Their fundamental differences are that *quarks* carry the colour charge and so feel the strong interaction, and that their electromagnetic charge is fractional in units of the charge of the electron, e. Due to the nature of the weak Interaction coupling the fermions are divided into left-handed doublets and right-handed singlets, and into three generations, of increasing mass. The minimal standard model assumes massless neutrinos and imposed the condition that there be no mixing between lepton generations[1]. Both can be incorporated into the SM easily. There is no need for the second and third generations in the SM. These arise from a combination of unexpected experimental discoveries of some of their elements, followed by theoretical postulation of the remaining ones. All the fundamental fermions of the model have by now been observed experimentally. They are listed, together with their quantum numbers, in Table 1.1.

---

[1] Resent results from Super-Kamiokande [8] on atmospheric neutrinos show evidence for massive neutrinos. This possibility will not be considered here as it has no impact on the results of this analysis.

Generation			**Quantum Numbers**			
1	2	3	T	T_3	Y	Q
	Leptons					
$\begin{pmatrix} \nu_e \\ e^- \end{pmatrix}_L$	$\begin{pmatrix} \nu_\mu \\ \mu^- \end{pmatrix}_L$	$\begin{pmatrix} \nu_\tau \\ \tau^- \end{pmatrix}_L$	$\frac{1}{2}$	$+\frac{1}{2}$ $-\frac{1}{2}$	-1	0 -1
e^-_R	μ^-_R	τ^-_R	0	0	-2	-1
	Quarks					
$\begin{pmatrix} u \\ d \end{pmatrix}_L$	$\begin{pmatrix} c \\ s \end{pmatrix}_L$	$\begin{pmatrix} t \\ b \end{pmatrix}_L$	$\frac{1}{2}$	$+\frac{1}{2}$ $-\frac{1}{2}$	$+\frac{1}{3}$	$+\frac{2}{3}$ $-\frac{1}{3}$
u_R	c_R	t_R	0	0	$+\frac{4}{3}$	$+\frac{2}{3}$
d_R	s_R	b_R	0	0	$-\frac{2}{3}$	$-\frac{1}{3}$

Table 1.1: Quantum numbers for the fermions in the standard model, where T and T_3 denote the weak isospin and its third component, Y denotes the weak hypercharge and Q the electric charge

Bosons

The spin-1 *vector* bosons of the SM describe the three forces of the model. The strength and range of these forces varies greatly at low energy scales. They are:

The **strong** force, which is the interaction between particles carrying the *color* charge. The corresponding bosons are *gluons* (g). They also carry the colour charge and so can interact with each other.

The **electromagnetic** force is the interaction between particles carrying electromagnetic charge via its neutral boson, the *photon* (γ).

The **weak** force is responsible for nuclear β decay and is mediated by the $W^\pm$ bosons.

The **electromagnetic** and **weak** forces have been unified via the **Electroweak** theory, which postulated the existence of a massive neutral vector boson, the Z^0, mediator of the weak neutral current interactions. The discovery of the Z^0 was a

Boson	Mass (GeV)	T	T_3	y	Q	**Interaction**
W^+	80.39 ± 0.06	1	$+1$	0	$+1$	Weak
Z^0	91.187 ± 0.002		0		0	Electroweak
W^-	80.39 ± 0.02		-1		-1	Weak
γ	0	0	0	0	0	QED
g	0	0	0	0	0	QCD
H	> 113.3 (95% *c.l.*)	$\frac{1}{2}$	$-\frac{1}{2}$	1	0	Yukawa

Table 1.2: Quantum numbers for the gauge bosons of the standard model. T and T_3 denote the weak isospin and its third component, y denotes the weak hypercharge and Q the electromagnetic charge. The values of the boson masses are taken from [9] where the masses of the $W^{\pm}$ and Z^0 are the world averages from direct and indirect measurements. The mass limit on the Higgs boson, derived from direct searches at LEP2, is taken from [10]

great triumph of this theory, which predicts and describes a wealth of **electromagnetic** and **weak** interactions.

The remaining boson in the SM is the scalar Higgs. It results from the spontaneous symmetry breaking mechanism by which the fermions and bosons of the SM acquire their mass. It is the only building block of the model yet to be directly observed, although tight experimental constraints exist regarding its mass. In Table 1.2 the bosons of the SM are listed with their quantum numbers, masses and the interaction they mediate.

1.2.2 Local Gauge Invariance: The $U(1)_Q$ Lagrangian

The properties of a relativistic quantum field theory can be described by a postulated Lagrangian[2] energy density $\mathcal{L}$. In the SM, the invariance of the theory under *local* gauge transformation is a requirement that plays a crucial role. As will be outlined for the case of QED, it results in the addition of fields to the theory. These fields will be directly related to the exchange of force between particles. First we start by considering a freely propagating fermion of mass m. This can be described by the

---

[2] In what follows this Lagrangian energy density will be referred to as "Lagrangian".

Dirac Lagrangian:

$$\mathcal{L}_D \;=\; i\overline{\psi}\gamma^\mu\partial_\mu\psi \;-\; m\overline{\psi}\psi \tag{1.1}$$

where the γ^μ are the Dirac gamma matrices and ψ is a four-vector wave function. By applying the Euler-Lagrange Equation (ELE) to 1.1 the equation of motion for ψ can be obtained. The generalised ELE is

$$\frac{\partial\mathcal{L}}{\partial\overline{\psi}} \;-\; \partial^\mu\left(\frac{\partial\mathcal{L}}{\partial(\partial_\mu\overline{\psi})}\right) \;=\; 0 \tag{1.2}$$

Applying this to Equation 1.1 yields the Dirac equation of motion for ψ:

$$(i\gamma_\mu\partial^\mu \;-\; m)\psi = 0\;. \tag{1.3}$$

A *local* gauge transformation, that is, a transformation which can vary according to space-time position, can be expressed mathematically as

$$\psi(x_\mu) \;\rightarrow\; \psi(x_\mu)' \;=\; e^{-iQ\rho(x_\mu)}\psi(x_\mu) \tag{1.4}$$

where Q is a constant and ρ is a function of x_μ. When a transformation of this type is applied to ψ the first term on the RHS of Equation 1.1 is not invariant as new terms arise during the transformation. Invariance is forced by postulating a new gauge field $A_\mu(x_\mu)$. This field is required to transform under the local gauge transformation defined in Equation 1.4 such that it cancels out the additional new terms. This can be achieved by requiring that $A_\mu(x_\mu)$ transform as

$$A_\mu \;\rightarrow\; A_\mu \;+\; \partial_\mu\rho(x_\mu) \tag{1.5}$$

and by replacing the derivative ∂_μ with the *covariant derivative*, $\mathcal{D}_\mu$:

$$\partial_\mu \;\rightarrow\; \mathcal{D}_\mu \;=\; \partial_\mu \;+\; iQA_\mu \tag{1.6}$$

This procedure of requiring local gauge invariance results in an additional term in Equation 1.1. This term gives the interaction between the Dirac fermion ψ and the postulated field A_μ:

$$\mathcal{L}_{int} \;=-\; Q\overline{\psi}\gamma_\mu\psi A^\mu \tag{1.7}$$

The field A_μ can be interpreted physically as the the field associated to the electromagnetic gauge boson, the *photon* γ, coupling to fermions with an electromagnetic charge of Q. A free Lagrangian for a massless spin-1 boson is

$$\mathcal{L}_\gamma \; = \; -\frac{1}{4}F_{\mu\nu}F^{\mu\nu} \tag{1.8}$$

This term describes the free propagation of the photon. Here $F_{\mu\nu}$ is the *electromagnetic field strength tensor* defined as

$$F_{\mu\nu} \; = \; \partial_\mu A_\nu \; - \; \partial_\nu A_\mu \tag{1.9}$$

and is invariant under the local gauge transformation 1.4. Adding the term $\mathcal{L}_{int}$ given in Equation 1.7 and the free photon propagation term $\mathcal{L}_\gamma$ given in Equation 1.8 to the Lagrangian 1.1 gives the complete QED Lagrangian:

$$\mathcal{L}_{QED} \; = \; i\overline{\psi}\gamma^\mu(\partial_\mu \; + \; iQA_\mu)\psi \; - \; m\overline{\psi}\psi \; - \; \frac{1}{4}F_{\mu\nu}F^{\mu\nu} \tag{1.10}$$

It must be noted that a mass term for the photon $\mathcal{L}_{m\gamma} \; \sim \; m^2 A_\mu A^\mu$ is not gauge invariant and so the photon must be massless. Replacing ∂_μ by the covariant derivative $\mathcal{D}_\mu$ yields the more compact formula

$$\mathcal{L}_{QED} \; = \; \overline{\psi}(i\gamma_\mu D^\mu \; - \; m)\psi \; - \frac{1}{4}F_{\mu\nu}F^{\mu\nu} \tag{1.11}$$

1.2.3 Renormalisation

Although all the features of a QFT are contained in the Lagrangian, calculations are performed with perturbative expansions in terms of the coupling constants. The various orders in the expansion correspond to Feynman diagrams with an increasing number of vertices and particle loops and the corresponding Feynman rules. Each order of the series must give finite answers in order that the theory produce sensible calculations. The gauge theories of the SM, in principle divergent, must be made finite through the technique of **renormalisation**. The unphysical infinities resulting from each order of perturbative expansion can be cancelled by a re-definition of quantities such as mass and charge. The infinities are simply absorbed into the physically measured masses and charges. The exceptional compatibility between the predictions of *QED* and experiment show that the technique, although intuitively awkward, is a valid one. The remaining issue, whether gauge theories like $SU(2)_L \otimes U(1)_Y$ and $SU(3)$ are actually renormalisable, was settled by t'Hooft [11, 12], who showed formally that all local gauge theories are renormalisable.

1.2.4 Electroweak Theory

Electroweak (EW) theory, formulated by Salam, Glashow and Weinberg [13, 14, 15], unifies the electromagnetic and weak forces. It is a locally gauge invariant under $SU(2)_{L(Weak\ Isospin)} \otimes U(1)_{Y(Weak\ Hypercharge)}$ transformations. This group structure accounts for and accurately describes all observed EW interactions. The full EW Lagrangian can be derived in a way similar to that of the QED one. The structure of the $U(1)_Y$ weak hypercharge group is the same as for the $U(1)_Q$ QED case. In a way analogous to that outlined in Section 1.2.2, local gauge invariance under $U(1)_Y$ is obtained by postulating a field B_μ and replacing the derivative ∂_μ by a covariant derivative in expressed in terms of ∂_μ, B_μ and a coupling strength constant. The B_μ field couples to fermions with strength $\frac{g'}{2}y$ where g' is a coupling constant and y is the weak Hypercharge defined as

$$y = 2(Q - T_3) \tag{1.12}$$

Here, Q is the electromagnetic charge and T_3 the third component of the weak Isospin, given in Table 1.1. A free field term $-\frac{1}{4}B^{\mu\nu}B_{\mu\nu}$ analogous to that shown in Equation 1.8 must be added to the Lagrangian to describe the propagation of the boson related to B_μ. The next requirement is that the Lagrangian be invariant under $SU(2)_L$ weak isospin transformations. Although the procedure is essentially the same as in $U(1)$ it has added complexity. Firstly, the Unitary transformation (*cf.* Equation 1.4) is now given by a 2×2 matrix:

$$\psi(x_\mu)_L \rightarrow \psi(x_\mu)' = e^{-i\frac{g}{2}\rho(x_\mu)\cdot\tau}\psi(x_\mu) \tag{1.13}$$

where ρ is now an arbitrary 3-vector in weak isospin space, τ is the vector of Pauli spin matrices, ψ is a doublet of *left-handed* Dirac fermion fields, and $\frac{g}{2}$ gives the coupling strength in a form similar to the Q in the QED $U(1)$ transformation. To ensure local gauge invariance under the transformation given by Equation 1.13 *three* fields W_μ^1, W_μ^2 and W_μ^3 are introduced. The derivative ∂_μ is replaced by a more complex covariant derivative defined as

$$\mathcal{D}_\mu = \partial_\mu + i\frac{g}{2}\tau \cdot \mathbf{W}_\mu \tag{1.14}$$

where $\mathbf{W}_\mu$ is the vector of the three W^i fields. The free propagation of the W^i is given by

$$-\frac{1}{4}\mathbf{W}_{\mu\nu}\mathbf{W}^{\mu\nu} \tag{1.15}$$

where

$$\mathbf{W}_{\mu\nu} = \partial_\mu \mathbf{W}_\nu - \partial_\nu \mathbf{W}_\mu - g\,\mathbf{W}_\nu \times \mathbf{W}_\mu \tag{1.16}$$

The general form of this field strength tensor differs from that of Equation 1.9 in that there is an extra term $g\ \mathbf{W}_\nu \times \mathbf{W}_\mu$. This term arises from the *non-Abelian* algebra of $SU(2)$ and means that the kinetic term 1.15 carries trilinear and quartic self-interactions of the $\mathbf{W}$ fields. An EW Lagrangian can now be written as

$$\begin{aligned} \mathcal{L}_{EW} &= i\overline{\psi}\gamma_\mu\partial^\mu\psi \\ &- \overline{\psi}_L\gamma_\mu(\frac{g}{2}\tau.\mathbf{W}^\mu + \frac{g'}{2}y_L\mathbf{I}B^\mu)\psi_L \\ &- \overline{\psi}_R\gamma_\mu\frac{g'}{2}y_R B^\mu\psi_R \\ &- \frac{1}{4}\mathbf{W}^{\mu\nu}\mathbf{W}_{\mu\nu} - \frac{1}{4}B^{\mu\nu}B_{\mu\nu} \end{aligned} \tag{1.17}$$

Here, the fields and quantum numbers have been explicitly divided into left- and right-handed to illustrate the chiral asymmetry of the $SU(2)_L \otimes U(1)_Y$ group. It must be noted that the elements of the Lagrangian contain no mass terms for fermions or bosons. Furthermore, no mass terms can be introduced by hand while maintaining local gauge invariance. The mechanism for mass creation will be discussed in Section 1.2.5.

The physical gauge bosons are given by linear combinations of the B_μ and W^i_μ fields. The charged $W^\pm$ bosons are obtained from:

$$W^\pm_\mu = \frac{1}{\sqrt{2}}(W^1_\mu \mp iW^2_\mu) \tag{1.18}$$

Both the photon field, A_μ, and the Z^0 field Z_μ couple to fermions of both chiralities. They can be expressed as orthogonal linear combinations of the neutral fields B_μ and W^3_μ:

$$A_\mu = W^3_\mu \sin\theta_W + B_\mu \cos\theta_W \tag{1.19}$$

$$Z_\mu = W^3_\mu \cos\theta_W - B_\mu \sin\theta_W \tag{1.20}$$

where θ_W is the Weinberg weak mixing angle. Expressing the Lagrangian 1.17 in terms of the physical fields 1.18, 1.20, and 1.19, gives the relation between the couplings of the W^i_μ fields g, the coupling of the B_μ field $g^{'}$ and that of the photon, e:

$$g \sin\theta_W \;=\; g' \cos\theta_W \;=\; e \tag{1.21}$$

Like the W^i_μ and B_μ fields, these "physical" linear combinations remain massless. The procedure by which mass is introduced in the following section.

1.2.5 The Higgs Mechanism

The mechanism to give masses to the gauge bosons $W^\pm$ and Z^0 while retaining a massless photon and conserving local gauge invariance stems from the principle of **spontaneous symmetry breaking**. This principle is outlined for scalar one-dimensional fields, followed by its generalisation to $SU(2)$ local gauge symmetry.

Spontaneous symmetry breaking

Starting from the simple case of scalar particles described by a Lagrangian

$$\mathcal{L} \;=\; T \;-\; V \;=\; \frac{1}{2}\left(\partial_\mu \phi\right)^2 \;-\; \left(\frac{1}{2}\mu^2\phi^2 \;+\; \frac{1}{4}\lambda\phi^4\right) \tag{1.22}$$

where λ (> 0) is the coupling strength of the four-particle vertex and the interpretation of μ depends on its sign: a positive μ^2 would give the scalar field ϕ a mass μ. An negative μ^2 opens the possibility to break the $\phi \to -\phi$ symmetry of 1.22. The potential V, seen in Figure 1.1, has a double minimum at

$$\phi \;=\; \pm\,\nu \tag{1.23}$$

where ν, the vacuum expectation value, can be expressed in terms of μ and λ:

$$\nu \;=\; \sqrt{-\mu^2/\lambda} \tag{1.24}$$

Now we arbitrarily choose one of the two minima to calculate the field fluctuations about the ground state. From a choice of two equivalent minima we have settled for one, thus "breaking" the symmetry. There is no loss of generality in the procedure

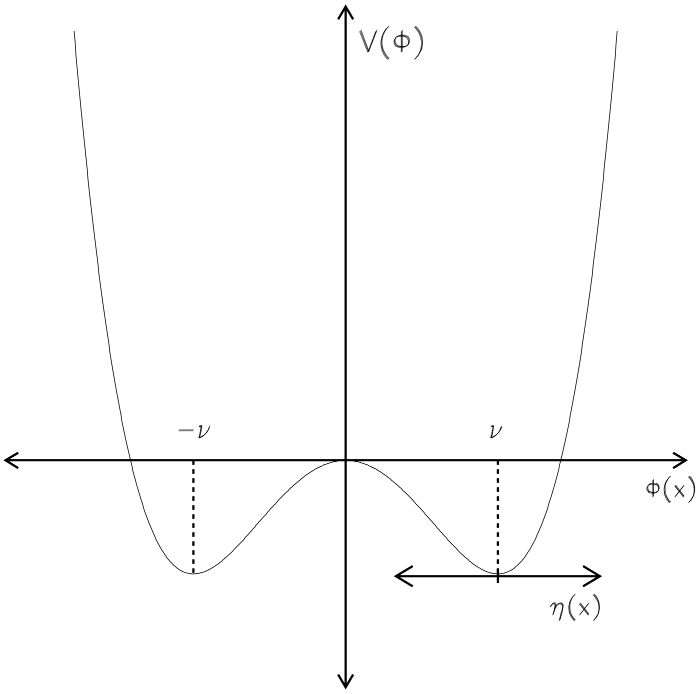

Figure 1.1: A $\frac{1}{2}\mu^2\phi^2 + \frac{1}{4}\lambda\phi^4$ potential for $\mu^2 < 0$. The potential has two minima at $\pm\nu$. The arbitrary choice of $+\nu$ to calculate the fluctuations about the ground state results in the "breaking" of the symmetry, which is now "hidden". In the generalisation to $SU(2)$ two complex scalar fields are used.

due to the symmetry of the Lagrangian. The choice of minimum is expressed as a simple transformation:

$$\phi(x) = \nu + \eta(x) \tag{1.25}$$

where η contains the fluctuations about ν. Substituting Equation 1.25 into the Lagrangian 1.22 yields

$$\overline{\mathcal{L}} = \frac{1}{2}(\partial_\mu \eta)^2 - \lambda\nu^2\eta^2 - \lambda\nu\eta^3 - \frac{1}{4}\lambda\eta^4 + constant \tag{1.26}$$

where the second term, $\lambda\nu^2\eta^2$, gives η a mass

$$m_\eta^2 = 2\lambda\nu^2 = -2\mu^2 \tag{1.27}$$

and the higher order terms are trilinear and quartic self-interactions. It must be stressed that the Lagrangians 1.22 and 1.26 are equivalent, however, the differences come about when perturbative theory is used, as an approximate solution, to calculate the fluctuations of the field about the minimum.

This principle can be easily generalised to local $SU(2)$ gauge symmetry. We start by defining a weak isospin doublet of complex scalar fields $\Phi(x)$. It has hypercharge $y = 1$, the upper component being positively charged and the lower one neutral. Expressing it in terms of real fields $\phi(x)_i$ gives:

$$\Phi(x) \;=\; \begin{pmatrix} \phi^+(x) \\ \phi^0(x) \end{pmatrix} \;=\; \frac{1}{\sqrt{2}} \begin{pmatrix} \phi_1(x) + i\phi_2(x) \\ \phi_3(x) + i\phi_4(x) \end{pmatrix} \tag{1.28}$$

These fields bring in extra terms to the $SU(2)$ Lagrangian:

$$\mathcal{L} \;=\; (D_\mu \Phi)^\dagger D^\mu \Phi \;-\; V(\Phi) \tag{1.29}$$

where D_μ is the covariant derivative 1.14 and

$$V(\Phi) \;=\; \mu^2 \Phi^\dagger \Phi \;+\; \lambda(\Phi^\dagger \Phi)^2 \tag{1.30}$$

with $\mu^2 < 0$ and $\lambda > 0$. This potential term is a complex equivalent of the potential V in Equation 1.22. Here, the minimum defines a complex circle:

$$\Phi^\dagger \Phi \;=\; \frac{1}{2}\left(\phi_1^2 \;+\; \phi_2^2 \;+\; \phi_3^2 \;+\; \phi_4^2\right) \;=\; -\frac{\mu^2}{2\lambda} \tag{1.31}$$

Now the symmetry is broken by the choice of a particular minimum about which to expand $\Phi(x)$ in terms of two new fields $\eta_1(x)$ and $\eta_2(x)$:

$$\Phi(x) \;=\; \frac{1}{\sqrt{2}} \begin{pmatrix} \phi_1(x) + i\phi_2(x) \\ \nu + \eta_1(x) + \eta_2(x) \end{pmatrix} \tag{1.32}$$

substituting 1.32 into 1.30 gives a potential

$$\begin{aligned} V \;&=\; \frac{mu^2}{s}\left(\phi_1^2 + \phi_2^2 + \eta_2^2 + (\nu + \eta_1)^2\right) && (1.33) \\ &\quad + \frac{\lambda}{4}\left(\phi_1^2 + \phi_2^2 + \eta_2^2 + (\nu + \eta_1)^2\right)^2 && (1.34) \\ &=\; \frac{-\mu^4}{4\lambda} \;+\; \lambda\nu^2\eta_1^2 \;+\; \lambda\nu\eta_1\left(\phi_1^2 + \phi_2^2 + \eta_1^2 + \eta_2^2\right) && (1.35) \\ &\quad + \frac{\lambda}{4}\left(\phi_1^2 + \phi_2^2 + \eta_1^2 + \eta_2^2\right)^2 && (1.36) \end{aligned}$$

This corresponds to a massive scalar particle η_1 with mass $\sqrt{2\lambda\nu^2}$ and three massless Goldstone bosons ϕ_1, ϕ_2 and η_2. We identify the massive scalar with the Higgs boson $h(x)$. The Goldstone bosons can be removed by applying a unitary gauge transformation to $\Phi(x)$ such that only the Higgs boson remains:

$$\Phi(x) \ \rightarrow \ U\Phi(x) \ = \ \frac{1}{\sqrt{2}} \begin{pmatrix} 0 \\ \nu \ + \ h(x) \end{pmatrix} \tag{1.37}$$

Applying the same transformation to the first term in Equation 1.29 gives the physical vector bosons $W^{\pm}$ and Z^0 their masses, while the photon remains massless:

$$M_W \ = \ \frac{g\nu}{2}, \ \ M_Z \ = \ \frac{\nu\sqrt{g^2 \ + \ g'^2}}{2}, \ \ M_\gamma \ = \ 0 \tag{1.38}$$

Using Equation 1.21 and eliminating ν gives the Born level relation between M_W and M_Z

$$M_W \ = \ M_Z \cos\theta_W \tag{1.39}$$

In this way, the three degrees of freedom related to the Goldstone bosons are given to the three physical vector bosons $W^{\pm}$ and Z^0, which, in becoming massive, get an extra degree of freedom in the form of a transverse polarisation state. The masses of the fermions come from the Lagrangian describing the interaction between the Higgs field and the fermion fields. Assuming the interaction to have a **Yukawa coupling** the Lagrangian can be expressed as

$$\mathcal{L}_{fH} \ = \ -g_f \left[(\overline{L}\Phi)R \ + \ \overline{R}(\Phi^\dagger L)\right] \tag{1.40}$$

$$= \ \frac{g_f}{\sqrt{2}} \left[\nu(\overline{f}_L f_R + \overline{f}_R f_L) \ + \ \overline{f}_L H f_R \ + \ \overline{f}_R H f_L\right] \tag{1.41}$$

where g_f if a dimensionless coupling constant. It is clear that the fermions have acquired a mass term

$$m_f \ = \ \frac{g_f \nu}{\sqrt{2}} \tag{1.42}$$

and that the coupling strength of fermions to the Higgs boson is given by m_f/ν.

1.3 The W boson

1.3.1 Introduction

In our current understanding, the W boson acts as the mediator of the weak force, responsible for nuclear β decay, μ, τ and decays of heavy quarks. Fermi's theoretical description of β decay was the first successful effort to explain the weak force.

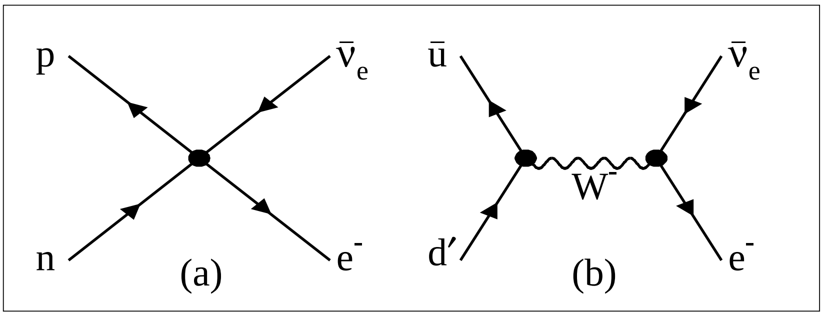

Figure 1.2: The Fermi four-point interaction **(a)** and the W mediated equivalent. The Fermi interaction is expressed in terms of nucleons n and p and not their constituent quarks for historical reasons.

However, fundamental problems within its formalism, as well as its inability to describe certain experimental observations, motivated the theoretical development which concluded in the current theory of electroweak interactions. This development is outlined below. The production and decay of W bosons is discussed, with emphasis on the case of W pairs in e^+e^- collisions at LEP2. The section is completed by a review of the importance of the measurement of $\mathrm{M_W}$ within the SM.

1.3.2 From Fermi's Theory to our Current Understanding

In Fermi's attempted theory of β radiation [16] the process $n \rightarrow pe^-\overline{\nu}_e$ is modelled as a four-point contact interaction, with matrix element of the form

$$\mathcal{M}_{fi} \sim G_F(\overline{\psi}_p\gamma_\mu\psi_n)(\overline{\psi}_e\gamma_\mu\psi_\nu) \tag{1.43}$$

where G_F is the Fermi coupling constant giving the strength of the interaction and the ψ_f are the Dirac fields for the proton (p), neutron (n), electron (e) and neutrino (ν). This point-like interaction is the product of the Dirac currents for the processes $n \rightarrow p$ and $\overline{\nu} \rightarrow e^-$ respectively. The Feynman diagram for this interaction can be seen in the left hand picture of Figure 1.2. However, this original matrix element does not allow for the parity violation observed experimentally in what was known as the $\theta - \tau$ puzzle. Introducing axial-vector terms allows for parity violation. The

$(1-\gamma_5)$ form chosen allows for maximal parity violation and for the chiral asymmetry observed in weak reactions:

$$\mathcal{M}_{fi} = \frac{G_F}{\sqrt{2}}(\overline{\psi}_p\gamma_\mu(1 - \gamma_5)\psi_n)(\overline{\psi}_e\gamma_\mu(1 - \gamma_5)\psi_\nu) \tag{1.44}$$

Although this matrix element now includes parity violation and chiral asymmetry, there remain fundamental problems. Firstly, the total cross section for tree-level $e^-\nu_e$ scattering diverges at high energies $\sqrt{s}$:

$$\sigma_{e+\overline{\nu}_e} = \frac{G_F^2 s}{\pi} \tag{1.45}$$

Viewed in terms of the partial waves this s dependence is a unitarity violation which means that the theory is non-renormalisable. Adding higher order diagrams to the process does not solve this problem. The first step is the inclusion of an intermediate vector boson to the matrix element. This boson must be massive in order to account for the short range of the weak force. The new matrix element is

$$\mathcal{M}_{fi} = \left[\frac{g}{\sqrt{2}}\overline{\psi}_u\gamma_\mu\frac{1}{2}(1 - \gamma_5)\psi_{d'}\right]\left[\frac{1}{M_W^2 - q^2}\right]\left[\frac{g}{\sqrt{2}}\overline{\psi}_e\gamma_\mu\frac{1}{2}(1 - \gamma_5)\psi_\nu\right] \tag{1.46}$$

where the Dirac fields for the neutron and proton have been replaced by those of the down (d') and up (u) quarks respectively. In the low energy regime the propagator tends to $\frac{1}{M_W^2}$. Comparison with Equation 1.44 gives the result

$$\frac{G_F}{\sqrt{2}} = \frac{g^2}{8M_W^2} \tag{1.47}$$

The inclusion of the massive propagator $(M_W^2 - q^2)^{-1}$ solves the unitarity problem in the $V - A$ theory at the tree level. The corresponding Feynman diagram can be seen on the right hand picture of Figure 1.2. However, when higher order diagrams are included unitarity is violated and the theory is non-renormalisable. These higher order divergences are cancelled by the inclusion of a massive neutral vector boson, the Z^0. The postulation of this boson led to the prediction of neutral currents, observed experimentally by the Gargamelle collaboration in 1973. The direct observation of the $W^\pm$ and Z^0 bosons by the UA1 [17] and UA2 [18] collaborations at CERN in 1983 proved the validity of the picture of electroweak interactions mediated by massive vector bosons.

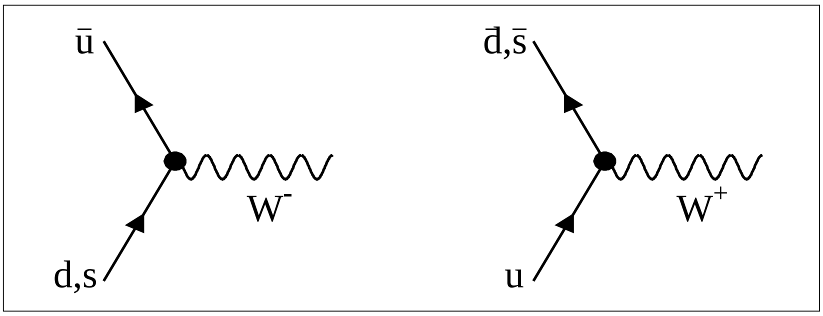

Figure 1.3: Production of single W^+ and W^- bosons via the Drell-Yan process in $p\overline{p}$ collisions.

1.3.3 W production and Decays

W production was first observed via the Drell-Yan process in $p\overline{p}$ collisions at the $Sp\overline{p}S$ at CERN. In this process, seen in Figure 1.3, valence quarks in the p and $\overline{p}$ combine to form the $W^{\pm}$ bosons. It has also been observed in e^+e^- colliders, where it is produced via the W radiation process seen in Figure 1.4 or as a t-channel intermediate boson in the $W^{\pm}e^{\mp}\nu_e$ processes seen in Figure 1.5. In LEP2 , pairs of W bosons are produced, to first order dominantly through the CC03 set comprised by t-channel neutrino exchange and s-channel Z^0 and γ exchange. These diagrams are shown in Figure 1.6, together with the s-channel Higgs boson exchange. The contribution from the latter is highly suppressed due to the small electron mass but it must be included to avoid unitarity problems at higher energies. Taking these three dominant (CC03) leading order contributions into account, the cross section for the production of W^+W^- pairs can be expressed in terms of each coherent contribution and their interference terms [19]:

$$\sigma_0(s, s_1, s_2) = \frac{g^4}{256\pi s^2 s_1 s_2}[a_{\gamma\gamma} + a_{ZZ} + a_{\gamma Z} + a_{\nu\nu} + a_{\nu Z} + a_{\nu\gamma}] \quad (1.48)$$

where s_1 and s_2 represent the energy scale of each W boson, and the a terms indicate the contribution of each of the CC03 Feynman diagrams squared: $a_{ZZ(\gamma\gamma)}$ is the s-channel Z^0 (γ) exchange, $a_{\nu\nu}$ corresponds to t-channel neutrino exchange, and the

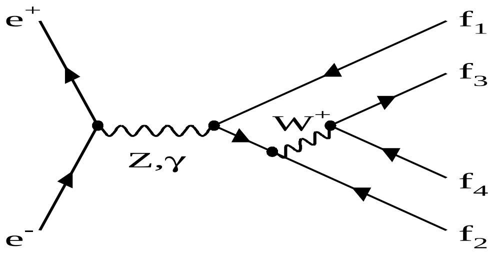

Figure 1.4: Feynman diagram for a singly-resonant W production process.

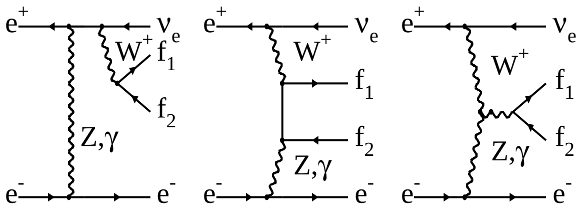

Figure 1.5: Feynman diagrams for t-channel exchange of W and neutral gauge bosons giving the "$We\nu$" final state

mixed terms symbolise the interference between pairs of diagrams. The full cross section depends on the available final states to which the W can decay, that is, on its width Γ_{W}, and can be expressed as a convolution of two Relativistic Breit-Wigners (RBW):

$$\sigma(s) \; = \; \int_0^s ds_1 \int_0^{(\sqrt{s}-\sqrt{s_1})^2} ds_2 \rho(s_1)\rho(s_2)\sigma_0(s,s_1,s_2) \tag{1.49}$$

where $\rho(s)$ is a RBW defined as

$$\rho(s) \; = \; \frac{\Gamma_W}{\pi M_W} \frac{s}{(s \; - \; M_W^2)^2 \; + \; s^2\Gamma_W^2/M_W^2}. \tag{1.50}$$

Here, the virtual propagator is expressed in terms of an s-dependent width, used to take into account higher order electroweak corrections in a similar way to the approach taken at LEP1 with the Z^0 boson [20]. The s-dependent width can be

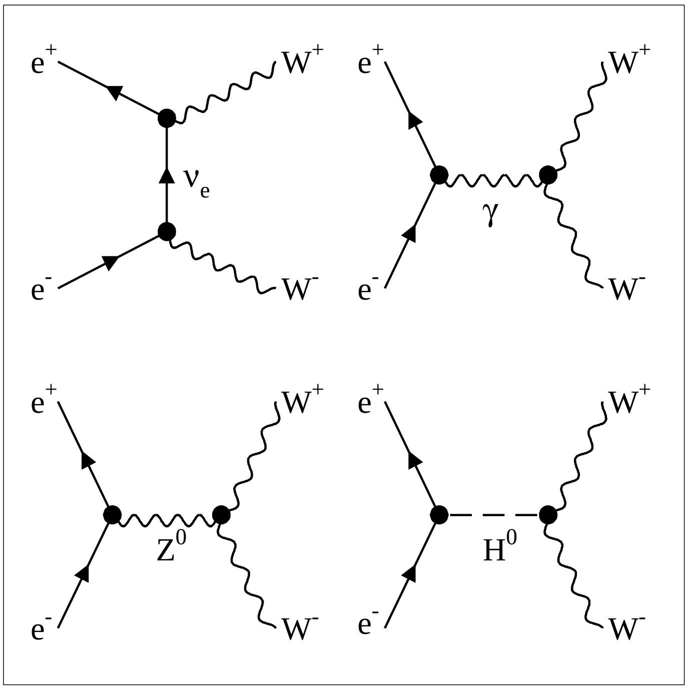

Figure 1.6: Leading order diagrams for the $e^+e^- \rightarrow W^+W^-$ process. The CC03 set, comprising t-channel neutrino exchange (top left), and s-channel γ and Z^0 exchange (top right and bottom left respectively), are shown together with the suppressed s-channel Higgs exchange.

expressed as:

$$\Gamma_W(s) = \frac{s\Gamma_W}{M_W}. \tag{1.51}$$

$\Gamma_{\rm W}$ for each decay channel can be calculated, ignoring QCD corrections and assuming massless fermions, using the matrix element from Fermi's Golden Rule:

$$\Gamma_{W^\pm \rightarrow f_i \bar{f}_j} = \frac{g^2 M_W}{48\pi}|V_{ij}|^2 C_f = \frac{G_F M_W^3}{6\pi\sqrt{2}}|V_{ij}|^2 C_f \tag{1.52}$$

where the second step results from using Equation 1.47, V_{ij} and C_f are one for leptonic decays, and represent the CKM matrix element for $q_i \rightarrow q_j$ and a color factor (= 3) respectively, in hadronic decays. Summing over all final states[3] and using the naive QCD correction we arrive at the familiar result

$$\Gamma_W = \frac{3G_F M_W^3}{2\pi\sqrt{2}}\left(1 + \frac{2\alpha_s(M_W^2)}{3\pi}\right) \tag{1.53}$$

---

[3] The production of top quarks is kinematically forbidden at LEP2 energies so the sum excludes all CKM matrix elements V_{qt}.

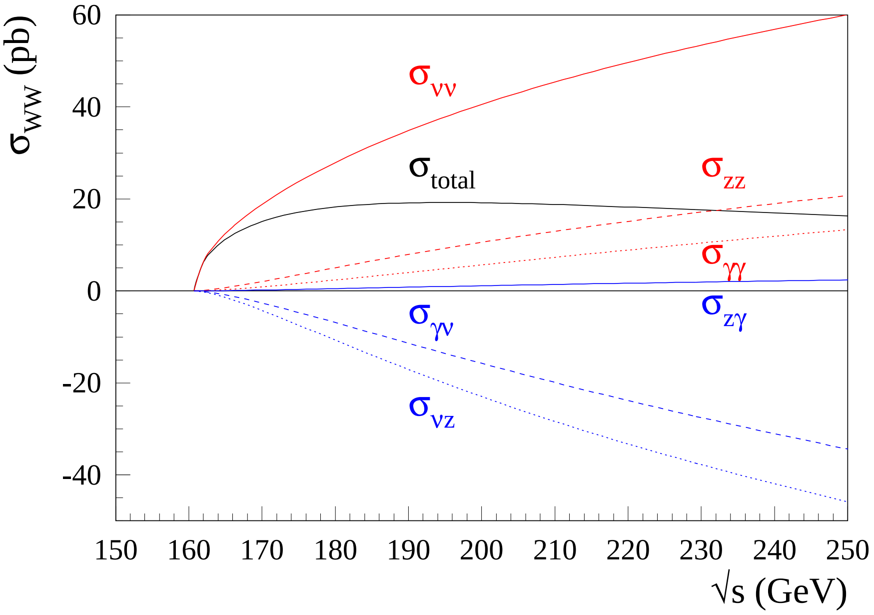

Figure 1.7: The $e^+e^- \rightarrow W^+W^-$ total cross section is shown at the Born level together with the six individual contributions from Equation 1.48.

where $\alpha_s(M_W^2)$ is the strong coupling constant evaluated at the mass of the W boson. The total Born level (on-shell) $e^+e^- \rightarrow W^+W^-$ cross section and its six constituent contributions from the CC03 set is shown in Figure 1.7. It can be seen that the negative interference terms $a_{\nu\gamma}$ and $a_{\nu Z}$ make the total cross-section non-divergent with $\sqrt{s}$. All cross sections are calculated using the analytical calculation program `GENTLE` [21]. An equivalent approach is to express the relativistic Breit Wigner in Equation 1.50 in terms of a fixed Γ_W propagator [19]:

$$\overline{\rho}(s) = \frac{1}{\pi}\frac{\overline{M}_W\overline{\Gamma}_W}{(s - \overline{M}_W^2)^2 + \overline{M}_W^2\overline{\Gamma}_W^2} \qquad (1.54)$$

where the *equivalent* mass and width are related to those in Equation 1.51 by:

$$\overline{M}_W = M_W - \frac{\Gamma_W^2}{2M_W} = M_W - 26.9\ MeV \qquad (1.55)$$

and

$$\overline{\Gamma}_W = \Gamma_W - \frac{\Gamma_W^3}{2M_W^2} = \Gamma_W - 0.7\ MeV \qquad (1.56)$$

This is of particular importance to the analysis presented here because it is the approach taken in the `EXCALIBUR` [22] four-fermion Monte Carlo event generator, used here both for the generation of signal and four-fermion background events and for the calculation of the matrix elements used for the reweighting method outlined in Chapter 5. However, a re-definition of $\mathrm{M_W}$ and Γ_W in the generator is performed to ensure that the physics is equivalent to the running width parametrisation. Therefore the results obtained with this analysis do not have to be corrected according to Equations 1.55 and 1.56.

Besides the inclusion of a finite W width Γ_W into the Relativistic Breit Wigner further corrections are required in order to correctly model the production of W^+W^- pairs with the required accuracy. These are higher order electroweak and QCD corrections. The electroweak part traditionally [19, 23] has been separated into

- *non-QED* EW corrections like massive fermion and vector boson loops in the $W^\pm$ and Z^0 propagators.
- Coulomb Correction: the virtual photon exchange between W bosons. Its effect falls with $\sqrt{s}$ as the W bosons become boosted with respect to each other.
- Initial state radiation (ISR), whose effect is to reduce the effective centre of mass energy ($\sqrt{s'}$), reducing the cross section.

This is the approach taken in the `GENTLE` analytical calculation program, used to produce Figure 1.8, which shows the W^+W^- cross section as a function of centre of mass energy with different corrections applied. All these corrections are discussed in detail in [19, 23]. However, in recent times there has been considerable progress in estimating the effect of higher order EW corrections as a whole with a series of more sophisticated calculations now available. Notably, `RacoonWW` [24] contains full one loop calculation to $\mathcal{O}(\alpha)$, plus real and non-factorisable virtual photon corrections. `YFSWW` has the leading corrections to higher order. The best current calculation of the CC03 cross section using the double-pole approximation for radiative corrections, obtained with the program `RacoonWW`, is between 2.5 and 3% lower than that

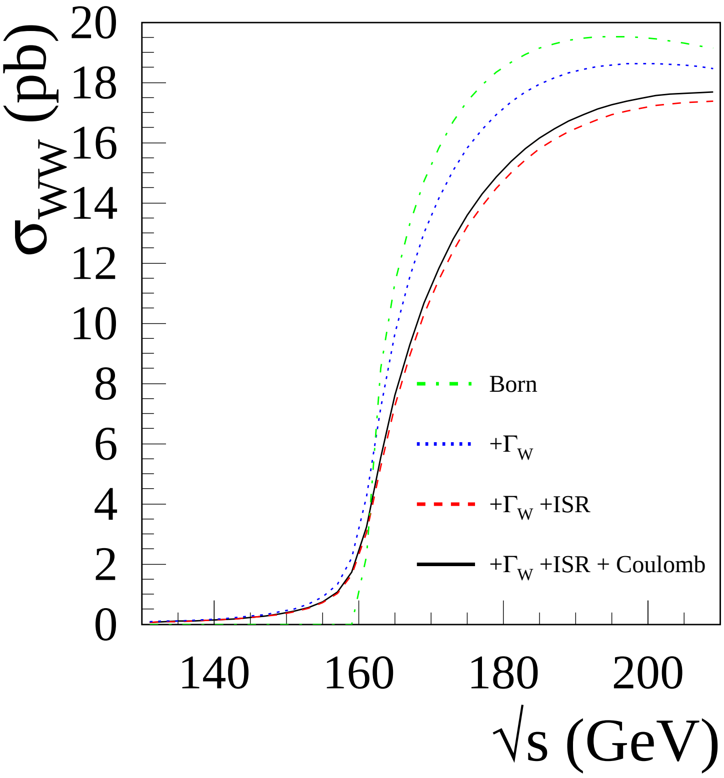

Figure 1.8: The $e^+e^- \rightarrow W^+W^-$ cross section is shown in different approximations: the Born on-shell ($\Gamma_W = 0$), Born off-shell, Born off-shell with Coulomb correction, and Born off-shell with Coulomb approximation and initial state radiation.

obtained with `GENTLE` [4]. This agrees with the calculations obtained with `YFSWW`. A detailed discussion of the new developments, including `RacoonWW` and `YFSWW`, and their numerical consequences can be found in [26] and references therein. The impact of this change in the theoretical predictions on W measurements will have to be assessed in the future.

Another important effect to take into account is the presence of diagrams which do not belong to the CC03 set but result in the same type of final states. These may be singly- or doubly-resonant charged current or neutral current processes. Since this thesis is only concerned with final events with a lepton, a neutrino and two quarks in

---

[4] However, it must be pointed out that semi-analytic calculations contemporary to `GENTLE`, like `WPHACT` and `WTO` gave results closer to the ones from DPA [25].

the final state, the only non-CC03 contribution comes from singly-resonant charged current diagrams like those responsible for W production in e^+e^- colliders in the pre-LEP2 era and which can be seen in Figures 1.4 and 1.5. Besides adding to the total cross section events with different topologies and $\mathrm{M_W}$ information, thereby distorting the BW shape of the mass distributions, these diagrams interfere with the CC03 set. These effects are particularly important for the $e\nu_e q\overline{q}$ final state, which has the largest non-CC03 contribution due to the $W^{\pm}e^{\mp}\nu$ set of diagrams, where the $e^{\mp}\nu$ system is non-resonant. The effect, found to be of the order of 50MeV at $\sqrt{s} = 172$GeV [4, 27], is largest near threshold but decreases with $\sqrt{s}$. To take all these effects into account events are generated using the full tree-level set of diagrams contributing to $l\nu q\overline{q}$ final states, thereby taking all contributions and interference terms into account. This is done using `EXCALIBUR`. Therefore, a "signal" event is now defined in terms of its final state and not its intermediate boson exchange process.

1.4 Importance of $\mathrm{M_W}$ in the Standard Model

A precise measurement of the W boson mass will provide a powerful constraint to the standard model. With our precise knowledge of parameters like the Fermi constant G_F, the weak mixing angle $sin^2\theta_W$, the fine structure constant $\alpha_{QED}(Q^2)$, and mass and width of the Z^0 boson, M_Z and Γ_Z, tight constraints are already placed on $\mathrm{M_W}$. Thus, its measurement can serve as a test of the internal consistency of the SM and provide constraints to unobserved particles, namely the Higgs boson. Starting with Equation 1.47 and using Equation 1.21 together with the $e = \sqrt{4\pi\alpha}$ we get the following relation between the Fermi constant, the weak mixing angle, the fine structure constant and $\mathrm{M_W}$

$$M_W^2 = \frac{\pi\alpha}{\sqrt{2}G_F sin^2\theta_W}\frac{1}{1 - \Delta r} \tag{1.57}$$

where Δr represents the contributions from higher order corrections from fermion and boson loops such as those in Figure 1.9. These loops are dependent on the masses of the **top** quark and the Higgs particle (m_t and M_H respectively) and that of any non-SM massive particle. Explicitly, the electroweak corrections depend on

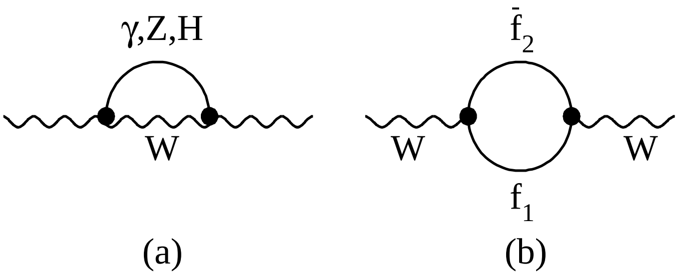

Figure 1.9: Feynman diagrams showing boson and fermion loop corrections to the W self-energy. These diagrams (predominantly those including top quarks and Higgs bosons) dominate the SM radiative Δr in Equation 1.57. Additional diagrams including massive non-SM particles can be probed with the measurement of M_W.

m_t^2 and $ln(m_h)$ [1]. It is through these corrections that the masses of the top , Higgs and M_W are related and constrained within the SM. Experimental knowledge of m_t and M_W can tightly constrain the mass of the hitherto unseen standard model Higgs, while a comparison between the directly measured value of M_W and the high precision indirect results from LEP1 and SLD can test the validity of the standard model. Furthermore, the presence of non-SM particles coupling to the W could add loop diagrams to those in Figure 1.9, potentially affecting the magnitude of Δr. Thus M_W can be used as a probe of new physics.

1.5 The Γ_W Measurement

The W width expression shown in Equation 1.53 gives a direct correspondence between M_W and Γ_W , albeit one which depends on the SM and which includes approximations to electroweak and QCD corrections. In this analysis the SM relation is assumed, together with its branching ratios. Γ_W is extracted from the invariant mass distribution of the W decay particles and not by a measurement of its individual cross sections. Hence, the measurement is performed in order to check the validity of 1.53 and the assumptions and approximations made to derive it.

Chapter 2

The LEP Accelerator and the LEP Beam Energy Measurement

2.1 Introduction

In this chapter the Lep accelerator will be described. Emphasis will be placed on the Lep beam energy calibration, in particular on the Lep Spectrometer, given its importance as a source of uncertainty in the measurement of the W mass.

2.2 The Accelerator

The Large Electron–Positron collider (Lep) is an e^+e^- collider located on the French-Swiss border at the European Laboratory for Particle Physics (known by its French acronym CERN) on the outskirts of Geneva, as shown in Figure 2.1. Its main ring has a circumference of 26.7 km making it the world's largest collider. Built on a stable layer of rock at an average depth of 100m below the surface, it comprises a series of alternated straight sections and arcs. The arcs contain some 3300 dipole magnets to bend the beams, quadrupole and sextupole magnets for focusing, and dedicated dipoles for correcting the horizontal and vertical position of the beams. The eight straight sections contain the Interaction Points (IPs) where the paths of the e^+, e^- beams traveling in opposite directions meet. In the four straight sections, where the multi-purpose detectors ALEPH, DELPHI, L3 and OPAL (ADLO) are situated, the beams are made to collide at the IPs. Otherwise they are steered away from each other at crossover to avoid unnecessary loss of beam current. In addition to the four detectors, the straight segments contain the RF cavities which restore the energy lost by the beams to synchrotron radiation. The reason for placing the detectors in the straight sections is to protect them from this synchrotron radiation. Before discussing the beam acceleration process in the main ring any further, the beam pre-acceleration and injection chain will be outlined.

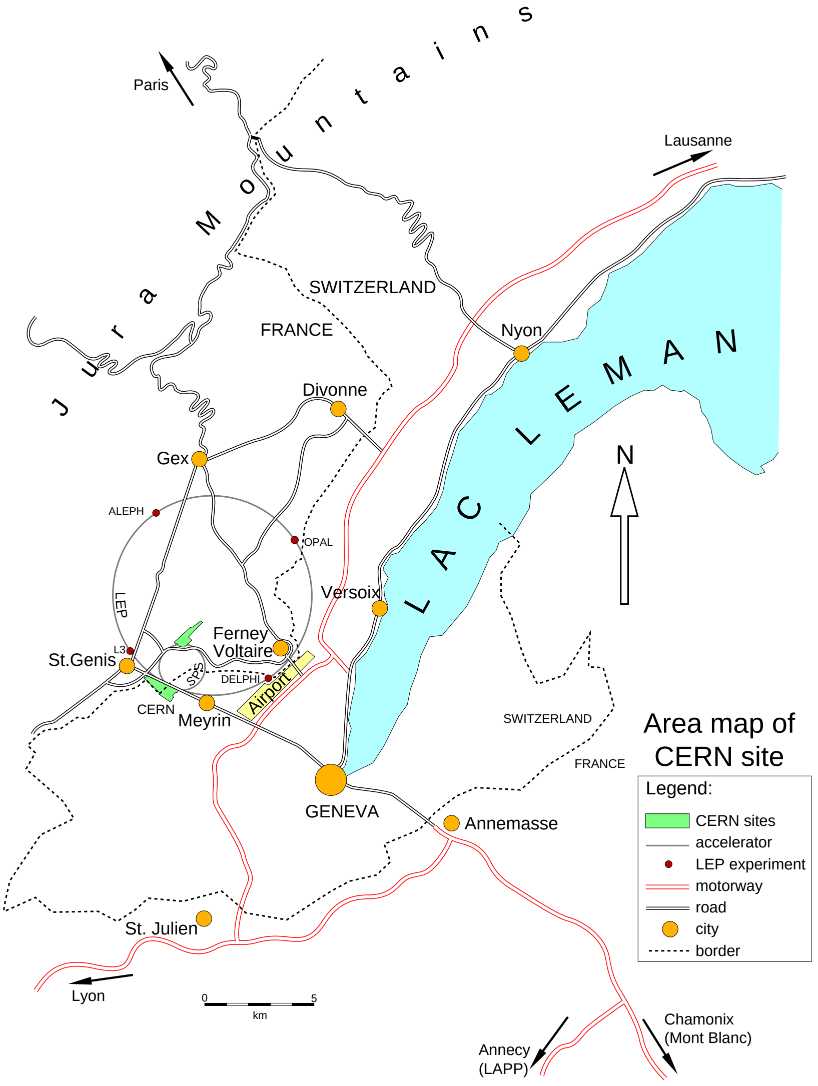

Figure 2.1: The location of the CERN laboratory and the LEP accelerator.

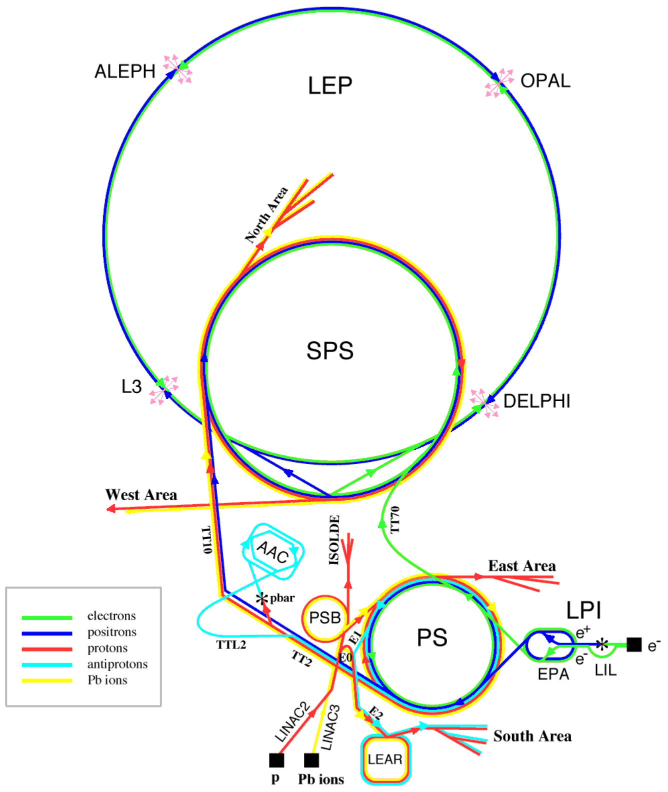

EPA - Electron Positron Accumulator
LEP - Large Electron Positron collider
LIL - LEP Injector Linac
LPI - LEP Pre-Injector
PS - Proton Synchrotron
SPS - Super Proton Synchrotron

Figure 2.2: A diagram of LEP with the pre–accelerators and injection system. The acronyms used for the accelerators which make up the LEP system are given. The other particle accelerators at CERN are also shown. This diagram is not to scale.

2.3 The e^+e^- Injection Chain

A schematic of the acceleration and injection chain into the LEP ring is shown in Figure 2.2. The process involves many accelerators which were already in existence before LEP. The injection and acceleration process can be summarised as follows:

- Electrons from a high intensity source are accelerated to an energy of 200 MeV by the LEP Injection LINAC (LIL). This electron beam is made to hit a tungsten target to produce positrons.

- A lower intensity source produces electrons. Both electrons and positrons are accelerated by the LIL to an energy of 600 MeV.

Year	Copper Cavities	Superconducting Cavities	E_{BEAM} (GeV)	$\int \mathcal{L}dt$ (pb^{-1})
1995	120	56	70.1	6.9
1996	120	170	86.2	23.4
1997	86	240	92.0	71.0
1998	48	272	94.4	181.9
1999	48	288	95.8	29.1
			97.8	85.4
			99.8	91.1
			100.8	44.0

Table 2.1: The RF cavity configuration of LEP (at the end of each year), the maximum E_{BEAM} and the integrated luminosity delivered to DELPHI in 1995 to 1999

- Both beams are stored in the Electron Positron Accumulator (EPA) until their currents are large enough.
- The beams are injected into the Proton Synchrotron (PS) and accelerated until they reach an energy of 3.5 GeV.
- The beams are moved into the Super Proton Synchrotron (SPS)and accelerated to an energy of 20 to 22 GeV. They are then injected into the main LEP accelerator.
- In the main accelerator the beams are ramped up in steps to nominal physics energy. During ramping the beams are deflected by electrostatic separators at the IPs in order to keep them from colliding.

After the acceleration cycle the beams are kept colliding at physics energy until they are lost or until the beam current is too low, in which case they are dumped and the cycle re-started.

2.4 The RF System

The increases in RF power in LEP have been have been driven by the objective to run at higher and higher centre of mass energies. Whereas during LEP1 operation 120 copper RF cavities with an accelerating field of 1.5 MVm^{-1} were sufficient, running at LEP2 energies has required a radical upgrade of the RF system, with the replacement of most Cu cavities by superconducting Nb-Cu and Nb ones with a maximum accelerating field of 7 MVm^{-1}, as detailed in Table 2.1. The main reason for such a significant increase in RF power is that the energy loss due to synchrotron radiation of a beam of energy E_{BEAM} following a curve of radius ρ is proportional to E^4_{BEAM}/ρ. So while the energy loss per turn in LEP1 was typically 0.13 GeV for an E_{BEAM} of 45 GeV, for an E_{BEAM} of 100 GeV it is $\sim$ 3 GeV. The increase in available accelerating potential and further improvements to the reliability of the accelerator allowed for stable running with beam energies of $\sim$ 94.3 GeV and up to $\sim$ 101 GeV in 1998 and 1999 respectively[1]. Furthermore, the integrated luminosities for these two running periods exceeded the anticipated values [28, 29].

2.5 Luminosity

The instantaneous luminosity, $\mathcal{L}$, of an accelerator is given, to a good approximation, by

$$\mathcal{L} = \frac{n_b I_b^2}{4\pi e^2 f \sigma_x \sigma_y}, \tag{2.1}$$

where n_b is the number of bunches per beam, I_b is the bunch current, e is the charge of the electron, f is the LEP revolution frequency (10.8 kHz) and σ_x and σ_y are the horizontal and vertical beam widths respectively. In 1998 and 1999 LEP ran in 4-bunch mode achieving instantaneous luminosities of $\sim 10^{32}$ $\mathrm{cm}^{-2}\mathrm{s}^{-1}$, close to a factor of 5 higher than at LEP1. This increase was driven by a reduction of the beam widths σ_x and σ_y and by an increase in the bunch current I_b. Typical values for these parameters during the 1998 and 1999 running periods were σ_x $\sim$170μm ($\sim$0.7 of LEP1 value), σ_x $\sim$3.5μm ($\sim$0.25 of LEP1 value), and I_b $\sim$800μm ($\sim$1.3 of LEP1 value). In order to control the beam width, a series of superconducting quadrupole magnets are used to tightly focus the beam. A further enhancement can be achieved by using the electrostatic beam deflectors. The improvements in focusing and bunch current are detailed in [30, 31, 28]. The integrated luminosities, $\int \mathcal{L}dt$, delivered to DELPHI between 1995 and 1999 are shown in Table 2.1.

---

[1] In 1999 LEP ran with stable luminosity conditions at four nominal energy points with beam energies of 96, 98, 100 and 101 GeV.

2.6 Energy Calibration

The LEP beam energy contributes directly to the overall uncertainty of the measurement of $\mathrm{M_W}$ due to the use of constrained kinematic fits to extract event by event observables, like the fitted invariant mass m_w. The contribution goes, to a good approximation, as:

$$\frac{\Delta \mathrm{M_W}}{\mathrm{M_W}} \approx \frac{\Delta E_{\mathrm{BEAM}}}{E_{\mathrm{BEAM}}}. \tag{2.2}$$

With an integrated luminosity of $\sim 700\mathrm{pb}^{-1}$ collected per experiment by the end of the LEP2 programme, the statistical uncertainty on $\mathrm{M_W}$ will be close to 21 MeV. To meet the target total uncertainty on $\mathrm{M_W}$ of $\sim$ 35 MeV the uncertainty on the beam energy must be controlled to $\Delta E_{\mathrm{BEAM}}/E_{\mathrm{BEAM}} \approx 10^{-4}$. During LEP1 the precision on E_{BEAM} was controlled to 2×10^{-5} [32]. Such precision is currently not possible at LEP2 for reasons that will be explained below, and new methods have been developed and implemented in the quest to reach the required sensitivity. First the salient points of the current energy calibration method will be outlined, and then some improvements will be discussed.

2.6.1 Resonant Depolarisation

At LEP1 the beam energy was measured to great precision using resonant depolarisation (RDP) [32]. This technique exploits the fact that the $e^{\pm}$ beams develop appreciable transverse polarisation due to the emission of synchrotron radiation as their trajectory changes in the magnetic field of the dipoles. The spin vectors precess about the field lines of the dipoles with a frequency given by:

$$f_p = f_{\mathrm{LEP}} \frac{(g_e - 2)}{2} \frac{E_{\mathrm{BEAM}}}{m_e c^2}, \tag{2.3}$$

where $(g_e - 2)/2$ is the anomalous magnetic moment of the electron, m_e is the mass of the electron and c is the speed of light, all known to great accuracy, and f_{LEP} is the LEP revolution frequency. The number of spin precessions per revolution around LEP is the *spin tune*, given by:

$$\nu_p = \frac{f_p}{f_{\mathrm{LEP}}}. \tag{2.4}$$

It is ν_p that is probed experimentally through RDP. By applying a transverse sinusoidal magnetic field of frequency f_{RDP} to the beam the polarisation can be destroyed. As the beam only passes through the depolarising region once per revolution of LEP, the condition for this depolarisation is that f_{RDP} divided by f_{LEP} match the non-integer part of ν_p. The integral part must be calculated by the use of flux loop and nuclear magnetic resonance (NMR) measurements, which are described in the following section. The measurement of the beam polarisation is performed with the LEP polarimeter apparatus [33]. It is a device which brings a circularly polarised laser beam into interaction with the electron and positron beams. The rate of Compton backscattered photons is monitored by a calorimeter as a function of the vertical direction for right and left handed laser beams. The asymmetry in the distributions is sensitive to the degree of transverse polarisation in the electron beam.

Using RDP, E_{BEAM} was determined to 1 part in 10^5 at LEP1 , greatly increasing the sensitivity of the high precision measurements carried out at the Z^0 resonance. Unfortunately the RDP technique is not applicable at LEP2 energies due to incoherent depolarisation effects caused by machine imperfections and which increase rapidly with beam energy. The result is that the $\sim$ 5% level of polarisation necessary for a reliable energy measurement has not been observed at beam energies beyond 61 GeV. Therefore the current strategy relies on NMR magnetic measurements and extrapolation.

2.6.2 The Extrapolation Method

Since E_{BEAM} is proportional to the magnetic field B integrated along the beam's trajectory l around LEP:

$$E_{\text{BEAM}} = \frac{e}{2\pi c} \oint_{\text{LEP}} B \cdot dl. \tag{2.5}$$

the beam energy can in principle be measured from estimates of $\oint_{\text{LEP}} B \cdot dl$. The integrated bending field is estimated from continuous measurements of the local magnetic fields by 16 NMR probes placed in some of the 3300 LEP main dipole magnets. The probes can measure the local field with a relative precision of $\sim 10^{-6}$

and can provide reliable measurements down to 40 GeV, although this minimum locking energy increases with radiation damage. For this reason probes have to be replaced through the year, but great care is taken to position them with accuracy in order not to be affected by variations in the local field in the vicinity of the probe. Even though the probes only sample a minute fraction of the total bending field, its relation to E_{BEAM} can be calibrated with great precision at low energies against measurements from RDP. Assuming a linear dependence of the local B field on the mean E_{BEAM}, each probe i is calibrated using:

$$E^{RDP}_{NMR\ i} = a_i B_{NMR\ i} + b_i, \tag{2.6}$$

during dedicated multi-point RDP fills, where the same beam is ramped to a set of nominal energies ranging from 41 to 61 GeV and RDP performed where possible. A fit to all available RDP energy points is made, regardless of the fill the data were taken in. In practice other time-dependent effects that affect the relation between the dipole field and the beam energy, such as the C corrections shown in Equation 2.7, are taken into account in the calibration 2.6, thereby normalising the calibration to a given set of conditions.

The beam energy model

Since the NMR probes only give a measurement of the contribution to the total bending field due to the main dipoles, all other effects that may contribute to $\oint B_{\mathrm{LEP}} \cdot dl$, as well as time-dependent effects which may alter the relation between $E_{\mathrm{BEAM}}(RDP)$ and each B_{NMR}, have to be taken into account separately and put into what is known as the *beam energy model* [32, 34], which gives the average beam energy around the accelerator as a function of time, $E_{\mathrm{BEAM}}(t)$. For LEP2, the model can be expressed as[2]:

$$\begin{aligned} E_{\mathrm{BEAM}}(t) &= (E_{\mathrm{initial}} + \Delta E_{\mathrm{dipole}}(t)) \\ &\quad \cdot(1 + C_{\mathrm{tide}}(t)) \cdot (1 + C_{\mathrm{orbit}}(fill)) \\ &\quad \cdot(1 + C_{\mathrm{h.corr.}}(t)) \cdot (1 + C_{\mathrm{QFQD}}(t)) \end{aligned} \tag{2.7}$$

---

[2] The beam energy model at LEP1 differed from Equation 2.7 in some aspects. The normalisation was treated differently because magnetic extrapolation was not necessary at the Z^0. Furthermore, the correction $\Delta E_{\mathrm{dipole}}(t)$ was implemented differently because of more sparse magnetic sampling.

where E_{initial} is the energy averaged from the $E^{RDP}_{NMR\ i}$, extracted from Equation 2.6, of each probe at the time when the dipole magnets have reached operating conditions. Here, equal weight is given to each probe in the average since each magnet behaves differently during LEP ramping. $\Delta E_{\text{dipole}}(t)$ gives the shift in energy due to changes in the bending field of the dipoles during a fill. These changes, due to temperature variations[3] and excitation of parasitic currents in the beam pipe, are considered to be traced by the calibrated NMRs and so are also calculated from a mean of the $E^{RDP}_{NMR\ i}$, this time with equal weight given to each of the octants, since these effects vary octant by octant [32]. The remaining terms in Equation 2.7 correct for other time-dependent effects:

$C_{\text{tide}}(t)$: The earth tides distort the shape of the LEP ring, effectively moving the quadrupole magnets with respect to the beam orbit. Beams passing off-centre through the quadrupoles sample more of the dipole component of the quadrupole field.

C_{orbit}: This term corrects for longer time scale horizontal drifts of the beam orbit and is evaluated for each fill.

$C_{\text{RF}}(t)$: This accounts for the changes in RF frequency during a fill which are made to optimise luminosity and to respond to RF trips.

$C_{\text{h.corr.}}(t)$: This term takes into account the extra bending field provided by the horizontal orbit corrector magnets which are used to steer the beam.

$C_{\text{QFQD}}(t)$: This accounts for the stray fields caused by the difference in the excitation currents used for focusing and defocusing quadrupole magnets in LEP.

All the above corrections are explained in detail in [32, 35, 36]. They apply to the measurement of the mean beam energy around the LEP. The evaluation of E_{BEAM} at any given point in the accelerator takes into account factors that give deviations from the mean beam energy as a function of the position along the circumference of LEP.

---

[3] The difference in the temperature coefficients in the core of the magnet and in the fringe field mean that there is a real change in $\Delta E_{\text{dipole}}(t)$ which is not traceable by the NMR probes. To give an idea of the magnitude of the effect, the LEP spectrometer magnet was found to have an effective temperature coefficient of $\sim 10^{-5} K^{-1}$ (see section 2.7.5)

The main factor behind these asymmetries is the uneven distribution of RF power around LEP. This is of particular importance to the spectrometer energy calibration, since it measures the centre of mass energy locally. The RF model [32, 34] provides the energy corrections and associated errors necessary to evaluate the beam energy of the electron and positron beams at each of the IPs. Conversely, it can be used to infer the average beam energy around LEP from a local measurement, like that provided by the spectrometer.

Testing the NMR calibration with the flux loop

In the RDP energy range, the relation between NMR values and E_{BEAM} is linear to a good approximation. The assumption is made that this linearity holds up to physics energies and the NMR values then play the leading role in the determination of E_{BEAM} values. This assumption can be checked against an independent measurement of the field integral. Each of the LEP main dipoles is fitted with a flux loop. The flux loops (FLs) can provide a measurement of $\sim$ 98% of the field of each of the 3300 main bending dipoles and $\sim$ 96% of the total bending field of the accelerator. They exclude the fringe fields of the main dipoles and the bending field from the weak dipoles placed at the ends of the arcs, and any bending field contribution provided by quadrupoles, sextupoles and dipole orbit correcting magnets.

The change in flux through the loops is measured during dedicated cycles where the magnets are ramped up through a series of nominal energy points including the RDP region and going up to physics energies. At each energy the cycle is paused for the NMR probes to lock and average values of their readings calculated. The linear extrapolation assumption can then be checked by fitting the NMR values in the RDP region to the 96.5% of the total bending field provided by the flux loops according to Equation 2.5, in a manner similar to 2.6:

$$E_{NMR\ i}(FL) = c_i B_{NMR\ i} + d_i. \tag{2.8}$$

Here, the flux loop reading has been represented as an energy by way of analogy with Equation 2.6. Then the prediction of the total field from the NMRs at physics energies can be compared to that given by the flux loop. The discrepancy between

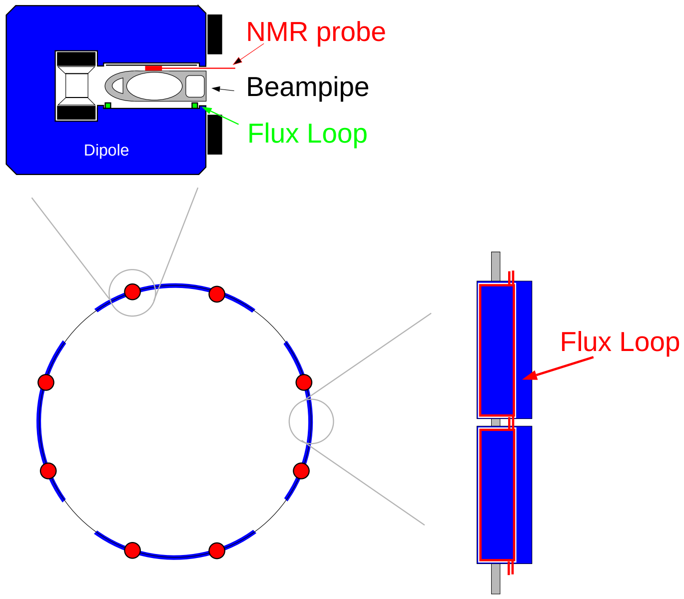

Figure 2.3: A schematic of the positioning of flux loops and NMR probes on a LEP main dipole.

the NMR and flux loop measurements, which can be seen for the 1999 data in Figure 2.4, lead to the dominant error on E_{BEAM} of 15 MeV in 1998 and 1999[4].

Since the uncertainty in the extrapolation, currently given by the flux loop experiments, is the dominant contribution to the total error on E_{BEAM}, alternative methods have been developed to perform independent measurements of E_{BEAM} at physics energies with a view towards improving the confidence in the extrapolation and thereby ensuring a total relative error of the order of 10^{-4}. Two such methods, the synchrotron tune Q_s and the LEP spectrometer, shall be described in the following sections, with emphasis placed on the latter. A third method, based on the reconstruction of the effective centre of mass energy from the three-body kinematics of the radiative two fermion $e^+e^- \to f\overline{f}\gamma$ process, can be performed by the individual experiments. For details of this method the reader is referred to [37, 38] and references therein.

---

[4] This is the dominant contribution to an error of 20 and 21 MeV in 1998 and 1999 respectively.

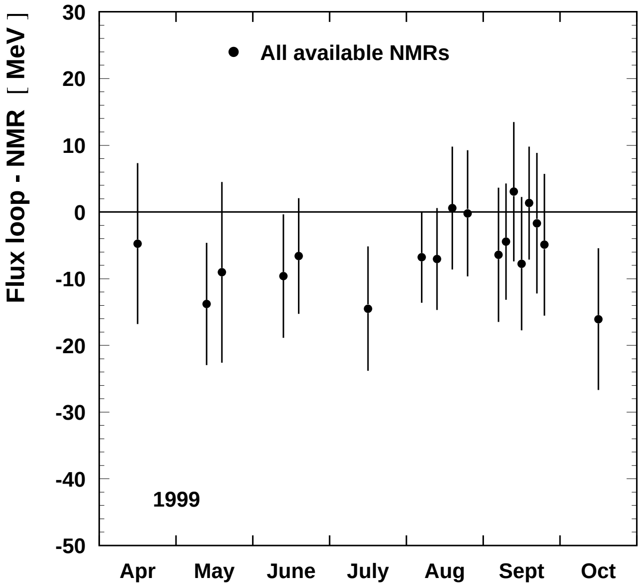

Figure 2.4: Residual difference between Flux Loop and NMR predictions of $\int B \cdot dl$ expressed as E_{BEAM}. Both methods are cross-calibrated in the RDP range and the results in the physics energy range compared. The plot shows the data taken in 1999.

2.7 The LEP Spectrometer

2.7.1 Introduction

The purpose of the LEP Spectrometer is to provide a direct measurement of E_{BEAM} at the $\mathrm{M_W}$ scale by measuring the local beam energy through:

$$E_{\mathrm{Spect}} = \frac{1}{\theta} \int B \cdot dl_{\mathrm{Spect}}, \tag{2.9}$$

where E_{Spect} now refers to the *local* beam energy as the beam traverses a bending field $\int B \cdot dl_{\mathrm{Spect}}$ and is deflected by an angle θ. The basic principle behind the spectrometer concept is shown in Figure 2.5. The spectrometer is integrated into the LEP magnet lattice. Two of the 3300 concrete LEP dipole magnets were replaced with a high precision steel dipole with twice the bending field, such that the beam deflection angle θ is fixed within the allowable variations of the beam orbit, while the integrated bending field $\int B \cdot dl_{\mathrm{Spect}}$ varies with the rest of the LEP dipoles as E_{BEAM} changes. Compared to the concrete core magnets, the steel one produces a field more uniform with respect to time and position, has a lower temperature

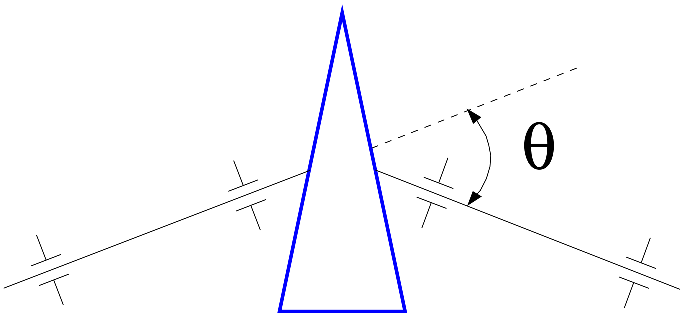

Figure 2.5: The spectrometer measures the beam deflection θ and the integrated bending field $\int B \cdot dl_{\mathrm{Spect}}$ of a dipole magnet in order to provide a measurement of the local beam energy.

coefficient, and does not have the long term drifts in field due to ageing which have been observed in the standard LEP dipoles. The general layout of the spectrometer is outlined below. There follows a section on the strategy used to measure E_{BEAM} with the spectrometer. The details of the measurements of the beam deflection and integrated bending field are given in Sections 2.7.4 and 2.7.5.

2.7.2 Layout

The LEP Spectrometer can be divided into beam bending and monitoring apparatus. A schematic of the layout is given in Figure 2.6. The bending apparatus consists of a 5.75m long C-shaped laminated steel dipole magnet. It is equipped with a water cooling system in order to maintain the temperature constant to within 1^{o}C, probes monitoring the temperature in different sections of the magnet, and four NMR probes placed in its core to monitor the changes in local fields in the magnet. Two types of NMR probes are used. These are referred to as “Range Type 1” and “Range Type 2” and they cover different ranges of magnetic field. There are two of each type mounted in the core of the magnet. Type 1 probes saturate at magnetic fields corresponding to nominal energies beyond $\sim$ 60 GeV, while type 2 probes are operational from $\sim$ 40 GeV upwards. However, with radiation damage, their locking threshold rises so the two types are necessary to ensure that readings are available for the full energy range under normal LEP running conditions. The integrated bending field of the magnet, $\int B \cdot dl_{\mathrm{Spect}}$, can be inferred from the local fields measured by the four NMR probes and other environmental variables, like the temperature of different parts of the magnet. The author developed the algorithms and software used for this purpose. The end fields and stray fields from the steel dipole and other magnets in the lattice are suppressed by a mu-metal shield which surrounds the beam pipe at either end of the magnet.

The beam monitoring apparatus consists of two arms of beam position monitors (BPMs). Each arm has three BPMs and is equipped with stretched wire position monitors, synchrotron radiation copper absorber blocks, temperature probes and a water cooling system. The BPMs are ~4m apart, giving a lever arm of ~10m. There is one arm at each end of the dipole magnet. The triplets of BPMs on each arm measure the beam trajectory at either side of the magnet and hence the beam deflection angle θ.

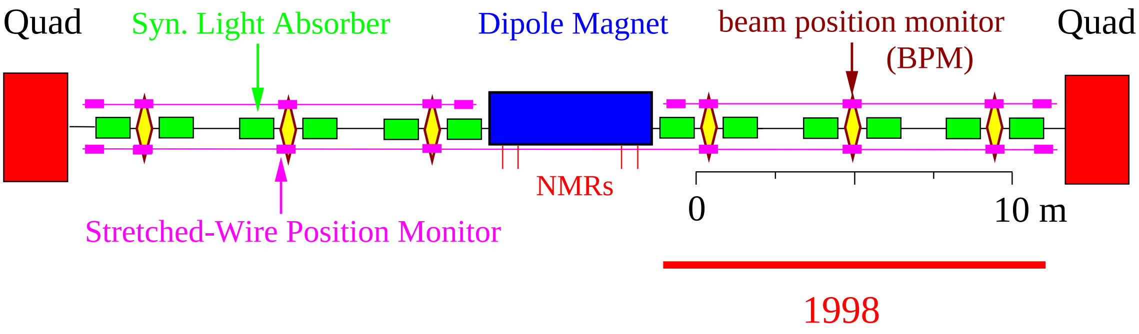

Figure 2.6: The layout of the LEP spectrometer showing the steel dipole magnet, the beam position monitors, the synchrotron radiation absorber blocks and the stretched wire position monitors. In 1998, a single-arm prototype was in place.

2.7.3 E_{BEAM} Measurement Strategy

The required accuracy on E_{BEAM} of 10^{-4} translates into a maximum relative error on the bend angle θ of 10^{-4}. Whereas an absolute precision on θ of this magnitude is unattainable, a high precision relative measurement is possible by calibrating the bend angle against RDP at low energies. The changes in deflection angle and $\int B \cdot dl_{\text{Spect}}$ can be then used to trace the beam energy as LEP is ramped up to physics energies. The strategy adopted can be visualised in Figure 2.7. It is summarised as follows:

- The beam is steered to the nominal trajectory and the BPM gain calibration is performed (see section 2.7.4).

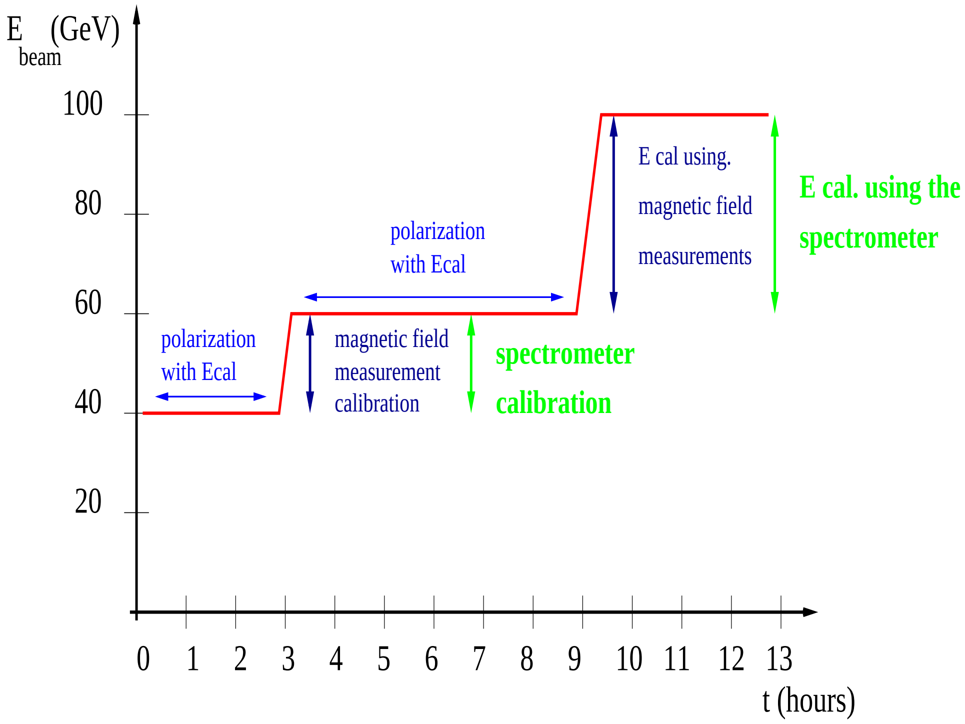

Figure 2.7: A schematic of the E_{BEAM} calculation using the spectrometer. The spectrometer is first calibrated against RDP measurements. The beam is then ramped to physics energies and the beam energy calculated using the spectrometer. Magnetic measurements with the NMR extrapolation method are performed in parallel and the two results compared.

- The Spectrometer is calibrated against RDP at low energies, E_{RDP}. Here, the local beam energy measured at the location of the spectrometer, octant 3 or P3, is translated to E_{BEAM} using the the RF model. This energy is calibrated against RDP, effectively constraining the beam deflection angle through Equation 2.9. This does away with the need to measure absolute deflection angles θ.

- The beam is ramped up to physics energies, E_{Phys} and steered to the nominal trajectory.

- The BPM gain calibration is performed again.

- The beam energy is adjusted by varying the RF frequency such that θ_{RDP} is close to θ_{Phys}.

- A relative beam energy measurement is performed from the *ratio* of the two bending angles θ_{RDP} and θ_{Phys}, and that of the bending fields of the dipole at both energies:
$$\frac{E_{Phys}}{E_{RDP}} = \frac{\int B \cdot dl_{\mathrm{Spect}}|_{E_{Phys}}}{\int B \cdot dl_{\mathrm{Spect}}|_{E_{RDP}}} \frac{\theta_{RDP}}{\theta_{Phys}}. \tag{2.10}$$
The dependence on the calibration of the absolute BPM gains is minimised in the limit that $\theta_{\mathrm{RDP}} = \theta_{\mathrm{Phys}}$, since large sources of error affecting the change in beam deflection, like the absolute gain and the change in BPM button signals, are avoided.

- The predicted mean beam energies for the calibrated spectrometer at low energy are then compared to those obtained from RDP to check for linearity.

- The mean beam energies predicted by the spectrometer, E_{Spect} at higher energies are compared to those obtained from the NMR model. Thus, provided the spectrometer behaves well in the RDP region, it serves as a test to confirm or reject the assumption of the linear relation between the NMRs and the LEP total bending field.

2.7.4 Measurement of Beam Deflection θ

The beam deflection is measured using three BPMs on either side of the dipole magnet, in areas of zero field. They are numbered 6, 5, 4, 1, 2, 3 in increasing z direction, that is, the direction of motion of the e^- beams. Their positioning relative to the dipole can be seen in Figure 2.6. The lever arm of each triplet is close to 10m. Given the target relative accuracy on E_{BEAM} of 10^{-4} and the relative accuracy on $\int B \cdot dl_{\mathrm{Spect}}$ of 3×10^{-5}, the required relative accuracy on the beam deflection angle θ is $\Delta\theta/\theta \sim 10^{-4}$. This translates to an accuracy of $\sim 1\mu$m in the measurement of the x position of the beam for each BPM. The BPMs must be stable at this level against mechanical and electronic drifts and fluctuations. The beam spectrometer energy calibration strategy used means that stability of this order is only required for a few hours while the spectrometer is calibrated against RDP (see section 2.7.3). However, with ~ 1 kWm^{-1} of power radiated as synchrotron light at physics energies, the whole spectrometer setup is in a very hostile environment. In order to keep thermal expansion of the BPM assemblies and the dipole magnet to a minimum, both are equipped with dedicated temperature sensors and water cooling stations. These allow temperature monitoring and control with higher accuracy than is possible with the standard equipment in the rest of LEP, giving the BPMs a thermal stability of $\pm 0.2^o C$. A stretched-wire positioning system measures any remaining thermal motion, which can be corrected for offline. The BPM buttons are protected from synchrotron light by copper absorbers (see Figure 2.8).

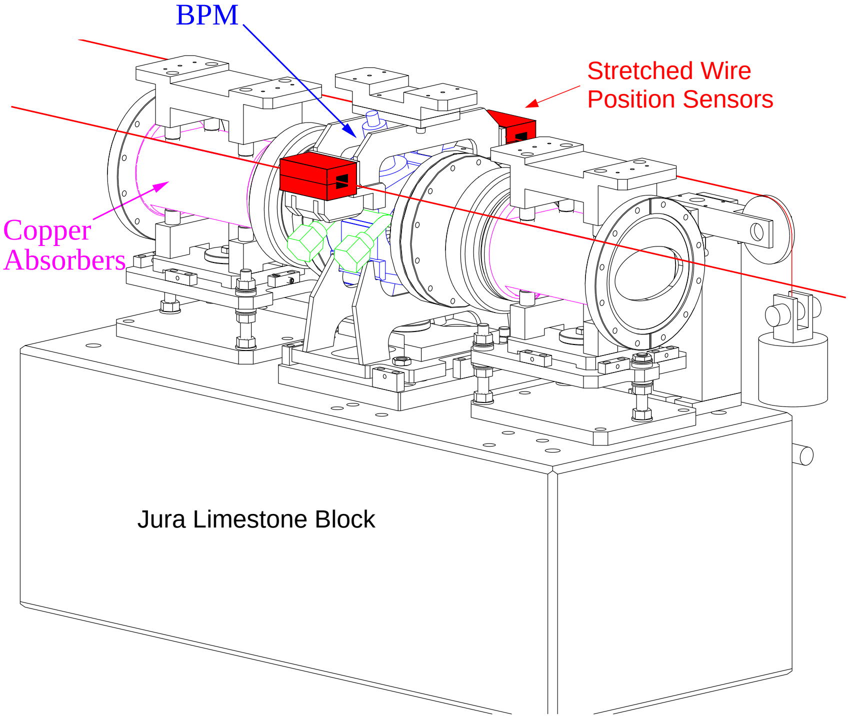

Figure 2.8: A BPM station showing the synchrotron light copper absorbers and the stretched-wire position sensors.

The bend angle θ is calculated from the sum of triplet angles on each arm of the spectrometer. Using small angle approximations, it can be expressed in terms of the x positions X_i measured by the BPMs on either side of the magnet:

$$\theta = \frac{(X_4 - X_6)}{2d_{BPM}} - \frac{(X_3 - X_1)}{2d_{BPM}}, \tag{2.11}$$

where X_6 (X_4) and X_3 (X_1) are the BPMs furthest (nearest) from the magnet on either side and d_{BPM} is the distance between two neighbouring BPM stations (≈4m).

In order for the absolute error on the calibration of the BPM electronics cards not to have a large impact on the accuracy of the beam position measurements, and to reduce the effects of beam orbit drifts, a relative calibration method using controlled beam trajectory shifts is applied [39] to each arm separately. The purpose is to calibrate the gain of the exterior BPMs, 1 and 3 (4 and 6), to the central one, 2 (5), on either side. Taking one arm of the spectrometer for clarity (BPMs 1 to 3), the calibration procedure is as follows:

- Angular bumps are applied to the beam in the xz plane about BPM2:

$$X_3 = -X_1; \; X_2 = 0. \tag{2.12}$$

- Parallel beam bumps in the xz plane are applied:

$$X_1 = X_2 = X_3. \tag{2.13}$$

- Equations 2.12 and 2.13 represent two ideal lines that define an ideal plane:

$$X_2 = \frac{X_1 + X_3}{2}. \tag{2.14}$$

  The angles of the corresponding measured lines to the ideal plane give the relative gains of the BPMs. The gains of BPMs 1 and 3 are calibrated to that of BPM 2, shifting the measured lines to match the ideal plane.

- The resolution of the calibrated BPM triplets, and hence that of the relative θ accuracy, is calculated from the triplet residuals after the beam calibration has been applied:

$$T = X_2 - \frac{(X_1 + X_3)}{2}. \tag{2.15}$$

The x position of the beams as measured by each of the three BPMs on one arm of the spectrometer during the beam bumps described above, as well as the triplet residuals before and after calibration, are shown in Figure 2.9. The relative accuracy estimated from expression 2.15 is of 300nm over 1 hour, with individual BPM scatters of ~200nm. Hence the required relative accuracy of $\sim 1\mu$m has been surpassed. The reproducibility of the cross-calibration before and after an energy ramp

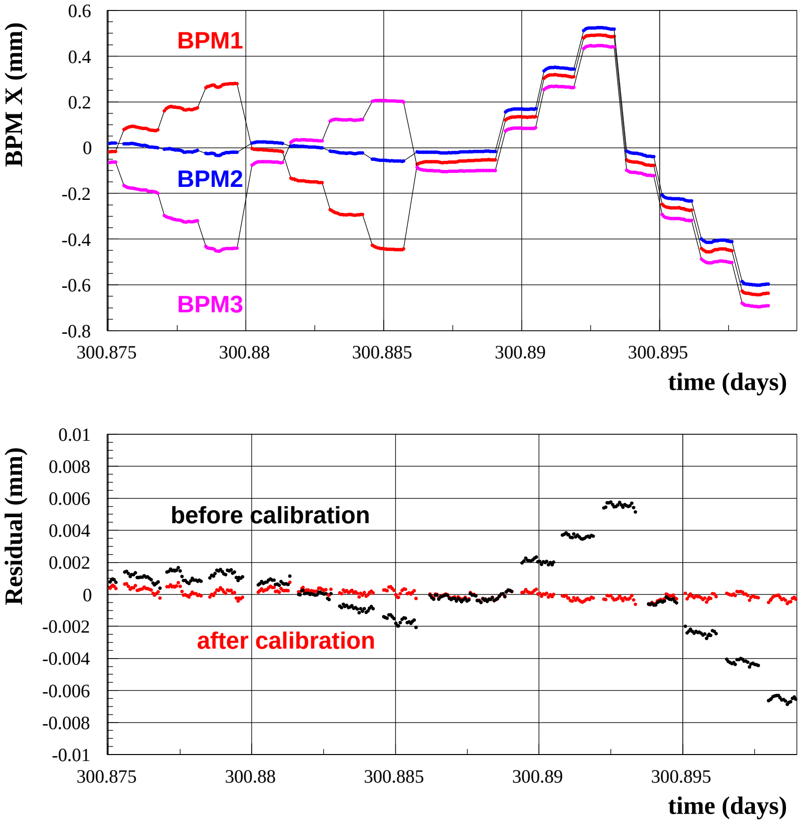

Figure 2.9: Beam based BPM gain cross-calibration. The beam is subjected to angular and parallel position changes which are followed by the three BPMs on one arm of the spectrometer (top). The triplet residuals before and after calibration are shown as a function of time (bottom).

is $\sim 10^{-3}$. The absolute gain can be calibrated using small frequency shifts δf_{RF} and comparing the fractional change in energy as determined by the spectrometer, given by

$$\frac{\delta E^{spect}_{\mathrm{BEAM}}}{E^{spect}_{\mathrm{BEAM}}} = \frac{\delta\theta}{\theta}, \tag{2.16}$$

to the fractional change in energy expected from the f_{RF} shift, given by

$$\frac{\delta E^{RF}_{\mathrm{BEAM}}}{E^{RF}_{\mathrm{BEAM}}} = -\,\alpha_c^{-1}\frac{\delta f_{RF}}{fRF}, \tag{2.17}$$

where α_c is the momentum compaction factor. The linear dependence between $\delta\theta/\theta$ and δf_{RF} can be seen in Figure 2.10. θ can then be calibrated to fit the expected slope, calculated in terms of f_{RF} and α_c.

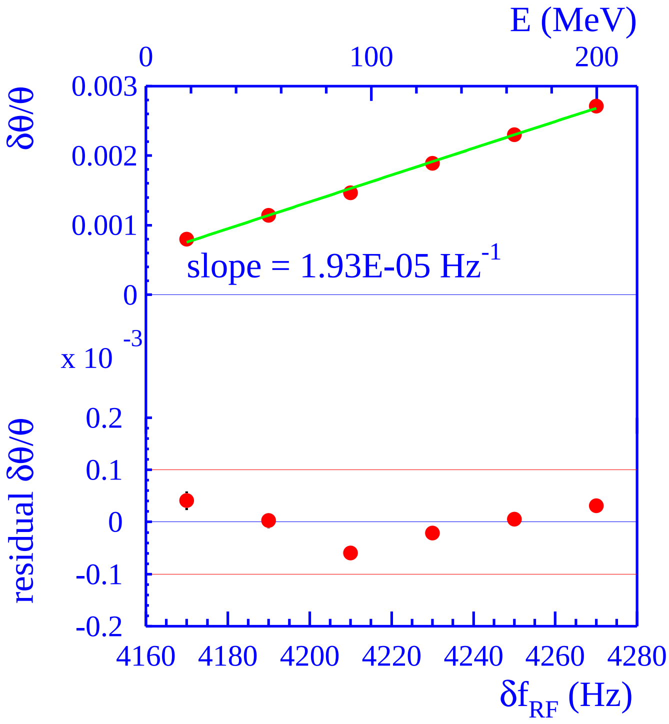

Figure 2.10: The observed relation between $\delta\theta/\theta$ and δf_{RF}. The slope depends on the absolute gain calibration of the BPMs. By fixing the slope to the expected value the absolute gain can be calibrated.

2.7.5 Measurement of $\int B \cdot dl_{\mathrm{Spect}}$

The precision to which $\int B \cdot dl_{\mathrm{Spect}}$ is known at different LEP regimes is crucial to the measurement of E_{BEAM} with the spectrometer. This section describes the procedures adopted to measure the integrated field of the dipole magnet under different conditions, how these measurements are related to those from the four NMR probes placed in the core of the magnet, and how the probes can be used to infer the integrated field of the magnet during LEP operations.

Mapping of the Spectrometer Dipole Magnet.

In order to have a precise knowledge of the integrated bending field of the LEP spectrometer magnet, $\int B \cdot dl_{\mathrm{Spect}}$, an extensive mapping campaign was carried out between December 1998 and February 1999 in the old Interacting Storage Rings (ISR) tunnel at CERN. $\int B \cdot dl_{\mathrm{Spect}}$ was measured in its totality under different temperatures and excitation currents. To achieve this, the magnet was scanned longitudinally by a measuring arm containing an NMR probe to measure local fields in its core with a relative precision of 10^{-6}, and with Hall probes to measure the fringe fields, which are too weak for NMR probes to lock, to a precision of $\sim 2.5 \times 10^{-4}$. The experimental setup for the mapping campaign is shown in Figure 2.11. Each standard

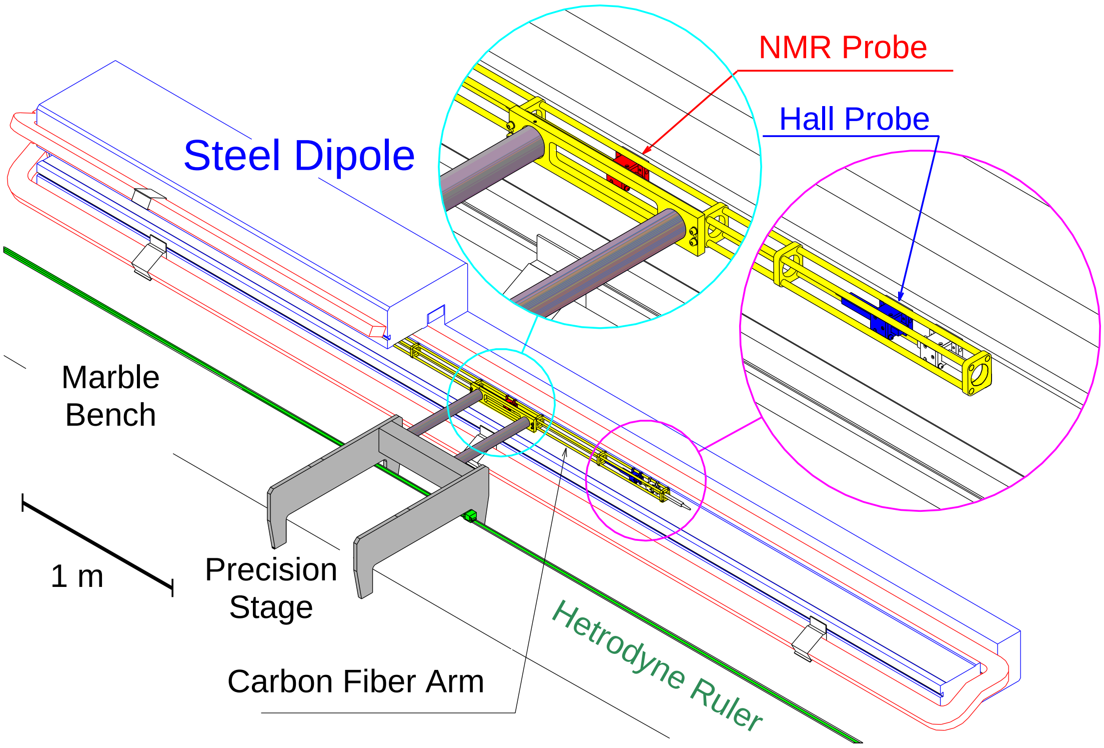

Figure 2.11: The Spectrometer mapping bench setup.

map contains a set of 552 readings taken at 1cm steps along the longitudinal axis of the magnet. The following quantities are logged: position, measured with a high precision ruler attached to the marble block (see Figure 2.11); NMR readings for the four stationary probes placed on the magnet; NMR and Hall probe readings for the moving arm; DC excitation current of the magnet; and temperatures for different parts of the dipole. During a standard map the temperature is kept constant to better than 1^{o}C. The probe readings from the scanning arm can be used to calculate integrated fields along the longitudinal direction of the magnet using the trapezium method. The arm NMR readings are used directly to give the field at the core of the magnet. As the precision of the Hall probes is very poor compared

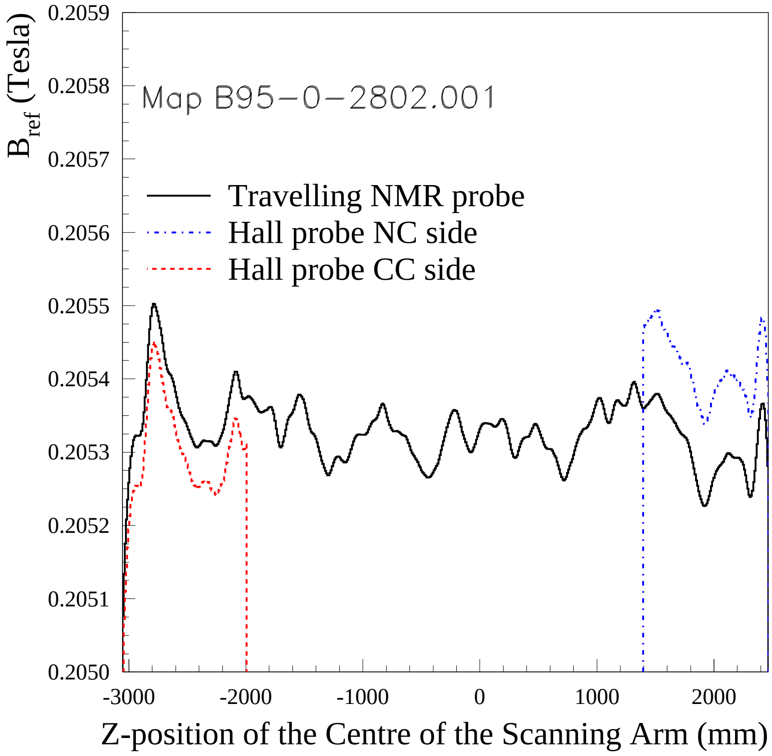

Figure 2.12: A magnet field map. The region of overlap between Hall and NMR probe readings points to discrepancies in the measured fields. These can be traced down to the inherent sensitivity of the Hall probes and a residual offset from mis-calibration. In practice, the offsets are corrected for and the scatter reduced by cross-calibration with the NMR. Since the fringe field only accounts for ∼ 10% of the total bending field this effect is not very significant.

to that of the NMR, it was necessary to calibrate them each map with the traveling NMR in a 150mm region of overlap at either end of the dipole, where both types of probe are operational. Figure 2.12 shows the discrepancy between Hall probe and NMR estimates of local fields in one map in the regions of overlap at either end of the magnet. As a first step, all Hall probe readings are scaled by a multiplicative factor $a_{Hall} = \overline{B^{Raw}_{HALL}}/\overline{B_{NMR}}$. A second effect discovered during the mapping campaign was that one of the Hall probes consistently gave field readings significantly different to zero in regions of the end-field where no field is expected, deep inside the mu-metal. Whether the effect was due to an instrumentation problem or to the existence of a real stray field was checked by performing measurements with an independent Hall probe in the region of interest. This experiment showed that the non-zero field was due to a problem with one of the Hall probes on the measuring arm, so a further correction b_{Hall} is applied to account for all offsets in the zero-field region. The offset is simply estimated from the mean value of the measured, local fields, $\overline{B_{Hall}^{mu-metal}}$, in a region ±65mm from the centre of the mu-metal, which is 845mm from the end of the magnet core. Both the a_{Hall} and b_{Hall} correction factors are calculated separately for each Hall probe and individually for each map. Each end-field reading from the Hall probes is then corrected for according to:

$$B_{Hall}^{Scale} = a_{Hall}(B_{Hall}^{raw} - b_{Hall}). \tag{2.18}$$

The relative RMS of the end-fields with and without these corrections, for maps taken at a nominal coil temperature of 34^oC^5, are shown in table 2.2. Although the calibration reduces the scatter, it is still large compared to that of the fields measured by the NMR probe, as can be seen in Table 2.3. However, the fact that the fringe field makes up only $\sim$ 10% of the total field means that the relative precision per map is $\sim 10^{-5}$, as was determined from the RMS scatter of maps taken under identical conditions. The end-field integrals are then re-evaluated from the scaled Hall probe readings using the trapezium method. The relative precision of these maps, determined by their reproducibility under "identical" conditions, ranges between 2×10^{-5} and 6×10^{-6} depending on the excitation current.

Stationary NMR probes

For each map, mean values of the B_{ref}^i fields measured by each one of the stationary NMR probes are also obtained after eliminating outliers and readings where probes were not locking[6]. While implementing this procedure, it was found that the scanning arm affects the local magnetic field seen by the stationary probes, as can be seen in Figure 2.13. The main effect is due to the passage of the traveling NMR probe over the reference ones. This effect disappears when the arm leaves

---

[5] The actual "nominal" temperature of a map refers to the mean temperature of the core of the dipole magnet. However, in the analysis that follows, only the temperature of the coil is used. For this reason, and to avoid confusion, the "nominal" temperatures given in what follows refer to coil temperatures only. The coil temperature is $\sim 4^oC$ higher than the core temperature.

[6] Non-locking NMR probes read out characteristic non-zero values which could be mistaken for genuine field values. Care has to be taken to identify these for each probe, and exclude them from the analysis.

Nominal Energy (GeV)	B_{Hall}^{raw}	$a_{Hall}B_{Hall}^{raw}$	$a_{Hall}(B_{Hall}^{raw} - b_{Hall})$
41	2.078×10^{-4}	1.806×10^{-4}	1.265×10^{-4}
44	2.497×10^{-4}	2.223×10^{-4}	2.264×10^{-4}
50	1.104×10^{-4}	8.866×10^{-5}	8.703×10^{-5}
55	1.325×10^{-4}	8.708×10^{-5}	6.537×10^{-5}
60	1.751×10^{-4}	1.450×10^{-4}	9.619×10^{-5}
70	1.085×10^{-4}	7.851×10^{-5}	4.958×10^{-5}
80	1.203×10^{-4}	9.302×10^{-5}	5.842×10^{-5}
90	8.317×10^{-5}	7.548×10^{-5}	4.356×10^{-5}
95	9.539×10^{-5}	7.446×10^{-5}	5.695×10^{-5}
100	2.642×10^{-4}	2.194×10^{-4}	6.762×10^{-5}
103	6.193×10^{-5}	5.425×10^{-5}	4.753×10^{-5}

Table 2.2: The relative RMS of the measured end-fields of maps for different nominal energies and for a nominal temperature of $34^o C$. The first column corresponds to end-fields where no correction has been applied to the Hall probes. In the second column the probes have been scaled with a slope to the traveling NMR. Finally, the third column shows the spread when both a scaling and an offset correction have been applied. This two-parameter scaling is applied to the data on a map-by-map basis.

the vicinity of the reference probes and so future readings are not compromised. The average B field for each stationary probe is therefore calculated from readings where the arm is at a distance of $\geq$1400mm from the probe. Thus we have obtained an integrated bending field, a set of mean local field readings from the stationary probes with associated errors from the standard deviation, plus the temperature and excitation current information logged during each map of the magnet. This information will be used to derive a model which can infer an integrated bending field during LEP operations.

Calibrating the stationary NMR probes against the measured $\int B \cdot dl_{\mathrm{Spect}}$

Each stationary NMR probe is calibrated against the integrated bending field obtained from the traveling NMR and the corrected Hall probe readings. Using maps taken under different excitation currents and environmental conditions, a two parameter fit is used to determine the relation between total integrated fields and the mean value of each of the stationary probes, assuming a linear dependence:

$$\overline{B_{ref}^{i}} = m_i \int B \cdot dl + c_i, \tag{2.19}$$

where the index i corresponds to the four reference NMR probes. The fit is performed in the full nominal energy range, $E_{nom} = 41 \rightarrow 103$ GeV, despite the fact that the

Nominal Energy (GeV)	$RMS(B_{core})$	$RMS(B_{end})$	$RMS(B_{total})$
41	2.724×10^{-6}	1.265×10^{-4}	1.024×10^{-5}
44	9.453×10^{-5}	2.264×10^{-4}	1.032×10^{-4}
50	1.857×10^{-6}	8.703×10^{-5}	7.293×10^{-6}
55	1.329×10^{-6}	6.537×10^{-5}	5.343×10^{-6}
60	5.589×10^{-5}	9.619×10^{-5}	5.688×10^{-5}
70	3.998×10^{-6}	4.957×10^{-5}	6.249×10^{-6}
80	3.573×10^{-6}	5.842×10^{-5}	6.192×10^{-6}
90	5.104×10^{-6}	4.356×10^{-5}	6.955×10^{-6}
95	1.120×10^{-6}	5.695×10^{-5}	5.383×10^{-6}
100	1.954×10^{-5}	6.762×10^{-5}	1.399×10^{-5}
103	8.246×10^{-7}	4.753×10^{-5}	4.151×10^{-6}

Table 2.3: The relative RMS of the core, end and total bending fields of the maps taken at $T = 34^oC$ is shown for different nominal energies.

probes do not necessarily lock at all energies. An estimate of the integrated field can then be obtained for each reference NMR probe:

$$\int B \cdot dl_{NMR\ i} = \frac{\overline{B^i_{ref}} - c_i}{m_i}, \tag{2.20}$$

The arithmetic mean of the $\int B \cdot dl_{NMR\ i}$ from locking probes is used as an estimate $\int B {\cdot} dl^{\mathrm{NMR}}_{\mathrm{Spect}}$ of the bending field of the magnet. The relative residuals of these estimates to the total measured integrated field, defined as:

$$Residual\left(\int B \cdot dl_{\mathrm{Spect}}\right) = \frac{\int B \cdot dl^{\mathrm{NMR}}_{\mathrm{Spect}} - \int B \cdot dl^{\mathrm{Meas}}_{\mathrm{Spect}}}{\int B \cdot dl^{\mathrm{Meas}}_{\mathrm{Spect}}}, \tag{2.21}$$

give an RMS of $\sim 2.8 \times 10^{-5}$ for the sample of all the maps. However, if the maps are split into two samples according to their running temperature it can be seen that each sample has residuals with an RMS of $\sim 1.7 \times 10^{-5}$ with mean values offset by $\sim 4.8 \times 10^{-5}$, as is shown in Figure 2.14. This effect is attributed to the difference in temperature coefficients between the core of the magnet and the end field, which gives temperature dependent field changes which are not traced by the reference NMR probes.

Temperature effects

The temperature of the magnet clearly has an effect on the relation between the measured integrated field and that inferred from the stationary probes. It is neces-

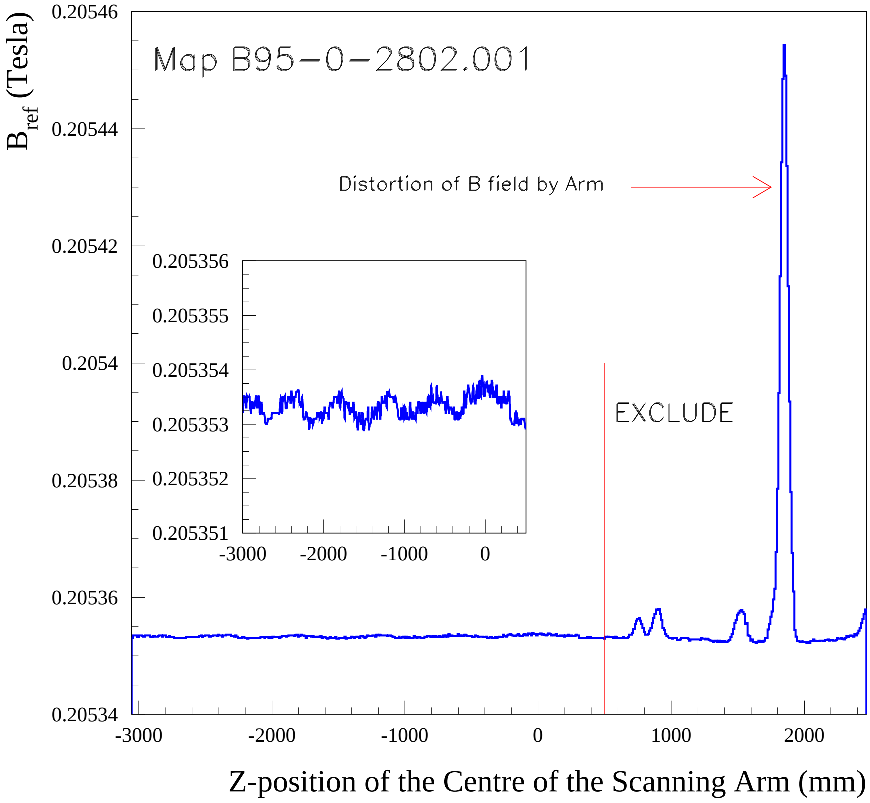

Figure 2.13: Value of the field, B^i_{ref}, in a stationary NMR probe as a function of the position of the moving scanning arm. The effect of the scanning arm as it passes over the stationary NMR probe can be seen as a series of bumps, each one corresponding to a magnetic element of the arm. The largest peak is due to the passage of the traveling NMR over the stationary one providing the field values. NMR readings from this region are excluded from the calculation of the mean. The inset shows the region which is included in the mean.

sary to account for this effect in the $\int B \cdot dl_{\text{Spect}}$ model. The procedure adopted to include temperature effects is outlined below.

Most standard maps were taken such that the temperature of the coil (T_{coil}) of the magnet was 34.0^{o}C to $\pm$0.2^{o}C (RMS). In order to gauge temperature dependent effects in the magnet, a series of maps with higher operating temperatures was also taken, this time with $T_{coil} \approx 42^o$C, but with a larger spread of $\pm 0.8^o$C (RMS). The reference NMR probes trace the field changes in the core of the magnet and so their readings vary with temperature T according to:

$$B^i_{ref}(T) \;=\; (1 + C^{core}_T \Delta T) B^i_{ref}(T_0) \;=\; \beta B^i_{ref}(T_0), \qquad (2.22)$$

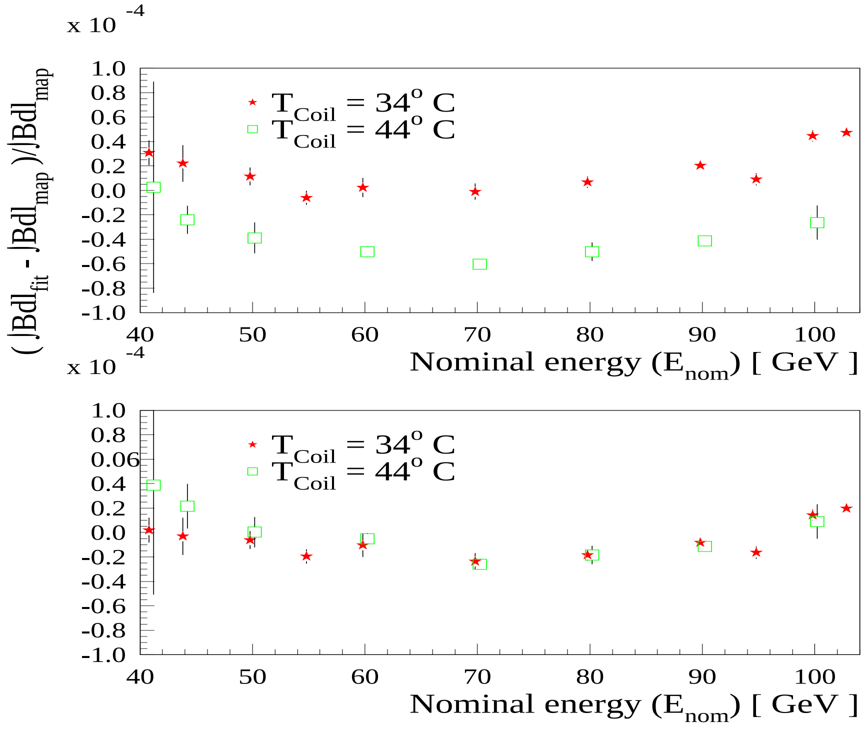

Figure 2.14: Relative residuals from Reference probe fits to measured integrated bending fields. Maps are separated according to temperature. The top plot shows the residuals from a fit where no temperature effects are taken into account. The bottom plot shows the residuals when fit coefficients and reference probe readings have been scaled according to Equation 2.32.

where C_T^{core} is the temperature coefficient of the core region, defined as $C_T^{core} = \Delta B/(B_0 \Delta T)$, ΔT is $(T - T_0)$, T_0 is $34^o C$, the mean coil temperature at which the standard maps were taken, B_0 is the B field measured at T_0 and $\beta = (1 + C_T^{core}\Delta T)$ is defined for simplicity. However, the change in total integrated field $\int B \cdot dl_{\mathrm{Spect}}$ has both core and end-field components and so its variation with temperature is more complex:

$$\begin{aligned}
\int B \cdot dl_{\mathrm{Spect}}(T) &= \{1 + \Delta T(f_{core} C_T^{core} + f_{end} C_T^{end})\} \int B \cdot dl_{\mathrm{Spect}}(T_0) \qquad (2.23)\\
&= \{1 + \Delta T(C_T^{core} + f_{end}(C_T^{end} - C_T^{core}))\} \int B \cdot dl_{\mathrm{Spect}}(T_0) \qquad (2.24)\\
&= \{\beta + \gamma\} \int B \cdot dl_{\mathrm{Spect}}(T_0),
\end{aligned}$$

where f_{core} and f_{end} are the fraction of $\int B \cdot dl_{\mathrm{Spect}}$ due to the core and end-fields respectively, *measured at* T_0, $\gamma = f_{end}(C_T^{end} - C_T^{core})\Delta T$, and the relation $f_{end} + f_{core} = 1$ has been used. The coil temperature T is the same for core and end-field[7].

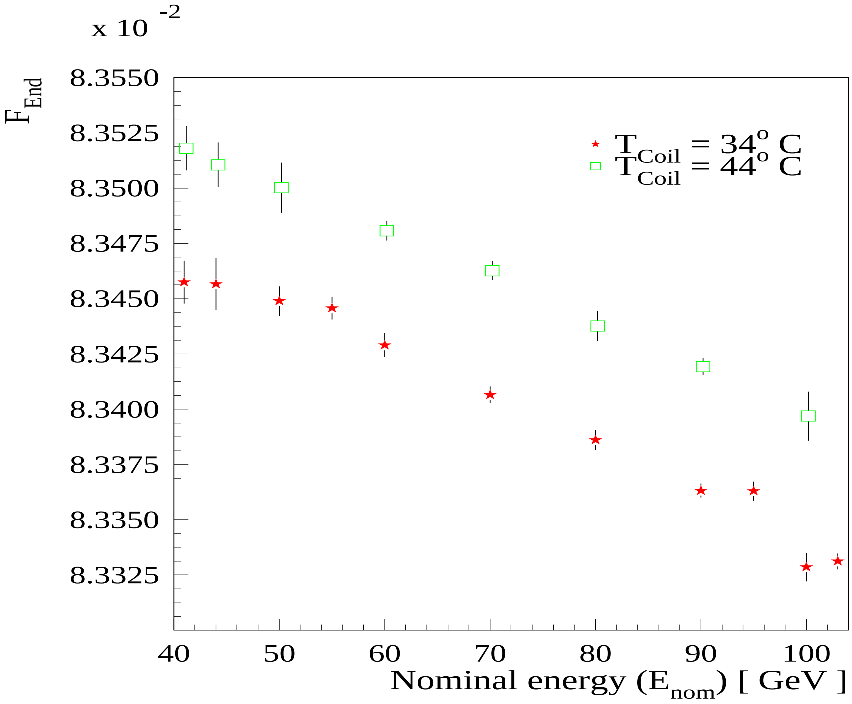

Figure 2.15: Fraction of the total bending field of the spectrometer dipole magnet due to the end-field contribution for the two temperature regimes.

In order to take these effects into account the relation 2.19 must be modified. This is achieved by transforming the B^i_{ref} values to an arbitrary reference temperature, T_0, before performing the linear fit in Equation 2.19. Requiring that the integrated field inferred from the reference probes through Equation 2.20 follows the temperature dependence given in Equation 2.25 yields:

$$\frac{\beta B^{i\ corr}_{ref} - c_i}{m_i} = \{\beta+\gamma\}\int B\cdot dl_{\mathrm{Spect}}(T_0) = \{\beta+\gamma\}\frac{B^i_{ref} - c_i}{m_i}, \tag{2.25}$$

where $B^{i\ corr}_{ref}$ are the transformed reference probe readings. A linear scaling factor α is sought such that $B^{i\ corr}_{ref} = \alpha B^i_{ref}$. Using Equation 2.25, α can be expressed as:

$$\alpha = \frac{(\beta+\gamma)(B^i_{ref}(T) - c_i) - c_i}{\beta B^i_{ref}(T)} \tag{2.26}$$

$$\approx 1 + \frac{\gamma}{\beta} \tag{2.27}$$

---

[7] A global temperature is used here so all temperature effects are absorbed into the temperature coefficients.

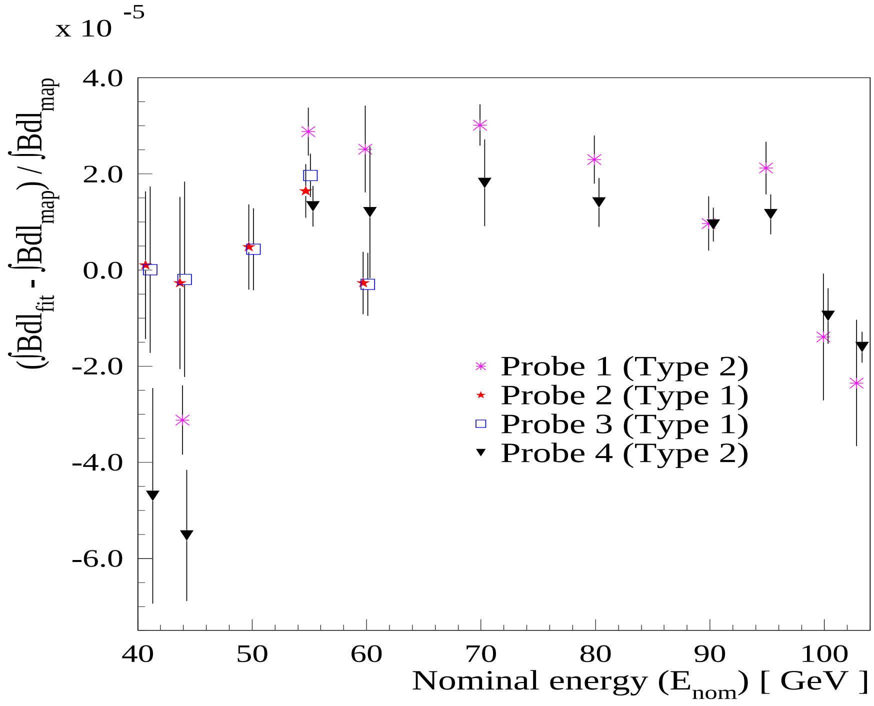

Figure 2.16: Relative residuals from the linear fit of each of the reference NMR probe readings to the measured integrated field. These residuals are used to provide probe-by-probe offset corrections before the probe estimates of $\int B \cdot dl$ are combined to get $\int B \cdot dl_{\text{Spect}}$.

$$= \quad 1 + \frac{f_{end}(C_T^{end} - C_T^{core})\Delta T}{1 + C_T^{core}\Delta T} \tag{2.28}$$

$$\approx \quad 1 + f_{end}(C_T^{end} - C_T^{core})\Delta T \tag{2.29}$$

where the approximations $c_i \approx 0$ and $1 + C_T^{core}\Delta T \approx 1$ have been made in going from 2.26 to 2.27 and 2.28 to 2.29 respectively. An effective temperature coefficient C_T^{eff} is then calculated by inspection of Equation 2.29:

$$C_T^{eff} = f_{end}(C_T^{end} - C_T^{core}), \tag{2.30}$$

Temperature coefficients C_T^{core} and C_T^{end} were estimated at each nominal energy point for which maps were taken at both nominal temperature values by performing a linear fit according to:

$$\int B \cdot dl = (C_T T + 1) \int B \cdot dl(T_0). \tag{2.31}$$

The fitted values are used to estimate the mean value of $(C_T^{end} - C_T^{core})$. This quantity, together with the mean values of C_T^{core} and C_T^{end}, is shown in Table 2.5. The

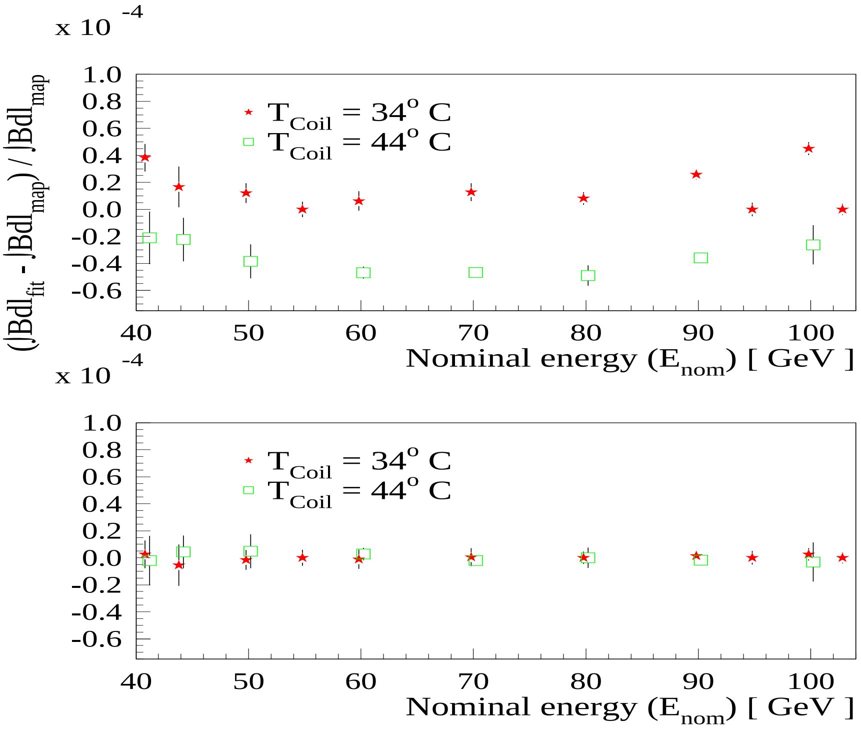

Figure 2.17: Relative residuals from Reference probe fits to measured integrated bending fields after correcting for probe-by-probe offset in bins of energy. As with Figure 2.14, the top plot shows the residuals from a fit where no temperature effects are taken into account, and the bottom plot shows the residuals when fit coefficients and reference probe readings have been scaled according to Equation 2.32.

reference NMR readings are then re-scaled according to:

$$B^{i\ corr}_{ref} = (1 + C^{eff}_{T}(T - T_0))B^{i}_{ref}, \tag{2.32}$$

before performing the linear fit defined by Equation 2.19. However, the calculation of C^{eff}_{T} has to account for the dependence of the fractional end field f_{end} on the magnet excitation current. The evolution of f_{end} with nominal energy for the two different temperature samples can be seen in Figure 2.15. It is clear that the f_{end} term in Equation 2.30 has a slope that has to be taken into account. The procedure followed is to perform a linear fit to relate f_{end} to the nominal energy, E_{nom}:

$$f_{end} = M_{end}(E_{nom} - 41\text{GeV}) + C_{end}. \tag{2.33}$$

The resulting coefficients are used to estimate the value of f_{end} given the nominal energy during a spectrometer measurement. They are summarised in Table 2.6. In

Probe (Type)	m (Tm^{-1})	c (T)	$\rho_{m,c}$
NMR_1 (2)	$17075532 \pm 7 \times 10^{-8}$	$-4312 \pm 8 \times 10^{-8}$	-0.991
NMR_2 (1)	$17068200 \pm 52 \times 10^{-8}$	$-1383 \pm 32 \times 10^{-8}$	-0.992
NMR_3 (1)	$17067944 \pm 26 \times 10^{-8}$	$-1659 \pm 16 \times 10^{-8}$	-0.991
NMR_4 (2)	$17079301 \pm 10 \times 10^{-8}$	$-3100 \pm 10 \times 10^{-8}$	-0.980

Table 2.4: The calibration parameters and correlation coefficients of the two parameter fit of mean NMR_{ref} values to the measured total bending fields. The fit is performed individually for each of the reference probes including every available energy point. For the Type 1 probes this means energies up to 60 GeV. The Type 2 probes were operational at all energies for the mapping campaign but radiation damage in the LEP tunnel increases their locking threshold.

Mean Temperature Coefficient	Value (K^{-1})
$\overline{C_T^{core}}$	$-8.62 \pm 4.52 \times 10^{-6}$
$\overline{C_T^{end}}$	$7.81 \pm 0.82 \times 10^{-5}$
$\overline{C_T^{end} - C_T^{core}}$	$8.67 \pm 0.56 \times 10^{-5}$

Table 2.5: Mean Temperature coefficients for the end and core fields of the LEP spectrometer magnet. Note the opposite signs of the end and core coefficients. The mean of the difference between core and end-field coefficients is is used to correct the $\int B \cdot dl$ of the magnet for temperature variations about 34^oC.

practice, the magnet current is used to get a value for the nominal energy using a linear factor. Then C_T^{eff} can be calculated using Equation 2.30.

The final coefficients m_i and c_i are shown in Table 2.4, together with their associated errors and correlations. In order to extract $\int B \cdot dl^{\mathrm{NMR}}_{\mathrm{Spect}}$ values from a given set of B_{ref} readings the scaling described in Equation 2.32 is applied before using the coefficients m and c. All three temperature coefficients are shown in Table 2.5. Note the opposite sign of the end and core field coefficients. The relative residuals with and without the temperature correction are shown in Figure 2.14.

Offset Corrections

After applying the temperature correction, the RMS of the relative residuals for the full sample is reduced from $\sim 2.8 \times 10^{-5}$ to $\sim 1.7 \times 10^{-5}$. The offset in the mean values is reduced from $\sim 4.8 \times 10^{-5}$ to $\sim 1.1 \times 10^{-5}$. It is clear that, with or without the temperature correction, the residuals reflect a nonlinearity in the relation between reference probe values and measured integrated bending field. The structure of the residuals for each one of the probes can be seen in Figure 2.16. For this reason, correction factors are calculated for the estimated field from each

T_{coil}	$M_{end}(\mathrm{GeV}^{-1})$	C_{end}	$\rho_{M,C}$
34	$-2.21 \pm 0.02 \times 10^{-6}$	$83470.35 \pm 1.06 \times 10^{-6}$	-0.926
44	$-2.07 \pm 0.03 \times 10^{-6}$	$83519.36 \pm 1.51 \times 10^{-6}$	-0.933

Table 2.6: The parameters and correlation coefficients of the linear fit of the fractional end-field of the spectrometer magnet, f_{end}, against the nominal energy. The coefficients correspond to Equation 2.33. Only the coefficients for the 34^oC maps are used for the analysis. The 44^oC coefficients are included to show that the slope is, to a good approximation, independent of temperature.

probe in bins of energy and applied to the estimation of the mean $\int B \cdot dl^{\mathrm{NMR}}_{\mathrm{Spect}}$. These corrections further reduce the RMS of the relative residuals to $\sim 1.1 \times 10^{-5}$, remove the overall bias, and do away with the need to reject outliers[8]. The residuals with the offset correction applied, with and without the temperature corrections, are shown in Figure 2.17.

In order to test the validity of the linear fit coefficients calculation and of the residual offsets correction, the fit defined by Equation 2.19 and the calculation of the residuals was carried out using half the available maps, and the remaining maps were fitted with all corrections applied. The resulting mean relative residual was found to be $(0.52 \pm 3.52(RMS)) \times 10^{-5}$ without offset corrections and $(0.30 \pm 1.23(RMS)) \times 10^{-5}$ with offset corrections, for all energies and operating temperatures. The residuals for both the full standard map sample and the independent subsample containing half the maps, after applying the offset corrections, can be seen in Figure 2.18. The reduction in the mean and RMS of the independent sample after applying the offset corrections gives an indication of the reproducibility of the structure of the residual distribution seen in figure 2.16 and underlines the validity of using such corrections.

Transverse position of the beam

In addition to temperature effects, any variation of the bending field strength in the transverse (x) and vertical (y) directions of the dipole magnet would give rise to changes in the relation between the NMR probe readings and the integrated bending field of the magnet. Since the beam necessarily describes a 3.8mrad arc inside the

---

[8] The outliers are caused by the large residuals shown by the Type 2 probes at energies under 50 GeV.

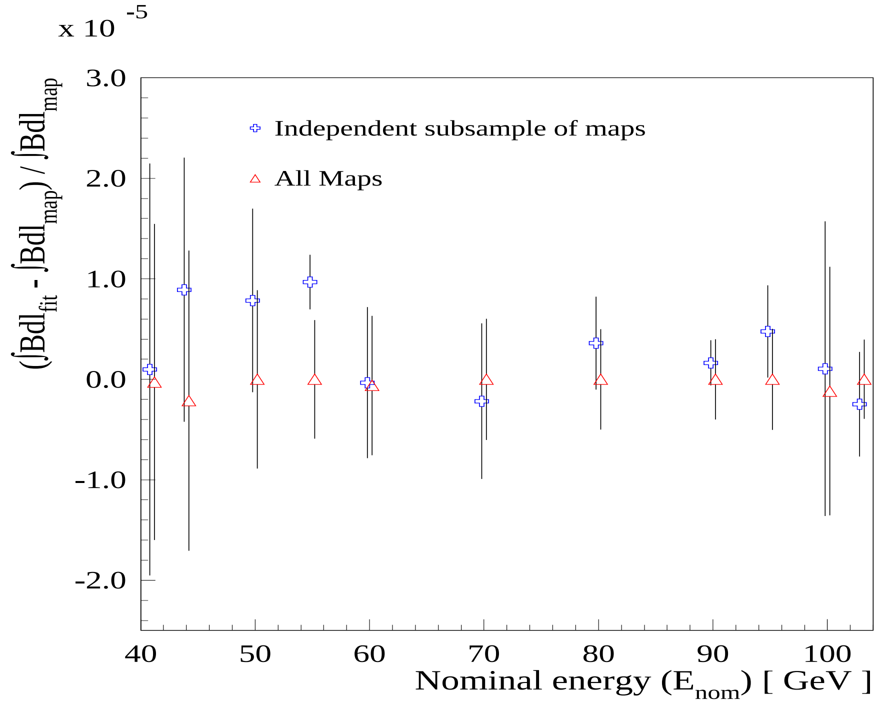

Figure 2.18: Relative residuals from Reference probe fits to measured integrated bending fields after correcting for probe-by-probe offset in bins of energy. Two sets of residuals are shown. The first corresponds to a subsample of ∼ 150 maps where the offset corrections and calibration coefficients from Equation 2.19 have been obtained from an independent sample of maps. The second set corresponds to the full sample of maps where the same sample has been used to calculate coefficients and offset corrections.

total dipole bending field, it probes regions displaced in x relative to the nominal axis along which the standard maps were taken. For a total bending field length of ∼6.2m the x displacement of the beam is ∼6mm. In order to take this effect into account, a series of maps were made with the measuring arm displaced in x. They covered a range of 20mm and were taken at three different excitation currents, corresponding to 45, 60 and 100 GeV. Whereas relative differences in end and core integrated fields of $\sim 10^{-5}$ were observed, the sign of the shifts is different between end and core fields and so largely cancels out. The relative shifts to the total bending field lie between 0.5×10^{-6} and 1.0×10^{-6}. Given the size of this effect, it was deemed unnecessary to include any modelling of the x dependence of the field into the $\int B \cdot dl_{\mathrm{Spect}}$ calculation.

The $\int B \cdot dl_{\mathrm{Spect}}$ model

Using the calibration coefficients calculated from Equation 2.19, mean values of the readings from each of the four reference NMR probes, the mean temperature of the coil of the magnet and the DC excitation current[9], $\int B \cdot dl^{\mathrm{NMR}}_{\mathrm{Spect}}$ can then be calculated as follows:

- Re-scale each of the mean NMR_{ref} values using the temperature correction described in Equation 2.32.
- Use the calibration coefficients from Table 2.4 and Equation 2.20 to estimate a total bending field $\int B \cdot dl_{NMR\ i}$ for each available reference NMR probe.
- Use the DC excitation current to calculate the nominal energy of the spectrometer magnet.
- Apply offset corrections to reduce the residuals seen in Figure 2.16 to each of the available $\int B \cdot dl_{NMR\ i}$ according to the nominal energy of the magnet.
- Take an arithmetic mean of the offset-corrected $\int B \cdot dl_{NMR\ i}$ to get $\int B \cdot dl^{\mathrm{NMR}}_{\mathrm{Spect}}$.

The relative accuracy on the prediction of the bending field of the spectrometer magnet from the $\int B \cdot dl_{\mathrm{Spect}}$ model can now be determined from the residuals of the independent samples of standard maps. It is found to be $1.2 \times 10^{-5}(RMS)$. However, the quantity of interest in performing a beam energy measurement with the spectrometer is the ratio of two integrated bending fields, one at resonant depolarisation and the other at physics energy. Therefore the error on E_{BEAM} due to the estimation of the bending field of the dipole is calculated from:

$$\frac{\int B \cdot dl_{meas}|_{E_{Phys}}}{\int B \cdot dl_{meas}|_{E_{RDP}}} - \frac{\int B \cdot dl_{Spect}|_{E_{Phys}}}{\int B \cdot dl_{Spect}|_{E_{RDP}}}, \tag{2.34}$$

where $\int B \cdot dl_{meas}$ is the integrated bending field of the spectrometer dipole as measured by the traveling arm. To estimate the mean and RMS of the quantity in expression 2.34, an independent sample of maps was separated according to nominal energy

---

[9] The DC excitation current is used in order to determine the nominal energy the spectrometer is operating under in order to apply the offset corrections given by the fit residuals seen in Figure 2.16.

Nominal E_{BEAM}	41	44	50	55	60
70	0.53 ±3.57	1.76 ±2.34	1.40 ±1.59	1.51 ±0.98	0.22 ±1.19
80	−0.50 ±3.92	0.83 ±2.28	0.68 ±1.57	0.88 ±0.72	−0.52 ±1.13
90	−0.14 ±4.33	1.49 ±2.66	1.12 ±1.62	1.31 ±0.48	−0.30 ±1.13
95	−0.87 ±4.66	−0.89 ±2.92	0.58 ±1.85	0.84 ±0.83	−0.81 ±1.32
100	1.44 ±4.25	1.64 ±3.69	0.74 ±3.22	1.57 ±2.68	−0.16 ±2.64
103	0.85 ±5.07	2.66 ±3.16	2.12 ±1.99	2.27 ±0.90	0.37 ±1.42

Table 2.7: The mean values of expression 2.34 are given in units of 10^{-5}. All errors are derived from the RMS spread of the results for all available combinations of maps, and give an indication of the accuracy to which the ratio between integrated bending fields can be predicted. The overall estimate of the accuracy for all combinations of maps is $\sim 3 \times 10^{-5}$.

into an E_{RDP} and an $E_{Physics}$ groups[10]. The quantity in expression 2.34 was evaluated for all possible cross-group combinations of maps. The mean and RMS were then calculated for all possible energy combinations. The results are summarised in Table 2.7. The overall evaluation of expression 2.34 is $(0.30 \pm 3.00) \times 10^{-5}$. The above procedure is a conservative indicator of the overall accuracy to which the NMR calculations can resolve ratios of bending fields, since it includes fill to fill variations in the bending field. Since the spectrometer is calibrated on a fill by fill basis during beam energy calibration, these variations are not present in the real calibration data. A similar study was performed with sets of maps taken during single magnet ramp cycles. However, the statistics of the study are small and no significant difference in the resolution could be observed.

Measurement of $\int B \cdot dl_{\mathrm{Spect}}$ with a Traveling Mole

In order to test the compatibility between the magnetic measurements carried out on the LEP spectrometer magnet at the ISR tunnel with the behaviour of the magnet

---

[10] The separation was done such that maps with nominal energies less than or equal to 60 GeV were included in the E_{RDP} group. All remaining maps were included in the E_{Phys} group.

inside the LEP tunnel, and as a cross check to the analysis described above, a separate campaign to map the total bending field of the magnet was carried out, this time with a chariot carrying NMR probes and moving along a mock beam pipe section. Such a device is known as a “magnet mole” or “traveling mole”. The details of this analysis can be found in [40]. Equipped with one Type 1 and one Type 2 NMR probe for measuring the core bending field, and with a search coil for measuring the fringe fields, the traveling mole was used to measure the integrated bending field of the spectrometer magnet both in the ISR tunnel and in LEP under different operating conditions. Linear fits like those defined by Equation 2.19 were performed and the residuals checked. It was found that the two mapping set-ups are compatible giving similar residual distributions. From fits to all available maps from both methods a relative error on the predicted bending field of 3×10^{-5} is obtained from the RMS of expression 2.34, in agreement with the resolution found using the measuring arm measurements. This is the only test of the reproducibility of field predictions after the magnet was moved to the LEP tunnel and it is chosen as the final estimate of the relative accuracy to which $\int B \cdot dl_{\mathrm{Spect}}$ can be predicted.

2.7.6 Analysis of 1999 Data

Five multi-point fills, including at least one RDP measurement and one high energy point, were taken in 1999. From these, the performance of the spectrometer in the RDP region was estimated. The spectrometer was found to be unbiased in this regime, with an uncertainty, given by the RMS spread of the results, of 8 MeV:

$$E_{Spect} - E_{RDP} = 3.0 \pm 8.0 \text{ MeV}(RMS), \tag{2.35}$$

The quantity $E_{Spect} - E_{RDP}$ is shown for the five fills in Figure 2.19. Two of these five multi-point fills were ramped to physics energies and spectrometer measurements carried out. Together with one two-point fill with one measurements at RDP energy and one at high energy, these fills were used to measure the deviation of E_{BEAM} as predicted by the spectrometer from the value predicted by the NMR extrapolation method. The results for each of the three fills can be seen in Figure 2.20. The

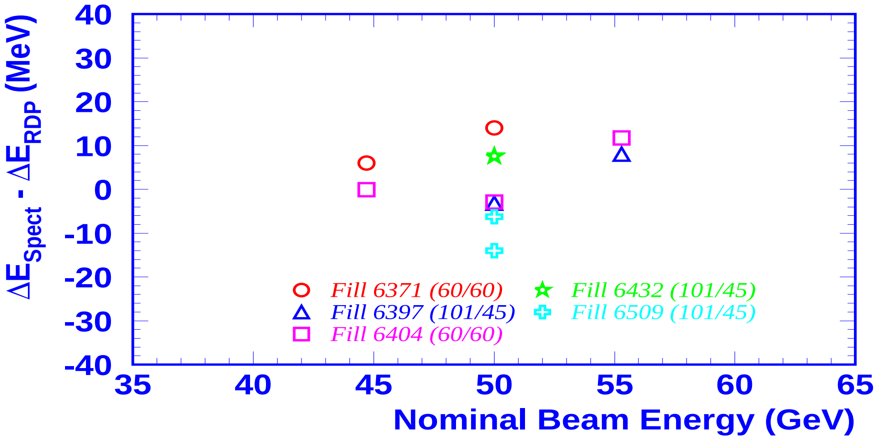

Figure 2.19: Difference between energy *intervals* measured by RDP and the LEP Spectrometer for different calibration energies. The first RDP point (41 GeV) is omitted as it is used to calibrate the spectrometer and so has zero difference by definition.

spectrometer is found to be unbiased with respect to the NMR method, this time with an RMS uncertainty of 15 MeV:

$$E_{Spect} - E_{NMR} = 0.5 \pm 15.0 \text{ MeV}(RMS), \tag{2.36}$$

It must be pointed out that these numbers are based on the limited statistics of the 1999 data sample. Therefore the uncertainty on the RMS spread of the results given in 2.35 and 2.36 is large. Furthermore, the Spectrometer is under development and the data analysis and calibrations are by no means final at the time of writing. Therefore all numbers concerning uncertainties are preliminary. No attempt has been made to assign an uncertainty from the BPM bend angle analysis or the RF corrections. Both are expected to be larger than the uncertainty due to the measurement and modelling of the integrated bending field presented in this analysis.

2.7.7 Conclusions

The integrated bending field of the spectrometer has been mapped. A model of the bending field during LEP operations has been developed and shown to give predictions of $\int B \cdot dl_{\text{Spect}}$ well within the tolerance required for the beam energy

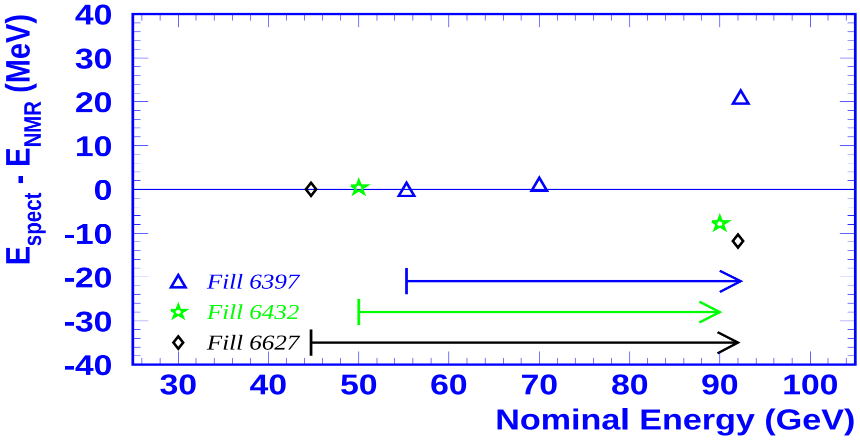

Figure 2.20: Difference between beam energy estimates from the LEP Spectrometer and the NMR method in fills with RDP and high energy points.

determination. The uncertainties due to the measurement of the bend angle of the beam and the RF model corrections used in the E_{BEAM} measurement strategy are under investigation. There are clear indications that these are larger than the uncertainty on $\int B \cdot dl_{\text{Spect}}$ and therefore the dominant sources of error. The data of 1999 has been analysed to test performance of the spectrometer. The 15.0 MeV error on $E_{Spect} - E_{NMR}$ given in Equation 2.36 gives a preliminary confirmation of the feasibility of the Spectrometer as a means to test the validity of the linearity assumption which forms the basis of the NMR extrapolation method. Although the statistics are limited and there is scope for improvement in precision, these first Spectrometer results seem to confirm the NMR extrapolation method.

2.8 The Synchrotron Tune Q_s

The Synchrotron tune Q_s is defined as the ratio of the synchrotron oscillation angular frequency of a bunch in a storage ring, Ω, and the revolution angular frequency, ω_{LEP} ($= 2\pi f_{LEP}$). It is an observable that is dependent on the energy loss per turn, U_0, which is itself directly dependent on the beam energy:

$$U_0 = \left(\frac{C_\gamma}{\rho}\right) E^4_{Beam}, \tag{2.37}$$

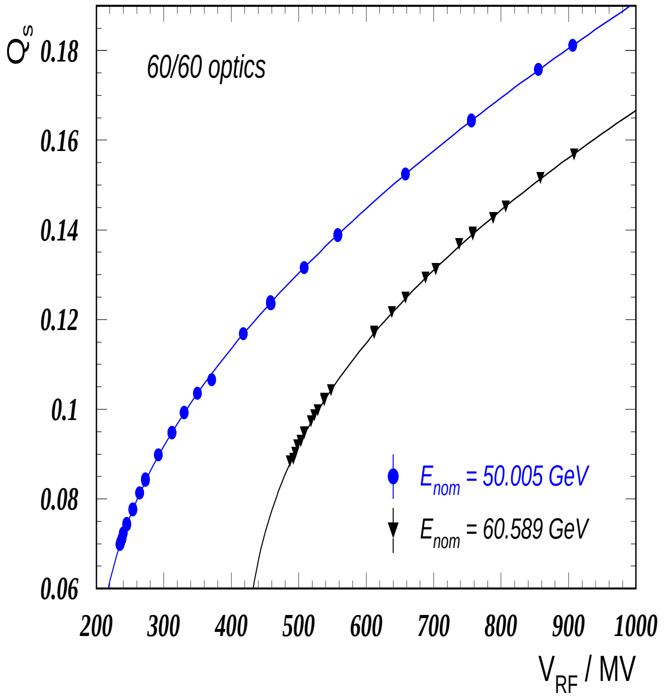

Figure 2.21: Measurements of Q_s as a function of the total effective accelerating voltage V_{RF}. Data points for two energies are superimposed on curves representing the fitted function described by Equation 2.38.

where C_γ is constant for each particle type and ρ is the mean bending radius of the charged particles. The synchrotron tune Q_s can be expressed as [41]:

$$Q_s^2 = \left(\frac{\alpha_c h}{2\pi E_{Beam}}\right)\sqrt{e^2V_{RF}^2 + bV_{RF}^4 - (U_0+K)^2}, \tag{2.38}$$

where α_c is the momentum compaction factor, h is the harmonic number[11], V_{RF} is the total RF voltage, and K takes into account energy losses due to sources different to synchrotron radiation in the LEP dipole magnets, like synchrotron radiation due to the dipole component of quadrupole and corrector magnets and the resistive part of the longitudinal impedance arising from beam-induced parasitic modes. The V_{RF}^4 term accounts for the inhomogeneous distribution of the RF voltage around LEP. Q_s is measured from a Fourier analysis of the measured phase difference between a bunch and the RF frequency. The Fourier analysis is performed with a spectrum

---

[11] The harmonic number h, relating the revolution frequency f_{LEP} and the RF frequency f_{RF} through $f_{RF} = hf_{LEP}$, is 31320 for the LEP ring.

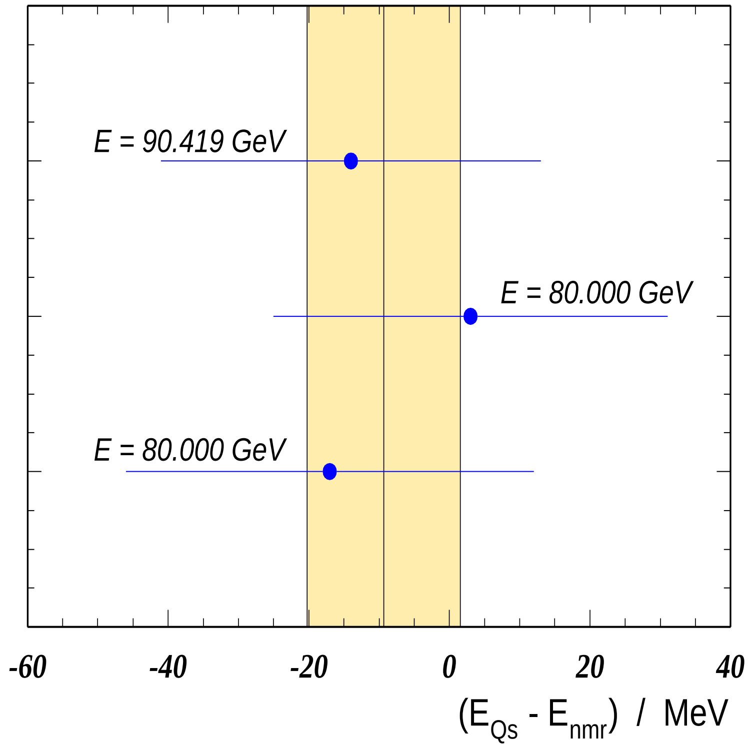

Figure 2.22: Differences between Q_s and NMR model measurements of E_{BEAM} for the three Q_s measurements performed in 1998 and 1999. The vertical line and band give the average value and statistical scatter of the measurements.

analyser, and the Q_s peak extracted manually, as spurious spikes in the signal make a fully automated measurement impossible. In practice the measurement is averaged over many turns and all bunches. The uncertainty on the measurement of Q_s is dominated by the manual reading, which has an RMS scatter of 3×10^{-4}. Q_s is fitted against V_{RF} according to Equation 2.38 in order to extract E_{BEAM}. Low energy voltage scans are made to calibrate V_{RF} against the NMR model. The measurement is then carried out with a voltage scan at high energy. The correction factors present in Equation 2.38 are obtained from dedicated measurements and from model simulations. A measurement with V_{RF} scans at two different energies can be seen in Figure 2.21. The sensitivity of this method is ~ 25 MeV and, to a good approximation, independent of energy. The sources of error are the statistical component which comes in as the error in the fit of expression 2.38, uncertainties in the modelling of the total additional energy loss K, the calibration of V_{RF} against the NMR model, and the determination of machine parameters α_c and ρ. There is scope for reducing the error by better understanding the systematic uncertainties.

This method was used to determine E_{BEAM} at high energy in 1998, 1999 and 2000. The results from the first two years can be seen in Figure 2.22. It can be seen that the agreement between the two methods is very good. The combined difference between the values of E_{BEAM} predicted by the Q_s method and the NMR model is:

$$E_{Q_S} \; - \; E_{NMR} \; = \; -9 \; \pm \; 11 \text{ MeV } (RMS). \tag{2.39}$$

With three measurements, the uncertainty on the RMS scatter of the measurements is quite large. However, the results seem compatible with the NMR model and very encouraging. At the time of writing further analysis involving the measurements taken in 2000 is underway with a view towards improving both the statistical and systematic sensitivity of the method.

Chapter 3

The DELPHI Detector

3.1 Introduction

This chapter contains a general description of the DELPHI detector. Only those sub-detectors relevant to the analysis presented here will be described. More detailed information about the whole detector can be found in [42, 43]. The Data Acquisition System (DAS) and the offline data processing stream will be outlined.

3.2 The Delphi Detector

DELPHI (DEtector with Lepton, Photon and Hadron Identification) is a 4π general purpose detector situated at interaction point 8 (IP8) on the LEP ring. It is the most complex of the four LEP experiments, containing the highest number of sub-detectors. This design was to combine good tracking efficiency and calorimetry over the greatest solid angle possible, precise micro-vertexing for identification of heavy quark decays, and particle identification over a large range of energy and momenta. The last requirement was the motivation to fit DELPHI with Ring Imaging Čerenkov detectors (RICH), a unique choice among LEP experiments. The detector consists of a cylindrical barrel region and two endcaps, which can be removed to allow access to the inner sub-detectors. The general layout of DELPHI can be seen in Figure 3.1. It has both a diameter and length of $\sim$ 10m and weighs $\sim$ 3500 tons. Its sub-detectors will be grouped, for this discussion, as trackers, calorimeters, muon system, luminometers, and RICHs. All except the RICHs and the VSAT luminometer will be

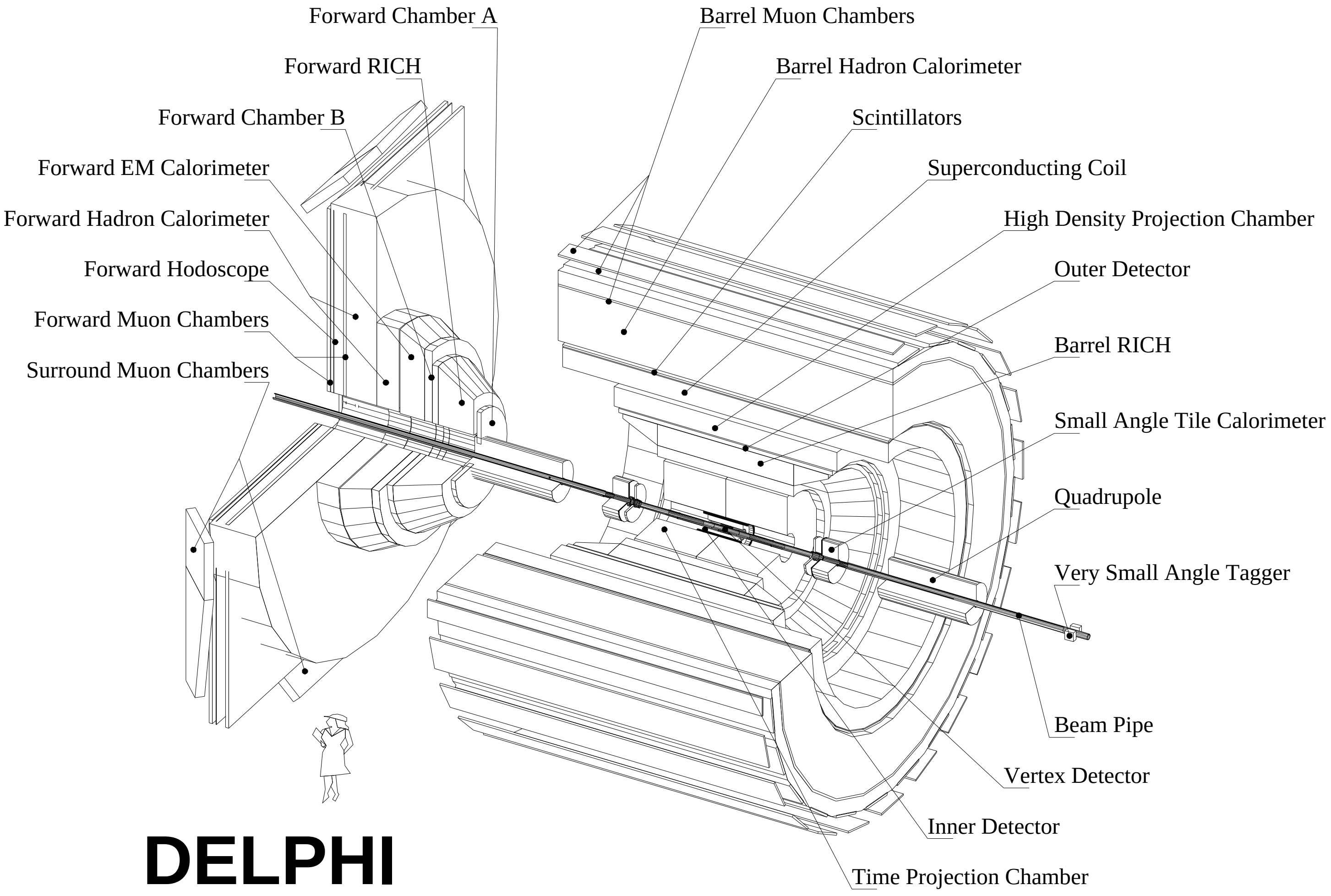

Figure 3.1: A view of the DELPHI detector showing the barrel section and one endcap.

discussed in the following sections, as no information from these sub-detectors is used for this analysis. The beryllium beampipe running down the centre of DELPHI has a radius 5.6 cm. The DELPHI Cartesian coordinate system is defined with the origin at the nominal interaction point, the z-axis in the direction of the incoming e^-, the x-axis towards the centre of LEP and the y-axis towards the surface. The (R, θ, ϕ) coordinate system is defined with the R and ϕ are polar coordinates lying on the x-y plane and the θ coordinate taken with respect to the z–axis. It can be seen in Figure 3.2.

3.3 Tracking Detectors

Tracking detectors exploit the ionising properties of charged particles passing through their active volumes. They are designed to maximise the tracking precision, which in principle requires more ionisation, while minimising the disturbances on the ionising particle due to its interactions with matter. This dictates that the detectors must find the highest controllable ionisation with the least possible mass within the active volume.

The tracking detectors are situated within a magnetic field. In DELPHI the field lines run parallel to the z direction, causing charged particles to describe curves in the xy plane. This curvature is used to estimate the charge and momentum of the particles. To this effect, DELPHI is equipped with the world's largest superconducting solenoid magnet, with a radius of 2.6 m and a length of 7.4 m . It produces a constant 1.23 T field. There are correcting coils at both ends of the solenoid to maintain the direction of the field parallel to the z axis in the end regions. The iron of the hadron calorimeter is also acts as the return yoke for the field. Table 3.1 summarises general characteristics of the tracking sub-detectors, including their angular acceptance and spatial resolution. The combination of track information from different sub-detectors is carried out in the Online and Offline Processing, which will be described in Section 3.8. The resolution of a track passing through all the tracking sub-detectors in the barrel region can be estimated from 45 GeV muons from Z^0 peak decays. The mean relative resolution on the inverse momentum, $\sigma(1/p)$, was found to be 2.6% [43].

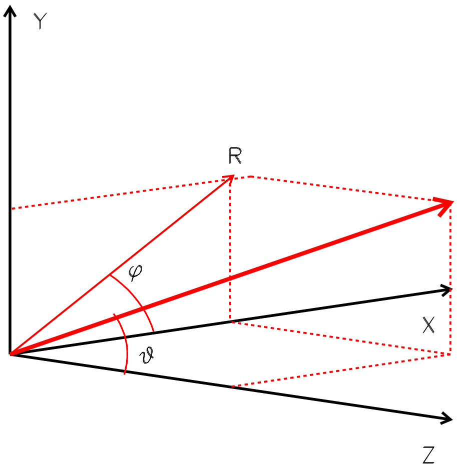

Figure 3.2: The DELPHI coordinate systems. The origin is the interaction point and nominal centre of the detector. The z direction points along the direction of the e^- beam, the x direction towards the centre of LEP , and the y direction towards the surface.

	Position		Acceptance θ $(+z)$ (°)	Maximum Number of points along track	Resolution per point (σ) (mm)
	R (cm)	$\lvert z\rvert$ (cm)			
VD	6.6/9.2/10.6	≤ 24	≥ 21	$R\phi$: 3 z: 3	$R\phi$: 0.008 z: 0.010
VFT	–	–	11 – 26	4	x, y: 0.1
ID drift	11.8 – 22.3	≤ 62	≥ 10	24	$R\phi$: 0.085
ID straws	23 – 28	≤ 105	≥ 15	5	$R\phi$: 2.4
TPC	35 – 111	≤ 134	≥ 20	$R\phi, z$: 16 $R\phi$: 192	$R\phi$: 0.23 z: 0.9
OD	198 – 206	≤ 232	≥ 43	$R\phi$: 5 z : 3	$R\phi$: 0.11 z: 44
FCA	30 – 103	155 – 165	11 – 33	6	0.3
FCB	53 – 195	267 – 283	11 – 35	12	0.25

Table 3.1: Specifications and performance of the DELPHI tracking sub-detectors as operated in 1996. The resolution in z is given for tracks which crossing the VD at 90°.

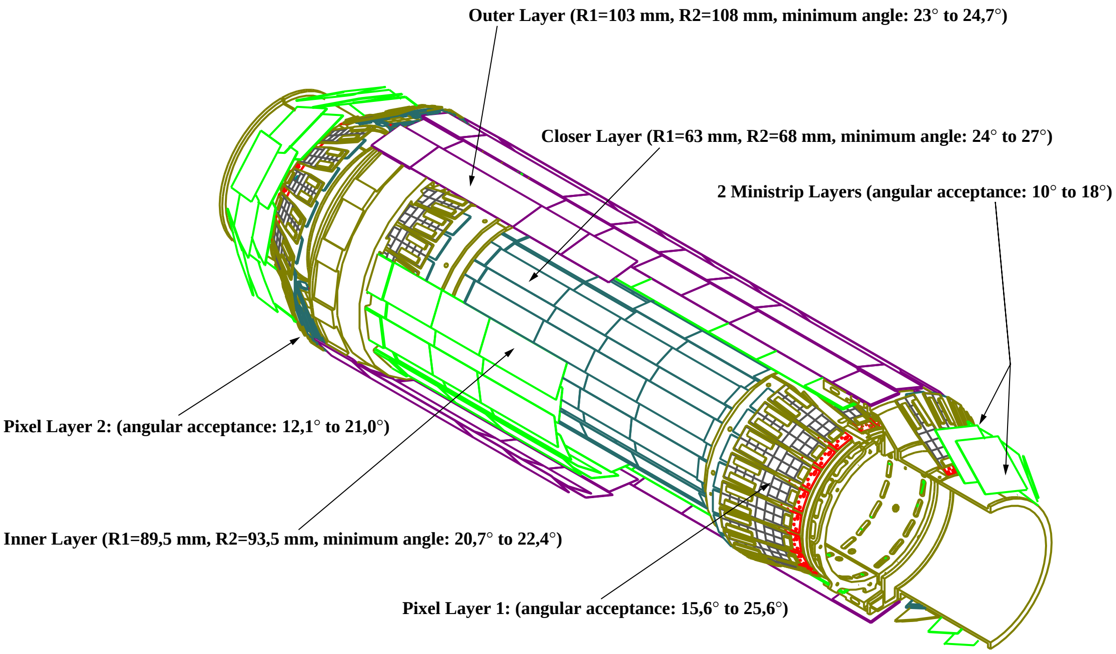

Figure 3.3: A diagram of the silicon tracker showing the 3 shells forming the barrel VD and the 4 layers of pixels and ministrip detectors which form the forward VFT .

3.3.1 The Silicon Tracker

In the spring of 1996 the silicon tracker was upgraded in order to improve the tracking, impact parameter resolution of secondary vertices, and the hermeticity in the forward regions of DELPHI [44]. This was achieved by replacing the old vertex detector (VD) by one twice its length, and by the addition of the Very Forward Tracker (VFT). Both sub-detectors are described below. The silicon tracker is illustrated in Figure 3.3, with details regarding the acceptance of its constituents.

Vertex Detector (VD)

The current VD uses the same module design as its predecessor, but the length of its outer layers has been doubled to 48 cm. It consists of three concentric shells of doped silicon ministrip detectors with average radii of 6.6, 9.2 and 10.6 cm. The polar angular acceptance is of $21° \leq \theta \leq 159°$. Parts of the old VD have been used to add double-sided readout to most of the inner layer. The detector elements in the outer layers are made of two back-to-back pieces of silicon with single readout, giving both $R\phi$ and z coordinate information. The detector elements in the central region of the middle layer are the only ones not to provide three dimensional information. The pitch of the ministrips parallel to the z axis is 25 μm with every other diode being read out. The pitch in Rz varies between 42 μm and 120 μm to optimise the resolution on tracks of different inclination. The use of double–sided readout in the inner layer and light mechanics in the whole detector is intended to minimise multiple scattering, thereby enhancing the resolution. The upgrade of the VD resulted in great improvements in vertexing resolution over a large polar range.

The Very Forward Tracker (VFT)

The VFT is made of two layers, named *crowns*, of silicon pixel detectors and two of silicon ministrip detector, placed at either end of the VD. Its installation was completed in time for the 1997 run. The ministrips are pitched at 100 μm and are placed back-to-back, with a stereo angle of 86° to aid pattern recognition. The pixel crowns consist of 1.2 million detector elements with an active area of 330 $\mu\text{m} \times 330$ μm. The angular acceptance of the VFT layers is between $10.0° - 25.6°$ in the $+z$ direction. Its inclusion had greatly increased the forward tracking and hermeticity of DELPHI.

3.3.2 Inner Detector (ID)

The ID consists of two concentric sections: an inner drift chamber and an outer straw tube detector. It measures the $R\phi$ coordinates of tracks, both for tracking and for trigger information. It was extended in the z coordinate in 1995 to match the extension of the silicon tracker. The drift chamber is composed of 24 azimuthal sectors, each containing 24 sense wires parallel to the z-axis. They are placed at intervals on the plane that bisects each sector longitudinally, giving up to 24 points for each track, subject to a left-right ambiguity. The drift field in each sector is proportional to the radial distance, R, such that the arrival times of the drift electrons at the sense wires from a single track are essentially simultaneous. This is to provide fast spatial information for the trigger.

The straw tube detector consists of 5 concentric layers of 192 tubes each. They enhance the $R\phi$ resolution of the detector and help solve the left-right ambiguities from the drift chamber.

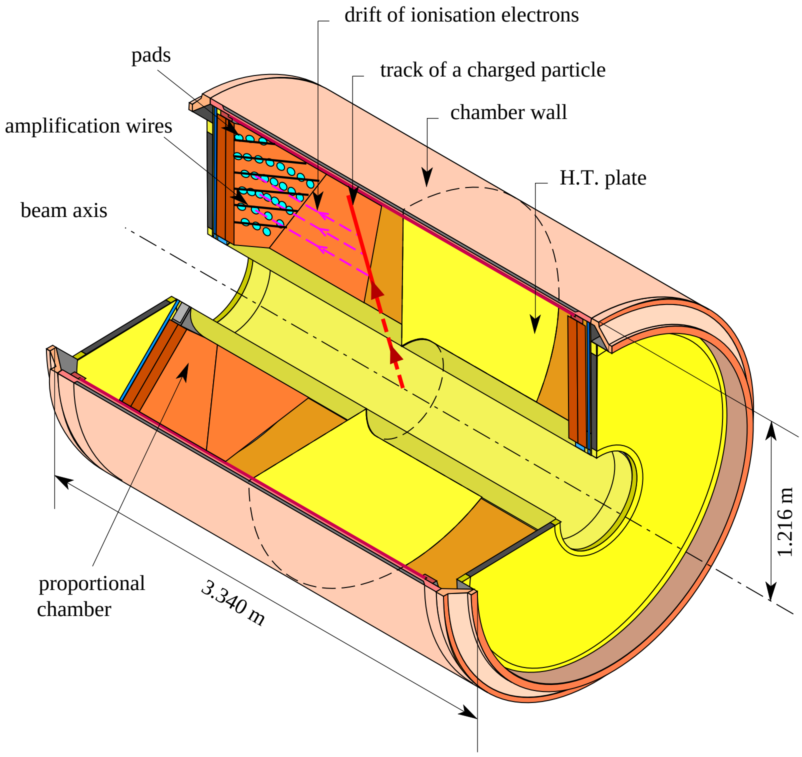

Figure 3.4: The interior of the Time Projection Chamber showing the passage of a charge particle and the subsequent shower of liberated electrons and ions.

3.3.3 The Time Projection Chamber (TPC)

The TPC is the principal tracking detector in Delphi. A cut away view of it can be seen in Figure 3.4. Its two drift chambers are symmetric about the $\theta = 90°$ plane and are separated by a high voltage plane, which gives reduced tracking efficiency at $\theta \approx 90°$. The drift volumes are filled with a 4:1 mixture of argon and methane and subject to a 187 Vcm^{-1} electric field parallel to the z axis. Electrons liberated by the traversing ionising particles drift towards the end planes at the end of each of the two sectors. The end planes are each divided into 6 azimuthal sectors. These are Multi Wire Proportional Chambers (MWPCs). Each sector has 192 sense wires, located 4 mm in front of the end plane. The end planes are divided into 16 circular rings made out of a total of 1680 cathode pads. The rings are equally spaced in R. The cathode pads collect the charge induced by the avalanche of the drift electrons as they approach the sense wires, providing an $R\phi$ measurement, typically consisting of up to 16 points per track. The z coordinate is determined from the time of arrival of the charge at the sense wires. $\frac{\mathrm{dE}}{\mathrm{d}x}$ information, which can be used for particle identification, is obtained from the magnitude of the charge deposited on the wires. The angular acceptance of the TPC is between polar angles of 20° and 160°.

3.3.4 The Outer Detector (OD)

There is no tracking information available from the volume of the Barrel RICH detector (BRICH). In the absence of BRICH, its volume would be filled my the TPC, which would consequently have better resolution. The Outer Detector (OD) is an extra tracking detector placed between the BRICH and the electromagnetic calorimeter. Its main purpose is to improve the resolution of the TPC and thus compensate for the presence of the BRICH. The OD consists of five concentric layers of limited streamer drift tubes. The layers are staggered with respect to each other to resolve left-right ambiguities. All the layers provide $R\phi$ information, and three of them use the time delay of the signal arriving at each end to estimate the z coordinate of the track. (R, ϕ, z) information can be quickly calculated and used for triggering decisions.

3.3.5 Forward Tracking Chambers

Each of the two DELPHI endcaps houses identical systems of tracking chambers. Each is composed into two sub-detectors, one on each side of the Forward RICH detector (FRICH).

Forward Chamber A (FCA)

The Forward Chamber A is placed next to the endcap of the TPC. It contains three modules made of 2 staggered layers of drift tubes operating in limited streamer mode. Each module is rotated by 120° with respect to its neighbours for improved pattern recognition.

Forward Chamber B (FCB)

FCB plays a similar role to the OD in the barrel region: it provides added tracking information to compensate for the volume occupied by the FRICH. It is a drift chamber divided into two independent semi–circular modules. Each module is equipped

Detector	Position		Acceptance	Depth		Energy Resolution
	r (cm)	$\lvert z \rvert$ (cm)	θ ($+z$) (°)	X_0	λ	$\sigma(E)/E$ (E in GeV)
HPC	208 – 260	≤ 254	≥ 43	18	0.6	$0.043 \oplus (0.32/\sqrt{E})$
FEMC	46 – 240	284 – 340	10 – 36.5	20	1	$0.03 \oplus (0.12/\sqrt{E}) \oplus (0.11/E)$
HCAL barrel	320 – 479	< 380	≥ 43	57	6	$0.21 \oplus (1.12/\sqrt{E})$
HCAL forward	65 – 460	340 – 489	10 – 43	57	6	–
STIC	6.4 – 41	218 – 249	1.7 – 10.6	27	–	$0.015 \oplus (0.135/\sqrt{E})$

Table 3.2: Specifications of the DELPHI calorimeters. Here, X_0 and λ are the radiation and interaction length respectively, both of which are defined in the text. A detailed account of the determination of the energy resolutions is given in [43].

with 12 planes of sense wires, located in the $R\phi$ plane. Each plane has a 120° offset in ϕ with respect to the previous one. Pairs of planes with wires parallel are staggered with respect to one another, to further aid the pattern recognition.

3.4 The Calorimetry

The calorimeter system at DELPHI measures the energies of electrons and photons (electromagnetic calorimeters), and charged and neutral hadrons (hadron calorimeters). It also serves as a veto for the muon tagging algorithms, since muons deposit little energy in them, unlike other particles. Table 3.2 shows the position, acceptance and resolution of the individual calorimeters.

3.4.1 Electromagnetic Calorimeters (ECALs)

The ECALs measure the electromagnetic showers that result from the interactions of photons and electrons with the nuclei inside their active volume. Energetic photons can create e^+e^- pairs when interacting with the active material of the ECAL. These electrons and positrons can emit *bremsstrahlung* photons, and this electromagnetic shower process can continue until the photons and electrons produced have not enough energy for further particle pair production. The shower can be initiated by a prompt photon or from a photon radiated by a prompt electron in the active

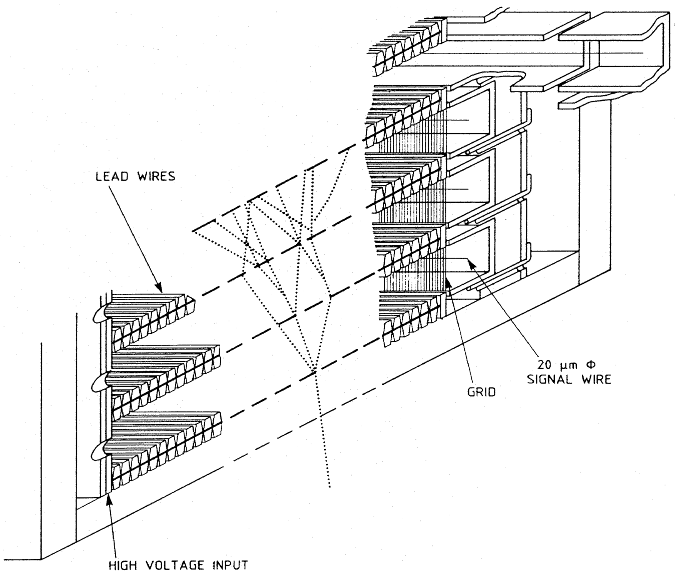

Figure 3.5: A cut away view of part of an HPC module including the development of an electromagnetic shower from an incident electron or photon.

volume of the calorimeter[1]. The ECALs are designed to absorb all the energy of a typical electron (positron) or photon, whose energy dependence is given by:

$$E(x) \quad = \quad E(0)e^{-\frac{x}{X_0}}$$

where $E(x)$ is the mean energy of a particle in a shower at a distance x from the shower origin, $E(0)$ is the incident energy of the electron or photon, and X_0 is the radiation length. A high value of X_0 gives a higher probability for all the energy of the incoming particle to be absorbed, but the ability to measure the energy itself is also an important consideration. In DELPHI two different ECAL designs are used for the barrel and endcap regions.

High density Projection Chamber (HPC)

The HPC is a time–projection sampling calorimeter situated in the barrel region of DELPHI. It provides three dimensional information on the development of electromagnetic showers. It is divided into six sectors in the z direction and 24 sectors in ϕ, making a total of 144 modules. Each of the modules is a trapezoidal volume with a width of 52 cm closest to the centre of DELPHI and 64 cm on the outside. Its

---

[1] Here, by "prompt" we refer to a particle that is not the product of showering in the calorimeters.

length and height are 90 and 47 cm respectively. The modules consist of 41 layers of lead wires immersed in a gas drift volume [2]. The lead volume provides the dense material in which e^+e^- production and electromagnetic showering occurs, while the gas serves to sample the magnitude and profile of the shower as it evolves through the different layers. The sampling and profiling technique is time projection. In a similar way to the TPC, the charge of the particles ionised in the gas volume is collected by a proportional chamber at the end of each module, as can be seen in Figure 3.5. The three–dimensional shower profiling allows for precise reconstruction of the direction of single photons and photon pairs coming from the decay of neutral pions. These leave no trace in the tracking system. The single–photon angular resolution is 1.0 mrad in θ and 1.7 mrad in ϕ. The shower profiling also gives some discriminating power to distinguish between charged pions and electrons.

Forward ElectroMagnetic Calorimeter (FEMC)

The FEMC detectors, located on each of the endcaps of DELPHI, are Čerenkov calorimeters. They consist of 4532 lead glass blocks on either side, each one being a wedge shaped truncated pyramid with a depth of 40 cm, which corresponds to 20 radiation lengths, pointing towards the interaction point. The blocks have a 1° ϕ twist with respect to each other to prevent particles escaping down the dead regions between them. The energy of particles is measured from the Čerenkov light they emit as they traverse the lead glass. The emitted photons are collected by photomultipliers. The energy of a shower is estimated after clustering the deposits in adjacent blocks and is calibrated using Bhabha events[3]. The energy resolution of the FEMC is degraded due to the presence of $\sim 2X_0$ of scattering material located between itself and the interaction point, in particular the end planes of the TPC and the FRICH.

3.4.2 Hadron Calorimeter (HCAL)

The HCAL is housed in the return yoke of the DELPHI solenoid magnet. It consists of two endcap sections containing 12 modules each, and a barrel section containing

---

[2] One gap between the lead wires, close to the expected maximum in shower activity, contains a layer of scintillator which provides trigger information.

[3] In the region where θ is below 32° the electron energy is greatly degraded by interactions with supporting structures of the TPC.

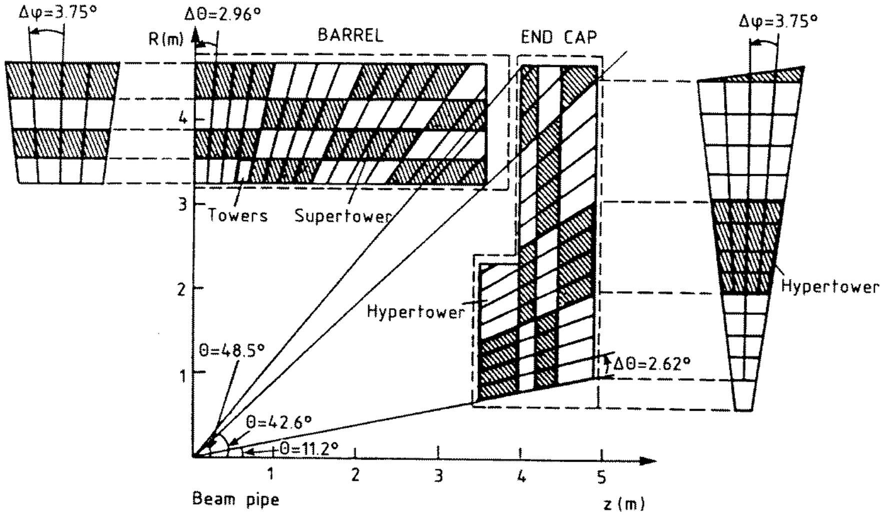

Figure 3.6: The HCAL readout geometry in the Rz plane. The diagram included both the barrel and the endcap region.

24. The sectors are azimuthal modules, with a further division defined by the xy plane in the barrel region. All sections follow the same design principle. The energy is measured by sampling secondary hadrons produced by inelastic interactions of the incoming particle with the atomic nuclei in the active material. In a similar manner to the development and profiling of electromagnetic showers in the HPC, the HCAL consists of layers of active material interspersed with a sampling detector. The active material is provided by 20 and 19 layers of 5 cm thick iron for barrel and endcap regions respectively. Between the iron planks are placed $\sim$ 19,000 8 cm wide gaseous drift tubes, operating in limited streamer mode. They vary in length between 40 and 410 cm. They are read out with copper readout boards such that each one covers a fixed angular range of 3.75 ° in azimuth and 2.96 ° in θ. They are segmented into towers pointing radially towards the interaction region. Boards from between 4 and 7 layers are read out together, depending on whether they are in the barrel or endcap region. The readout geometry can be seen in Figure 3.6. An independent system is in place to read out the cathodes of individual streamer tubes, improving the granularity of the detector and allowing for better $\pi - \mu$ separation. This system has been in place since 1994. The HCAL has a depth of approximately six interaction lengths λ^4. This means that very few particles except muons penetrate beyond the

---

[4] λ is defined as the mean free path between interactions in the active material.

	Position r (cm)	Position $\lvert z \rvert$ (cm)	Acceptance θ $(+z)$ (°)	No. Points along Track	Resolution per point σ (mm)
MUB	~ 445	≤ 385	$52 - 128$	$2 - 6$	$r - \phi$: 1.5 z: 10
MUF	$70 - 460$	463/500	$9 - 43$	$4(x, y)$	x, y: 1.0
MUS	550	487	$42 - 53$	2	10×10

Table 3.3: Specifications of the DELPHI muon chambers. The resolution quoted for the MUS is given in the local coordinate system of each chamber.

HCAL.

3.5 The Muon Chambers (MUC)

Since muons are practically the only particles to penetrate through all the calorimeters, the MUC are the outermost sub-detector in DELPHI . The basic identification procedure is to associate hits in the MUC system to an extrapolated track, taking into account the return field of the solenoid magnet in the HCAL and the scattering of the muon as it traversed the material in the different sub-detectors. The MUC consists of three separate sets of chambers corresponding to different solid angle regions. Their specifications can are summarised in Table 3.3.

3.5.1 Barrel Muon Chambers (MUB)

The Barrel Muon Chambers were designed and built in Oxford. During the lifetime of DELPHI the Oxford group was responsible for their running and for the offline muon analysis software. The MUB consists of a set of drift chambers split into 24 azimuthal sectors. Each sector is divided in half at the $z = 0$ plane and contains three sets of modules. The layout of the modules within a sector can be seen in Figure 3.7. The outer and peripheral modules have seven drift chambers each, arranged in two staggered layers. The inner modules are inside the iron of the HCAL and consist of 14 drift chambers set in three staggered layers. Only two of the three layers are read out. The third one is placed as a precautionary measure. Since these drift chambers are not accessible for repair, in case of a malfunction in one of them another one from the redundant layer can be brought online. The peripheral modules are offset

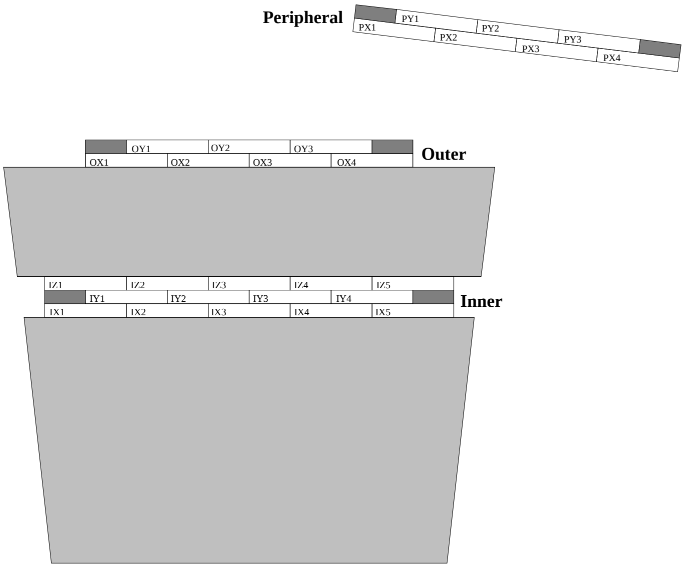

Figure 3.7: An xy view of the layout of a MUB sector. The grey shading indicates the position of the HCAL.

in ϕ with respect to the other two in order to cover the azimuthal region out of the acceptance of the inner and outer modules. The staggered setup of the different layers is to resolve the left-right ambiguities of single drift chambers.

Each chamber consists of a volume of gaseous mix (85.5% argon, 8.5% methane and 6% carbon dioxide) which charged particles ionise, an anode wire running along the centre of the chamber parallel to the z axis, and cathode grading strips running along the inner walls of the chamber. The anode wire is kept at a nominal voltage of 6.15 kV in operating conditions, so that the chambers operate in the proportional streamer mode. The drift field is kept constant at 400 Vcm^{-1} by the copper grading strips. The $R\phi$ coordinate is given by the time delay in the signal on the cathode wire with respect to the beam cross-over (BCO) and is used for triggering decisions. The z coordinate is calculated by the relative time difference in the arrival of a signal at either end of the chamber. To this effect, one of the cathode grading strips is set up as a delay line which picks up a signal from the avalanching electrons from the gas. A cross section of a typical chamber can be seen in Figure 3.8.

3.5.2 Forward Muon Chambers (MUF)

The MUF consists of two planes of limited streamer drift chambers on each endcap. Their design is similar to that of the MUB chambers. The planes are divided into

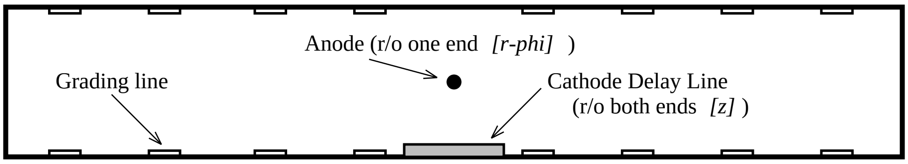

Figure 3.8: A cross-section view of a MUB drift chamber

quadrants, each containing two layers of 22 drift chambers. The layers are orthogonal to each other to provide xy information. The inner plane of the MUF is inside the iron of the HCAL.

3.5.3 Surround Muon Chambers (MUS)

The MUS was added in 1994 to cover the solid angle region not covered by the MUB and MUF, around $\theta \sim 45$ ° and $\theta \sim 135$ ° at the top, bottom, left and right of each endcap. It consists of four modules on each endcap, each one containing two staggered layers of streamer tubes identical to those used for the sampling detectors in the HCAL.

3.6 The STIC Luminometer

The Luminosity measurement at DELPHI is performed by measuring the small angle Bhabha scattering cross section ($e^+e^- \to e^+e^-$). This method is the same one used for the high precision measurement made at LEP1 [45]. A precise knowledge of the beam parameters, of the theoretical expectation of the cross section, coupled with the clean experimental signature, which results in high purity of signal, and the high statistics yielded by the process, allow for a very precise measurement. Bhabha scattering is dominated by QED processes at low angles, allowing for a precision of 0.25% at LEP2 energies [46]. The dominant uncertainties are the focusing effect of the quadrupole focusing magnets and the precision of the knowledge of the geometrical acceptance of the STIC. The STIC is a low angle electromagnetic calorimeter used for the luminosity measurement and to increase the hermeticity of DELPHI, providing measurements down to ~ 2 ° from the beam pipe. Its precise acceptance, resolution and position inside DELPHI are shown in Table 3.2. It is a

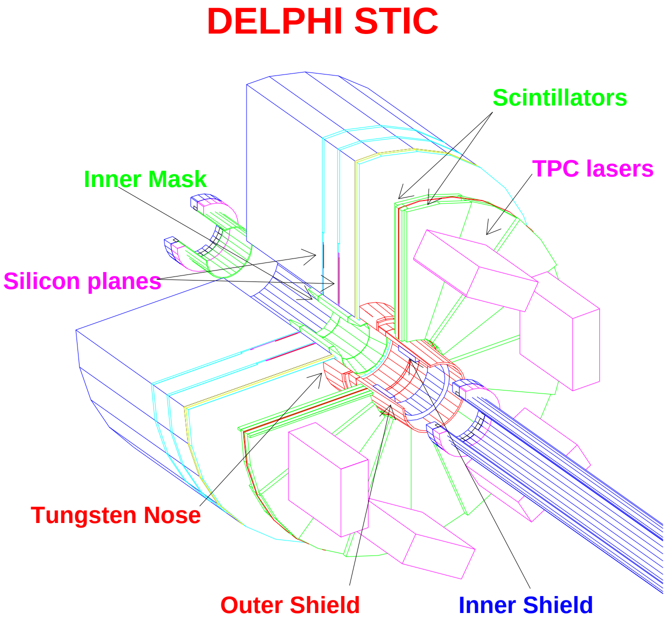

Figure 3.9: A cut away diagram of an arm of the STIC detector showing its main features.

lead/scintillator sampling calorimeter, consisting of two hemispheres of 94 alternating layers of lead and scintillator. Each layer is 3 mm thick. The scintillator layers are segmented into independent sectors to give the readout a tower structure with little cross–talk between channels. Particles from the electromagnetic shower, that develops as the electrons and photons interact with the nuclei in the lead plates, act on the scintillator. The light emitted is collected and taken to the back of the detector by some of the 1200 wavelength shifting optical fibres that run through the detector along the R direction[5]. This particular setup of alternating active material and sampler, traversed by optical waveguides, is known as the *shaslik* geometry. It allows for good photon collection efficiency and energy resolution without compromising hermeticity. The STIC is fitted with two layers of silicon detector to improve the reconstruction of shower direction and profile. Two planes of scintillator are placed in front of it to distinguish between incoming charged and neutral particles. The layout of one end of the STIC can be seen in Figure 3.9. A detailed account of its design and performance can be found in [47].

---

[5] the geometry of the detector has a ϕ twist to reduce the chance of particles escaping through the fibre channels or the gap between upper and lower hemisphere.

3.7 Online System

The Data Acquisition System (DAS) controls the storing of data from all the sub-detectors in DELPHI at every BCO. The trigger selects what data are stored and which are thrown away. All data are kept until the low level trigger reaches a decision. If the decision is to trigger on an event, the DAS then controls the merging and storage of the data. The BCO occurs every 22 μs [6], while the time taken to read out all the data from all the detectors is ~3.5 ms. The requirement for fast triggering decisions to minimise the dead time of the detector is met by dividing the trigger into four levels, which are described in the following section.

The Trigger

The four levels of the trigger are labelled T1, T2, T3, and T4, in order of increasing selectivity. T1 and T2 operate synchronously with the BCO. T1 is a loose pre-trigger, performing a logical OR based on triggering criteria for the ID, TPC ($\theta \geq 43^\circ$), OD, HPC scintillator, MUB, FCA, FCB, FEMC or STIC [7], reaching a decision $\sim$ 3.5 μs after the BCO. The rate of positive decisions passed on to T2 is ~700 Hz. T2 uses information from the TPC, HPC, HCAL and MUF sub-detectors and uses correlations between the data from different sub-detectors to make a decision. It typically takes ~40 μs to make a decision, at a rate between 5 and 10 Hz. T3 uses more detailed information from the sub-detectors to halve the rate of T2.

T4 uses event reconstruction algorithms to search for events with no good tracks or insignificant energy deposits. It is only run after tests have been performed to show that it will cause no loss of genuine physics events.

The DAS

The DAS is responsible for controlling the trigger system, described above, and managing the data flow. It controls the local data acquisition systems from the sub-detectors and provides their timing. The whole DAS, from individual sub-detectors

---

[6] This is with LEP running in four-bunch configuration.

[7] There is additional information available to the trigger from 2 scintillator detectors in DELPHI, which are situated between the solenoid and the HCAL in the barrel (Time Of Flight or TOF), and between the HCAL and the second MUF plane in the endcaps (Forward HOdoscope or HOF).

upwards, is based on FASTBUS crates. Most front-end sub-detector modules have four local buffers which can store one event each. If a logical AND of the BCO-synchronised T1 and T2 decisions is positive, data taking is paused for a few milliseconds while the data of each sub-detector is read out into one of the four local buffers (if any are available) in its crate processor. Otherwise, all the sub-detector electronics are reset readying DELPHI for data taking with little dead time. The T3 decision is made after $\sim$300 μs so the chance of all buffers being full at the moment of a positive T2 decision is very small. If the T3 decision is positive the data are passed on to a global event buffer where the data from the sub-detectors are merged and transferred to the surface through an optical link. In case of a negative T3 decision, the buffers for that event are cleared in the front-end of each detector. T4 then decides whether the data are interesting enough to be stored locally on disk and then copied on to tape at the main CERN site at Meyrin. In that case, the data are ready to be put through the offline event reconstruction `DELANA`, performed on the DELPHI computer farm.

The operation of each sub-detector is constantly monitored by Slow Controls. Quantities such as high voltage power supplies, gas systems, DAS electronics, background levels, *etc*, are available in real-time to prevent damage to the detectors and to ensure efficient running.

The specifications and performance of the DELPHI DAS, trigger and Slow Control systems are found in [43] and the references therein. The DAS data taking efficiency ranges between 90 and 95%.

3.8 The Offline Processing

The DELPHI event reconstruction program `DELANA` [48] takes the vast amount of information contained in the raw data, consisting of individual channel signals, times and pulse heights, and makes charged tracks and neutral energy clusters. Particle identification is also performed at this stage. This processing of the raw data can be summarised as follows:

- **Track Data Objects (TDs).** The calibration of the sub-detectors is used to construct TDs in each sub-detector separately. TDs typically consist of coordinates of individual hit wires or energy deposits in calorimeter sectors or layers.

- **Track Element reconstruction.** The TDs from each sub-detector are analysed individually to link points into Track Elements (TEs). For the trackers, the TEs are short track segments, while for the calorimeters they are clusters of energy. Of particular importance to the DELPHI track reconstruction are TEs formed from hits in the TPC, or from hits in both the ID and OD (ID∩OD) or VD and ID (VD∩ID).

- **Full Track Fit.** TEs from the TPC, (ID∩OD), or (VD∩ID), are used as the starting point in a search for longer cross-detector tracks. Matched TEs are called Track Strings (TS) and are passed on to the global track fit, where left-right or z coordinate ambiguities are resolved. The resulting fitted track is called a TK.

- **TK Association.** The final step is to associate TKs with calorimetric energy deposits, muon chamber or RICH hits. To this effect, TKs are extrapolated into the calorimeters and energy deposits (calorimeter TEs) are associated to them. Simple particle identification information like $\frac{\mathrm{d}E}{\mathrm{d}x}$ from the TPC and RICH and muon chamber information are associated to TKs. Unassociated calorimeter TEs are clustered into neutrals.

The principal `DELANA` output is the Data Summary Tape (DST), which provides data that can be used for basic physics analyses. An added layer of central processing is implemented with the program `DSTANA`. It applies corrections to detector distortions and irregularities that have not been applied at the `DELANA` level, re-fits the TKs and performs the necessary associations. Thus, the data can be corrected for calibration distortions discovered after the `DELANA` output has been produced. Standard particle identification, such as muon, electron and b quark tagging is also repeated here. These can all be re-run at further stages in the analysis stream. The electron and muon identification are discussed in Section 4.2. The output of the `DSTANA` processing is the eXtended Short DST (XSDST) and is the starting point of the analysis presented here. A series of offline analysis tools are used for analysing the XSDST. This analysis relies on a chain of `PHDST` [49], `SKELANA` [50] and the W physics analysis code `WWANA` [51] .

Chapter 4

Data Selection

4.1 Introduction

This analysis uses standard track, run and event selection used and developed by the W team, in addition to DELPHI electron and muon identification routines. This chapter is intended to give a brief overview of these data selection tools. The reader is referred to more detailed accounts of these three aspects. The selection and treatment of tracks and calorimetric clusters, available as a standard option in the `SKELANA` XSDST reading program, is documented in [50, 52]. The electromagnetic clustering and electron and photon ID are performed with the package `REMCLU`, which is documented in [6]. The muon ID procedures are described in detail in [7, 43]. The event selection was developed for the W cross section measurement and is now standard for the $l\nu q\bar{q}$ and $q\bar{q}q\bar{q}$ channels. Some modifications have been made for this analysis, but the main features are the same. For a full account of the event selection and its application to the cross-section measurement see [53, 54].

4.2 Track Selection, Lepton and Photon ID

4.2.1 Track Selection

The track selection is applied to tracks reconstructed with the `DELANA` off-line analysis package [43] and has the aim of ensuring that tracks in simulated events provide a good description of tracks seen in real data events. This requirement should translate into a good agreement in global event properties. The track selection is implemented in order to reject badly modelled tracks in the data, without affecting the information carried in any given event. These tracks are typically badly reconstructed ones, fake tracks resulting from electronics noise, and tracks reconstructed from hits due to cosmic rays impinging on the detector. Therefore they carry little information concerning the underlying physics of the event. Details of the track selection can be found in [4, 52]. This section will provide an overview of the main cuts and criteria applied to charged and neutral tracks in the selection used for this analysis.

Charged Tracks

Charged tracks are selected according to their impact parameters in the $R\phi$ ($IP_{R\phi}$) plane and in the z (IP_z) direction, their momentum p_{track} and associated error Δp_{track}, and some criteria on the detectors contributing hits to the track. The requirements for the standard track selection used by the W team are:

- $IP_{R\phi} \ < \ 4cm$
- $IP_z \ < \ 4cm \times sin\theta$
- $\frac{\Delta p_{track}}{p_{track}} \ < \ 1.0$
- $0.1\text{GeV} \ < \ p_{track} \ < \ 1.5 \times E_{beam}$

The following tracks are rejected:

- ID$\cap$VD only tracks with no z information
- VD only tracks

Tracks failing the maximum momentum cut are re-fitted using the event primary vertex as a constraint. Rejected tracks are considered for the neutral track selection.

Neutral Tracks

The neutral track selection is based on the energy deposited in the calorimeters by neutral clusters. In addition to the neutral tracks reconstructed by `DELANA`, tracks failing the charged track selection but with an associated calorimetric energy deposit of more than 5 GeV are converted into neutral tracks by extrapolating the energy deposit back to the event vertex. The new track is then subject to the standard neutral track selection. Minimum energy cuts are placed on the HPC, FEMC, and STIC. In order to be selected, calorimetric showers must satisfy one of the following:

- $E_{HPC} > 0.3$ GeV
- $E_{FEMC} > 0.4$ GeV
- $E_{STIC} > 0.3$ GeV

For HCAL energy deposits a noise rejection algorithm is applied based on the shower's energy, its number of hits, and its longitudinal centre of mass.

Off-Momentum Electrons

The abundance of off-momentum electrons from the beam impacting on the STIC is such that there is a distinct possibility that this might happen in coincidence with physics events. Whereas the energy spectrum of these electrons is quite broad, they are forward peaked to such a degree that they can be suppressed by cutting out all STIC energy showers with polar angles lower than 3^o [55]. This cut is applied in this analysis.

4.2.2 Lepton Identification

Muon Tagging

The DELPHI muon chambers (MUC) are shielded by the iron in the Hadron Calorimeter (HCAL) and therefore in a very clean environment. Although the vast majority of hits in the MUC are due to muons passing through the chambers, there is a residual activity caused by hadronic punch-through pions from HCAL showers. This motivates the quality criteria placed on the association between MUC hits and tracks extrapolated from the DELPHI trackers, since signals from punch-through hadrons have more scatter with respect to extrapolated tracks than signals from muons of the same momentum [43].

Tracks are extrapolated from the central detectors taking into account the return field of the solenoid magnet. The errors on the track parameters are propagated using their covariance matrix. An error from the multiple scattering along the extrapolation region is included. The extrapolation gives $R\phi$ and z (x and y) coordinates at each MUB or MUS (MUF) layer and the ϕ and θ direction of the extrapolated track together with the error matrix at the innermost layer. Potential hits in the MUC layers are searched for and a χ^2 between the extrapolated track and the hit, χ^2_{hit}, calculated. These χ^2 values can then be used to reject "bad hits", the definition of which depends on the tag demanded by the user and controls the degree of hadron contamination in a muon candidate sample[1]. A global χ^2 fit is performed using the extrapolated tracks, "good hits", and the errors and correlations on those quantities. In the case of non-convergence of the fit the hit with the highest χ^2_{hit} is excluded. This procedure is repeated until the fit converges. The global χ^2, χ^2_{glob}, is used to select the best hit in the case where there are more than one in a layer and to resolve the left-right ambiguities in layers. Ambiguities resulting from the association of one hit to more than one track are dealt with by assigning the hit to the track with the most associated hits. Failing that, the χ^2_{glob} values are used to resolve the ambiguity. Recent studies of the efficiencies of muon tagging and track reconstruction have been performed at LEP2 using data from 1997 and 1998 [56, 57]. These point to differences in the efficiencies in data and Monte Carlo simulation. These are corrected for in the standard W^+W^- DELPHI common analysis stream. This analysis uses the "Very Loose" tag, with an muon identification efficiency of $\sim$ 98% within the acceptance of the DELPHI detector.

Electron and Photon Tagging

This analysis makes use of `REMCLU`[6], an electromagnetic cluster reconstruction package designed specifically for the LEP2 environment. Previously existing electromagnetic shower recognition tools `ELECID` , `FWELID` and `PXPHOT`, comprising the `ELEPHANT` [58] package, were developed and optimised for LEP1, where electrons

---

[1] The tags are named, in order of increasing purity, "Very Loose" (VL), "Loose" (L), "Standard" (S) and "Tight" (T).

were either inside hadronic jets, or isolated in QED events with very low multiplicity. In the LEP2 environment the final states available for e^+e^- interactions are more and high multiplicity events with high energy electrons and/or photons are quite common. These high multiplicity events are mainly due to two types of process: four fermion ones with two quarks, one or two electrons and possibly a photon of considerable energy in the final state; and radiative returns to the Z^0 resonance, characterised by two or more jets and at least one hard ISR photon, which typically falls outside the acceptance of the detector. Furthermore, it is these types of events which are of interest to this analysis. `REMCLU` treats electromagnetic showers in the barrel and end-cap regions differently. This package is relatively new to DELPHI and was incorporated into this analysis at an early stage. This analysis has served as a test to assist in the development of the `REMCLU` package, which is explained in some detail in this section.

- **HPC Electrons**. All tracks identified as muons are vetoed. Tracks with a momentum lower than 30 GeV are treated with the LEP1 tool `ELECID`, which uses E/p, dE/dx and shower profiling information from the TPC and matching of tracks to EM showers in z and ϕ. Tracks selected as "loose" `ELEPHANT` electrons are selected as `REMCLU` "tight" electrons. Tracks of a higher momentum are subject to a new tagging algorithm. The energy of photons in an angular region in θ and ϕ around the track is added to the energy associated to the track, resulting in a new cluster with energy E_{clus}. The angular region is symmetric in θ ($\pm 2^o$) and asymmetric in ϕ to take into account the bending of the track in the magnetic field of DELPHI. It is parametrised as $-2^o < (\phi_\gamma - \phi_e) \times q_e < 5^o$ where ϕ_γ and ϕ_e are the azimuth angles of the photon and electron respectively and q_e is the charge of the electron. The total energy inside this region is required to be greater than 10 GeV with a ratio to the track momentum, E_{clus}/p_{track} of at least 0.5. The HCAL energy deposits in a 5^o cone around the track have to be less than 10% of E_{clus} for the cluster to be tagged as a "tight" electron. Otherwise it receives a "loose" electron tag. The energy of the cluster, E_{clus}, is corrected for cracks in the HPC and low energy non-linearities. The energy associated to the new electron candidate is calculated from a weighted mean of the momentum of the track and the corrected energy of the cluster deposited in the HPC. The weight given to the latter is obtained from the magnitude of the correction, such that energy deposits from clusters with high correction factors receive small weights.

- **HPC photons**. Neutral HPC clusters with an energy greater than 500 MeV are put through transverse and longitudinal shower profiling algorithms derived from `PXPHOT`. The transverse profiling is based on the spread of energy deposits with respect to the shower direction and also includes a veto to double-peaked deposits which are likely to be due to two photons from π^0 decays. The longitudinal development relies on the sampling provided by the HPC pad rows with signal and on the centre of gravity of the shower along its direction. Photon candidates close to z or ϕ cracks have more relaxed selection criteria. Such candidates are given “loose” photon tags even if they don’t meet the criteria. However, showers of energies below 25 GeV are still subject to the longitudinal profile cuts to eliminate low energy backgrounds.

- **Forward Region Electrons and Photons**. The electromagnetic shower reconstruction efficiency in the forward region is less than in the barrel due to the lower number of tracking layers at small polar angles and to the presence of between one and two radiation lengths of material between the tracking and the FEMC calorimeter. This material leads to early showering of electromagnetic particles, difficulties in associating tracks to energy clusters, and the scattering of particles with a consequent loss in track finding efficiency and momentum resolution. The reconstructed electron momentum resolution in the forward region is poorer than the corresponding energy resolution measured in the FEMC, so the forward region algorithm starts from calorimeter deposits.

  The first step is to re-cluster FEMC showers. Showers with energy less than 3 GeV or with more than 10% coming from HCAL deposits are rejected from the clustering to exclude muons. The most energetic shower is used as a seed, and the secondary showers lying within an angular region in θ and ϕ around its centre are clustered with an iterative procedure which starts from the most energetic one. At each step the energy of the cluster and its direction are re-computed. Secondary showers not belonging to the cluster are added to it if they lie in a cone of 7^o around the cluster direction and have a transverse momentum relative to it of less than 3 GeV. Tracks associated to the new cluster are then searched for in order to establish whether it is a photon or electron candidate. In order to cut out tracks resulting from early showering, track elements (TEs, see Section 3.8) from the innermost detectors are required. Different requirements on the TEs and polar range lead to "loose" or "tight" electron or photon tags. The direction of the cluster is obtained from the direction of the measured tracks associated to it. For this purpose it is necessary to perform a track selection based on impact parameter, ϕ, the error on ϕ, p_{track}/E_{clus} and the θ position of the track. This rejects long tails in the ϕ and θ resolution distributions of electrons as has been seen by checking the acoplanarity and acollinearity of Bhabha events. The energy of the clusters was calibrated using radiative Bhabha events with both electrons and a photon falling within the acceptance of the detector and lying on one plane. If no missing momentum down the beampipe is assumed the topology is over-constrained by the directions of the particles and the centre of mass energy. In this way, the energies of the particles can be calculated independently of calorimetric deposits[2]. Thus, the energy resolution can be calculated in a large energy range in different angular regions of the FEMC. The angular regions are chosen to coincide with material in front of the FEMC and its own natural boundaries, resulting in a more accurate assessment of the energy resolution. Its dependence on the measured energy E is parametrised according to

$$\frac{\sigma_E}{E} = \sqrt{\left(\frac{A}{\sqrt{E}} + B\right)^2 + \frac{0.2^2}{E}} \tag{4.1}$$

for each angular region. This parametrisation has the same functional form as that used for the FEMC shower energy calibration given in [43]. The parameters A and B obtained for different angular regions are shown in Table 4.1.

---

[2] Here, the direction of the electrons is computed with tracking information only.

		$10^o < \theta < 15^o$	$15^o < \theta < 32^o$	$32^o < \theta < 35^o$
Data	A	0.299	0.131	0.152
	B	0.050	0.040	0.045
Monte Carlo	A	0.293	0.137	0.154
	B	0.051	0.048	0.050

Table 4.1: FEMC cluster resolution parameters from fits to Equation 4.1.

After this data estimate of the energy resolution from Bhabha events has been performed, discrepancies between the energy scale and resolution in data and Monte Carlo Bhabha events are observed. These lead to the necessity to apply corrections to the Monte Carlo. The corrections and impact on the sensitivity of the $\mathrm{M_W}$ and Γ_W measurements are discussed in Section 6.2.

4.3 Run Selection

A standard run selection is applied on the XSDST to ensure that all the relevant subdetectors to this analysis are operational. This is to exclude data which, due to various malfunctions of different subdetectors, could have large inefficiencies, dead regions, biases, noise, and sub-standard tracking and pattern recognition. Besides the effect this has on selected events, the main point is that these short lasting effects cannot be easily modelled in the simulation and so can give rise to hidden biases in the measurements presented here. There are two run selections used as standard within the W team [59]: a hadronic one, intended for $\mathrm{W^+W^-} \rightarrow \mathrm{q\bar{q}'\bar{q}q'}$ analyses, and a semi-leptonic one, intended for the $\mathrm{W^+W^-} \rightarrow l\nu q\bar{q}'$ channel. The former is a subset of the latter and excludes the electron and muon tagging criteria. The semi-leptonic run quality selection is summarised in Table 4.2. Runs must satisfy all the run quality criteria before being considered for the analysis. The treatment of the MUC quality differs from that of the other detectors listed above in that inefficiencies due to abnormal running of the chambers are estimated and corrected for in the analysis stream.

Semi-leptonic W team Run Selection		
Selection	Detectors	Status known
Barrel Tracking	TPC $\cap$ (VD $\cup$ ID $\cup$ OD)	$> 90\%$
Forward tracking	FCA $\cup$ FCB	$> 90\%$
Calorimetry	HCALB $\cap$ HCALF	$> 90\%$
	HPC $\cap$ FEMC	$> 90\%$
Muon Chambers	MUB, MUF, MUS	Efficiencies re-scaled in simulation

Table 4.2: Semi-leptonic run selection requirements on different DELPHI subdetectors. A logical AND of all the above requirements must be satisfied for a run to be included in the analysis.

4.4 $l\nu q\overline{q}$ Event Selection

4.4.1 Introduction

The event selection used in this analysis is based on that used for the W^+W^- cross section determination at DELPHI[54]. It uses an Iterative Discriminant Analysis (IDA) to construct a discriminating variable from a set of event observables. It was developed from analyses previously used in DELPHI for Higgs searches [60]. The theory behind discriminant analyses (DAs) and its implementation to the selection of W^+W^- events is discussed below.

4.4.2 Motivation

The event selection has the purpose of classifying events as "signal" or "background". Typically, this is done in terms of a large set of event observables, which define an N-dimensional space, where N is the number of observables under consideration. Events are defined by an N-dimensional vector $\vec{\mathbf{x}}$, and their populations by a Probability Density Function (PDF) $P(\vec{\mathbf{x}})$. In a cut-based analysis, a sequence of cuts is applied to a population with a view to excluding events according to some pre-established criteria regarding the desired purity or efficiency[3], in a sense constructing an N-dimensional boundary which defines which events will be classified as signal and which as background.

There are two problems with such a procedure. First, that it is difficult to take into account the correlation between the observables and hence to tune the cuts

---

[3] The Purity **P** is defined as the ratio between the number of "signal" events and the total number of events selected. The efficiency ϵ is defined as the fraction of selected signal events from a sample. Both are typically calculated from simulation.

for optimal performance: the order in which the cuts are applied and tuned might lead to different results and this is not always transparent. Second, N-dimensional boundary, constructed out of flat, orthogonal surfaces, is not necessarily an optimal discriminator, if we make the fair assumption that the PDFs of signal and background are not box-shaped. The DA deals with both these problems by providing an automated way of defining the N-dimensional boundary in a way that provides optimal discrimination. We take the particular example of the Linear Discriminant Analysis (LDA), in which the high dimensionality of the problem is elegantly dealt with by constructing a flat N-dimensional plane boundary. Then we generalise to the Polynomial Discriminant Analysis (PDA), the method used here.

Linear Discriminant Analysis

Given PDFs $P_S(\vec{\mathbf{x}})$ and $P_B(\vec{\mathbf{x}})$ for signal (S) and background (B) respectively, defining the distribution of signal and background populations in two clusters, we want to find the optimal separation between S and B. We define the optimal separation as that which gives the highest purity $\mathbf{P}$ for a given efficiency ϵ. The Neyman-Pearson Lemma [61] states that the optimal separation is achieved with an N-dimensional boundary of constant likelihood ratio:

$$\kappa(\vec{\mathbf{x}}) = \frac{P_S(\vec{\mathbf{x}})}{P_B(\vec{\mathbf{x}})} \tag{4.2}$$

where $\kappa(\vec{\mathbf{x}})$ is a scalar which is determined by the desired selection efficiency. The PDFs are assumed to be Gaussian and can be expressed as

$$P(\vec{\mathbf{x}}) \propto exp\left[-\frac{1}{2}(\vec{\mathbf{x}} - \vec{\mathbf{x}}^0)^T V^{-1}(\vec{\mathbf{x}} - \vec{\mathbf{x}}^0)\right] \tag{4.3}$$

where $\vec{\mathbf{x}}^0$ and V are the mean and error matrix of the distribution. Stating Equation 4.2 in terms of the Gaussian PDF 4.3 and taking the natural logarithm of the resulting equation gives

$$ln(\kappa) = -\frac{1}{2}(\vec{\mathbf{x}} - \vec{\mathbf{x}}^0_S)^T V_S^{-1}(\vec{\mathbf{x}} - \vec{\mathbf{x}}^0_S) + \frac{1}{2}(\vec{\mathbf{x}} - \vec{\mathbf{x}}^0_B)^T V_B^{-1}(\vec{\mathbf{x}} - \vec{\mathbf{x}}^0_B) \tag{4.4}$$

where the means of the S and B distributions, $\vec{\mathbf{x}}^0_S$ and $\vec{\mathbf{x}}^0_B$, and their error matrices, V_S and V_B, have been stated explicitly. It can be shown that [53], if the two error matrices are assumed to be identical (and = V) the constant log-likelihood ratio boundary can be expressed as

$$\Omega \;=\; \vec{\mathbf{x}}^T V^{-1} \Delta \vec{\mathbf{x}}^0 \;=\; \vec{\mathbf{a}} \cdot \vec{\mathbf{x}} \tag{4.5}$$

where $\Delta\vec{\mathbf{x}}^0$ is the difference between the means of the S and B populations, $(\vec{\mathbf{x}}^0_S - \vec{\mathbf{x}}^0_B)$, $\vec{\mathbf{a}} = V^{-1}\Delta\vec{\mathbf{x}}^0$ and all constant terms have been absorbed into Ω. Equation 4.5 defines an N-dimensional plane which will discriminate between S and B. The degree to which the separation is optimal depends on the validity of the two assumptions made in deriving Equation 4.5, namely, that the PDFs are Gaussian, and that they have the same error matrix. As we shall see, in practice, strictly satisfying these assumptions is not vital to the performance of the method if the DA is generalised to higher orders.

Polynomial and Iterative Discriminant Analysis

Any deviations of the data S and B samples from the assumptions stated above result in a degraded performance of the method. Using higher order surfaces instead of the plane defined in Equation 4.5 can help compensate for any such degradation. In fact, in the case where the signal and background PDFs are Gaussian but have different error matrices, the optimal separation boundary is no longer a plane, but a quadratic surface. The approach taken is to generalise the LDA to higher orders. We start by defining a quadratic surface, where the linear part retains the structure of the LDA and the second order part is general:

$$\Omega_2 \;=\; \vec{\mathbf{x}}^T (\vec{\mathbf{a}} \;+\; \hat{b}\vec{\mathbf{x}}) \tag{4.6}$$

Here, $\hat{b}$ is an $N \times N$ matrix containing coefficients of the $x_i x_j$ and x_i^2 terms in the surface. In order to use the same mathematics as in the LDA, a second, equivalent definition of the higher order surface can be made: a new space, including the higher order terms, is constructed, and LDA applied, and the surface can now be expressed as a plane of dimensionality higher than N. In the quadratic case,

$$\Omega_2 \;=\; \vec{\mathbf{b}} \cdot \vec{\mathbf{y}} \tag{4.7}$$

where $\vec{\mathbf{b}}$ is a vector containing the coefficients of the x_i, $x_i x_j$ and x_i^2 components of the new event vector $\vec{\mathbf{y}}$. By re-defining the space of observables to include the higher order terms in the vector $\vec{\mathbf{y}}$, Equation 4.7 can be trivially generalised to higher orders. A new error matrix must be defined in order to follow the LDA formalism. A linear combination of the inverse S and B error matrices is made:

$$V^{-1} \ = \ \beta V_S^{-1} \ + \ (1 \ - \beta) V_B^{-1} \ , \tag{4.8}$$

where β ranges between 0 and 1 and is tuned to give the best performance.

We have started from an LDA in which, given two assumptions, the optimal separation boundary can be found analytically. We have then generalised to higher orders to compensate for loss of performance due to non-validity of the assumptions in the data populations. By constructing a space of higher orders we have retained the one-dimensional structure of the LDA, at the price of one tunable parameter β. The Polynomial Discriminant Analysis lacks the rigour of the LDA, but has been shown to give sizeable improvements in discriminating power. Added performance can be found by carrying out the PDA in steps, re-assessing the mean values $\vec{\mathbf{x}}_S^0$ and $\vec{\mathbf{x}}_B^0$ and the error matrix V each time. This is known as Iterative Discriminant Analysis (IDA) for historical reasons, although there is no real iteration involved.

4.4.3 Application to the Selection of $\mathrm{l}\bar{\nu}_\mathrm{l}\mathrm{q}\bar{\mathrm{q}}'$ Events

Signal $\mathrm{l}\bar{\nu}_\mathrm{l}\mathrm{q}\bar{\mathrm{q}}'$ events are characterised by the presence of two or more jets from the hadronically decaying W boson, a high energy lepton, and high missing momentum from the W decay into a charged lepton and a neutrino, which escapes undetected. Initial state radiation (ISR) photons can also leave a signature in the calorimeters of DELPHI or escape undetected down the beampipe. In the latter case the photons are also a source of missing momentum.

Separate IDA selections have been developed for each of the three $\mathrm{l}\bar{\nu}_\mathrm{l}\mathrm{q}\bar{\mathrm{q}}'$ decay channels, corresponding to leptonic decays of W bosons into electrons, muons and multi-prong taus (referred to henceforth as “hadronic taus”). There is one tuning for 1998 data and one for the four centre of mass energy points of the 1999 running period. The latter is referred to as the 200 GeV tuning for simplicity.

The first step in the event selection process is to identify an electron, muon or hadronic tau lepton in an event. Electrons and muons are tagged using the standard particle ID packages described in Section 4.2. Further requirements on their energy/momentum and isolation are made before deciding whether the events can be considered for pre-selection. The tagging of hadonic taus is more involved. First, events are clustered into jets using the `LUCLUS` algorithm with a clusterisation scale d_{ij} of 6.5 GeV. Then the following selection criteria are imposed on the jets:

- Jet charged multiplicity ≤ 5
- Jet total multiplicity ≤ 10
- Jet total momentum ≥ 5 GeV

Jets satisfying these criteria are tagged hadronic tau candidates.

Once a lepton candidate has been found, the highest energy photon candidate is searched for. `REMCLU` neutral energy clusters satisfying the following criteria are tagged as photon candidates:

- Tight `REMCLU` photon tag
- Energy ≥ 5 GeV
- Isolation angle from tracks with momentum greater than 1GeV of at least 15^o
- Total energy from unassociated deposits in a surrounding 15^o cone of no more than 1GeV

The candidate photon with the highest energy is selected.

The `DURHAM` track clustering algorithm is used to force two jets from all the tracks in the event except those tagged as muons or those forming part of electron or photon clusters or tau jets. The events are then ready for the pre-selection. It must be stressed that the lepton identification and selection is not exclusive, so events can be ambiguously tagged. It is only at the selection stage that any ambiguity is resolved.

The pre-selection itself consists of a series of sequential cuts which are applied in order to eliminate large amounts of background without compromising efficiency,

189 GeV IDA pre-selection			
Event Variable	$\mathrm{e}\overline{\nu}_{\mathrm{e}}\mathrm{q}\overline{\mathrm{q}}'$	$\mu\overline{\nu}_{\mu}\mathrm{q}\overline{\mathrm{q}}'$	$\tau\overline{\nu}_{\tau}\mathrm{q}\overline{\mathrm{q}}'$
Lepton Energy/Momentum (GeV)	≥ 20	≥ 20	≥ 10
Cos(θ_{lepton})	≤ 0.92	-	-
Transverse Energy (GeV)	≥ 50	≥ 40	≥ 40
Total Jet Multiplicity	≥ 4	≥ 4	≥ 4
Charged Jet Multiplicity	≥ 1	≥ 1	≥ 1
Total Event Multiplicity	-	-	≥ 14

Table 4.3: Pre-selection cuts for the 200 GeV IDA tuning.

200 GeV IDA pre-selection			
Event Variable	$\mathrm{e}\overline{\nu}_{\mathrm{e}}\mathrm{q}\overline{\mathrm{q}}'$	$\mu\overline{\nu}_{\mu}\mathrm{q}\overline{\mathrm{q}}'$	$\tau\overline{\nu}_{\tau}\mathrm{q}\overline{\mathrm{q}}'$
Lepton Energy/Momentum (GeV)	≥ 20	≥ 17	-
Cos(θ_{lepton})	≤ 0.92	-	-
Transverse Energy (GeV)	≥ 50	≥ 40	≥ 40
Visible Energy (GeV)	-	≥ 60	-
Total Jet Multiplicity	≥ 4	≥ 4	≥ 4
Charged Jet Multiplicity	≥ 1	≥ 1	≥ 1
Total Event Multiplicity	-	-	≥ 14
Successful Kinematic Fit (Constraints)	2C	2C	1C

Table 4.4: Pre-selection cuts for the 200 GeV IDA tuning

and to ensure good agreement between real and Monte Carlo data in the variables to be used for the IDA. The cuts are listed in Tables 4.3 and 4.4. The pre-selection has negligible impact on the final selection of events [62]. The three $\mathrm{l}\overline{\nu}_{\mathrm{l}}\mathrm{q}\overline{\mathrm{q}}'$ IDA selections are applied to all events passing the pre-selection, starting with the $\mathrm{e}\overline{\nu}_{\mathrm{e}}\mathrm{q}\overline{\mathrm{q}}'$, followed by the $\mu\overline{\nu}_{\mu}\mathrm{q}\overline{\mathrm{q}}'$ and hadronic $\tau\overline{\nu}_{\tau}\mathrm{q}\overline{\mathrm{q}}'$ channels. Events passing one selection are not considered for the remaining ones. The backgrounds in the $\mathrm{l}\overline{\nu}_{\mathrm{l}}\mathrm{q}\overline{\mathrm{q}}'$ are QCD events with two or more jets in the final state, $e^+e^- \rightarrow Z^0/\gamma \rightarrow q\overline{q}(\gamma)(g)$, four fermion processes such as $\nu\nu q\overline{q}$ or $l^+l^-q\overline{q}$, and $\mathrm{W}^+\mathrm{W}^-$ events decaying into non-$\mathrm{l}\overline{\nu}_{\mathrm{l}}\mathrm{q}\overline{\mathrm{q}}'$ final states. Genuine $\mathrm{l}\overline{\nu}_{\mathrm{l}}\mathrm{q}\overline{\mathrm{q}}'$ events selected under the wrong lepton hypothesis could also be construed as background, but in general the $\mathrm{M_W}$ information carried by the hadronic system merits their inclusion into the analysis as signal events. The Probability Density Function used in order to fit the $\mathrm{M_W}$ and Γ_{W} parameters and described in Chapter 5 takes into account the presence of these events. Since the efficiency with which leptons can be identified at DELPHI varies greatly between families, and the level of their corresponding backgrounds differs considerably, the three IDA selections used here will be explained separately. For completeness, the 189 and 200 GeV tunings are be will be described.

4.4.4 IDA Tunings

The details of the tunings can be seen in Table 4.5. The variables used for each of the tunings in Table 4.5 are standard ones used in sequential cut selections [4, 5]. They are, for the $\mathrm{e}\overline{\nu}_{\mathrm{e}}\mathrm{q}\overline{\mathrm{q}}'$ tunings,

IDA tuning characteristics						
Channel	$\mathrm{e}\overline{\nu}_{\mathrm{e}}\mathrm{q}\overline{\mathrm{q}}'$		$\mu\overline{\nu}_{\mu}\mathrm{q}\overline{\mathrm{q}}'$		$\tau\overline{\nu}_{\tau}\mathrm{q}\overline{\mathrm{q}}'$	
Tuning	189	200	189	200	189	200
Degree	2	2	3	2	2	2
Steps	2	3	2	2	2	3
Variables	9	10	8	9	11	12

Table 4.5: Characteristics of the different $\mathrm{l}\overline{\nu}_{\mathrm{l}}\mathrm{q}\overline{\mathrm{q}}'$ IDA tunings.

- Electron energy
- Electron isolation angle θ_{iso}, defined as the angle between the electron direction and the nearest track of momentum greater than 1 GeV.
- Missing momentum magnitude, $|P_{miss}|$. The missing momentum vector is is opposite in direction and of equal magnitude to the sum of the momenta of all the tracks in the event.
- Cosine of missing momentum polar angle, $cos\theta_{P_{miss}}$.
- Angle between electron and missing momentum.
- Angle between electron and nearest jet.
- Angle between jets (200 GeV tuning only).
- Normalised effective centre of mass energy $\sqrt{s'/s}$, calculated using the algorithm described in [63].

- Transverse energy E_{trans} (189 GeV tuning only).
- Visible energy E_{vis} (200 GeV tuning only).
- 2 constraint kinematic fit mass. See Sec. 4.5.

For the $\mu\overline{\nu}_{\mu}\mathrm{q}\bar{\mathrm{q}}'$ tunings, we have:

- Muon momentum.
- Muon isolation angle θ_{iso}.
- Missing momentum $|P_{miss}|$.
- Cosine of missing momentum, $cos\theta_{P_{miss}}$.
- Angle between muon and missing momentum.
- Angle between muon and nearest jet.
- Normalised effective centre of mass energy $\sqrt{s'/s}$.
- Transverse energy E_{trans}.
- Visible energy E_{vis} (189 GeV tuning only).
- 2 constraint kinematic fit mass (200 GeV tuning only).

And finally, for the multi-prong $\tau\overline{\nu}_{\tau}\mathrm{q}\bar{\mathrm{q}}'$ tunings the variables are

- Tau jet momentum.
- Energy of tau jet deposited in electromagnetic calorimeters.
- Energy of tau jet deposited in hadron calorimeters.
- Tau jet multiplicity.
- Tau jet polar angle θ_{τ} (189 GeV tuning only).
- Missing momentum $|P_{miss}|$,
- Cosine of missing momentum, $cos\theta_{P_{miss}}$.

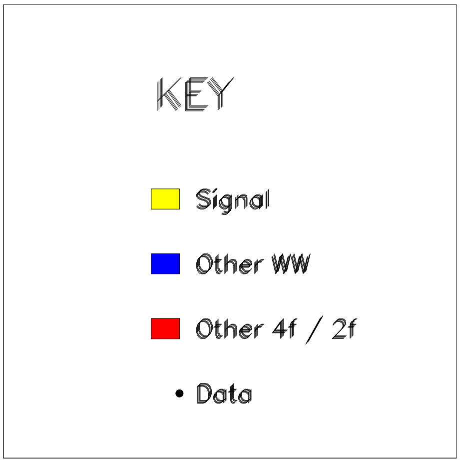

Figure 4.1: Key to plots 4.2 to 4.20, showing data and Monte Carlo distributions of IDA selection variables and discriminants.

- Angle between non-tau jets.
- Angle between tau jet and nearest non-tau jet (200 GeV tuning only).
- Normalised effective centre of mass energy $\sqrt{s'/s}$.
- Transverse energy E_{trans} (189 GeV tuning only).
- Visible energy E_{vis}.
- 1 constraint kinematic fit di-jet mass.

The variables for the $\mu\overline{\nu}_{\mu}\mathrm{q\bar{q}'}$ and $\tau\overline{\nu}_{\tau}\mathrm{q\bar{q}'}$ have similar definitions to those used in the $\mathrm{e}\overline{\nu}_{\mathrm{e}}\mathrm{q\bar{q}'}$ selection. The spectra of these variables, for data and both signal and background Monte Carlo samples, together with the scalar discriminant variables Ω_N, constructed using an IDA mechanism of order N according to the Nth order generalisation of equation 4.6, are shown before and after the IDA selection, in Figures 4.2 to 4.20. The key for the plots is shown in Figure 4.1. The 200 GeV plots contain 200 GeV data and Monte Carlo simulation only.

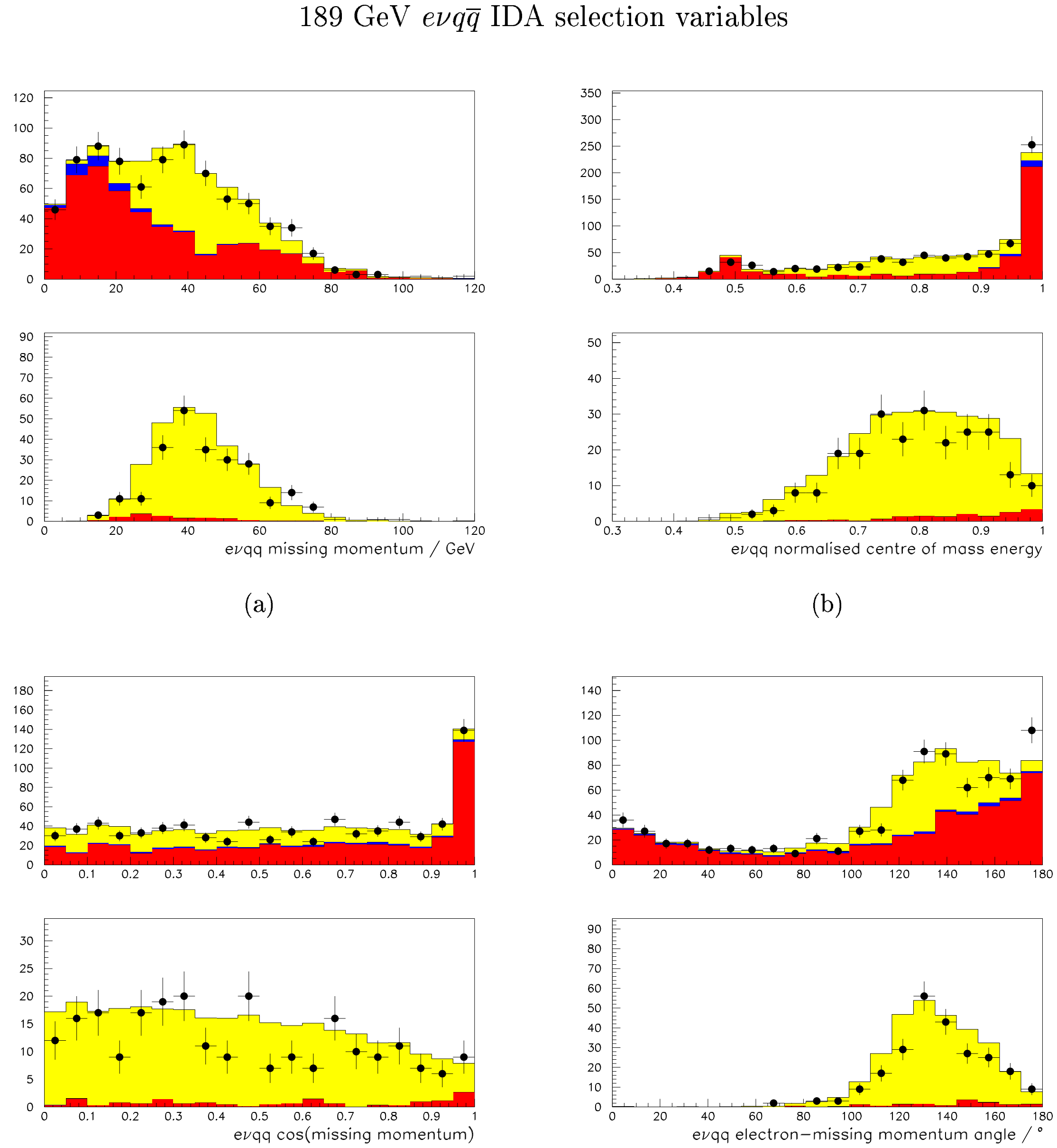

(a) (b)

(c) (d)

Figure 4.2: $e\overline{\nu}_e q\bar{q}'$ missing momentum p_{miss} (a), $\sqrt{s'}/\sqrt{s}$ (b), $cos(p_{miss})$ (c) and electron-p_{miss} angle (d) distributions for 189 GeV data and Monte Carlo simulation before (top) and after (bottom) the IDA selection.

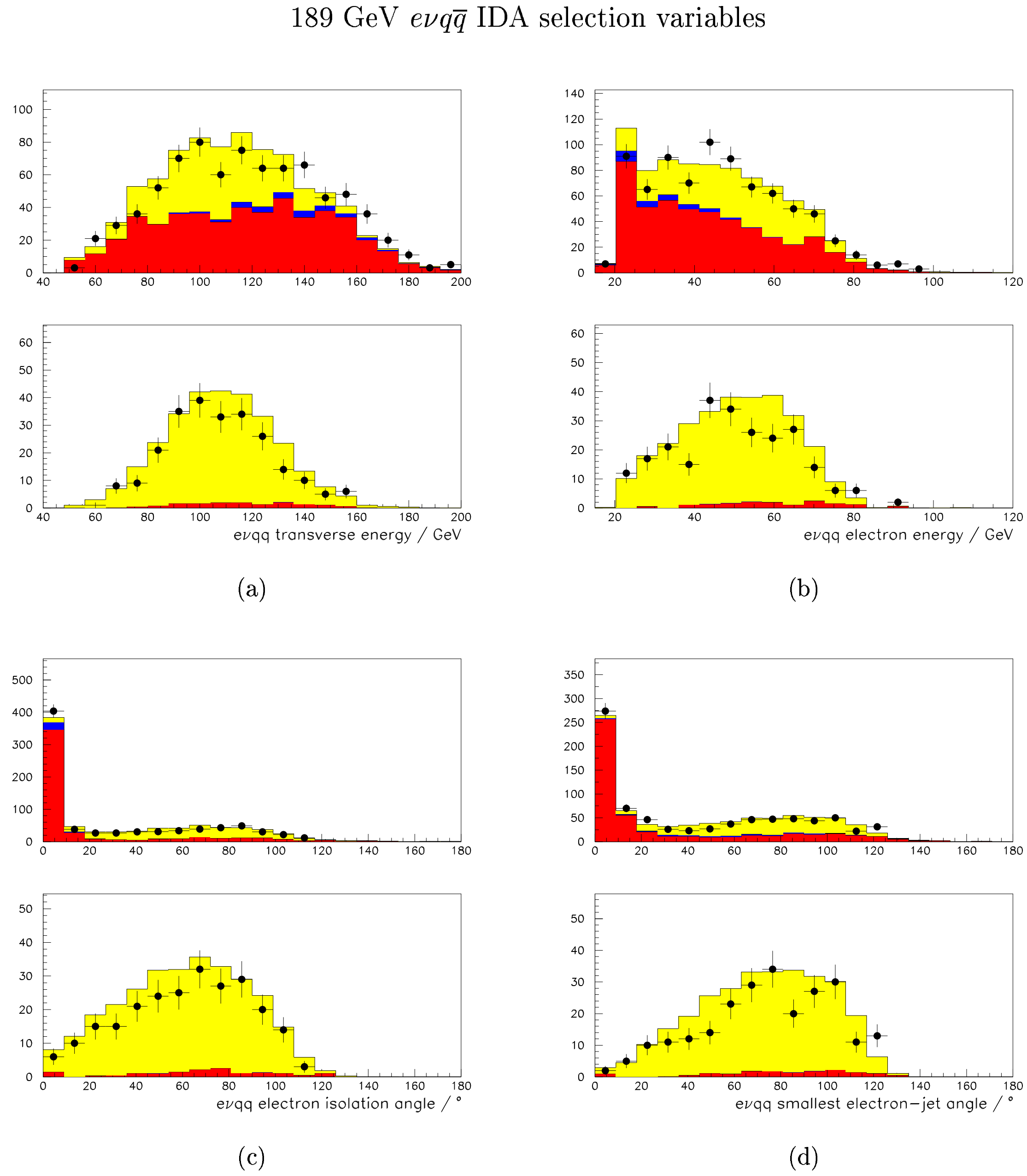

(a) (b)

(c) (d)

Figure 4.3: $e\overline{\nu}_e q\bar{q}'$ transverse energy (a), electron energy (b), isolation angle (c), and smallest electron-jet angle (d) distributions for 189 GeV data and Monte Carlo simulation before (top) and after (bottom) the IDA selection.

189 GeV $e\nu q\overline{q}$ IDA selection variables

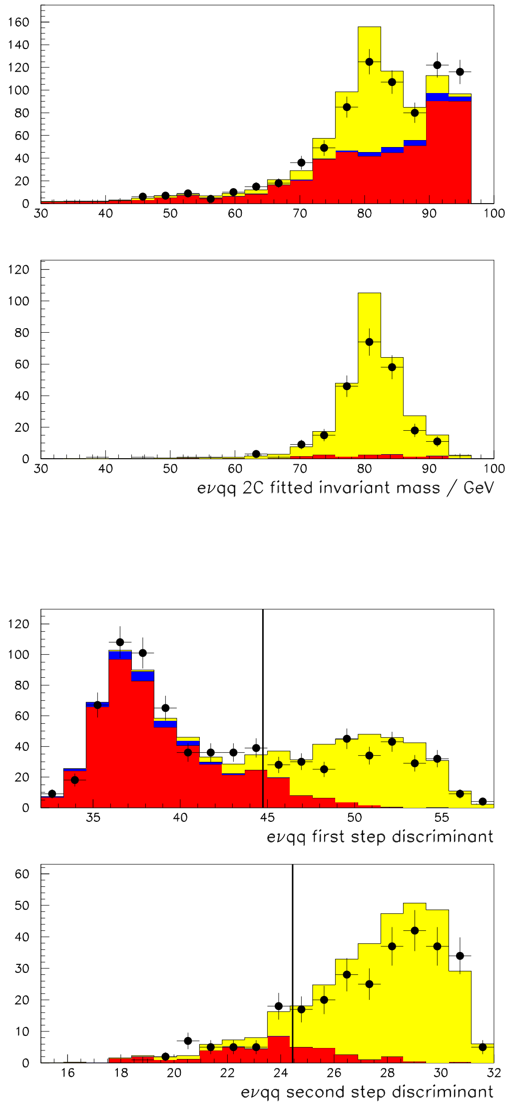

Figure 4.4: $e\overline{\nu}_e q\overline{q}'$ 2C fitted mass before (first from top to bottom) and after (second from top to bottom) IDA selection, the first (third from top to bottom) and second (bottom) step IDA discriminant distributions for 189 GeV data and Monte Carlo simulation.

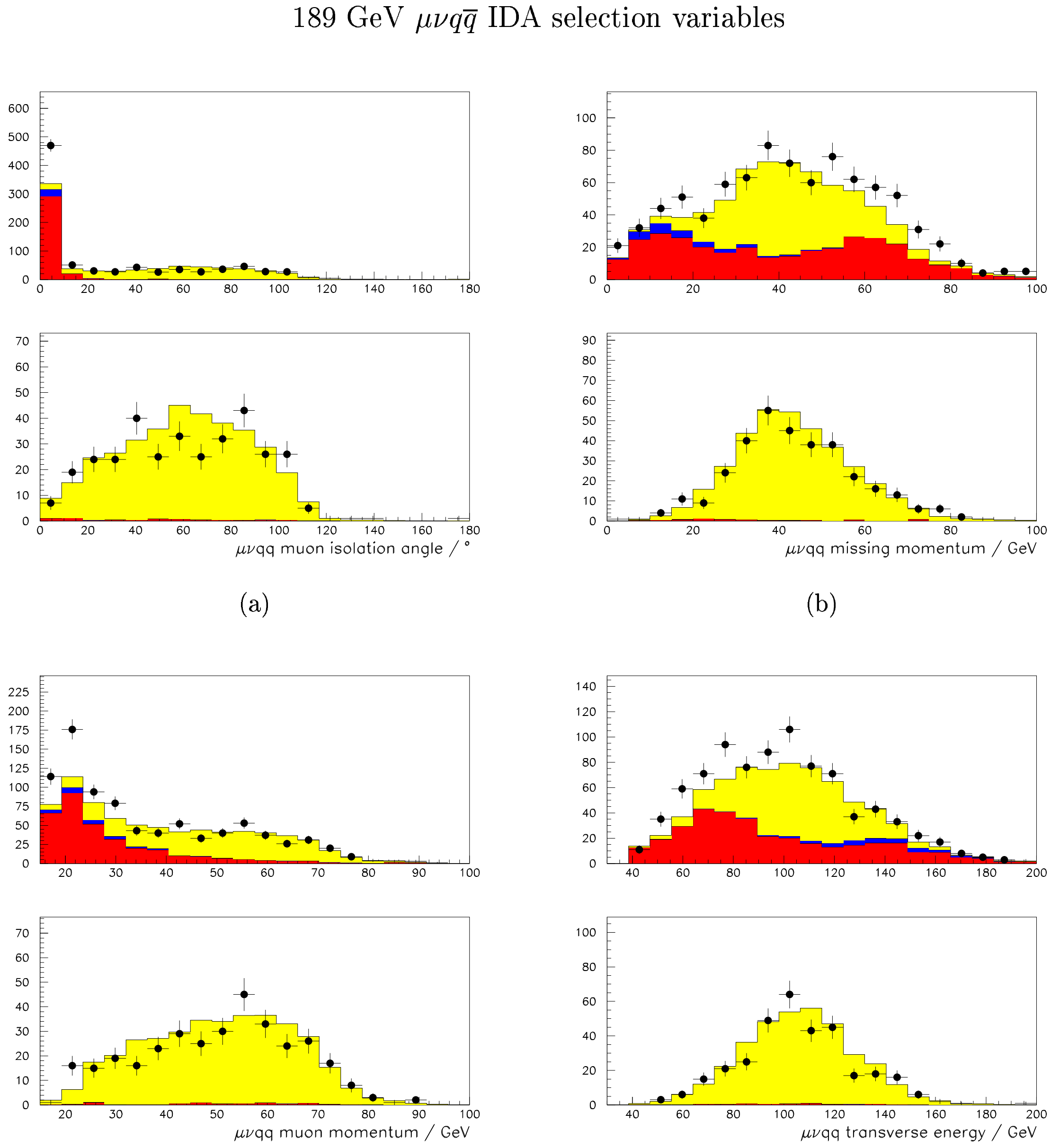

(a) (b)

(c) (d)

Figure 4.5: $\mu\overline{\nu}_\mu q\overline{q}'$ isolation angle (a), missing momentum p_{miss} (b), muon momentum (c), and transverse energy (d) distributions for 189 GeV data and Monte Carlo simulation.

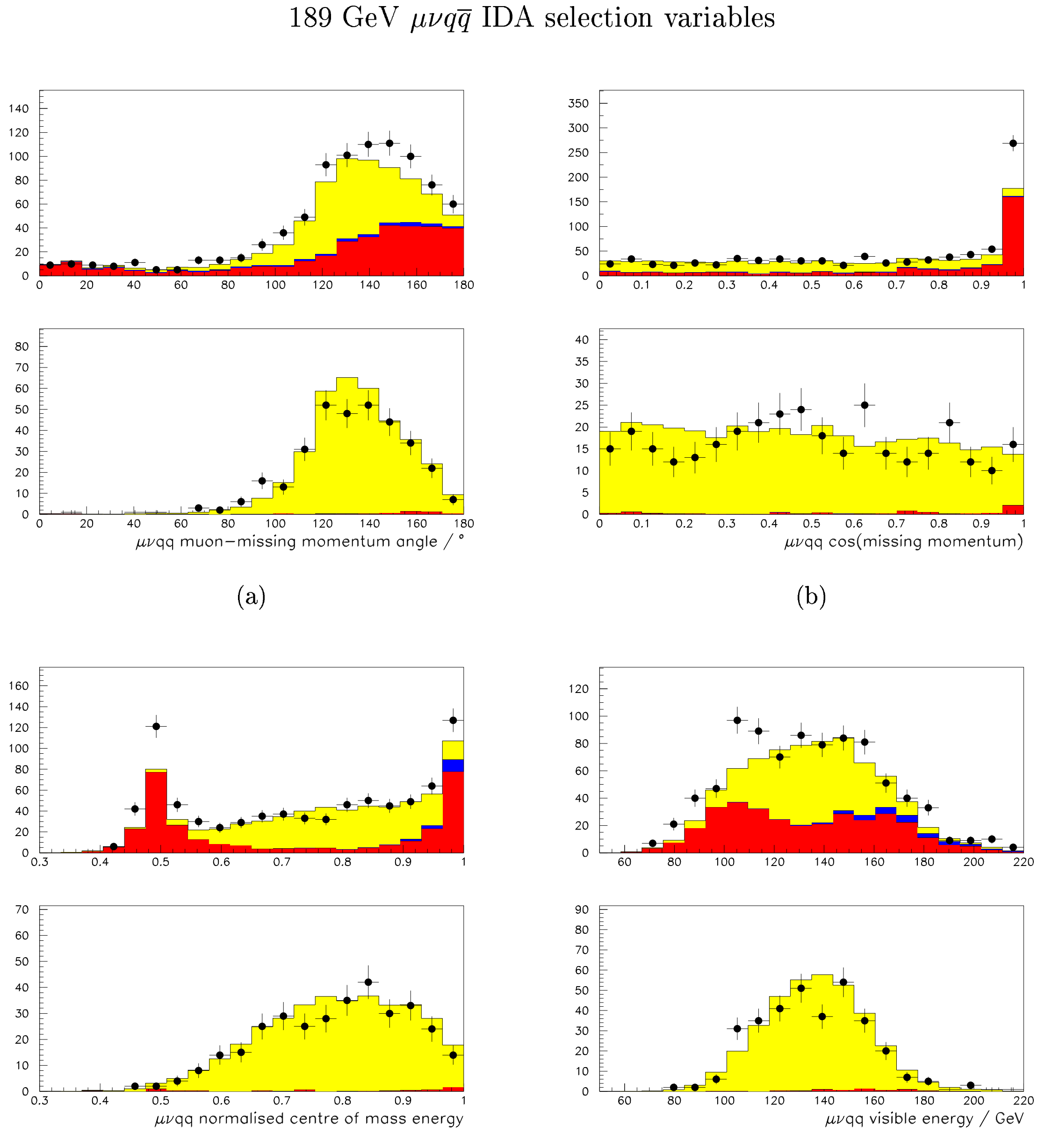

(a) (b)

(c) (d)

Figure 4.6: $\mu\overline{\nu}_\mu q\bar{q}'$ muon-p_{miss} angle (a), $cos(p_{miss})$ (b), $\sqrt{s'}/\sqrt{s}$ (c) and visible energy (d) distributions for 189 GeV data and Monte Carlo simulation before (top) and after (bottom) IDA selection.

189 GeV $\mu\nu q\overline{q}$ IDA selection variables

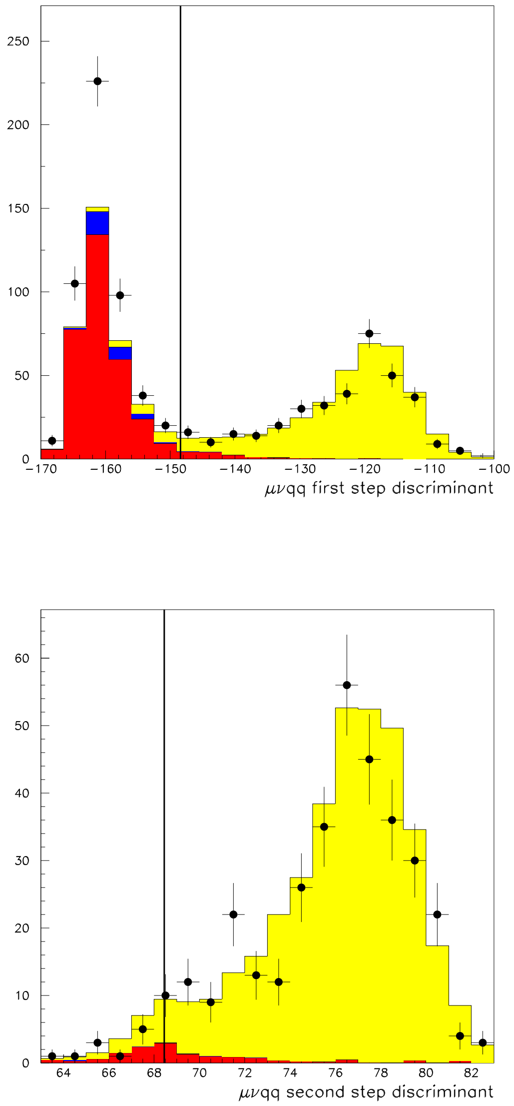

Figure 4.7: $\mu\overline{\nu}_\mu q\bar{q}'$ first (top) and second (bottom) step IDA discriminant distributions for 189 GeV data and Monte Carlo simulation.

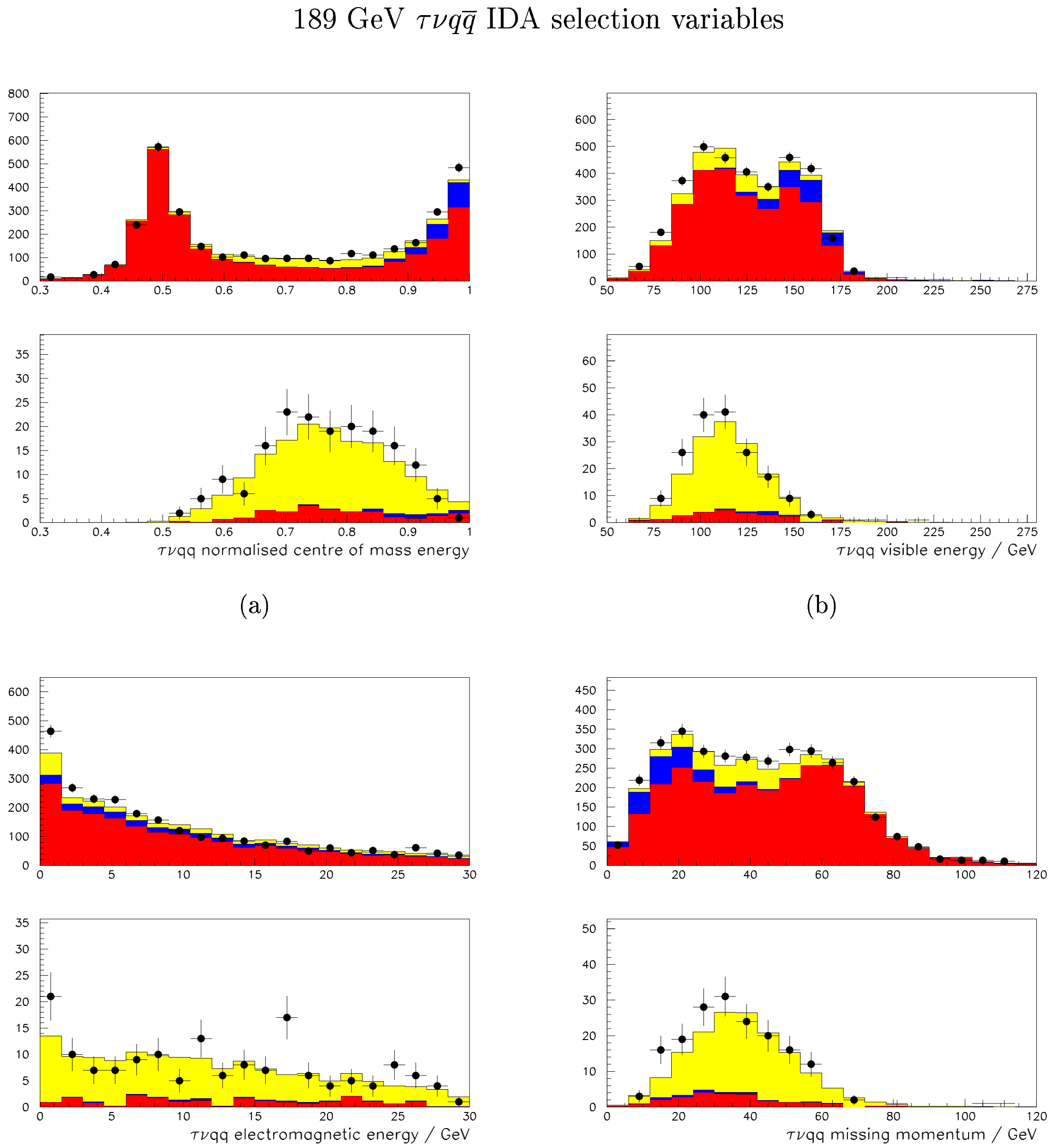

(a) (b) (c) (d)

Figure 4.8: $\tau\overline{\nu}_\tau q\bar{q}'$ $\sqrt{s'}/\sqrt{s}$ (a), visible energy (b), energy deposited in electromagnetic calorimeters (c) and missing momentum p_{miss} distributions for 189 GeV data and Monte Carlo simulation before (top) and after (bottom) IDA selection.

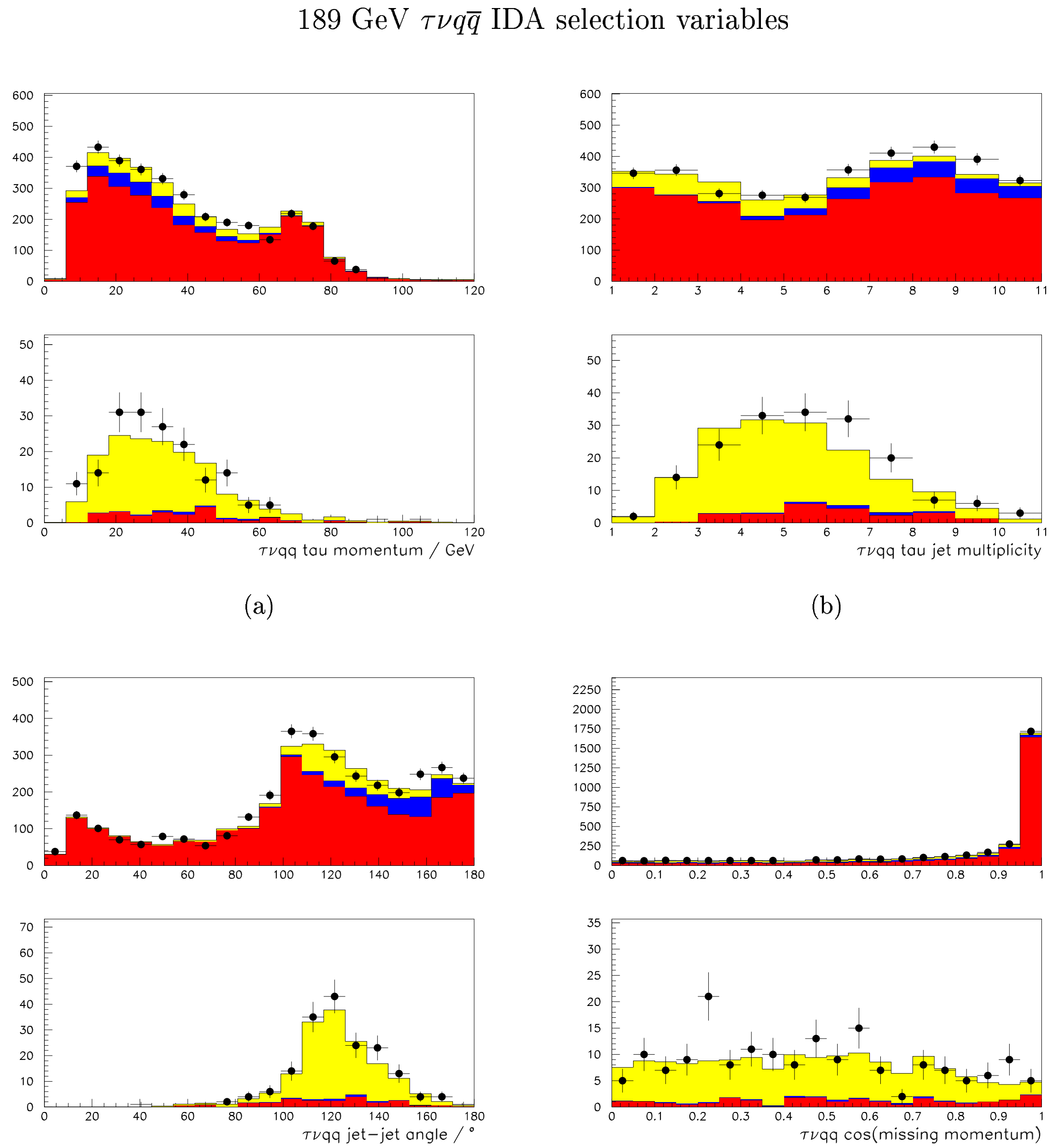

(a)

(b)

(c)

(d)

Figure 4.9: $\tau\overline{\nu}_\tau q\overline{q}'$ τ-jet momentum (a), τ-jet multiplicity (b), jet-jet angle (c), and $cos(p_{miss})$ (d) distributions for 189 GeV data and Monte Carlo simulation before (top) and after (bottom) IDA selection.

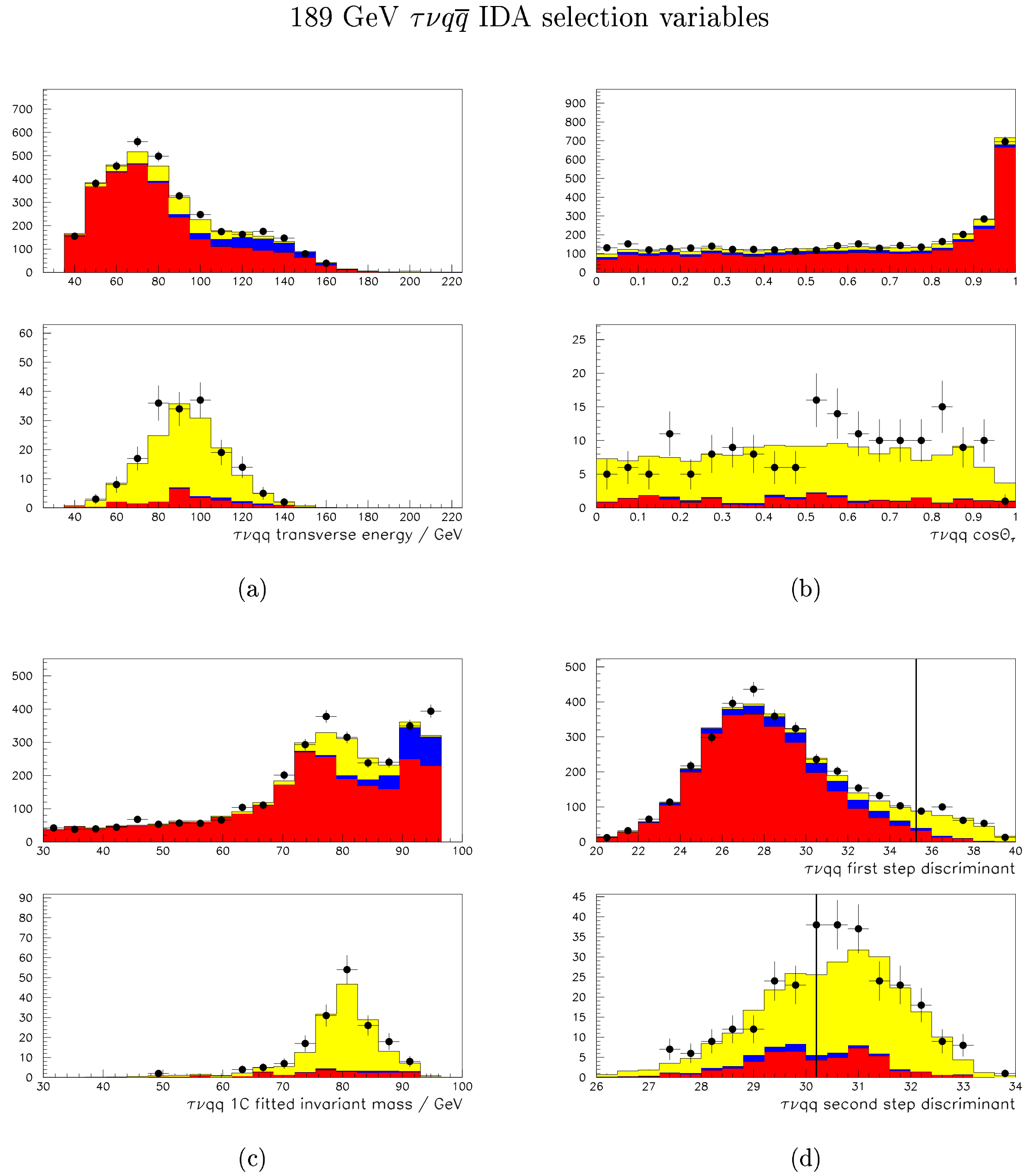

(a) (b)

(c) (d)

Figure 4.10: $\tau\overline{\nu}_\tau q\bar{q}'$ transverse energy (a), τ polar angle (b), 1C fitted jet-jet mass (c) before (top) and after (bottom) IDA selection, and first (top) and second (bottom) step IDA discriminants (d) for 189 GeV data and Monte Carlo simulation.

200 GeV $e\nu q\bar{q}$ IDA selection variables

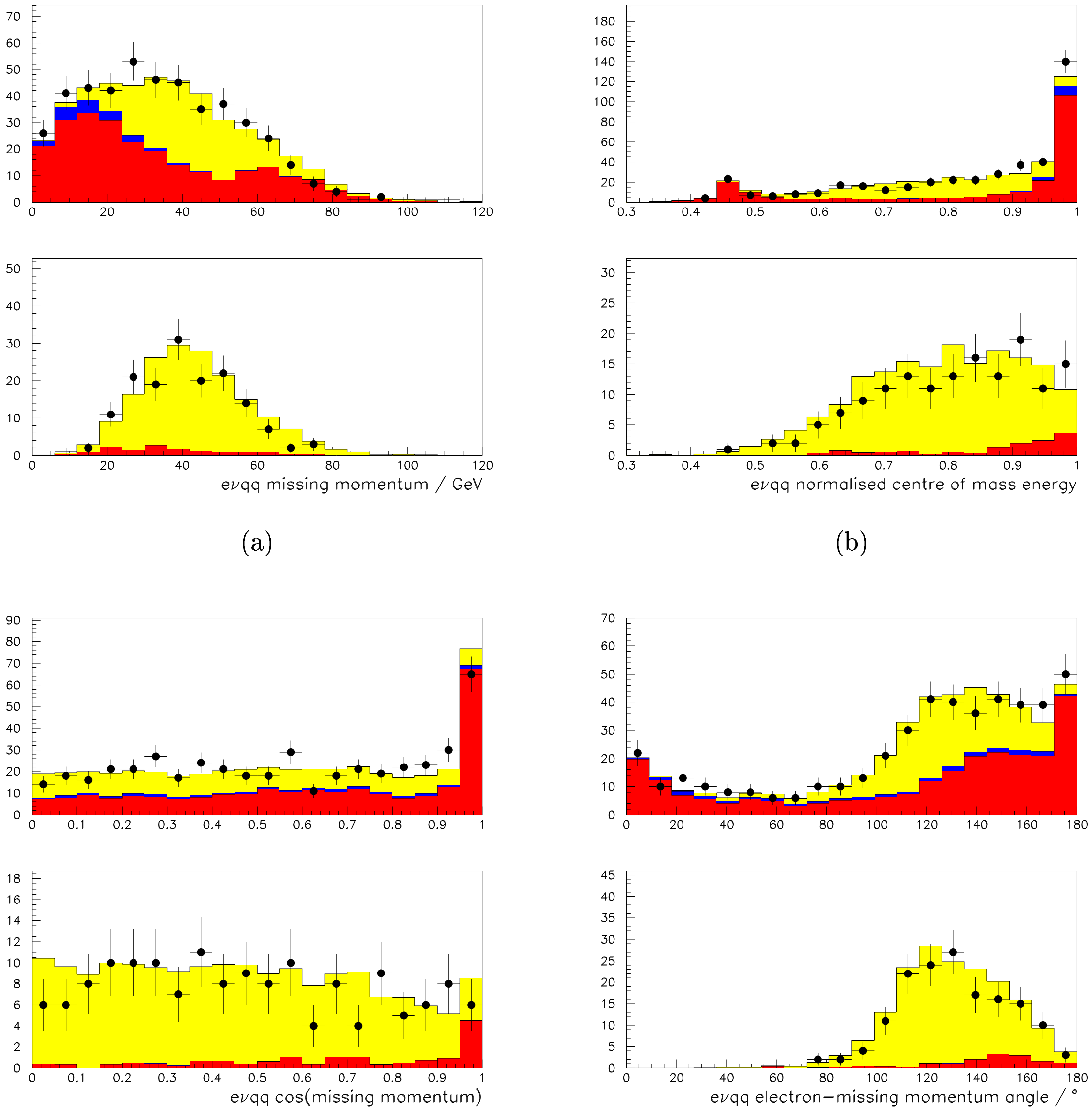

(a) (b)

(c) (d)

Figure 4.11: $e\bar{\nu}_e q\bar{q}'$ missing momentum p_{miss} (a), $\sqrt{s'}/\sqrt{s}$ (b), $cos(p_{miss})$ (c), and electron-p_{miss} angle (d) distributions for 200 GeV data and Monte Carlo simulation before (top) and after (bottom) IDA selection.

200 GeV $e\nu q\overline{q}$ IDA selection variables

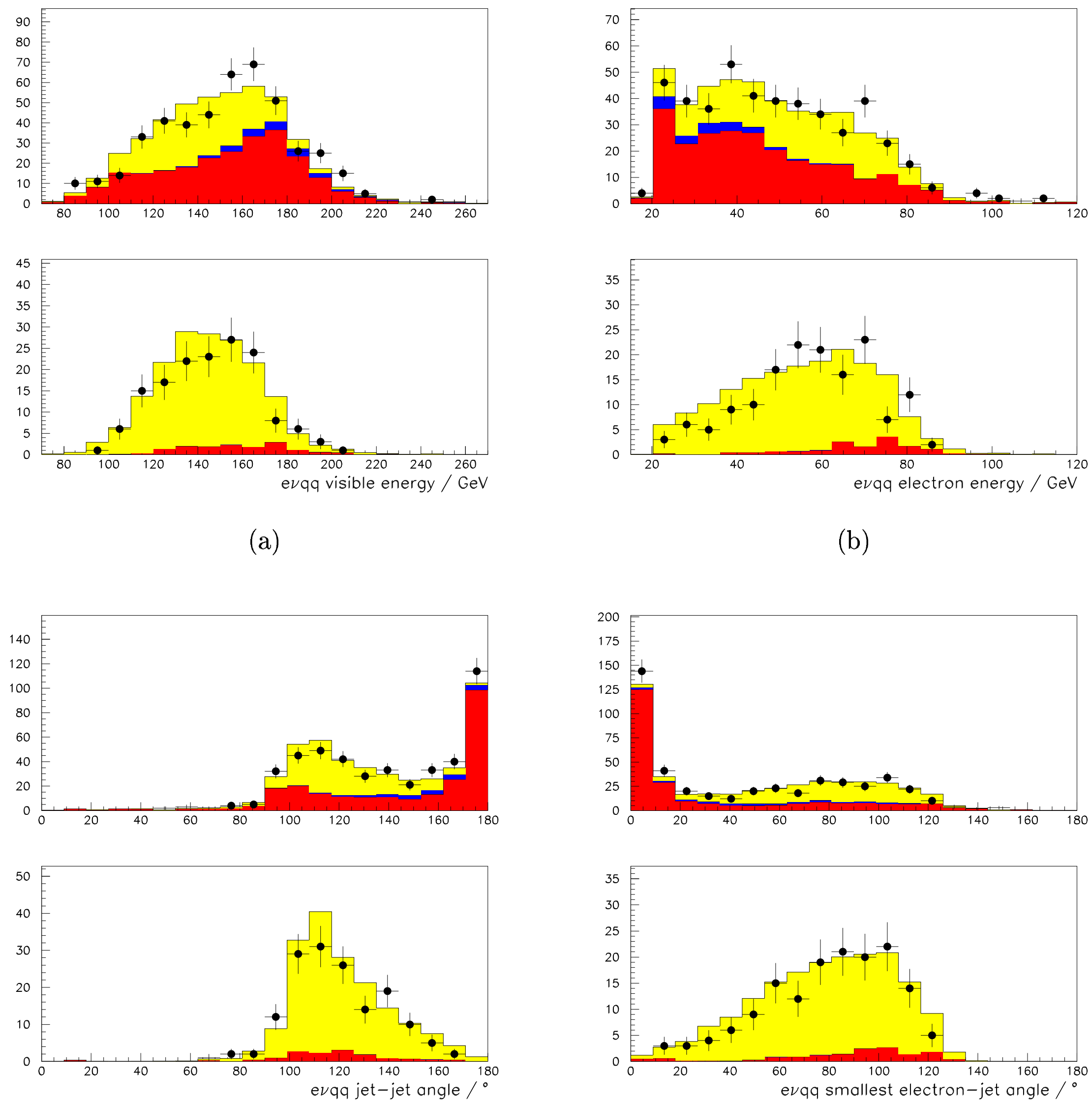

(a) (b)

(c) (d)

Figure 4.12: $e\overline{\nu}_e q\bar{q}'$ visible energy (a), electron energy (b), jet-jet angle (c), and electron-jet angle (d) distributions for 200 GeV data and Monte Carlo simulation before (top) and after (bottom) IDA selection.

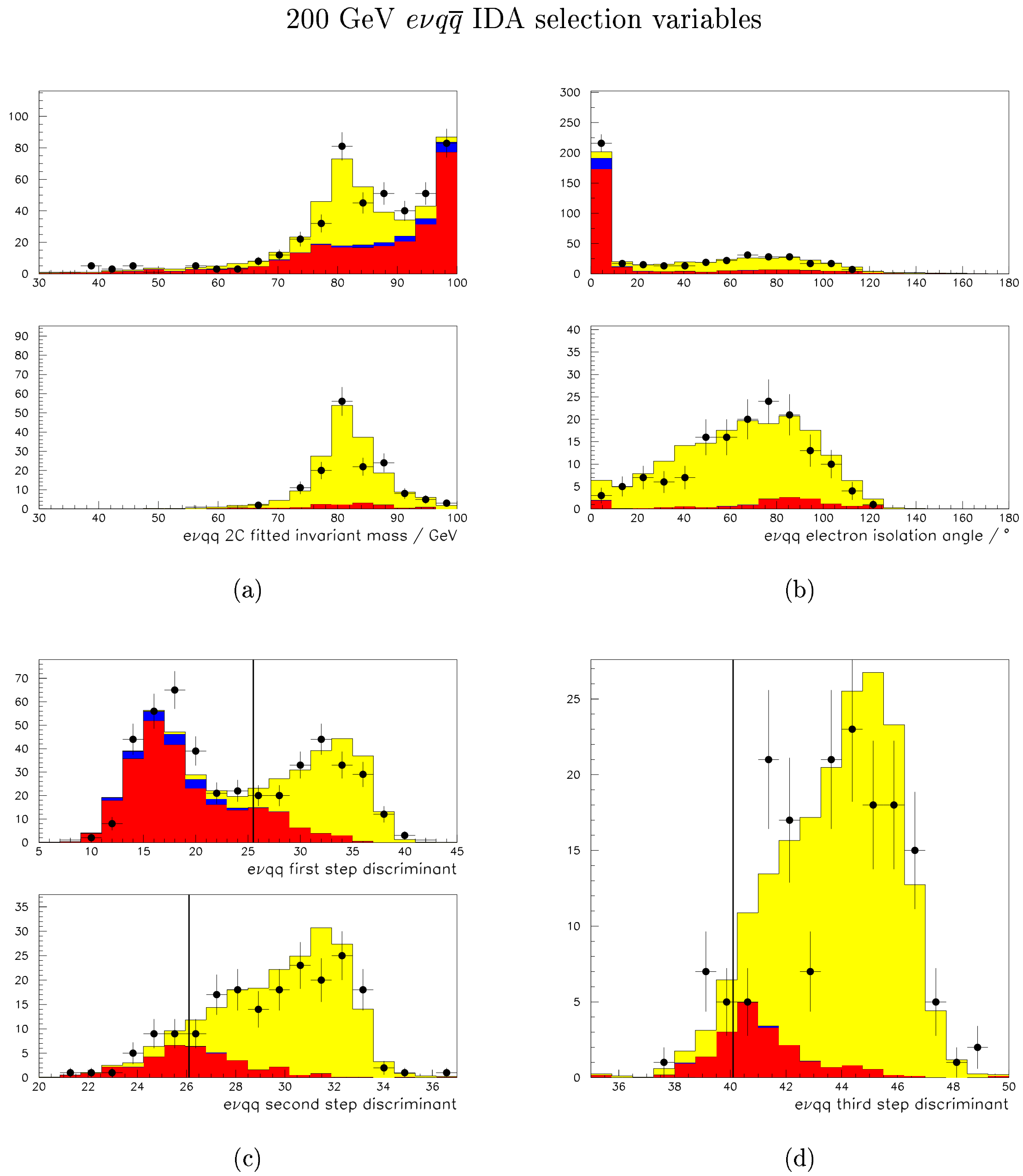

Figure 4.13: $\mathrm{e}\overline{\nu}_{\mathrm{e}}\mathrm{q}\overline{\mathrm{q}}'$ 2C fitted mass (a), electron isolation angle (b) distributions before (top) and after (bottom) IDA selection, first (plot c, top), second (plot c, bottom) and third (d) step IDA discriminant distributions.

200 GeV $\mu\nu q\overline{q}$ IDA selection variables

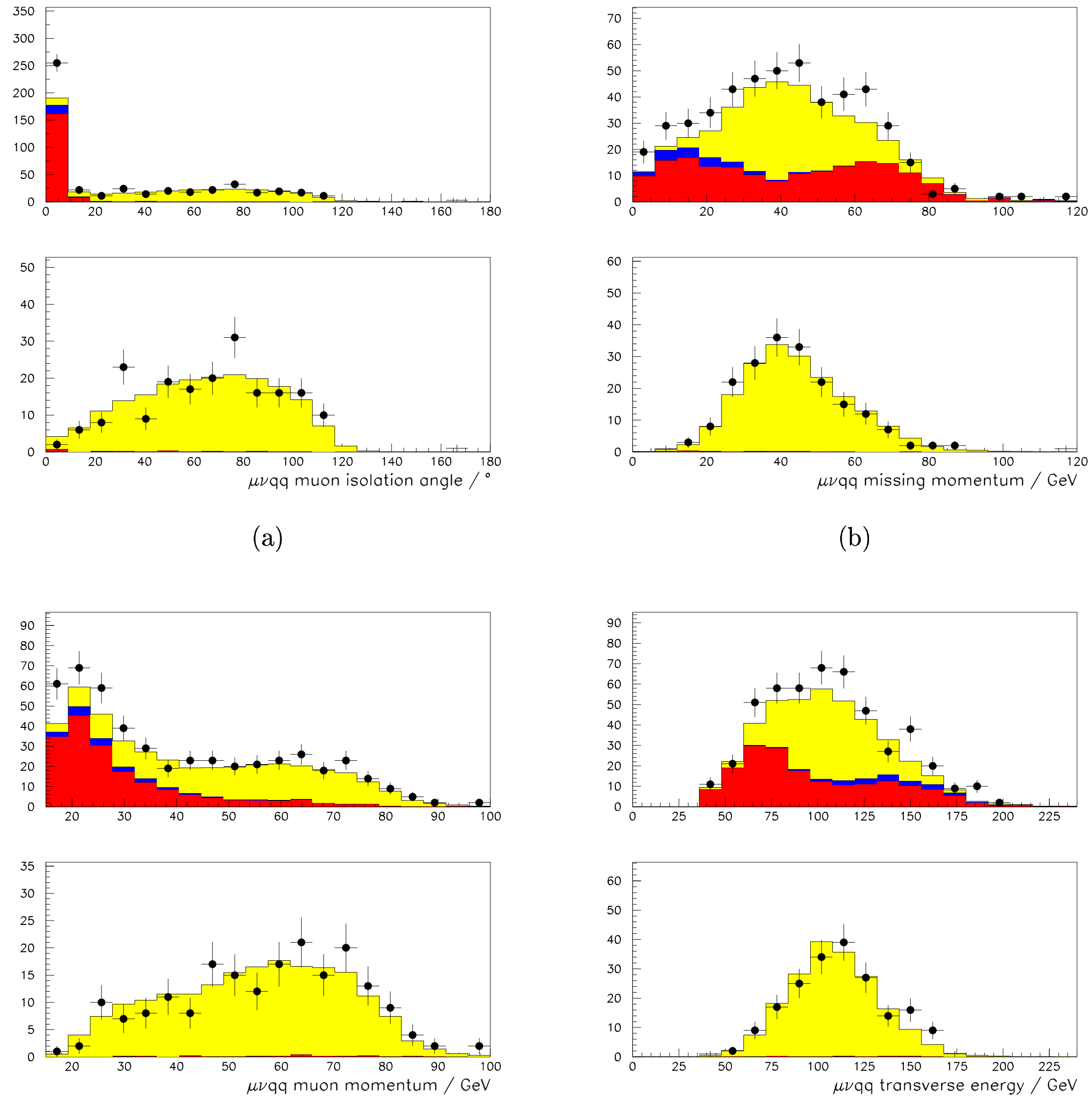

(a) (b)

(c) (d)

Figure 4.14: $\mu\overline{\nu}_\mu q\bar{q}'$ visible muon isolation angle (a), missing momentum p_{miss} (b), muon momentum (c), and transverse energy (d) distributions for 200 GeV data and Monte Carlo simulation before (top) and after (bottom) IDA selection.

200 GeV $\mu\nu q\bar{q}$ IDA selection variables

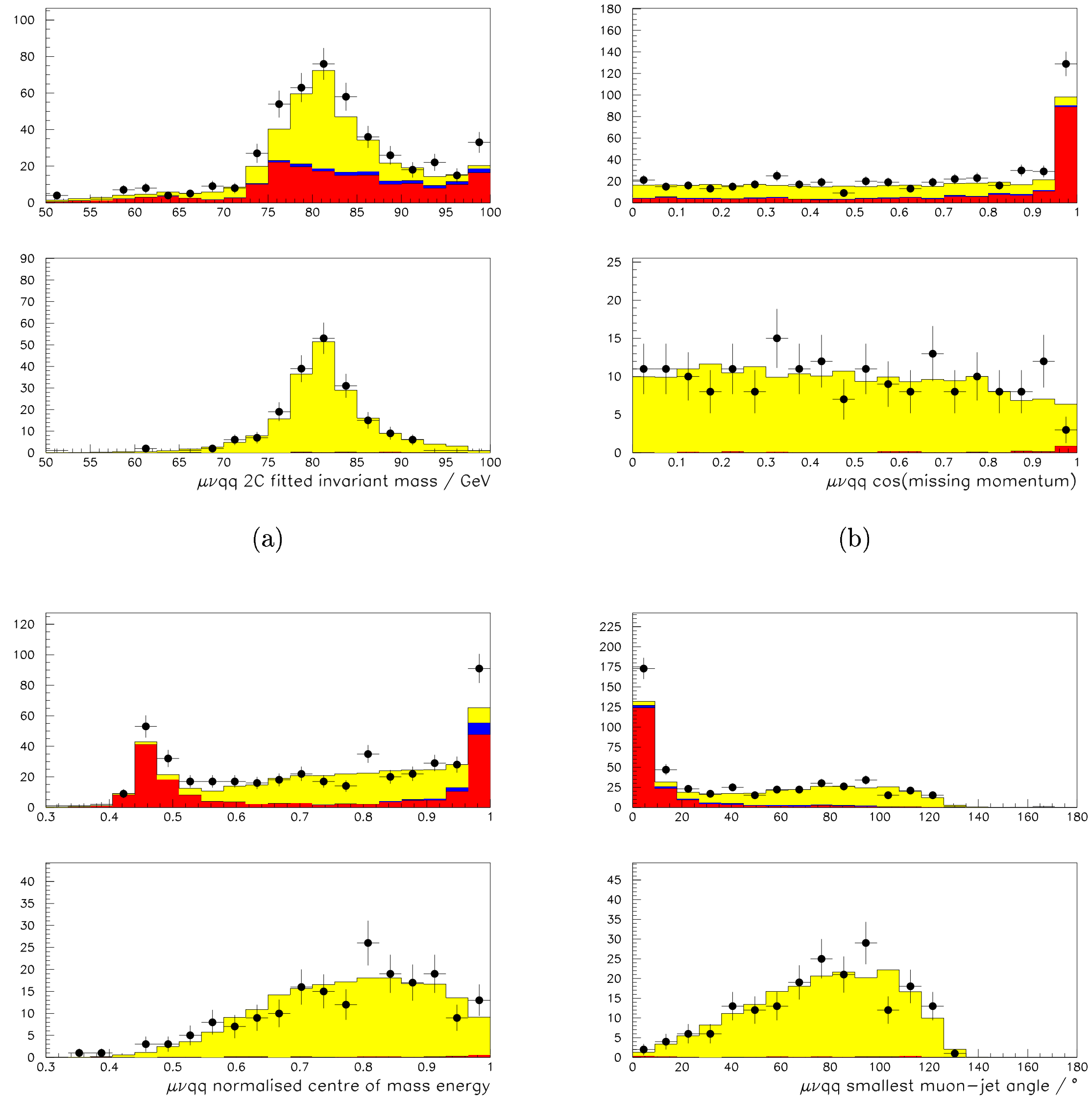

(a) (b)

(c) (d)

Figure 4.15: $\mu\overline{\nu}_{\mu}\text{q}\bar{\text{q}}'$ 2C fitted mass (a), $cos(p_{miss})$ (b), $\sqrt{s'}/\sqrt{s}$ (c), and smallest muon-jet angle (d) distributions for 200 GeV data and Monte Carlo simulation before (top) and after (bottom) IDA selection.

200 GeV $\mu\nu q\overline{q}$ IDA selection variables

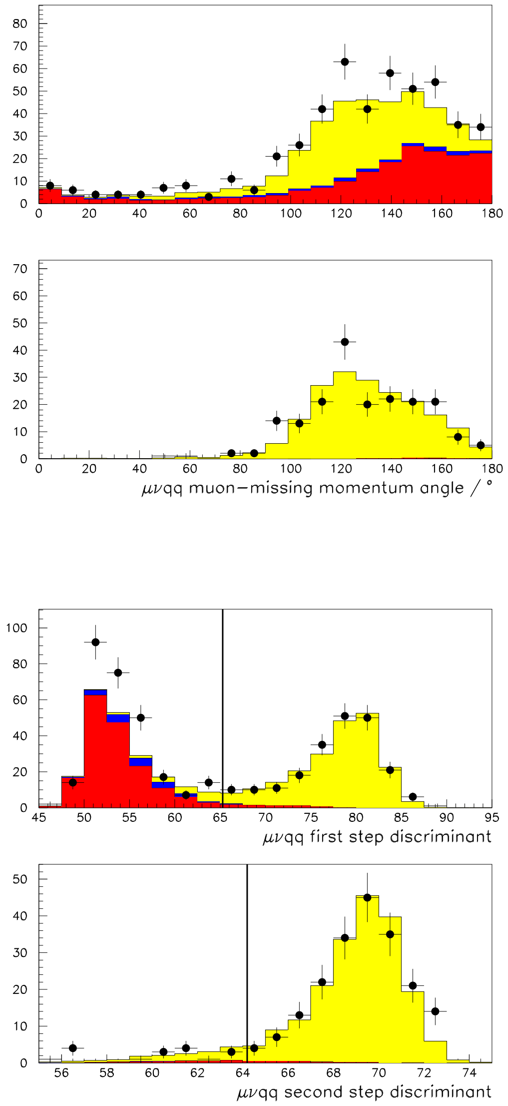

Figure 4.16: $\mu\overline{\nu}_{\mu}$q$\bar{\text{q}}'$ muon-p_{miss} angle before (top) and after (second from top to bottom) IDA selection, and first (third from top to bottom) and second (bottom) step IDA discriminant distributions for 200 GeV data and Monte Carlo simulation.

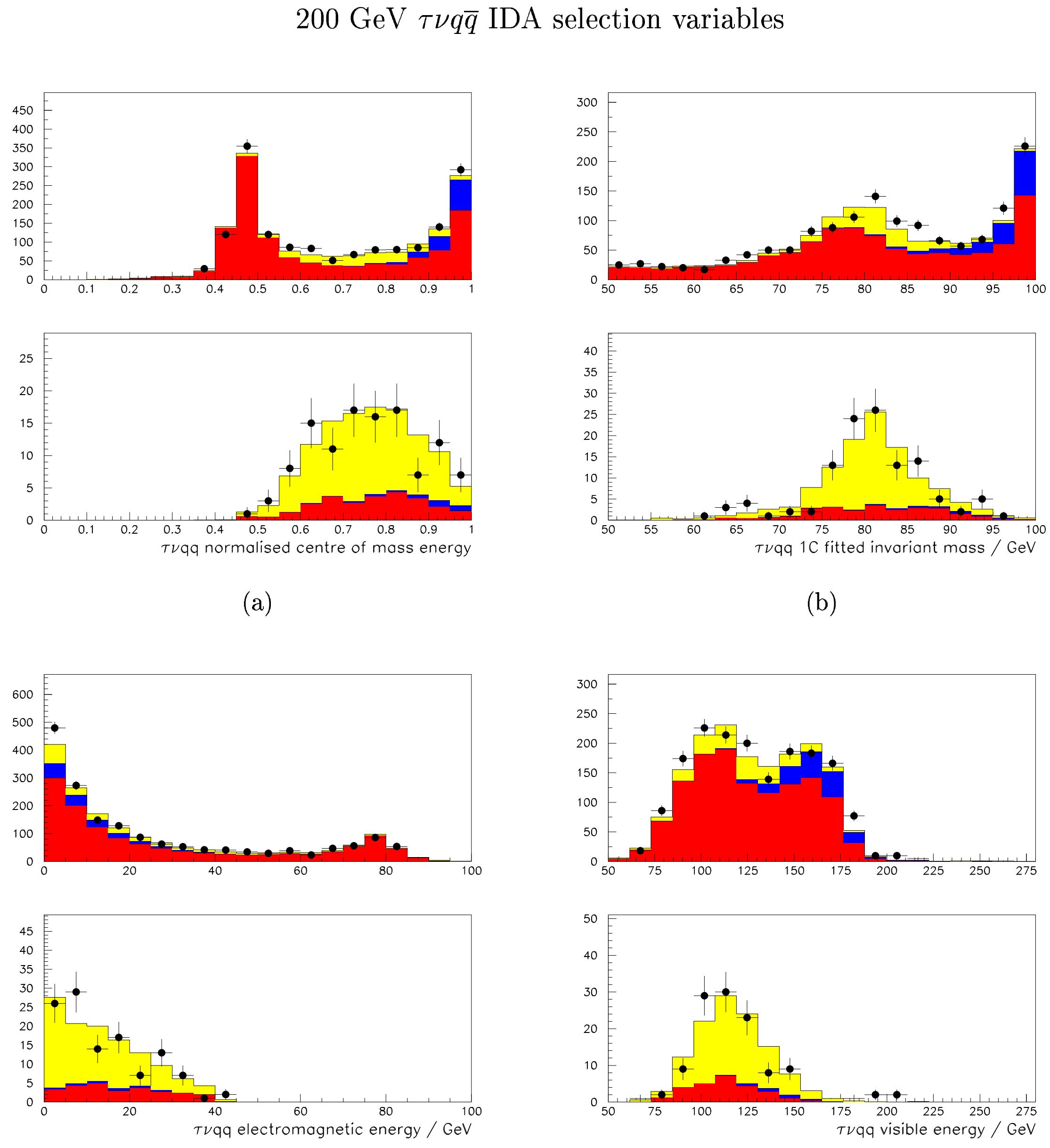

(a)

(b)

(c)

(d)

Figure 4.17: $\tau\bar{\nu}_\tau q\bar{q}'$ visible $\sqrt{s'}/\sqrt{s}$ (a), 1C fitted mass (b), energy deposited in electromagnetic calorimeters (c), and visible energy (d) distributions for 200 GeV data and Monte Carlo simulation before (top) and after (bottom) IDA selection.

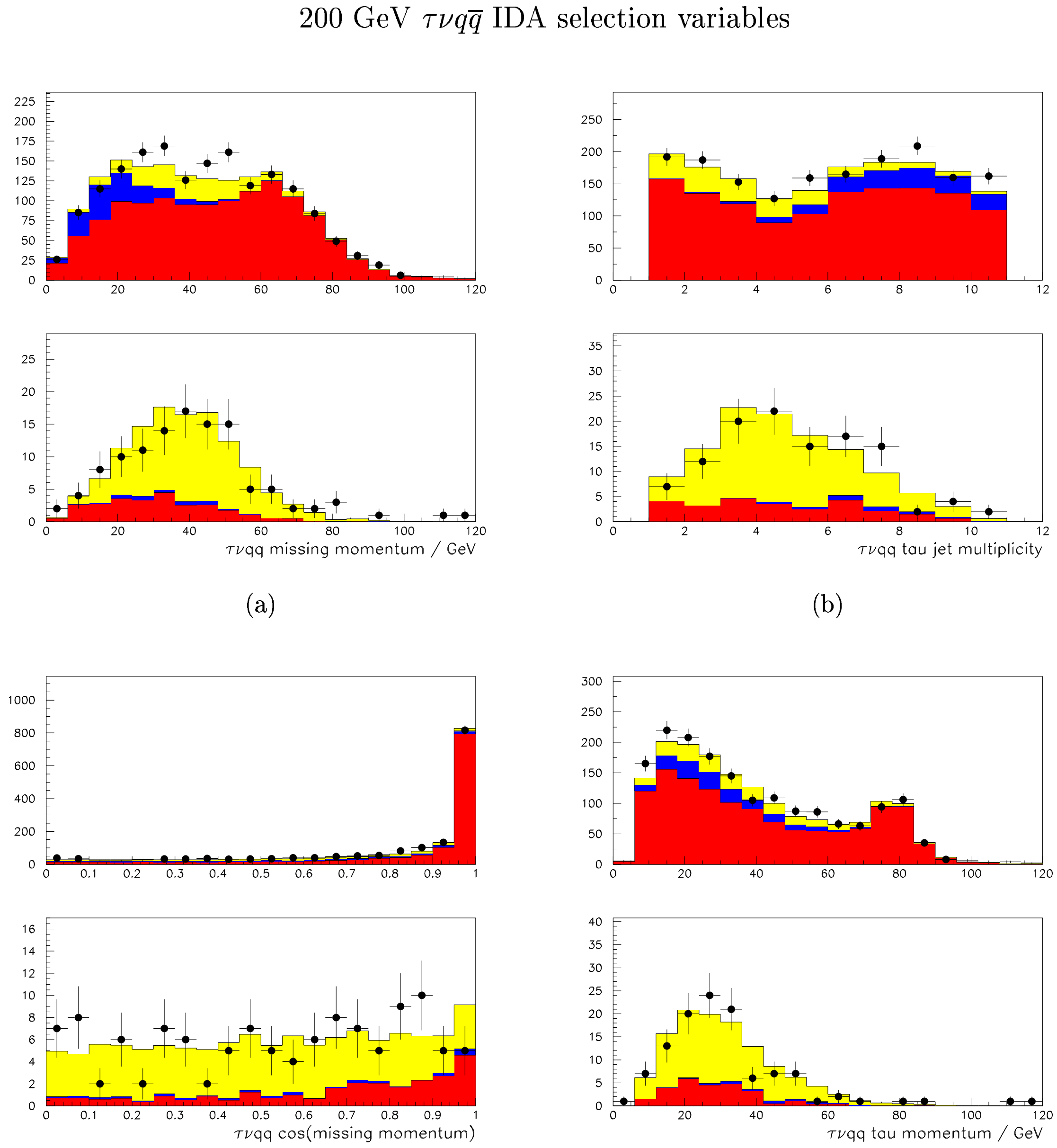

(a) (b)

(c) (d)

Figure 4.18: $\tau\overline{\nu}_\tau q\bar{q}'$ missing momentum p_{miss} (a), τ-jet multiplicity (b), $cos(p_{miss})$ (c), τ-jet momentum (d) distributions for 200 GeV data and Monte Carlo simulation before (top) and after (bottom) IDA selection.

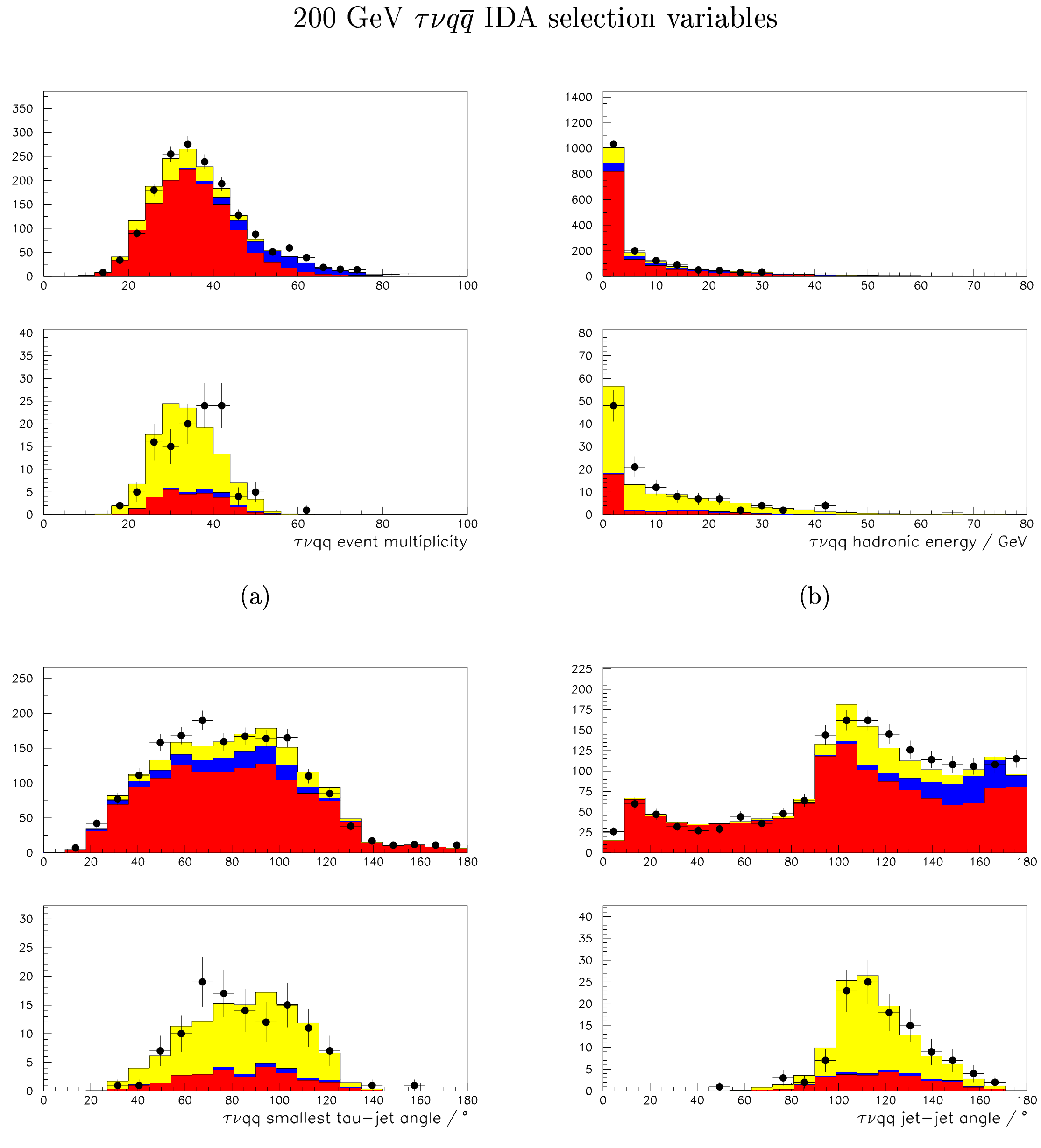

(a) (b)

(c) (d)

Figure 4.19: $\tau\overline{\nu}_{\tau}\mathrm{q}\bar{\mathrm{q}}'$ multiplicity (a), energy deposited in hadronic calorimeters (b), angle between τ-jet and nearest jet (c), jet-jet angle (d) distributions for 200 GeV data and Monte Carlo simulation before (top) and after (bottom) IDA selection.

200 GeV $\tau\nu q\overline{q}$ IDA selection variables

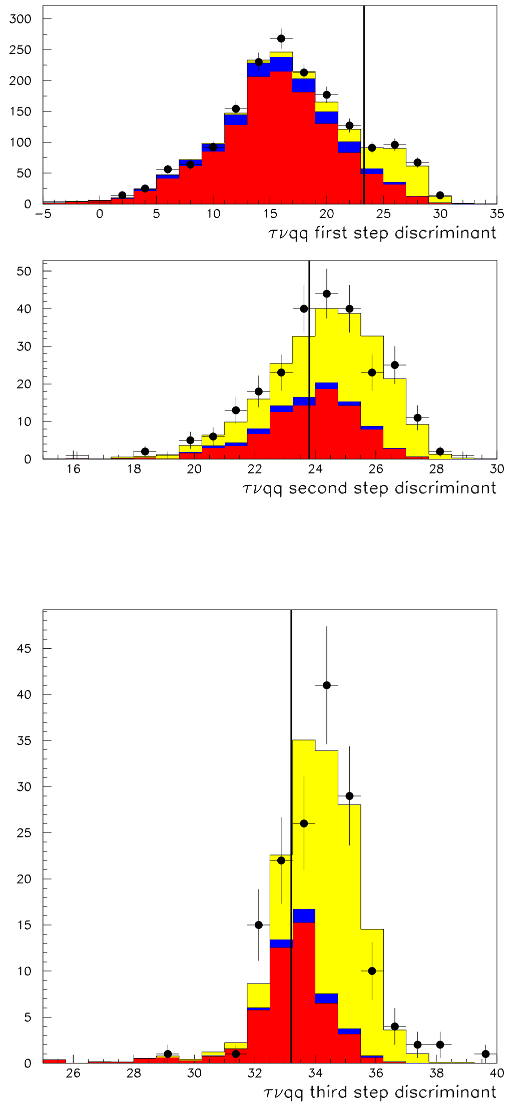

Figure 4.20: $\tau\overline{\nu}_{\tau}\mathrm{q}\bar{\mathrm{q}}'$ first, second and third step IDA discriminant distributions for 200 GeV data and Monte Carlo simulation (top to bottom).

It is clear from the plots that there is an excess of low isolation angle and low momentum $\mu\bar{\nu}_\mu \mathrm{q\bar{q}'}$ events before the IDA selection is performed. This is due to a deficient modelling of punch-through pions in the simulation [62]. The excesses are in background dominated regions and so their effect on the analysis presented here is assessed by scaling the background and checking the effect on the final IDA selection. The effect is reduced after applying the first step discriminant cut and found to be negligible after the full selection. Nevertheless, the error on $\mathrm{M_W}$ and Γ_W stemming from the uncertainty in the level of the background is evaluated in Section 6.4.

4.4.5 Performance

The selections have been applied to Monte Carlo samples in order to estimate their efficiency and purity. For this purpose, signal and background samples independent to those used for tuning the IDA have been used. The efficiencies and visible background cross sections are summarised in Tables 4.6 and 4.7. The efficiencies are given in terms of $\mathrm{W^+W^-}$-like truth processes. In the case of the $\tau\bar{\nu}_\tau \mathrm{q\bar{q}'}$ channel the truth category includes all types of τ decay. The truth categories for all final states

M.C. Truth Process	Selection channel		
	$\mathrm{e}\bar{\nu}_\mathrm{e} \mathrm{q\bar{q}'}$	$\mu\bar{\nu}_\mu \mathrm{q\bar{q}'}$	$\tau\bar{\nu}_\tau \mathrm{q\bar{q}'}$
	Efficiencies (%)		
$\mathrm{e}\bar{\nu}_\mathrm{e} \mathrm{q\bar{q}'}$	65.33 ± 0.51	0.41 ± 0.07	3.34 ± 0.19
$\mu\bar{\nu}_\mu \mathrm{q\bar{q}'}$	0.10 ± 0.03	88.28 ± 0.36	0.76 ± 0.10
$\tau\bar{\nu}_\tau \mathrm{q\bar{q}'}$	3.86 ± 0.21	4.95 ± 0.24	30.2 ± 0.50
$\mathrm{q\bar{q}'\bar{q}q'}$	0.01 ± 0.01	0.01 ± 0.01	0.29 ± 0.03
$l\bar{\nu}_l \bar{l}\nu_l$	–	–	–
	backgrounds (fb)		
$q\bar{q}$	62.4 ± 11.4	20.8 ± 6.6	126.9 ± 16.2
$\mathrm{e^+e^-q\bar{q}'}$	41.5 ± 6.8	–	10.1 ± 3.4
$\mu^+\mu^-\mathrm{q\bar{q}'}$	0.1 ± 0.1	28.6 ± 0.7	0.7 ± 0.1
$\tau^+\tau^-\mathrm{q\bar{q}'}$	0.8 ± 0.1	1.5 ± 0.1	7.1 ± 0.2
$\nu\bar{\nu}\mathrm{q\bar{q}'}$	0.4 ± 0.1	–	9.0 ± 0.6
$\gamma\gamma$	–	–	–

Table 4.6: 189 GeV IDA Selection Performance

M.C. Truth Process	Selection channel		
	$\mathrm{e}\overline{\nu}_{\mathrm{e}}\mathrm{q}\bar{\mathrm{q}}'$	$\mu\overline{\nu}_{\mu}\mathrm{q}\bar{\mathrm{q}}'$	$\tau\overline{\nu}_{\tau}\mathrm{q}\bar{\mathrm{q}}'$
	Efficiencies (%)		
$\mathrm{e}\overline{\nu}_{\mathrm{e}}\mathrm{q}\bar{\mathrm{q}}'$	65.30 ± 0.58	0.25 ± 0.06	2.80 ± 0.20
$\mu\overline{\nu}_{\mu}\mathrm{q}\bar{\mathrm{q}}'$	0.16 ± 0.05	86.40 ± 0.44	0.89 ± 0.12
$\tau\overline{\nu}_{\tau}\mathrm{q}\bar{\mathrm{q}}'$	0.23 ± 0.10	2.94 ± 0.22	37.9 ± 0.62
$\mathrm{q}\bar{\mathrm{q}}'\bar{\mathrm{q}}\mathrm{q}'$	0.02 ± 0.01	–	0.49 ± 0.05
$l\overline{\nu}_l\bar{l}\nu_l$	–	–	–
	backgrounds (fb)		
$q\bar{q}$	106.3 ± 12.8	13.86 ± 4.6	246.4 ± 19.5
$\mathrm{e}^+\mathrm{e}^-\mathrm{q}\bar{\mathrm{q}}'$	51.9 ± 6.9	–	20.8 ± 4.9
$\mu^+\mu^-\mathrm{q}\bar{\mathrm{q}}'$	–	20.6 ± 0.6	1.4 ± 0.2
$\tau^+\tau^-\mathrm{q}\bar{\mathrm{q}}'$	1.4 ± 0.1	1.1 ± 1.1	13.4 ± 0.3
$\nu\bar{\nu}\mathrm{q}\bar{\mathrm{q}}'$	–	0.1 ± 0.1	11.6 ± 1.0
$\gamma\gamma$	23.2 ± 9.5	–	11.6 ± 6.7

Table 4.7: 200 GeV IDA Selection Performance

defined in terms of the primary final state four fermions in $e^+e^- \rightarrow f\overline{f}f\overline{f}$ processes where all tree level Feynman diagrams are included. However, the IDA has been tuned to select CC03 events since it is these that carry the most information about the W boson. However, the efficiencies quoted here only differ significantly from CC03 ones in processes with an electron and an electron neutrino in the final state. The fully hadronic $\mathrm{q}\bar{\mathrm{q}}'\bar{\mathrm{q}}\mathrm{q}'$ final state also includes non-interfering contributions from the NC02 set of Feynman diagrams. These are events with two intermediate Z^0 bosons where the final state set of quarks cannot be reached through the CC03 set of Feynman diagrams. Thus, the NC02 $\mathrm{q}\bar{\mathrm{q}}'\bar{\mathrm{q}}\mathrm{q}'$ background is included in the $\mathrm{q}\bar{\mathrm{q}}'\bar{\mathrm{q}}\mathrm{q}'$ entries of the efficiency matrix. The contamination due to the remaining backgrounds is given in terms of visible cross sections. The performances quoted here are those obtained using the standard $\mathrm{W}^+\mathrm{W}^-$ cross section selection. As is shown in Chapter 5, further cuts are applied to selected events before the $\mathrm{M_W}$ and Γ_{W} fits are performed. The resulting changes in efficiency and purity are fully taken into account.

4.5 Treatment of Selected Events

Events have been selected according to their characteristics in the observables listed in Section 4.4.4. The M_W and Γ_W fits that will be performed with the events rely on distributions of observables that have a high M_W and Γ_W dependence. As is shown in Section 5.7.5, the most sensitive observable is the W boson invariant mass, defined as

$$m^2 = E^2 - p^2 \tag{4.9}$$

The invariant mass spectrum is sharply peaked and so has a well defined node and width. However, there are experimental factors that contribute to a distortion of the spectra[4]. These are:

- Biases and resolution effects on lepton energy or momentum measurement.
- Loss of energy and/or tracks down the beampipe or through gaps in the DELPHI detector.
- Energetic ISR photons escaping undetected down the beam pipe.
- The presence of one energetic neutrino from the leptonic W decay. This goes undetected.
- Resolution of jets energy measurement.

The above factors contribute to smear and bias the invariant mass distributions of the leptonic and hadronic systems. In the case of the di-jet system, Monte Carlo studies show the measured jet energy is considerably lower than the true primary quark energy. This biases the invariant mass distribution towards lower values. The jet energy resolution effects broaden the distribution. In the leptonic system, the electron and muon energy resolution is considerably better than the jet one, and the bias correspondingly smaller. A problem arises from the presence of the neutrino, whose four momentum is not well determined. This is due to the presence of further sources of missing momentum, such as ISR, which is typically emitted down the beam pipe.

---

[4] We refer to a spectra here as we are considering two W bosons per event and hence, two invariant masses.

Although the fit method presented in Chapter 5 is unbiased and designed to take all such effects into account, its sensitivity depends greatly on the shape of the invariant mass distribution and so is limited by resolution effects. However, extra information may be added to the calculation of the invariant mass. Using knowledge of the centre of mass energy of the e^+e^- collisions, we can apply two sets of constraints. First, we impose conservation of energy, that is, that the sum of the energy of the "particles"[5] and any detected ISR photon is equal to twice the measured LEP beam energy. Second, we impose conservation of momentum, whereby the vectorial sum of the momenta of particles and ISR photon must be zero. These four constraints assume that there are no ISR photons escaping down the beampipe and thus approximately assigns the missing momentum to the neutrino. A fifth constraint is applied to improve the invariant mass resolution: the masses of the leptonic and hadronic systems are required to be the same. Given that the width of the invariant mass distribution is dominated by the detector resolution effects it is not unreasonable to treat the W bosons in an event as on-shell and assign the two masses to be equal. This results in the reconstruction of only one W invariant mass for each event.

The constraints and the calculation of the invariant masses are obtained by performing a constrained kinematic χ^2 fit using `PUFITC+` [64]. The inputs are the measured directions and energies or absolute momenta of the particles and ISR photon candidate, and the errors associated to each of those quantities. In the case of jets the errors are parametrised as a function of the jet polar angle. The initial neutrino momentum vector is taken from the event missing momentum, but is given a large error so that it has little pull on the result from the χ^2 fit. The τ lepton is treated as a jet as it has well defined direction but undefined energy. The details of the kinematic fit can be found in Appendix B. By considering the errors on the measured quantities in the event the kinematic fit exploits the precision in the electron energy or muon momentum, and in the quark or τ jet direction measurements.

The improvement in the determination of the invariant mass can be seen in Figure 4.21, which shows the di-jet mass resolution before and after the kinematic fit. The kinematic fit yields an improved measurement of a set of event observables.

---

[5] we consider as particles the jets and leptons from which the invariant masses can be obtained.

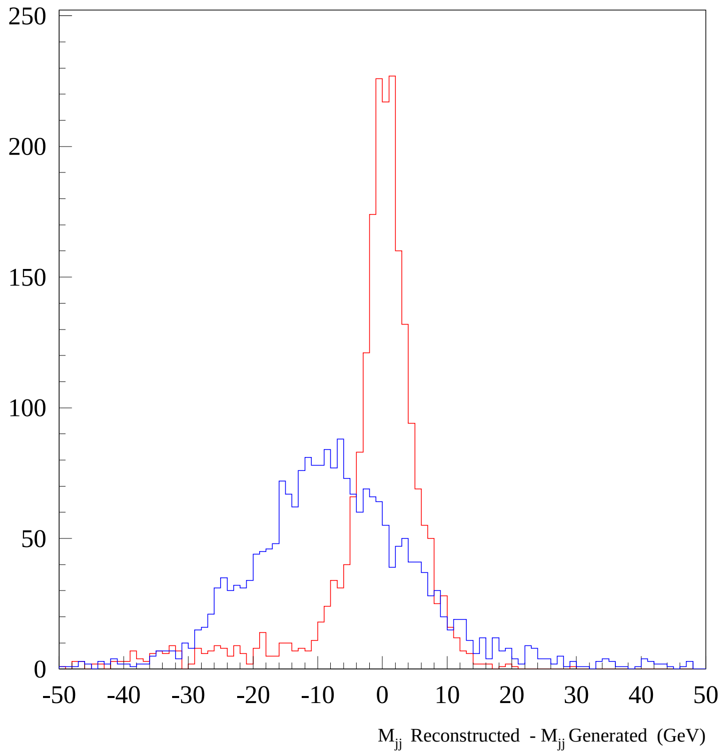

Figure 4.21: The di-jet invariant mass resolutions before (dark line) and after (light line) a constrained kinematic fit has been performed. Besides improving the resolution, the kinematic fit reduces the bias in the reconstructed mass.

Of particular importance to this analysis are the invariant masses resulting from different constraints, and the error on these quantities. The price to pay for the gains resulting from the constrained fit is the direct dependence of the fitted kinematical variables on the LEP beam energy. The uncertainty in the energy calibration now enters directly into the sensitivity with which parameters can be fitted from the kinematical variable distributions[6]. Its effect on the M_W measurement is discussed in section 6.5.

---

[6] There is an indirect dependence on the beam energy due to the calibration of the momentum and energy scale of jets and and leptons and photons (See Chapter 6). This dependence is, however, not a dominant factor in the error associated to these calibrations.

Chapter 5

The M_W and Γ_W Fitting Method

5.1 Introduction

This chapter describes the fitting method used to extract $\mathrm{M_W}$ and Γ_W from $e^+e^-\rightarrow \mathrm{W^+W^-}\rightarrow \mathrm{l}\overline{\nu}_\mathrm{l}\mathrm{q\bar{q}'}$ events selected at centre of mass energies between 189 and 202 GeV. Section 5.4 will introduce the basic principles behind non-parametric methods for probability density estimation and their application to parameter fitting and unfolding. In Section 5.4.2 an unbinned maximum likelihood method will be described in detail. A simpler binned maximum likelihood method, used as a cross check, will also be described. Tests of the performance and consistency of the methods will be shown in Section 5.6 . Their implementation to the measurement of $\mathrm{M_W}$ and Γ_W in semi-leptonic $\mathrm{W^+W^-}$ events will be described in Section 5.7 . The results of the method applied to data from the 1998 and 1999 running periods (corresponding to $\sqrt{s}$ ranging between 189 and 202 GeV) will be presented in Chapter 7.

5.2 Conventions

The methods for parameter fitting and unfolding described in the following sections are generalisable to different kinds of problems and so are outlined in terms of abstract sets of observables and parameters. In what follows, $\mathbf{\Omega}_i$ represents a vector of observables $(\omega_1, \omega_2, \omega_3, ..., \omega_{N-1}, \omega_N)$ for an event i and $\tilde{\mathbf{\Omega}}_i$ represents the corresponding vector after experimental resolution and acceptance effects. When stated explicitly, elements of $\tilde{\mathbf{\Omega}}$ are written in lower case. $\mathbf{\Lambda}$ represents any vector of underlying parameters which define the physics behind the distributions of $\mathbf{\Omega}^1$. Elements of $\mathbf{\Lambda}$ are written in upper case.

5.3 The Maximum Likelihood

The Maximum Likelihood method assigns the probability that an event described by a set of observables $\mathbf{\Omega}$ came from a distribution defined by a set of parameters $\mathbf{\Lambda}$ according to a probability density function (PDF) $\mathbf{P}(\mathbf{\Omega}|\mathbf{\Lambda})$. This PDF must be normalised to 1 over the full space of observables $\mathbf{\Omega}$ and for all physical values of the parameters $\mathbf{\Lambda}$:

$$\int P(\mathbf{\Omega}|\mathbf{\Lambda})d\mathbf{\Omega} \; = \; 1 \tag{5.1}$$

The value of $\mathbf{\Lambda}$ which maximises the likelihood L is the fitted value. The Likelihood is then defined as the collective probability of the data sample to come from the distribution with parameters $\mathbf{\Lambda}$:

$$L(\mathbf{\Lambda}) \; = \; \prod_{i=1}^{n} P(\mathbf{\Omega}_i|\mathbf{\Lambda}) \tag{5.2}$$

where $\mathbf{\Omega}_i$ is the value of the observables $\mathbf{\Omega}$ of the i^{th} event in a sample of n. The value of $\mathbf{\Lambda}$ which maximises the likelihood L is the fitted value, $\mathbf{\Lambda}_{fit}$. In practice the quantity $-2\ln L$ is maximised as it behaves like a χ^2 (provided L is Gaussian-like) and the evaluation of the statistical error becomes straight-forward with most function evaluation and minimisation algorithms [61, 65, 66].

The differences between the methods mentioned above lie mainly in the means used to calculate $\mathbf{P}(\mathbf{\Omega}|\mathbf{\Lambda})$. So far in DELPHI, for the official $\mathrm{l\overline{\nu}_l q\bar{q}'}$ $\mathrm{M_W}$ and Γ_W extraction analysis, the PDF has been calculated from a convolution technique. This combines physics functions with phase-space factors, a Gaussian event-by-event resolution function and, more recently, ISR spectra. For a detailed discussion of one

---

[1] In this specific case, either $\mathrm{M_W}$ or Γ_W.

such method see [4]. The non-parametric methods favoured in the other LEP collaborations are more similar to the analysis presented here.

5.4 Non Parametric Methods for Parameter Fitting

The Maximum Likelihood is commonly used by all four LEP experiments for the extraction of $\mathrm{M_W}$ and Γ_W. ALEPH [67] and OPAL [68] both use binned likelihoods as their official method, while L3 [69] and DELPHI [70] make use of unbinned likelihoods. In what follows, both binned and unbinned non parametric methods will be outlined with particular attention being paid to the method which forms the basis for this analysis, the *Kernel Method* .

In non-parametric methods, the functional form of the probability density function (PDF) is not specified *a priori* but is derived from data[2] distributions [71]. The basic principle is to model the PDF which generated the data distributions without making any assumptions as to its form. In practice, the PDF will be constructed from Monte Carlo samples which describe the underlying physics of interest as well as the detector response. In this way detector and physics effects which are difficult to parametrise (ISR, FSR, 4f interference, etc.) are included directly in the PDF to the extent of the validity of the Monte Carlo model. Consequently any biases arising from such effects should be eliminated. The approach taken here is to approximate the PDF at any given point i in a space constructed from $\mathbf{\Omega}$ as the local density of Monte Carlo population in the vicinity of i . This can be expressed in terms of the fraction of Monte Carlo events lying inside a region R surrounding i :

$$P \approx \frac{\mathbf{N}_{inR}}{\mathbf{V} N_{total}} \tag{5.3}$$

where V is the volume of the region R and $\mathbf{N}_{total}$ is the total Monte Carlo population. Equation 5.3 relies on two fundamental assumptions: the real PDF must

---

[2] To maintain the generality of this discussion, we refer to "data", which can be real or Monte Carlo simulation. In the context of $\mathrm{M_W}$ and Γ_W determination the data used is simulation. This will be made clear in following sections.

vary linearly within R and the number of Monte Carlo events in R must be large enough that statistical fluctuations are negligible. Thus R plays a crucial role in the method. It is also clear that large Monte Carlo statistics, $\mathbf{N}_{total}$, are always desirable, particularly if the $\mathbf{\Omega}$ is to be generalised to many dimensions. By using this non parametric approximation we get closer to the exact underlying PDF at the expense of some dependence on the statistics of the reference Monte Carlo sample. Two different approaches are outlined in what follows: the *Kernel* and the *Binned* Methods. Their main conceptual difference concerns the way in which the region R is defined and hence the way the PDF is constructed. In the limit of $R \to 0$ both are equivalent.

5.4.1 Constructing a Space from a Set of Observables

The region R and volume $\mathbf{V}$ in Equation 5.3 are evaluated in a space $\mathbf{\Omega}'$ constructed from the set of observables in $\mathbf{\Omega}$. The reasons for this are twofold: different observables carry different sensitivity to the parameters $\mathbf{\Lambda}$ and so can be chosen to carry more or less weight when the space is constructed, and for practical reasons it is necessary to maintain a high enough density of Monte Carlo events in all regions of space being considered for the fit. So the space $\mathbf{\Omega}'$ is simply constructed by scaling the elements of $\mathbf{\Omega}$ as needed:

$$\mathbf{\Omega}' = \vec{\alpha} \cdot \mathbf{\Omega} \tag{5.4}$$

where the elements of $\vec{\alpha}$ can be used as tuning parameters of the fit. This scaling is analogous to the choice of bin-widths for the different dimensions of a binned analysis.

5.4.2 The Kernel Method

If the region R is centred on the data point i the number of events N_{inR} can be given by a *Kernel function* $K(\mathbf{\Omega}'_i)$ such as a hypersphere function such as that represented schematically in Figure 5.1:

$$K(\mathbf{\Omega}'_j - \mathbf{\Omega}'_i) = \begin{cases} 1 & |\mathbf{\Omega}'_j - \mathbf{\Omega}'_i| < r \\ 0 & |\mathbf{\Omega}'_j - \mathbf{\Omega}'_i| \geq r \end{cases} \tag{5.5}$$

where $\mathbf{\Omega}'_j$ is the vector of scaled observables for a Monte Carlo event j, and $|\mathbf{\Omega}'_j - \mathbf{\Omega}'_i|$

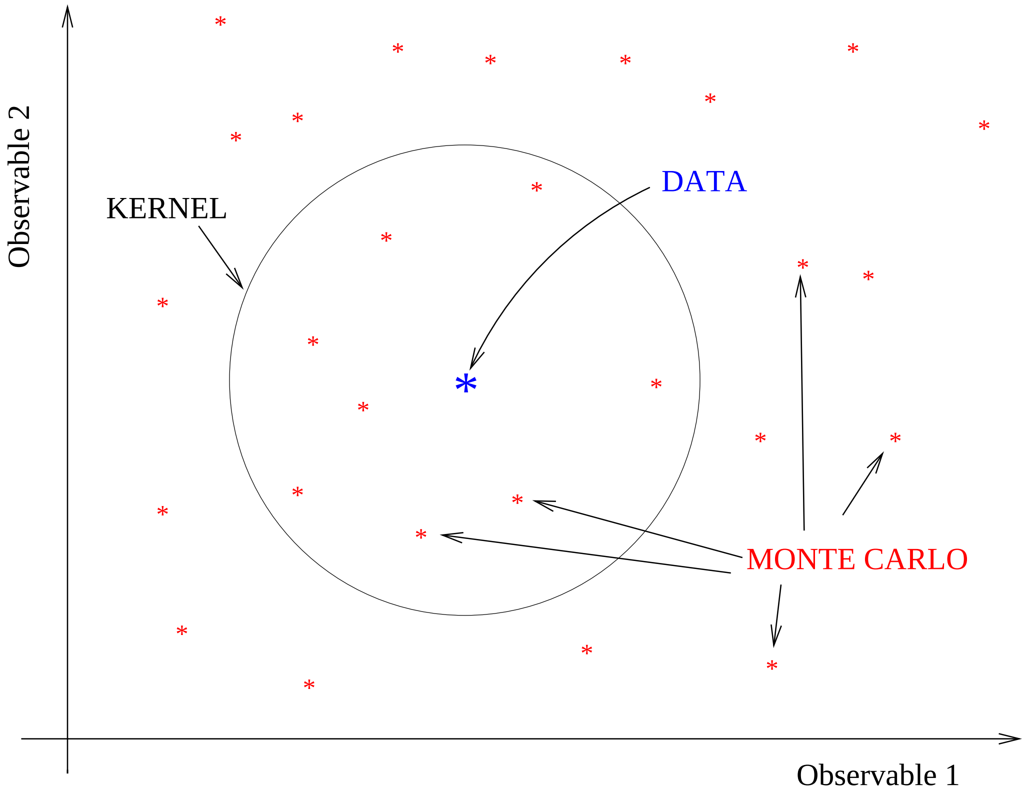

Figure 5.1: A two-dimensional Kernel function. The discrete boundary of the kernel serves to define the local density of Monte Carlo events in the vicinity of the data point.

is the Euclidean distance between $\mathbf{\Omega}_i^{'}$ and $\mathbf{\Omega}_j^{'}$. From Equation 5.5 it is clear that the number of Monte Carlo events N_i inside the region R surrounding i is simply:

$$N_i \;=\; \sum_{j=1}^{N_{total}} K(\mathbf{\Omega}_j^{'} - \mathbf{\Omega}_i^{'}) \tag{5.6}$$

and the approximate PDF becomes:

$$\mathbf{P}(\mathbf{\Omega}_i^{'}|\mathbf{\Lambda}) \approx \frac{1}{N_{total}} \sum_{j=1}^{N_{total}} \frac{1}{V_i} K(\mathbf{\Omega}_j^{'} - \mathbf{\Omega}_i^{'}) \tag{5.7}$$

Smoothing the PDF

One disadvantage of this type of Kernel is that the resulting PDF may have discontinuities due to the discrete boundaries of the cells. These discontinuities may be eliminated by increasing the radius r of the kernels. The effect of increasing

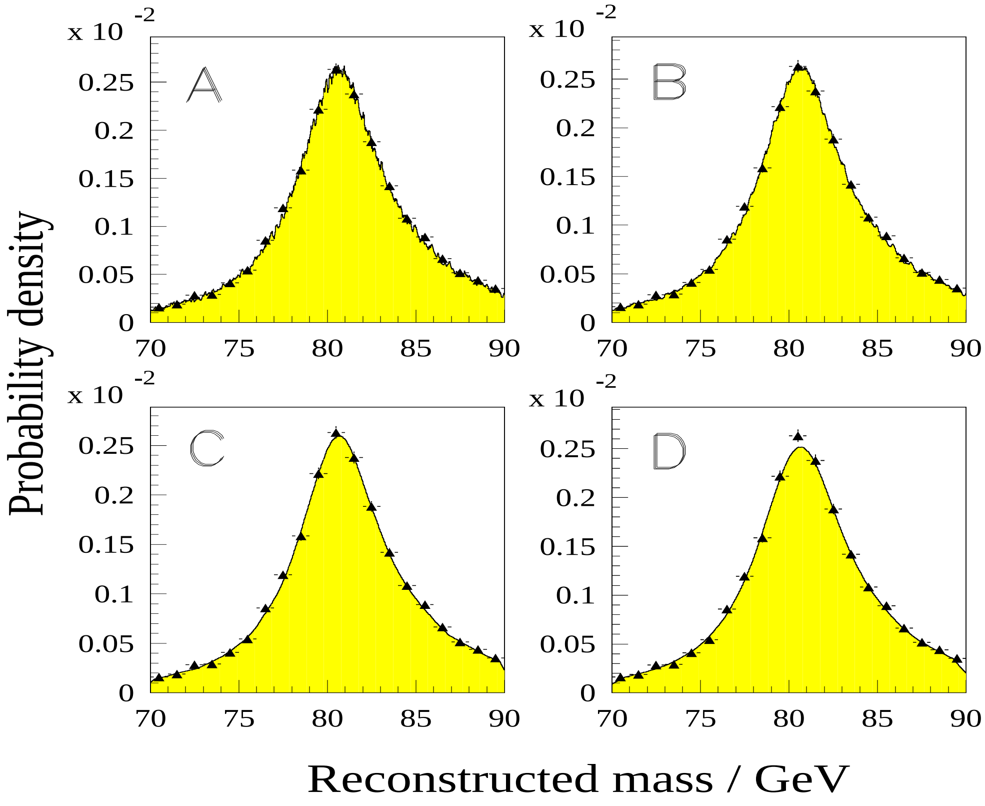

Figure 5.2: Several one-dimensional PDFs constructed from the same Monte Carlo sample are shown as a shaded histogram. The observable from which they are constructed is the measured W mass after the 2C kinematic fit. The triangles show a binned Monte Carlo data distribution as an approximation to the "true" distribution which the PDF should model. Note how the PDF reproduces the statistical noise in the reference Monte Carlo sample. Plots A,B,C and D correspond to hypersphere kernels of radius of 50, 100, 500 and 1000 MeV respectively. The effect of increasing the width of the hypersphere kernels smoothes out the irregularities in the PDF but rapidly distorts its shape leading to a bias and loss of sensitivity.

the kernel width is shown in fig. 5.2 . As the kernels get larger, and their overlap increases, the discontinuities in the resulting PDF disappear. Unfortunately, so does the sensitivity to the observed data distribution. It can be seen that the distribution is being over-smeared and, besides the expected loss in sensitivity to $\mathbf{\Lambda}$, a large bias can be induced as the "average" local density approximation expressed in Equation 5.3 starts diverging from the "true", unknown PDF. One way of coping with this problem is to choose a non-discrete Kernel function, where instead of a

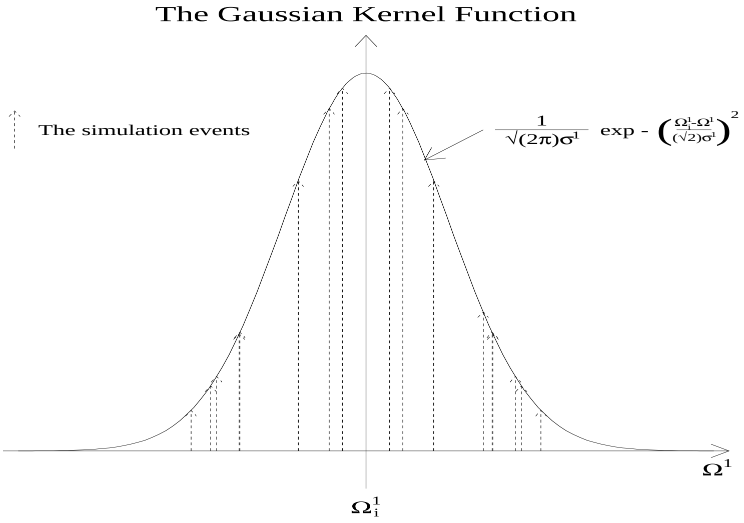

Figure 5.3: A 1-D Gaussian Kernel. Reference Monte Carlo Events are weighted according to the specified Gaussian function. This choice of Kernel smoothes the statistical fluctuations in the reference sample without increasing the effective size of the volume.

hypersphere the cell is defined as a Gaussian centered on data point i :

$$K(\mathbf{\Omega}_j^{'} - \mathbf{\Omega}_i^{'}) \;=\; \frac{1}{(2\pi\sigma^2)^{d/2}} exp\{-\frac{(\mathbf{\Omega}_j^{'} - \mathbf{\Omega}_i^{'})^2}{2\sigma^2}\} \tag{5.8}$$

where σ is the width of the Gaussian kernel and plays the role of a smoothing parameter analogous to the radius of the hypersphere kernel defined in Equation 5.5 or the bin-width in the method outlined in the following Section, and d is the number of dimensions of the space of scaled observables $\mathbf{\Omega}^{'}$. A one-dimensional sketch of the Gaussian kernel is shown in fig. 5.3. The effect of this change in the kernel function can be appreciated in fig. 5.4. It can be seen that the discontinuities have been smoothed out, making the PDF less sensitive to the statistical noise of the reference Monte Carlo, while maintaining the effective size of the volumes. Thus the bias which would be introduced by simply increasing the size of the hypersphere kernel is avoided by this procedure. Besides its smoothing effect, the Gaussian kernel gives more weight to the Monte Carlo events that are closer to the data point. Fig. 5.5 shows the PDFs that result from Gaussian kernels of different widths σ .

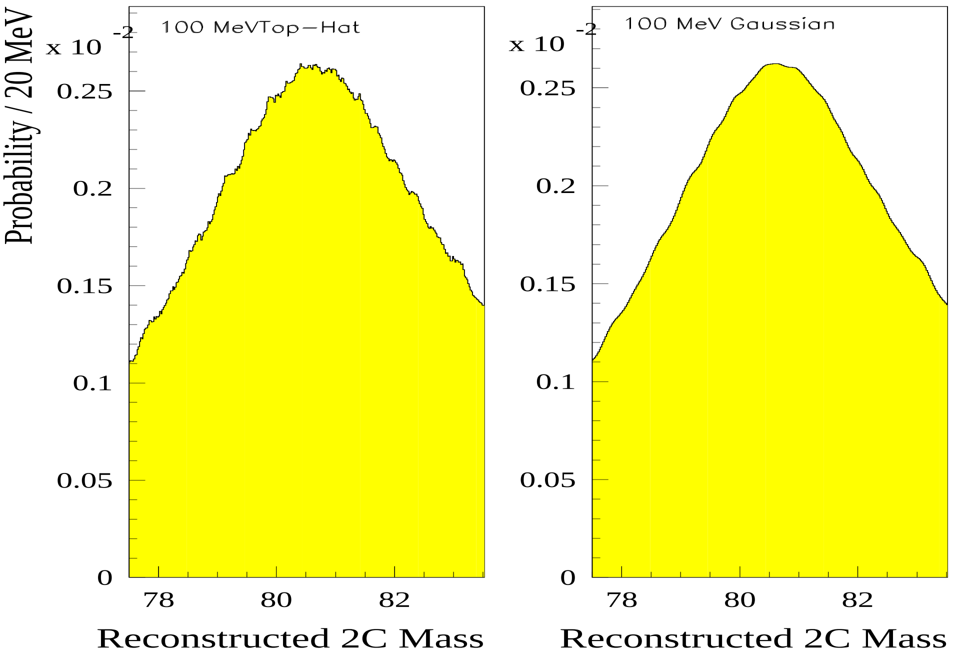

Figure 5.4: Two PDFs are constructed from the same reference Monte Carlo sample but with different kernel functions. The plot on the left shows the PDF constructed from the Hypersphere Kernel while the plot on the right shows that constructed from a Gaussian one. The radius and width are both 100 MeV so the visible smoothing is entirely due to the choice of kernel function.

Ensuring Normalisation of the PDF

Due to the finite effective size of the kernel cells, the approximate PDF defined by Equation 5.7 does not necessarily satisfy the normalisation condition 5.1 automatically. The problem arises from the presence of boundaries in the Ω space, be them physical limits of the variables or cuts applied in the analysis. When events lie near the boundaries, their kernel volumes can lie partially across the boundary, in an area of space with no reference Monte Carlo population, resulting in an underestimation of the PDF in these regions. The magnitude of the problem depends directly on the size of the kernel cells. The two distinct types of boundaries can be compensated for with two different solutions. For boundaries created artificially by cuts, the procedure adopted is simply to omit making the cuts on the reference Monte Carlo sample and to apply them only to the data samples to be fitted. In this way, the region beyond the boundary is populated by reference Monte Carlo events and

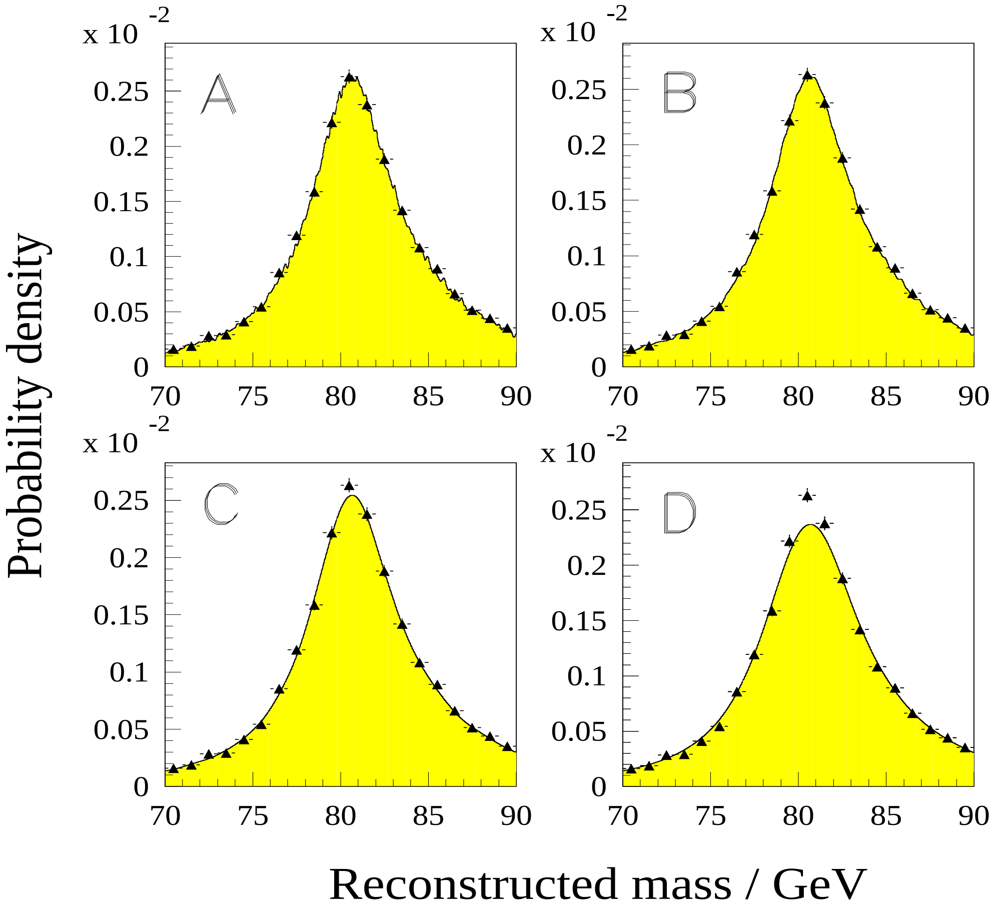

Figure 5.5: Several PDFs constructed from the same Monte Carlo sample are shown in the shaded histogram. A binned Monte Carlo data distribution (triangles) is overlaid to show the agreement between the PDF and the data it is trying to model. Plots A to D correspond to Gaussian kernels of width 50, 100, 500, and 1000 MeV respectively. Increasing the width of the Gaussian kernels smoothes out the irregularities in the PDF but rapidly distorts its shape.

so the probability for boundary events gets correctly calculated. A schematic of this method can be seen in Figure 5.6. The total number of reference Monte Carlo events, N_{total}, is then re-scaled to the number lying inside the cuts.

The problem concerning physical boundaries, like phase-space or unphysical values of any of the observables, requires an artificial compensation as there are no reference Monte Carlo events beyond these boundaries. The procedure adopted is to create a "ghost" data event by reflecting the data point across the boundary, and then to evaluate a complementary probability in the normal manner. This is then added to the original, underestimated one. This has the effect of increasing

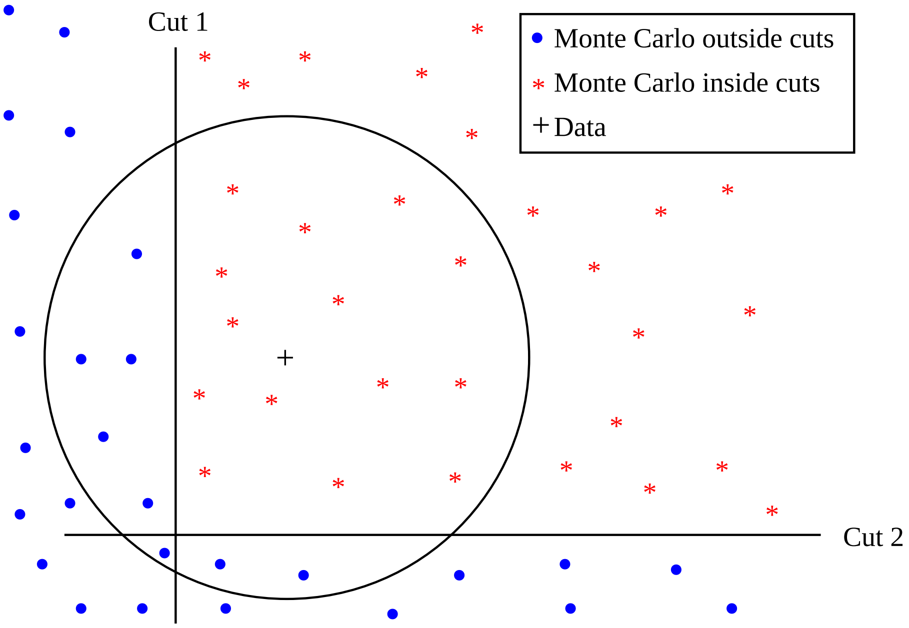

Figure 5.6: A data point lying close to the boundaries imposed by cuts on observables. The red stars are reference Monte Carlo lying within the cuts. A probability calculated using these events only will be underestimated. The blue stars are reference Monte Carlo events which would fail the cuts. When these are included a correct evaluation of the probability for the data event is obtained. The extra reference events are taken into account in the normalisation of the PDF.

the weight of reference events near the boundaries to make up for the empty zones of the kernel volumes. The *ghost event* method can be visualised in Figure 5.7.

Tuning Parameters

Once a choice of Kernel Function has been made, there are two tuning parameters of the method, both of which control the cell occupancy. In the set-up chosen, these are the radius of the Kernel cell, and the scaling of the real observables used to construct the space $\mathbf{\Omega}'$. These two parameters are important in controlling or limiting any biases and non-linearities, as is shown in the following sections.

5.4.3 The Binned Likelihood

In this method the regions R are replaced by predetermined, fixed bins covering the $\mathbf{\Omega}$ region of interest with no overlap[3]. An advantage of such a method is that

---

[3] There is no need to construct a space $\mathbf{\Omega}'$ in the binned method since the bin sizes can be chosen in order to give more or less weight to any observable ω_i

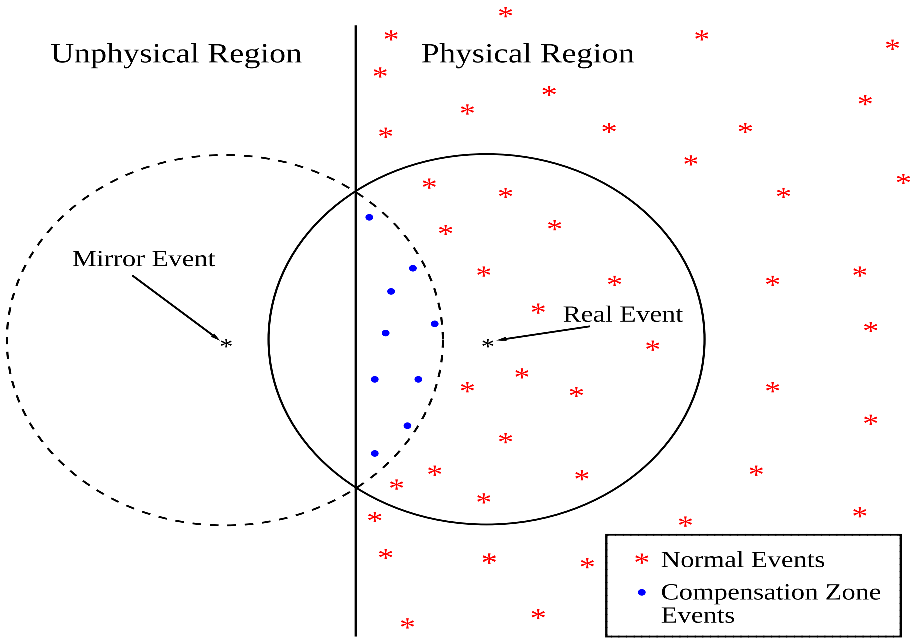

Figure 5.7: A data point lying near a physical boundary. As there are no reference Monte Carlo events in the unphysical region, some of them must be used to compensate for the resulting underestimation of the probability. A mirror event is used to construct the ghost kernel, represented here by the dashed circle. The probability for the event is the sum of the probabilities estimated using both kernels. In effect this amounts to using the reference events in the region of overlap twice.

once data and reference Monte Carlo events have been assigned to bins their $\mathbf{\Omega}$ information can be discarded, making it in general faster than unbinned methods. Furthermore, it is possible to directly compute a χ^2 to see how good the fit to the data is. Here, the PDF is simply defined as

$$\mathbf{P}(\mathbf{\Omega}_i|\mathbf{\Lambda}) \;=\; \frac{1}{N_{total}} \sum_{j=1}^{N} \frac{1}{V_i} N_{in\ bin} \tag{5.9}$$

This PDF differs from those described previously in that the “average” PDF is computed for arbitrary bins. The result is that data events which may look different will get assigned the same probability if they fall in the same bin. This loss of potentially useful information can only have a negative effect on the sensitivity of the method compared to an unbinned likelihood. On an event by event basis binning can introduce an extra source of bias in the estimation of the PDF. In the ideal case where the true PDF behaves continuously in the range of R and its second derivative

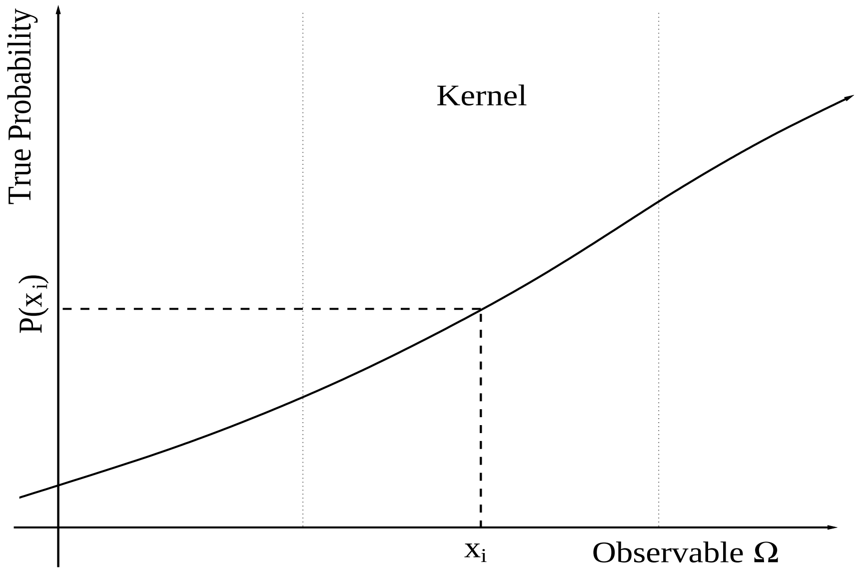

Figure 5.8: Variation of the true PDF inside the Kernel cell. The PDF at the data point is approximated as the mean PDF over the whole cell. This approximation holds exactly if the true PDF behaves linearly inside the cell.

is negligible the kernel methods described in the previous section provide an unbiased estimate of the PDF *at* each data point $\mathbf{\Omega}_i$ because the region R is centered on $\mathbf{\Omega}_i$. This can be visualised in figure 5.8. As point $\mathbf{\Omega}_i$ does not lie in the centre of the bin, it gets assigned the wrong probability. However, a lot of this biasing effect is diluted by the other events in the bin, making the average bias smaller. Unfortunately, the bias now depends on the first derivative of the *data* distribution in the bin while there is only a second and higher derivative dependence in the Kernel methods. Either way, the fact that there is a miscalculation of the PDF on an event-by-event basis means that the resolution is reduced even if there turns out to be no overall bias.

Another problem inherent to all binned methods is their granularity which may make the measurement of subtle effects impossible or unreliable. Fig. 5.9 shows how the PDF reproduces the structure and discontinuities of the bins. However, the binned likelihood method is used by two of the four LEP collaborations to extract $\mathrm{M_W}$ and Γ_W and an exploration of this method within DELPHI could shed some light on the apparent differences in $\mathrm{M_W}$ sensitivity in the semi-leptonic channel between experiments. It also provides a very fast cross-check analysis, both for the

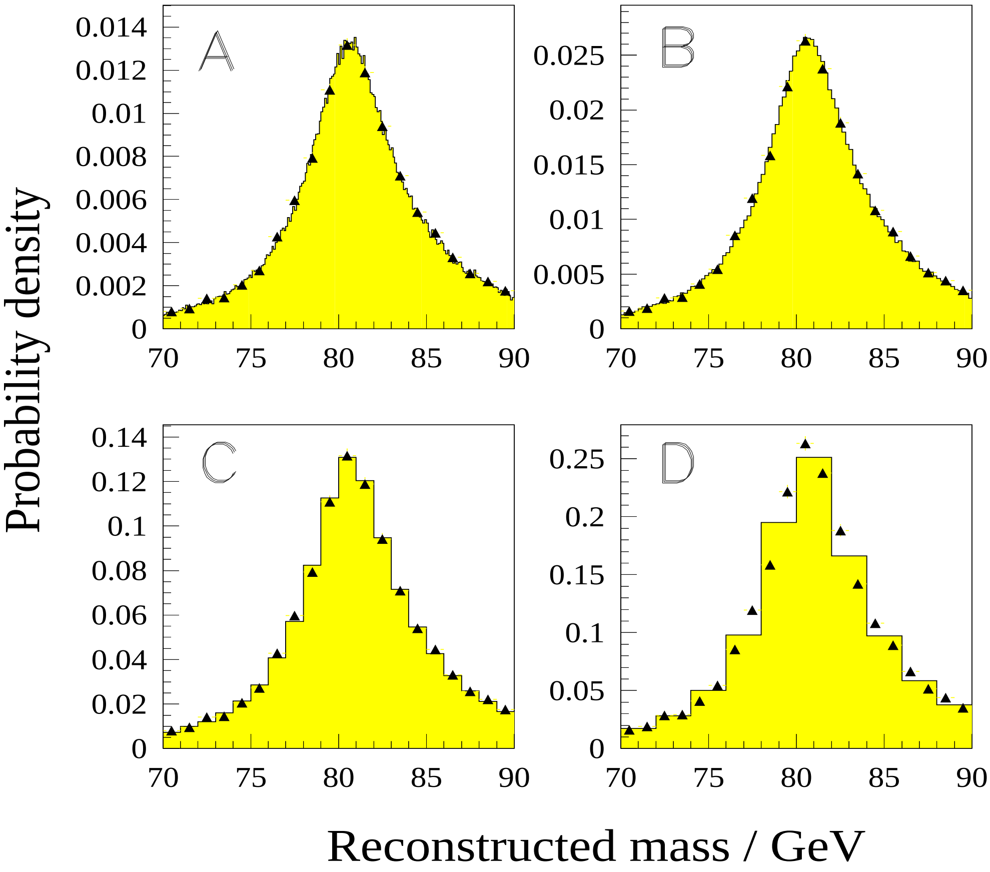

Figure 5.9: A 1-D PDF constructed from bins. The shaded histogram shows the PDF while the triangles show a binned Monte Carlo data distribution. Plots A, B, C and D correspond to bin widths of 100, 200, 1000 and 2000 MeV respectively. The PDF clearly reproduces the discontinuities of the bins.

Delphi official one and for the unbinned likelihood with a Kernel function, which forms the core of this analysis.

5.5 Introducing the Λ dependence into the PDF

In Section 5.4 a general description of non-parametric methods to construct a PDF $\mathbf{P}(\mathbf{\Omega}|\Lambda)$ has been made. This chapter will describe the way in which the dependence of the PDF on the parameters $\mathbf{\Lambda}$ to be measured is introduced. It was already mentioned that in these non-parametric methods the Monte Carlo distribution which best describes the data is searched for, and its generation parameters $\mathbf{\Lambda}_{Gen}$ are then said to be the fitted values of $\mathbf{\Lambda}$. In practice one sample is taken and reweighted according to different values of the parameters $\mathbf{\Lambda}'$. Each event is assigned a weight $\mathcal{W}(\mathbf{\Lambda}, \mathbf{\Lambda}_{Gen}, \alpha)$:

$$\mathcal{W}(\mathbf{\Lambda}, \mathbf{\Lambda}_{Gen}, \alpha) = \frac{\frac{d\sigma}{d\alpha}(\mathbf{\Lambda}, \alpha)}{\frac{d\sigma}{d\alpha}(\mathbf{\Lambda}_{Gen}, \alpha)} \tag{5.10}$$

where α is a vector of variables describing the event. These can be any set of event variables sensitive to $\mathbf{\Lambda}$. However, they must not be confused with the set of observables $\mathbf{\Omega}$, since the α are not necessarily the observables that are measured experimentally and from which the PDF is determined. The approximate PDF first described in Equation 5.3 can now be written as:

$$\mathbf{P} \approx \frac{\mathcal{W}_{inR}}{\mathbf{V}\mathcal{W}_{total}} \tag{5.11}$$

In figs. 5.10 and 5.11 the effect of reweighting on the generated and reconstructed mass spectrum of a Monte Carlo sample can be seen. The reweighting technique allows for a smooth and continuous variation in the PDF as a function of $\mathbf{\Lambda}$ and removes the necessity to generate samples at many different values of $\mathbf{\Lambda}$. There is, however, a loss of statistical significance in a Monte Carlo sample as $\mathbf{\Lambda}$ diverges from $\mathbf{\Lambda}_{Gen}$. This can be taken into account by using the concept of *equivalent number of events* N_{eq} which is defined as [72]:

$$N_{eq} = \frac{(\sum_{i=1}^{N} \mathcal{W}_i)^2}{\sum_{i=1}^{N} \mathcal{W}_i^2} \tag{5.12}$$

Here, the ensemble of N weighted events has the same statistical power as N_{eq} events

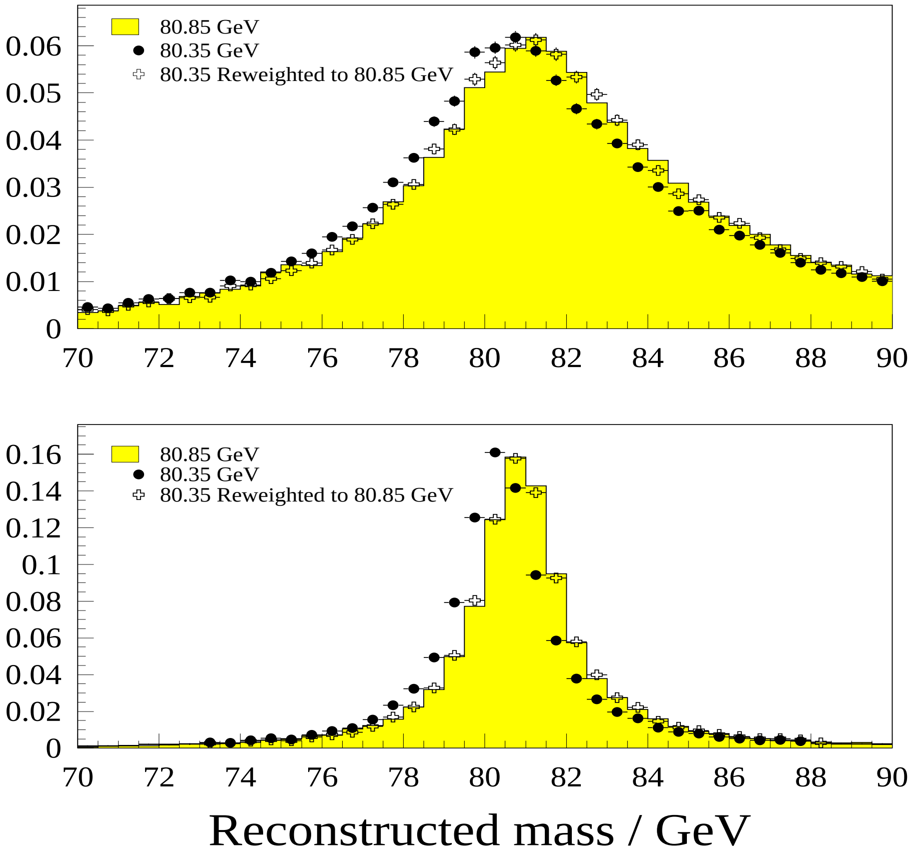

Figure 5.10: Reweighted M_W spectra: The first plots show a sample generated at $M_W = 80.85$ GeV (solid histogram) together with one generated at $M_W = 80.35$ GeV (black circles) and then reweighted to $M_W = 80.85$ GeV (open crosses). The spectra correspond to reconstructed m_W after 2C kinematic fit (top) and average generated m_W (bottom)

with unit weight. Equation 5.12 is derived in Appendix A as Equation A.8. This is of particular importance if a sample is being reweighted to different $\mathbf{\Lambda}$ values in order to do calibration studies of any type of fit method, as in Section 5.6. The weights $\mathcal{W}_i$ are re-scaled such that their sum is N_{eq}:

$$\sum_{i=1}^{N} \mathcal{W}_i' = \alpha \sum_{i=1}^{N} \mathcal{W}_i = \frac{(\sum_{i=1}^{N} \mathcal{W}_i)^2}{\sum_{i=1}^{N} \mathcal{W}_i^2} \tag{5.13}$$

and the re-scaling factor α can be seen to be

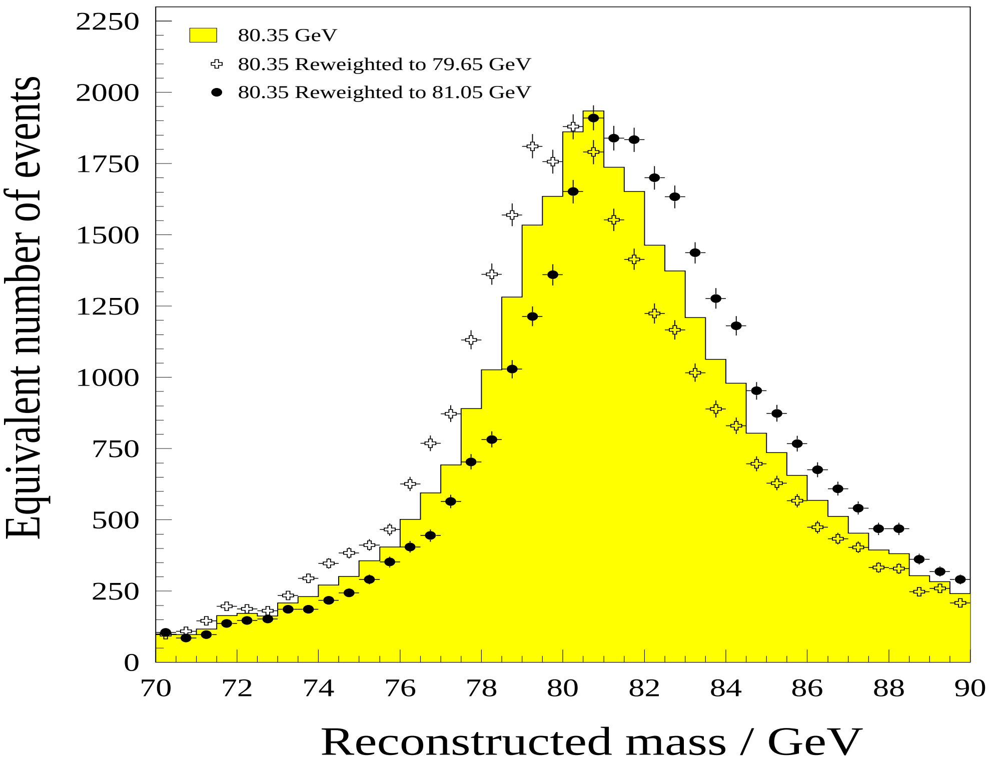

Figure 5.11: Reweighted m_W spectra: the same sample has been reweighted to two different values of M_W

$$\alpha = \frac{\sum_{i=1}^{N} \mathcal{W}_i}{\sum_{i=1}^{N} \mathcal{W}_i^2} \tag{5.14}$$

Concerning the reference Monte Carlo sample used to construct the PDF, it can be seen from equations 5.11 and 5.14 that the scaling factor will drop out in the normalisation and so in principle is not needed. However, in the case where many reference Monte Carlo samples generated with different values of $\mathbf{\Lambda}$ are being used in combination, the re-scaling factor shown in Equation 5.14 must be calculated separately for each sample before their weights are combined in the estimation of the PDF. This is because the evolution of the ratio N_{eq}/N_{tot} as a function of $\mathbf{\Lambda}'$ is different for samples generated at different $\mathbf{\Lambda}_{Gen}$. By applying the re-scaling to the different samples individually one ensures that they will all have the appropriate

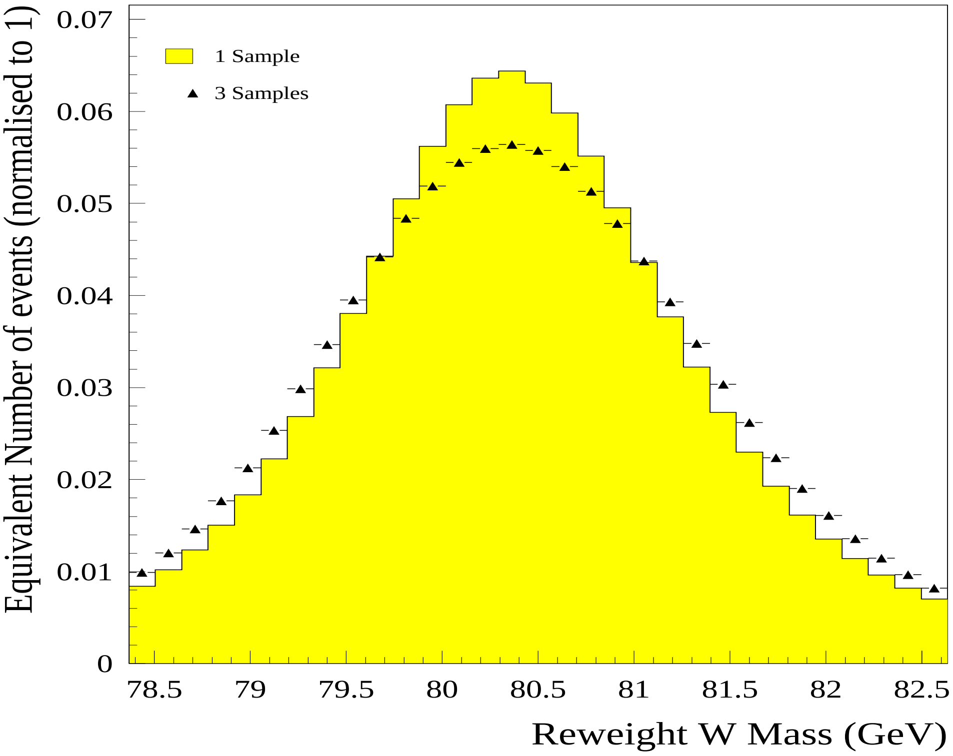

Figure 5.12: The equivalent number of events as a function of reweighting $\mathrm{M_W}$ is shown for a sample generated at M_W = 80.35 GeV (solid histogram) and for three samples generated at M_W = 79.85, 80.35 and 80.85 (triangles).

relative weight. Furthermore, the number of equivalent events must be taken into account when trying to estimate the systematic error due to the statistics of the reference sample. In fig. 5.12, the equivalent number of events for two reference samples is shown as a function of $\mathrm{M_W}$. It is clear that as one reweights further away from the generator values of $\mathbf{\Lambda}$, the effective statistics of the reference sample decrease.

5.6 Tests of the Method: Bias and Sensitivity

This section will describe the tests carried out to evaluate the consistency of the method, its sensitivity to fit parameters $\mathbf{\Lambda}$, and to evaluate any offset to be applied to the parameters. For these purposes two distinct Monte Carlo tests are performed:

fits to a single large calibration sample and fits to a large number of data-sized samples.

5.6.1 Calibration Fits to a Large Monte Carlo Sample

In order to evaluate any potential bias on Λ and to have an estimate of the statistical error on that bias, a fit to an independent calibration sample of known Λ is performed. The error on the bias is simply the statistical error from the fit. Similarly, in order to evaluate the *linearity* of the method, that is, the variation in the bias on Λ as a function of Λ, fits to samples with different input values of Λ are performed. This can be done by generating independent Monte Carlo samples or by reweighting one sample to different values of Λ. A linear χ^2 fit is then performed to extract the slope m and offset c between the "true" generation value of the parameter, Λ_{true} and its corresponding fitted value Λ_{fit}:

$$\Lambda_{true} \; = \; m(\Lambda_{fit} \; - \; \Lambda_0) \; + \; c \; + \; \Lambda_0 \tag{5.15}$$

where Λ_0 is an arbitrary constant chosen such that c is the bias at or near Λ_{Gen}. These fits contain simulation events of both signal and background, where the background events are weighted according to

$$\mathcal{W}_{Bck} \; = \; \frac{\mathcal{L}_{WW}}{\mathcal{L}_{Bck}} \tag{5.16}$$

Here, the $\mathcal{L}$ denote the generation luminosities of the samples. The results from fits to independent samples and to one sample reweighted to different Λ values are summarised in Section 5.7.7.

5.6.2 Fits to a large number of data-sized samples

To calculate the sensitivity σ_Λ of an estimator $\hat{\Lambda}(\tilde{\mathbf{\Omega}}'_i)$ empirically many fits to data-sized samples S_i are performed. The ensemble of results $\Lambda_i = \hat{\Lambda}(S_i)$ is used to determine the variance V $(= \sigma^2_\Lambda)$:

$$V \; = \; <\hat{\Lambda}^2> - <\hat{\Lambda}>^2 \tag{5.17}$$

where the angular brackets denote expectation values. An unbiased estimator of the variance V is the sample variance $\hat{V}$, which is [73]:

$$\hat{V} = \frac{M}{(M-1)}\frac{1}{(1-\rho)}(\overline{\Lambda^2} - \overline{\Lambda}^2) \tag{5.18}$$

where M are the number of data-sized samples and ρ is the correlation coefficient, assumed to be equal for all pairs of samples. This is the expression used to estimate the sensitivity of the fit, which is now $\sqrt{\hat{V}}$. The variance of $\hat{V}$ is then given by:

$$V(\hat{V}) = \frac{2\sigma_\Lambda^4}{M-1} \tag{5.19}$$

and that of σ_Λ by

$$V(\sigma_\Lambda) = \frac{\sigma_\Lambda^2}{2(M-1)} \tag{5.20}$$

Equation 5.20 is used to estimate the error on the expected error of the fit and is independent of any correlation ρ. To construct a large ensemble of data-size samples clearly requires large Monte Carlo statistics. This potential problem can be addressed by resampling according to the Bootstrap method [74, 75]. Here, the M data-sized samples containing n events are drawn *at random* from a large Monte Carlo sample containing N_{cal} events, like the one used for the calibration studies shown in Section 5.6.1. In this particular case, the samples were drawn without replacement, i.e. one event cannot occur more than once in the same sample. In this way, events are shared between the samples M, introducing some correlation ρ that depends on n and N_{cal}. This correlation will clearly affect the variance expressed in 5.18. The correlation between two samples i and j is defined as the fraction of shared events between the samples:

$$\rho = \frac{n}{N_{cal}} \tag{5.21}$$

given simply by the probability of an event from S_i to be in S_j. This approximation assumes that an event would carry the same weight in any given sample S_i. From equations 5.19,5.20 and 5.21 it is clear that the knowledge of the sensitivity of the method can be increased arbitrarily by the use of this resampling technique since the correlation ρ is independent of M.

Besides testing the sensitivity of the method empirically, the Bootstrap resampling technique was also used to check the reliability of the errors coming from the maximum likelihood fit, σ_{fit}. The ensemble of M $\sigma_{fit\ i}$ values should be compatible with the standard deviation or sensitivity of the ensemble of fitted M values $\mathbf{\Lambda}_{fit\ i}$, within the errors given by Equation 5.20. This can be checked by computing the $Pull_{\ i}$ of the entries in the ensemble thus:

$$Pull_{\ i} \; = \; \frac{\Lambda_{fit\ i} - \Lambda_{true}}{\sigma_{fit\ i}} \tag{5.22}$$

The *Pull* distributions should be Gaussian and their width be compatible with unity if the fit errors $\sigma_{fit\ i}$ are to be considered reliable.

5.7 Applying the method to $\mathrm{M_W}$ and Γ_W

The PDF for an event characterised by a given set of experimental observables $\tilde{\mathbf{\Omega}}$ and a set of Standard Model parameters $\mathbf{\Lambda}$ is given by the non-parametric *kernel* or *binned* expressions defined in the previous sections. These non-parametric PDFs are constructed with $l\nu q\bar{q}$ simulation events and do not include background from other SM processes. The estimation of the background PDF is presented in 5.7.3. The final likelihood expression must take the signal and background PDFs into account. It is discussed in Sections 5.7.1 to 5.7.4. The choice of observables $\mathbf{\Omega}$ for the fit and the tests on bias and sensitivity are described in Sections 5.7.5 and 5.7.7 respectively. In both, ample use is made of the tests described in Section 5.6. All the fits in these sections are carried out using the Gaussian kernel to construct the PDF unless otherwise stated. In all cases, the binned method was found to give compatible results. The reference samples used to construct the signal PDF are discussed in 5.7.6.

5.7.1 The Likelihood Expression

The probability for observing an event i with observables $\tilde{\mathbf{\Omega}}$ is given by:

$$\mathcal{P}(\tilde{\mathbf{\Omega}}_i) = \mathbf{P}_{l\nu q\bar{q}} P(\tilde{\mathbf{\Omega}}_i|\mathbf{\Lambda}) + (1 - \mathbf{P}_{l\nu q\bar{q}}) B(\tilde{\mathbf{\Omega}}_i) \tag{5.23}$$

where:

- $P(\tilde{\mathbf{\Omega}}_i|\mathbf{\Lambda})$ is the PDF for observing a signal event with observables $\tilde{\mathbf{\Omega}}$ for a given SM parameter set $\mathbf{\Lambda}$. This PDF is given by the non-parametric methods described in previous sections.
- $B(\tilde{\mathbf{\Omega}}_i)$ is the PDF for observing a background event with observables $\tilde{\mathbf{\Omega}}_i$ and is constructed from the individual PDFs for each type of background as is described in Section 5.7.3.
- $\mathbf{P}_{l\nu q\bar{q}}$ is the probability that event i is an $l\nu q\bar{q}$ event and is determined from the selection discriminant D as outlined in Section 5.7.4.

5.7.2 Calculating the Weights

The weights $\mathcal{W}$ given to each event are estimated from the differential cross section for the process $e^+e^- \to f_1 f_2 f_3 f_4$:

$$\mathcal{W}(\mathbf{\Lambda}, \mathbf{\Lambda}_{Gen}, \mathbf{p}^\mu, \mathbf{f}) = \frac{\frac{d\sigma}{d\mathbf{p}^\mu}(\mathbf{\Lambda}, \mathbf{p}^\mu, \mathbf{f})}{\frac{d\sigma}{d\mathbf{p}^\mu}(\mathbf{\Lambda}_{Gen}, \mathbf{p}^\mu, \mathbf{f})} \tag{5.24}$$

Where $\mathbf{\Lambda}$ now refers to $\mathrm{M_W}$ or Γ_W, and $\mathbf{p}^\mu$ represents the four-momentum of the four final state fermions $\mathbf{f}$. The differential cross sections include all tree-level Feynman diagrams that contribute to the final state given by $\mathbf{f}$. All non- $\mathbf{\Lambda}$-dependent factors remain unchanged and thus cancel out in the ratio. The weights then depend only on the matrix element for the process and, if $\mathbf{\Lambda}$ includes $\mathrm{M_W}$, on the weak mixing angle $sin^2\theta_W$. In the DELPHI tuning of the `EXCALIBUR` generator, $sin^2\theta_W$ is defined using the α normalisation scheme[4]:

$$sin^2\theta_W = \frac{\pi\alpha_{QED}(2M_W)}{\sqrt{2}M_W^2 G_\mu}. \tag{5.25}$$

---

[4] In the on-shell or G_μ normalisation scheme, $sin^2\theta_W = 1 - M_w^2/M_z^2$.

The weight can be expressed as:

$$\mathcal{W}(\mathbf{\Lambda}, \mathbf{\Lambda}_{Gen}, p_i^\mu, f_i) \ = \ \frac{sin^{-8}\theta_W(M_W)|\mathcal{M}(\mathbf{\Lambda}, p_i^\mu, f_i)|^2}{sin^{-8}\theta_W(M_{WGen})|\mathcal{M}(\mathbf{\Lambda}_{Gen}, p_i^\mu, f_i)|^2} \tag{5.26}$$

The squared matrix elements $\mathcal{M}$ are calculated using the `EXCALIBUR`[22, 76] four-fermion generator.

5.7.3 Parametrising the Background

In Chapter 4, efficiencies and purities for each of the three $l\nu q\overline{q}$ final states were presented. It can be seen that these vary considerably from the cleanest ($\mu\nu q\overline{q}$) to the least clean ($\tau\nu q\overline{q}$) decay channel. In Tables 4.6 and 4.7 it can also be seen that, besides the contamination from non-$\mathrm{l\overline{\nu}_l q\overline{q}'}$ processes, there is some cross-talk between signal channels (seen as the off-diagonal elements in the $\mathrm{l\overline{\nu}_l q\overline{q}'}$ efficiency matrix). These $\mathrm{l\overline{\nu}_l q\overline{q}'}$ misidentified events carry some $\mathbf{\Lambda}$ information. On the other hand, non-$\mathrm{l\overline{\nu}_l q\overline{q}'}$ events, be they non-$\mathrm{W^+W^-}$ or non-$\mathrm{l\overline{\nu}_l q\overline{q}'W^+W^-}$ final states, will carry no such information. For this reason, these two types of backgrounds are treated differently.

$\mathrm{l\overline{\nu}_l q\overline{q}'}$ background

This consists of $l\nu q\overline{q}$ events selected under the wrong lepton hypothesis. Here, the lepton has been misidentified but the $q\overline{q}$ remains essentially unperturbed, although there is a small effect due to the fact that the selection includes lepton and jet information as a whole, and also due to the fact that the wrong lepton has been selected and excluded before clustering the jets.

In the case of multi-prong $\tau\nu q\overline{q}$-hypothesis events, some tracks belonging to a jet may have been assigned to the hadronic τ and hence essentially lost, while for single-prong leptonic taus it is typically the genuine electron or muon that gets lost[5].

---

[5] As is mentioned in Chapter 4, τ leptons carry no weight in the kinematic fit. This is due to the undetected neutrinos forming part of their decay chain. So the event mass is defined by the hadronic system.

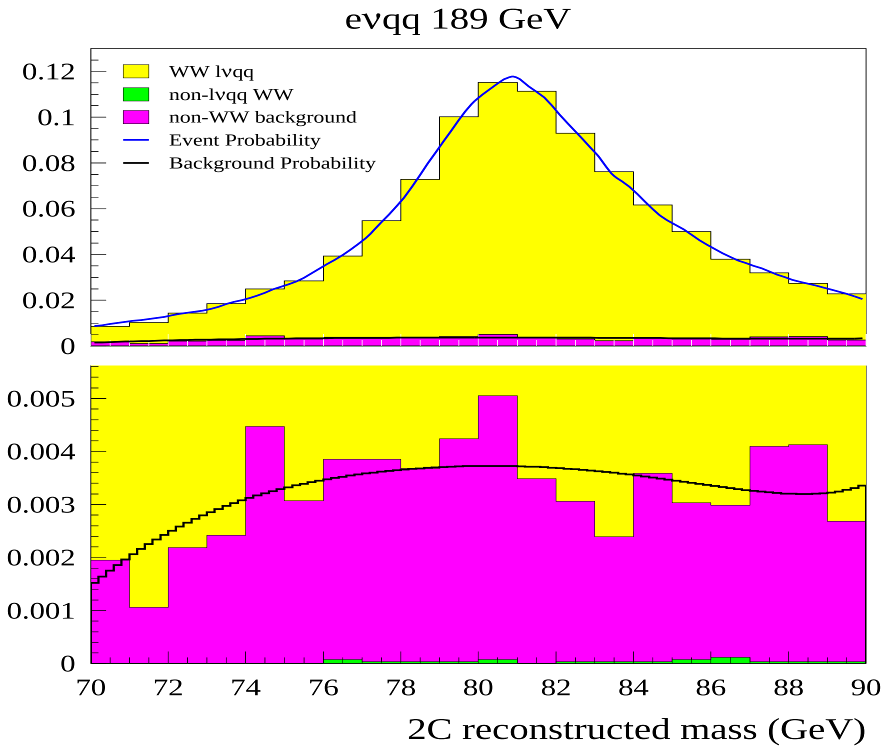

Figure 5.13: Signal and background 2C mass distribution for $e\nu q\bar{q}$ simulation are shown with the corresponding signal and background probabilities calculated from the kernel method and the polynomial parametrisation respectively

The non-parametric method presented here takes such $\mathbf{\Lambda}$-dependent contamination into account by construction: the reference Monte Carlo sample includes the right proportion of $\mathrm{l\bar{\nu}_l q\bar{q}'}$ signal and background and these are reweighted in the normal way.

Due to the intricacies of reweighting methods, badly reconstructed events from the reference sample can bring in instabilities without contributing any improvements to the overall sensitivity. By excluding non-$\mathrm{l\bar{\nu}_l q\bar{q}'}$ $\mathrm{W^+W^-}$ events from the reference sample this problem is partially avoided. Thus, non-$\mathrm{l\bar{\nu}_l q\bar{q}'}$ $\mathrm{W^+W^-}$ background is treated separately.

Non-$\mathrm{l\bar{\nu}_l q\bar{q}'}$ background

Background events of this type are taken not to carry any useful $\mathbf{\Lambda}$ information and so are given a non-$\mathbf{\Lambda}$-dependent contribution to the PDF described in previous

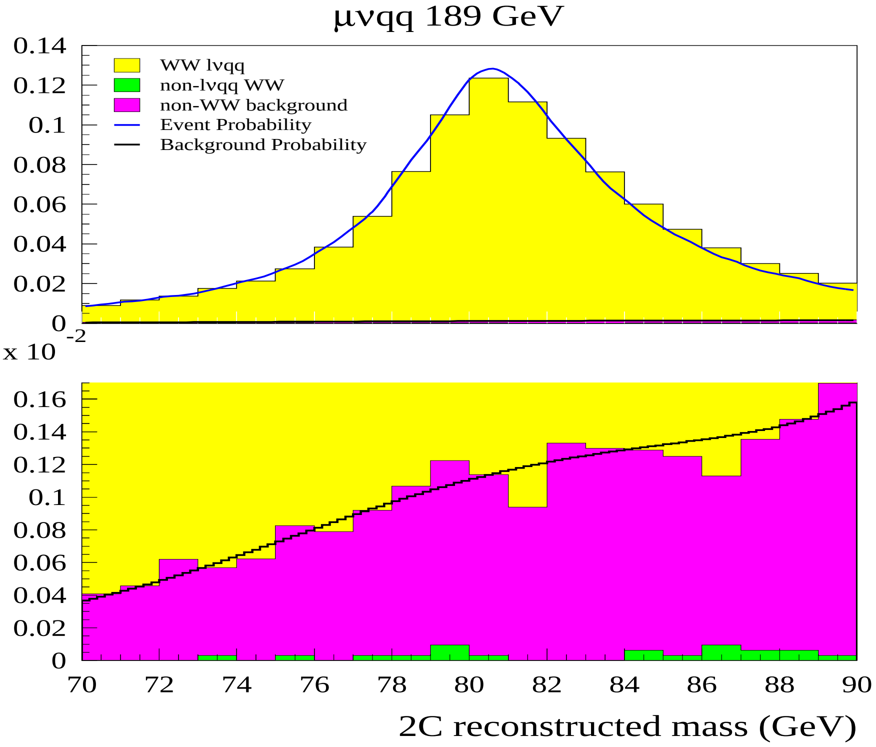

Figure 5.14: Signal and background 2C mass distribution for $\mu\nu q\bar{q}$ simulation are shown with the corresponding signal and background probabilities calculated from the kernel method and the polynomial parametrisation respectively

sections (where any mention of backgrounds was avoided for didactic purposes).

These backgrounds are simply parametrised in the 2C fit mass axis (m_W) and assumed to be flat in any other dimension. The parametrisation is carried out by fitting a quartic polynomial to histograms of the m_W distributions of each of the k backgrounds considered:

$$b_k^1 = \sum_{i=1}^{5} a_{i-1} m_W^{i-1} \tag{5.27}$$

where the a_n coefficients are chosen to satisfy:

$$\int_{m_a}^{m_b} b_k^1 dm_W = 1 \tag{5.28}$$

where m_a and m_b are the lower and upper cuts on the reconstructed 2C mass and the superscript on b_k signifies that the parametrisation represents the first variable. The second dimension is simply a constant $b_k^2 = c_0$ chosen to satisfy a normalisation

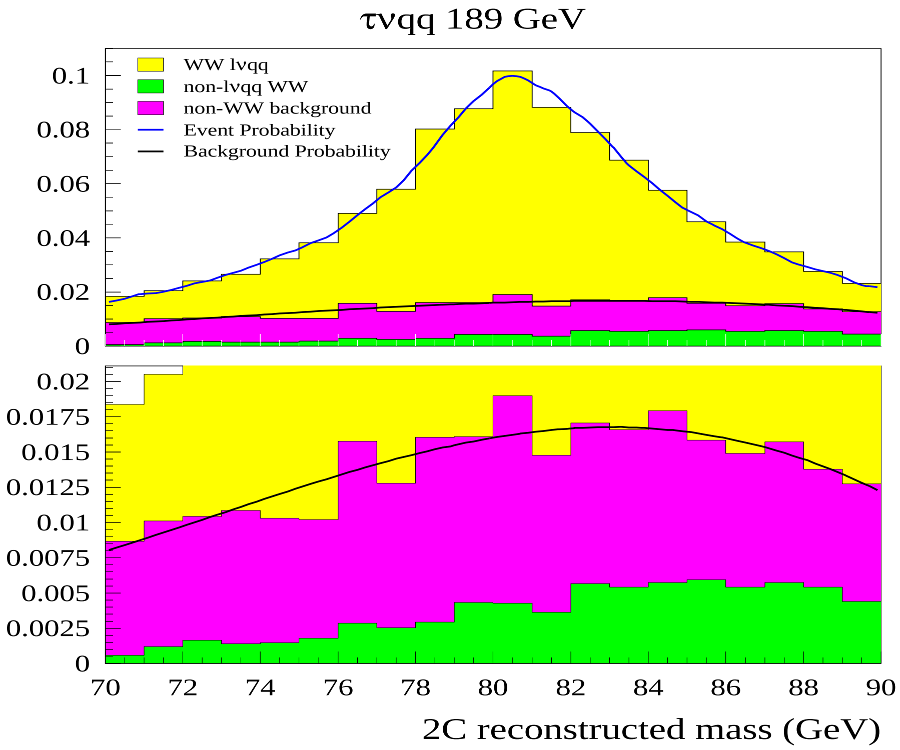

Figure 5.15: Signal and background 2C mass distribution for $\tau\nu q\overline{q}$ simulation are shown with the corresponding signal and background probabilities calculated from the kernel method and the polynomial parametrisation respectively

condition:

$$\int_{v_a}^{v_b} b_k^2 dv = 1 \qquad (5.29)$$

where v is the second variable. The two dimensional background PDF for background k is simply the product of b_k^1 and b_k^2 weighted to the overall purity of k, Pur_k, as defined in Chapter 4. The total background PDF is then obtained from the sum of the individual ones, normalised to one:

$$B(\tilde{\Omega}_i) = \frac{1}{\kappa} \sum_{k=1}^{N_{bck}} Pur_k b_k^1(\tilde{\Omega}_i) b_k^2 \qquad (5.30)$$

where $\kappa = \sum_{k=1}^{Nbck} Pur_k$. In this way, an overall normalised background PDF in terms of the observables of the fit is obtained for use with the event-by-event multivariate discriminant-based $l\nu q\overline{q}$ probability described in Section 5.7.4. The results of these parametrisations can be seen in figures 5.13 to 5.15, where Monte Carlo distributions

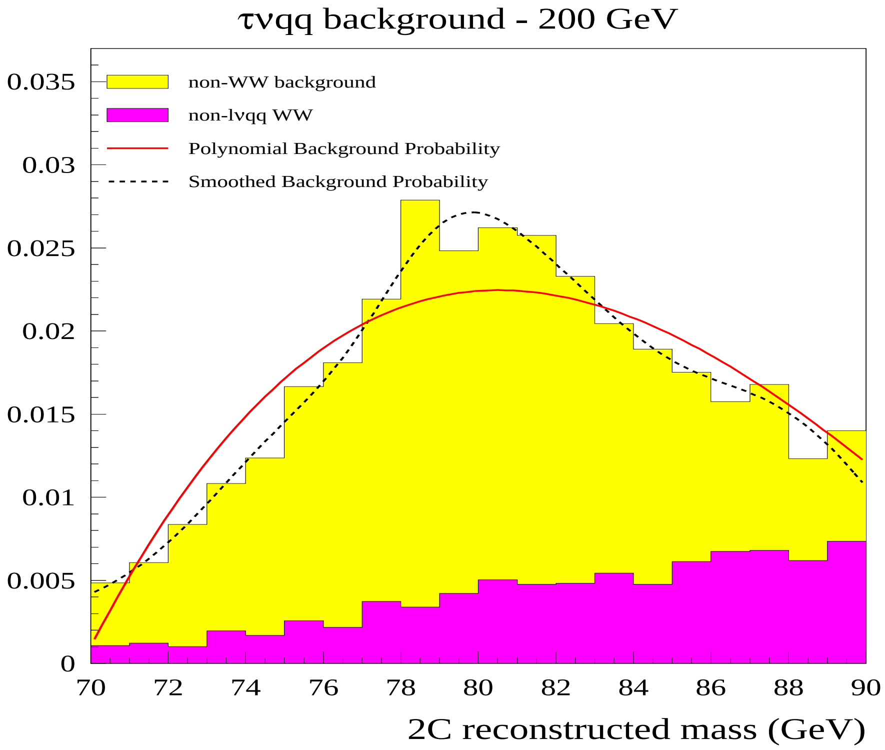

Figure 5.16: 200 GeV $\tau\nu q\overline{q}$ Monte Carlo background with 3rd degree polynomial and multi-quadratic smoothed density functions. The polynomial description does not model the peaked structure of the 2C background mass distribution adequately, and so it is necessary to use the smoothed function, shown here as a dashed line.

and parametrisations for $\sqrt{s}$ = 189 GeV are shown. The simple parametrisation is seen to give a good description of the background shape. However, when the same procedure is applied to Monte Carlo data corresponding to the 1999 running period centre of mass energies it is at once apparent that it does not give a good description of the $\tau\nu q\overline{q}$ background, the polynomial parametrisation failing to reproduce its sharply peaked structure. Furthermore, the lower selection purity for this channel at this higher energy regime means that the fit is more sensitive to the accuracy in the description of the background shape. Therefore, a different procedure is applied to $\tau\nu q\overline{q}$-hypothesis selected events. A smoothed distribution representing the background is obtained by fitting a Multiquadratic Radial Basis function to a 1-dimensional histogram of the background distribution [77]. This results in a better description of the background, as can be seen in figure 5.16. The same technique is applied to 1998 $\tau\nu q\overline{q}$-hypothesis events for consistency.

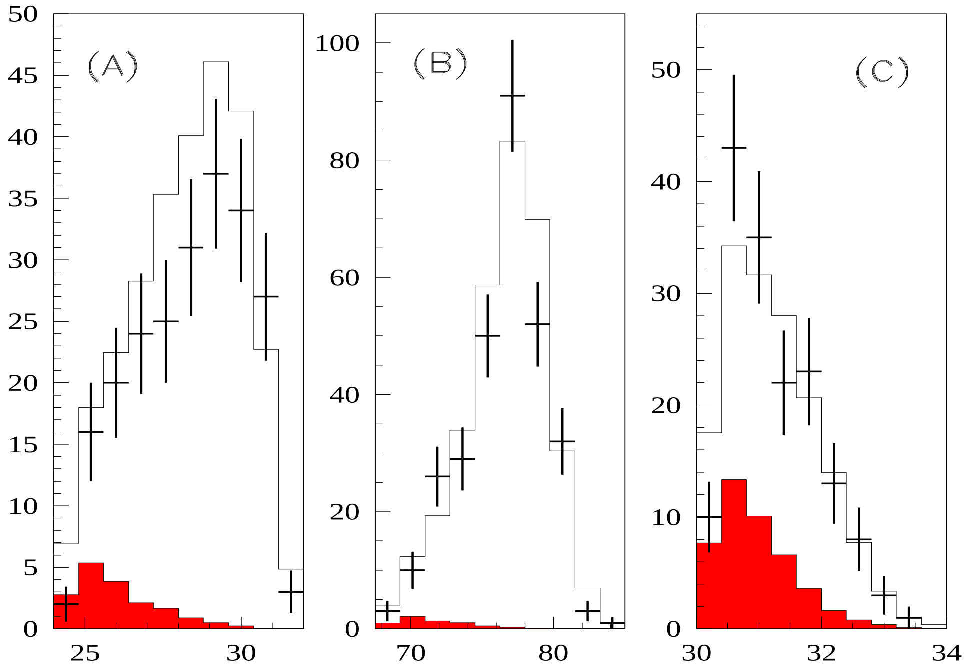

Figure 5.17: Histograms of the IDA discriminating variable D_{IDA} for the $e\nu q\bar{q}$ (A), $\mu\nu q\bar{q}$ (B), $\tau\nu q\bar{q}$ (C), decay channels at 189 GeV. The solid histogram shows the expected distributions from Monte Carlo given the data integrated luminosity. The shaded histogram corresponds to all non-$l\nu q\bar{q}$ background and the points with errors are the real data.

5.7.4 l$\nu q\bar{q}$ Purity Estimation

The IDA selection discriminant D_{IDA} is constructed in order to obtain the highest discriminating power from the information contained in a variety of experimental observables and so provides an efficient one-dimensional purity estimator for any given event. Histograms of the discriminating variable distributions for the three $l\nu q\bar{q}$ decay channels, including both Monte Carlo and real data events, can be seen in Figure 5.17. A procedure which can be adopted is to estimate purities in bins of D_{IDA} from Monte Carlo according to

$$\mathbf{P}_{l\nu q\bar{q}} = \frac{n_{l\nu q\bar{q}}}{n_{l\nu q\bar{q}} \; + \; \sum_{i=1}^{k} n_k} \tag{5.31}$$

where k is the number of background processes considered and includes events coming from charged-current $\mathrm{W^+W^-}$-like decays into final states other than $l\nu q\bar{q}$, and

n represents the selected events for each process after normalising to the same luminosity. Then a polynomial is fitted to the resulting histogram, as shown in Figure 5.18. However, when the resulting parametrisation is used to estimate the purity in bins of event reconstructed mass m_W, it becomes apparent that there is a mass dependence in this event purity estimator. This mass dependence has two problems. In the first place, the Likelihood Expression 5.23 is no longer automatically normalised. Second, when convoluted with $P_{l\nu q\bar{q}}$ and $(1 - P_{l\nu q\bar{q}})$ respectively, the signal and background PDFs get distorted from their original shape, creating a bias instead of an improvement in sensitivity. The distortion of the background PDF $B(\tilde{\Omega}_i)$ for the $e\nu q\bar{q}$ can be seen in Figure 5.19. To avoid this problem, the mass dependence of the D_{IDA} purity estimator has to be corrected out. Thus the final $P_{l\nu q\bar{q}}$ calculation is carried out in three steps:

- Calculate a purity $\tilde{P}_{l\nu q\bar{q}}(D_{IDA})$ ($\tilde{P}(IDA)$ in short) in bins of D_{IDA} from Monte Carlo and fit a fourth degree polynomial to the distribution.
- Use $\tilde{P}_{IDA}$ to estimate mean purities $< \tilde{P} >$ for Monte Carlo data in bins of reconstructed mass m_W to get a hybrid D_{IDA} probability distribution in terms of mass, $\tilde{P}_{l\nu q\bar{q}}(m_W)$ ($\tilde{P}(m_W)$ in short).
- Estimate for each event the scaled purity:

  $$P_{l\nu q\bar{q}} = P_{l\nu q\bar{q}}^{Glob} \frac{\tilde{P}(IDA)}{\tilde{P}(m_W)} \tag{5.32}$$

  where $P_{l\nu q\bar{q}}^{Glob}$ is the global $l\nu q\bar{q}$ purity estimated from all Monte Carlo events using Equation 5.31 with no binning.

Using this procedure, the $P_{l\nu q\bar{q}}$ distribution is made, to a good approximation, flat in the m_W axis while keeping the discriminating power of the D_{IDA} variable which is uncorrelated to m_W, although the binning involved in the above procedure dilutes some of this power. In this way we can take advantage of some event purity information while ensuring the normalisation of the likelihood expression and maintaining the overall shape of the signal and background PDFs in the m_W axis. Since the IDA tuning used for the 1999 running period ($\sqrt{s} = 192 - 202$ GeV) is different to that used for 1998 ($\sqrt{s} = 189$ GeV) the above procedure is repeated separately for each running period.

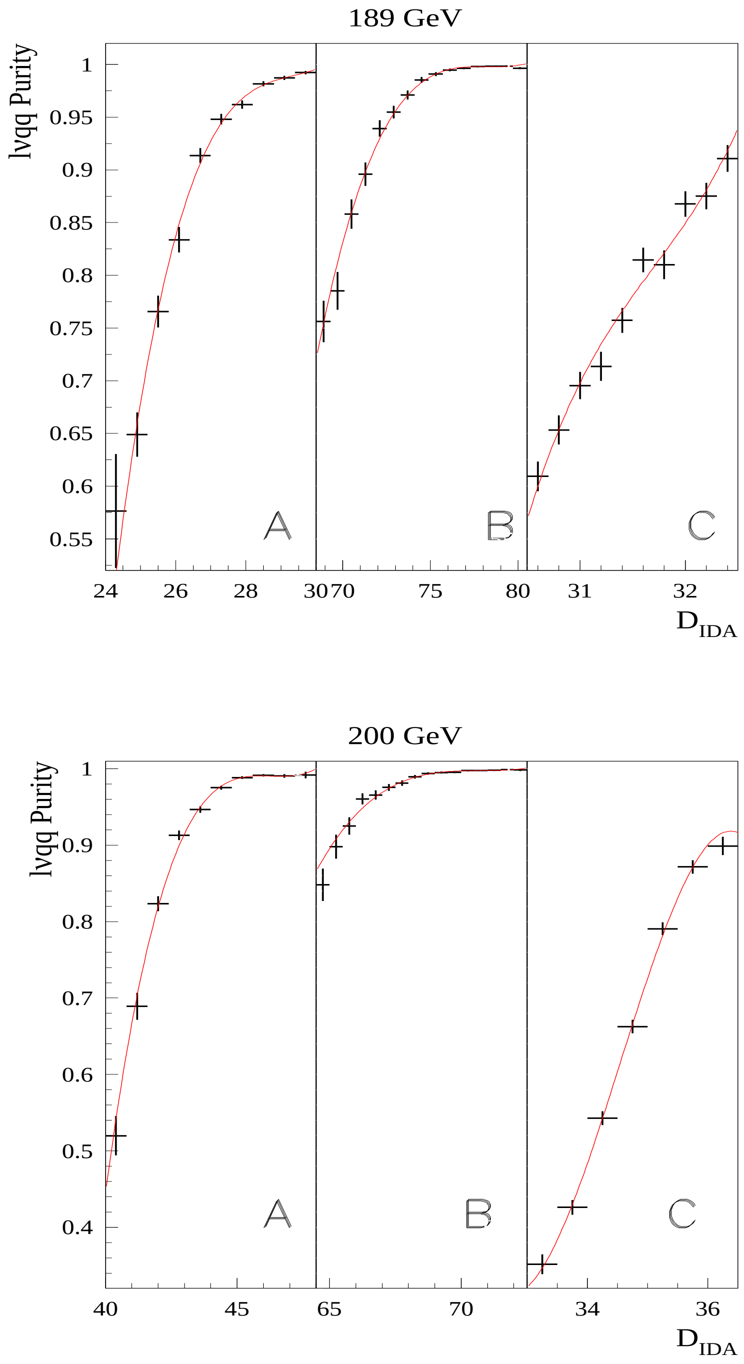

Figure 5.18: $P_{l\nu q\bar{q}}$ as a function of the discriminating variable D_{IDA}. The three plots on each graph correspond to the purity for selecting any $l\nu q\bar{q}$ event under the $e\nu q\bar{q}$ (A), $\mu\nu q\bar{q}$ (B), and $\tau\nu q\bar{q}$ (C) hypotheses before the mass dependence of the purity estimator has been corrected for. The points with errors are Monte Carlo data and the lines represent the corresponding polynomial parametrisation, for each of the two IDA tunings performed at 189 GeV (top) and 200 GeV (bottom).

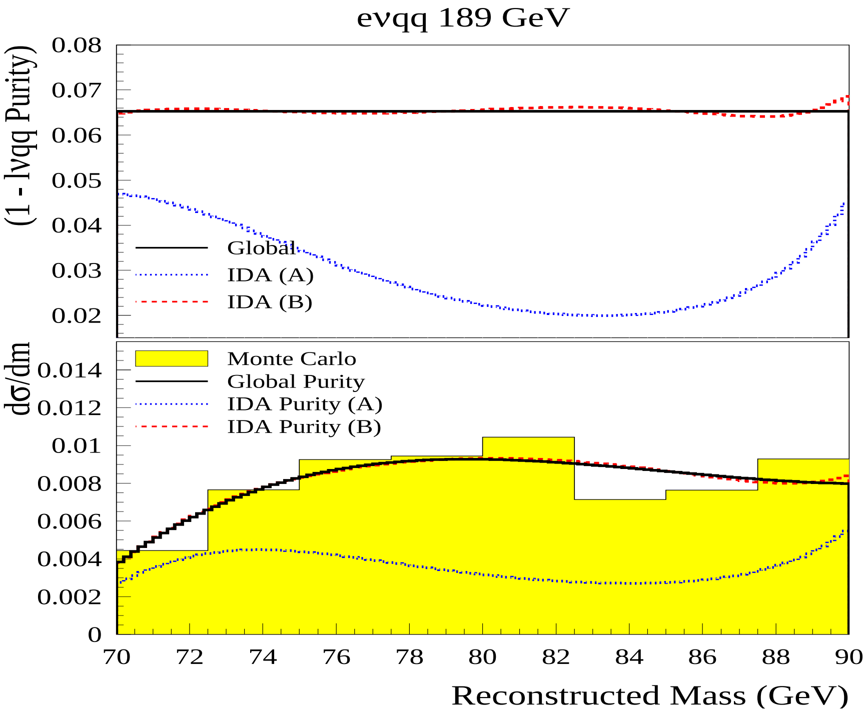

Figure 5.19: Plots of background parametrisations in the $e\nu q\bar{q}$ channel. For all plots, probabilities and purities were estimated for equally spaced points along the reconstructed 2C mass (m_W) axis. The top plot shows the background probability ($1 - P_{l\nu q\bar{q}}$) as a function m_W. The three curves correspond to the global purity, to the D_{IDA} based purity projected on to the m_W axis (labeled IDA (A) in the plot), and to the corrected D_{IDA} (IDA (B)) purity. The correction takes out most of the mass dependence of the ($1 - P_{l\nu q\bar{q}}$) estimator. The bottom plot shows a histogram of background Monte Carlo events. Superimposed are the background probabilities obtained from the product of the corresponding background purities from the top plot, and the background PDF $B(\tilde{\Omega}_i)$. It is clear that not only does the mass dependence of ($1 - P_{l\nu q\bar{q}}$) distort the background probability distribution, but it causes a normalisation problem.

5.7.5 Choosing the variables in $\tilde{\Omega}$

Due to their sharply peaked nature, the reconstructed event mass distributions carry the most $\mathrm{M_W}$ and Γ_W information in a $\mathrm{W^+W^-}$ data sample. As was shown in Section 4.5 there are several ways of reconstructing invariant masses according to the constraints imposed in the kinematic fit, notably the 5-constraint reconstructed mass m_w (where conservation of energy and momentum, and the equal mass constraints are imposed), and the 4-constraint masses m_{w1} and m_{w2} (where conservation of energy and momentum has been imposed), unambiguously identified as $m_{l\nu}$ and

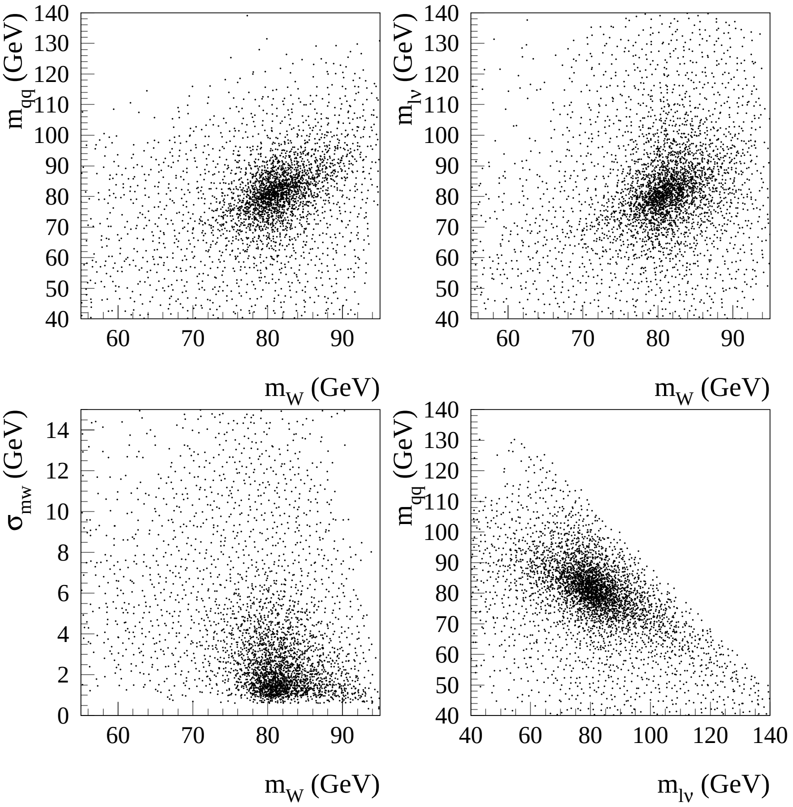

Figure 5.20: Scatter plots of different pairs of event observables $\tilde{\Omega}$ considered for the fit. Whereas all $\tilde{\Omega}$ carry some $\mathrm{M_W}$ and Γ_W information, correlations between them limit any gains in sensitivity obtained by doing a fit in a bi-dimensional space of observables. Furthermore, regions of low Monte Carlo density can compromise the stability of the method and have to be eliminated by imposing further cuts, resulting in a loss of statistics. The sensitivity of each pair of observables is estimated empirically through Monte Carlo experiments.

$m_{q\bar{q}}$ in the $l\nu q\bar{q}$ channel[6]. It was also shown that m_w shows a better resolution than either $m_{l\nu}$ or $m_{q\bar{q}}$ and is therefore an obvious choice of first variable.

The 2nd variable should then be chosen to maximise the sensitivity of the method to $\mathrm{M_W}$. However, the correlation between m_W and the other variables limits any gains in sensitivity and so the course taken is to also try out combinations with first variables different to m_W.

The other variables considered were the 4-constraint W-boson masses $m_{l\nu}$ and

---

[6] We refer to 5 and 4-constraint masses. However, the neutrino momentum is not known, resulting in the loss of three constraints. Hence the masses can be referred to as 2 and 1-*constrained*. The presence of a τ lepton further reduces the number of constraints by one.

$m_{q\bar{q}}$, and the error on the 5-constraint event mass, σ_{mw}. To give an idea of the degree of correlation between different observables, Figure 5.20 shows scatter plots of m_w against the three other variables under consideration, as well as one of $m_{l\nu}$ vs. $m_{q\bar{q}}$, for a 189 GeV $\mathrm{W^+W^-}$ sample of events selected under the $\mu\nu q\bar{q}$ hypothesis.

Using the Bootstrap resampling method, as outlined in Section 5.6.2, the sensitivity of the fit with different pairs of variables was calculated in order to choose the most optimal set of observables and the best tune of the fit parameters. For this experiment, twenty thousand samples of 300 $l\nu q\bar{q}$ selected events were formed. The loss of selection efficiency due to the extra cuts imposed for each fit tuning were taken into account and the size of each fitted sample reduced accordingly. However, the overall selection efficiency differences across decay channels were not taken into account and so the sensitivities obtained through this experiment serve only as an indicator of the best fit set-up for one given channel, and do not show how the channels compare to each other.

In order to isolate the sensitivity of the method to the $l\nu q\bar{q}$ signal, background events were excluded from the samples and only the signal PDF was used to estimate the event probabilities. For each choice of variables and decay channel, the Kernel cell width and $\tilde{\Omega}$ scaling factors and cuts were tuned to achieve an acceptable linearity using a linear fit with reweighting of the data, described in Section 5.6.1. The reweighting method was used in this instance because the strong correlation between the different calibration samples, made from exactly the same events, gives a clear indication of systematic non-linearities and instabilities for any given combination of variables and tuning.

Once a set-up had been found where the linearity of $M_W(fit)$ against $M_W(true)$ was within 5% of unity, the resulting bias parameters were used to correct each of the fitted values and errors from the Bootstrap experiment. The results are shown on table 5.1, together with the sensitivity to single variables.

Some entries in the sensitivity table are missing. There are two reasons for this. Firstly, for some combinations of variables and decay channels an acceptable linearity was not obtainable with the available reference Monte Carlo samples. But the main reason is that, in the case of $\tau\nu q\bar{q}$ events, the leptonic 1C mass $m_{l\nu}$ carries

Variables		Channel		
Variable 1	Variable 2	$e\nu jj$	$\mu\nu jj$	$\tau\nu jj$
m_W	σ_{mW}	264 ± 1	229 ± 1	270 ± 1
	$m_{q\bar{q}}$	270 ± 1	240 ± 1	N/A
	$m_{l\nu}$	284 ± 1	246 ± 1	N/A
	m_W	279 ± 1	244 ± 1	304 ± 1
$m_{q\bar{q}}$	$m_{l\nu}$	300 ± 1	270 ± 1	N/A
	$m_{q\bar{q}}$	665 ± 1	611 ± 1	703 ± 2
$m_{l\nu}$	$m_{l\nu}$	821 ± 1	$706 \pm X$	N/A

Table 5.1: Sensitivity to M_W in MeV for all channels and different combinations of two variables. The data samples include only $l\nu q\bar{q}$ events. Each bootstrap sample is constructed from 300 randomly selected events chosen with the σ_{WW} selection. The events are then put through a further set of cuts tuned to ensure stability and linearity of the fit for each channel and combination of variables. Entries where both variables are the same correspond to fits in 1 dimension.

no $\mathrm{M_W}$ information: its spectrum is constrained by $m_{q\bar{q}}$, the detected ISR photon and the centre of mass energy, and not by the four-momentum of the candidate τ.

It should be pointed out that these estimates of the resolution were only used for the choice of variables for the final fit, and not as an estimate of the final resolution of the method. The final resolution estimates, including background and expected numbers of selected events for each channel separately, are estimated and summarised for each chosen set-up in following sections.

The best choice of two variables is the 5-constraint fitted mass, m_W, and its corresponding error, σ_{mW} for all the decay channels.

5.7.6 Reference Samples

The methods presented above require large statistics for the reference sample. These are needed in order to minimise the systematic error due to limited Monte Carlo statistics in the reference sample, and to avoid the instabilities arising from the fact that statistical fluctuations in an unweighted sample can be greatly magnified under reweighting. Significant statistics are also needed in order to satisfy the conditions of high kernel occupancy and small kernel size outlined in Section 5.4.

Since non-parametric methods are not used for $\mathrm{M_W}$ and Γ_W extraction in DELPHI, the statistics of the official Monte Carlo samples are suitable only for tuning, calibration and some studies of systematic effects. It was therefore necessary to generate dedicated samples for this analysis.

An approach taken in the past in Triple Gauge Coupling (TGC) analyses has been to use a fast parametrisation of the detector response, `FASTSIM`[78][7], instead of the full detector simulation `DELSIM`[79]. Given the sensitivity of TGC analyses at LEP and the fact that they rely on angular information of the four fermions from a W^+W^- decay, whose modeling in a fast simulation is sufficiently accurate, this approach was found to have little detrimental effect on the quality of the analyses after some careful tuning [5]. However, the reconstruction of the invariant mass of W^+W^- events depends greatly on lepton and jet energies and on missing energy. Therefore an optimal description of the detector and its response to different types of charged and neutral particles with a large momentum spectrum is required.

For this reason it was necessary to generate large Monte Carlo samples using `DELSIM`. This was only possible with the use of large PC clusters running the `Linux` operating system[8]. About 1 million $l\nu q\bar{q}$ events were generated at centre of mass energies of 189 and 200 GeV, and at three values of M_W (79.85, 80.35 and 80.85 GeV) . The 189 GeV sample was used for the analysis of the 1998 data set while the second one was used for that of 1999. Smaller samples of $\approx$ 100K events were generated at different values of M_W and Γ_W for the calibration studies presented in Section 5.6, together with samples with different values of fragmentation parameters, used for the study of systematic errors due to hadronisation effects. With these statistics it is possible to perform the fit in two dimensions without loss of stability.

However, it must be pointed out that, for technical reasons beyond the scope of this manuscript, it was not possible to port the 1998 version of the `DELSIM` and `DELANA` chain to `Linux`. Therefore the reference samples generated for the analysis of the 1998 data ($\sqrt{s}$ = 189 GeV) are essentially 1999 Monte Carlo samples generated at 1998 energies. The main differences in the versions of the simulation and reconstruction chains are in the HCAL section of `DELSIM` and in the Forward Tracking from `DELANA`, both of which changed from 1998 to 1999. Furthermore, the official

---

[7] In `FASTSIM` the detector response is modelled by a simple parametrisation of the detector geometry followed by tuned smearings of the momenta and energies of particles.

[8] `Linux` is a freely available, open source clone of the `UNIX` operating system, written to run on personal computer processors of varying specifications and architectures.

DELPHI 1998 and 1999 `EXCALIBUR` samples differ in the version of the hadronisation package used, while all the reference samples generated for this analysis use the newer `PYTHIA` version. However, tests carried out on control Z^0 peak $q\bar{q}(g)$ events showed no visible differences in the two hadronisation packages [80]. Nonetheless, the fact that there are differences in the reconstruction software between the years means that the reference samples generated at $\sqrt{s}$ = 189 GeV are not compatible with the official DELPHI simulation or the real data corresponding to that centre of mass energy. This is the most likely cause for a bias, which is discussed below.

5.7.7 Bias and Expected Sensitivity

The tests described in Section 5.6 were used to determine the linearity and bias of the method with respect to $\mathrm{M_W}$ and Γ_W for the three $l\nu q\bar{q}$ decay channels at nominal centre of mass energies of 189 (corresponding to 1998 data), and 192, 196, 200 and 202 GeV (corresponding to 1999 data).

In order to determine the linearity and bias of the fit, official DELPHI Monte Carlo samples are used both for signal and background. Official signal samples are only generated with $\mathrm{M_W}$ values of 80.35, 79.35 and 81.35 GeV, and the latter two are outside the region in which the fit method behaves reliably for $\mathrm{M_W}$. Furthermore, the corresponding values of Γ_W are too close to provide enough of a lever arm. Therefore, the procedure adopted was to use the 80.35 GeV samples and reweight them to values of $\mathrm{M_W}$ between 79.65 and 81.05 GeV and values of Γ_W between 1 and 5 GeV.

Cross-check fits were performed with private $l\nu q\bar{q}$ samples generated at $\mathrm{M_W}$ = 79.85, 80.35 and 80.85 GeV for the $\mathrm{M_W}$ calibration, and at widths of 1.00, 2.09 and 3.00 for the Γ_W calibration and found to be compatible with the results from the reweighting calibration method.

The offset and slope of the reweighting calibration fits can be seen in Tables 5.2 and 5.4 for the $\mathrm{M_W}$ fit and in Tables 5.3 and 5.5 for the Γ_W fit. Plots showing the offsets as a function of $\mathrm{M_W}$ and Γ_W are shown in Figures 5.22 and 5.23 respectively.

As mentioned in Section 5.7.6, the reference samples generated at $\sqrt{s} = 189$ GeV for the 1998 data are not entirely compatible with the official DELPHI ones or with the processing applied to real or Monte Carlo data . For this reason, an overall

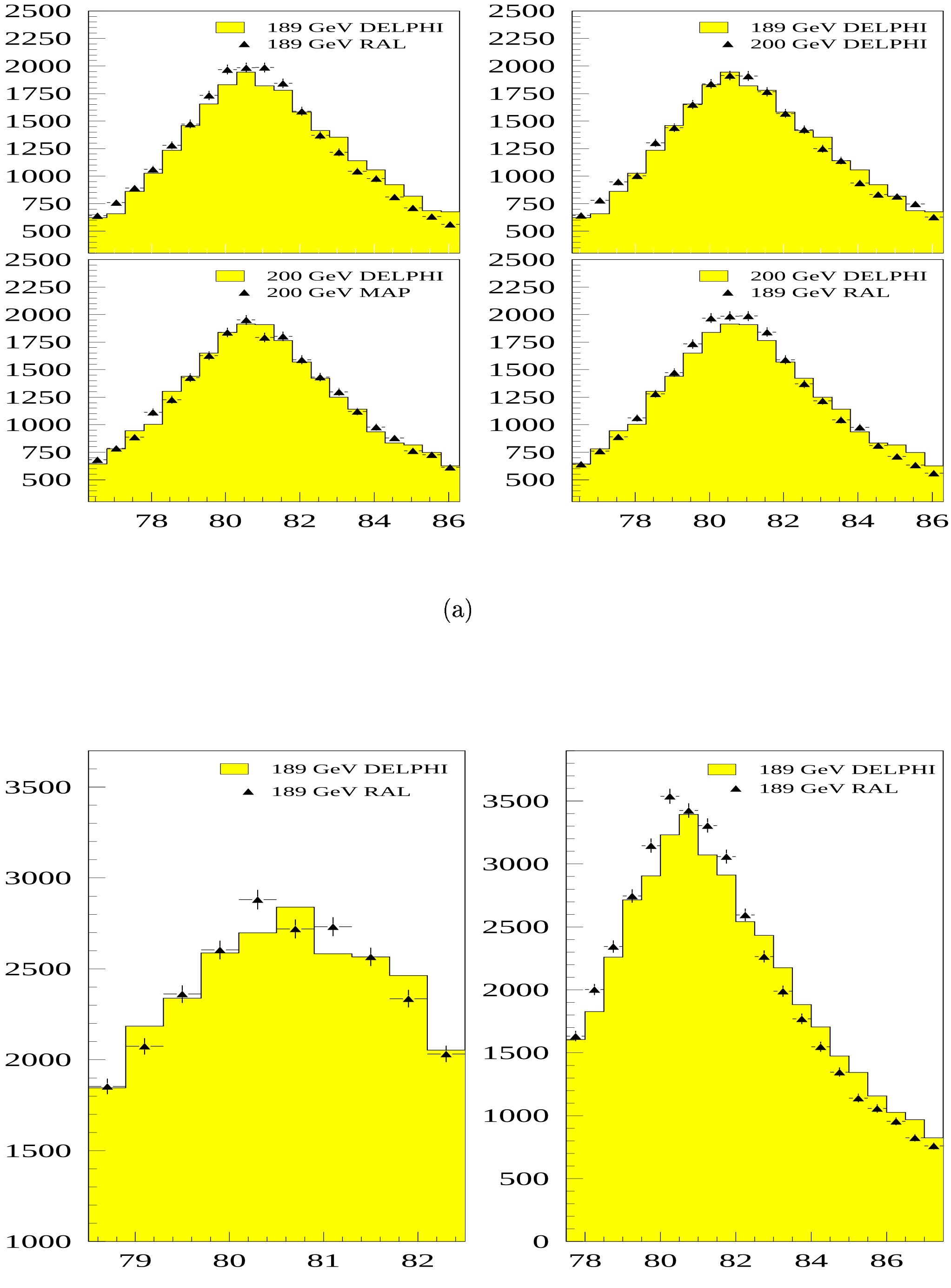

(a)

(b)

Figure 5.21: Comparison between official DELPHI W^+W^- samples and private reference ones (denoted RAL). All events have been selected under the $\mu\nu q\bar{q}$ hypothesis. In plots **(a)** official and private samples generated at $\sqrt{s}$ = 189 and 200 GeV are compared against each other. There is good agreement between samples generated at 200 GeV. However, the discrepancy between the official 189 GeV sample and the private one is clear. In plots **(b)** the comparison of the 189 GeV samples can be seen in more detail. In the peak region (left) there seems to be no noticeable bias. In the high mass tail region (right) the discrepancy is clear and consistent .

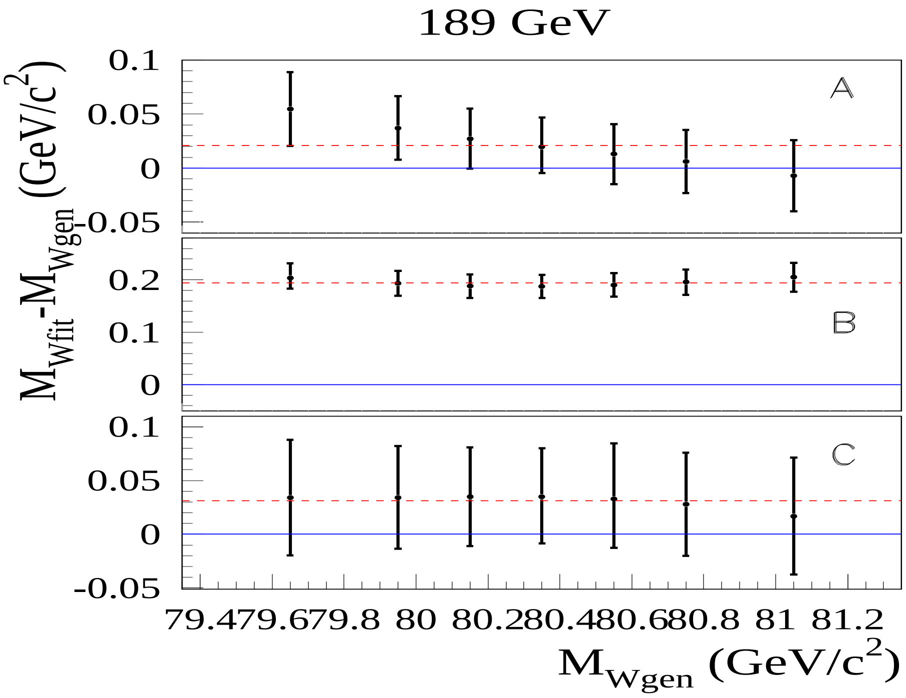

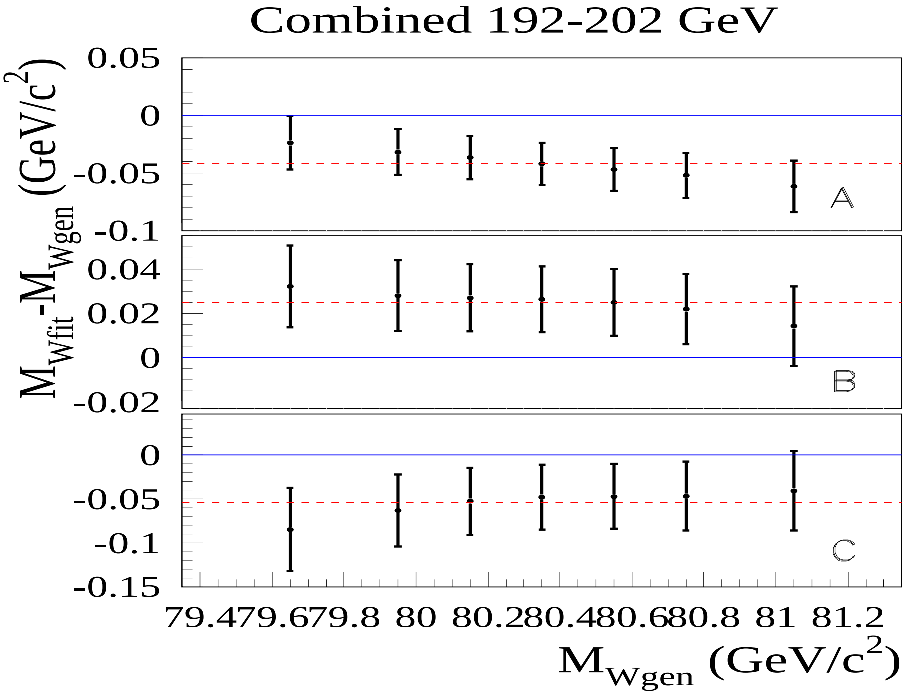

Figure 5.22: Offsets in $\mathrm{M_W}$ as a function of true mass. The plots correspond to the $e\nu q\bar{q}$ (A), $\mu\nu q\bar{q}$ (B) and $\tau\nu q\bar{q}$ (C) decay channels at a centre of mass energy of 189 GeV (top) and a combination of 192, 196, 200 and 202 GeV (bottom). The solid line marks zero offset. The dashed line indicates the offset from the linear fit to the points assuming a slope of 1.

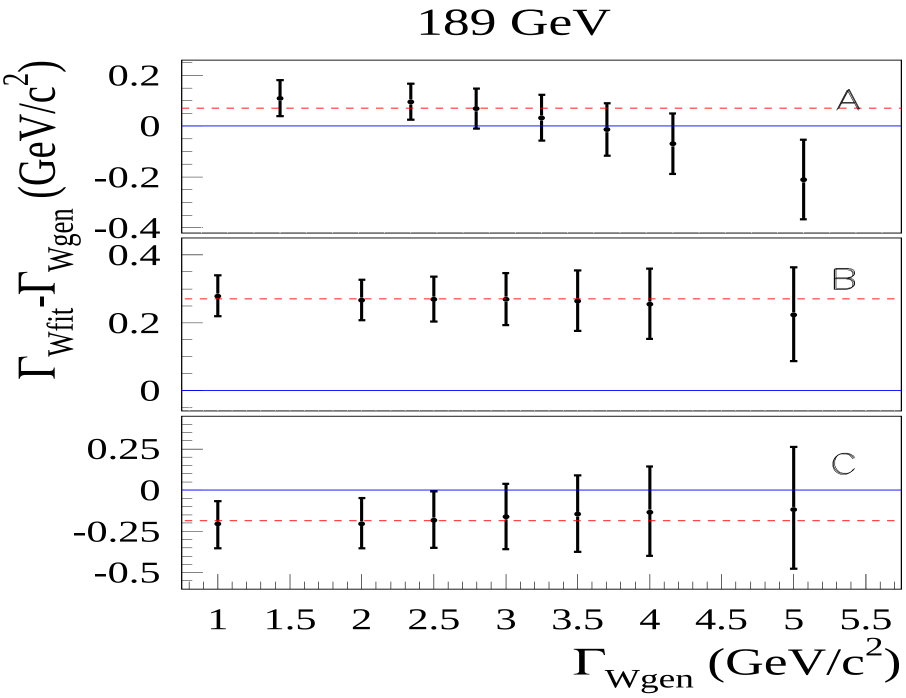

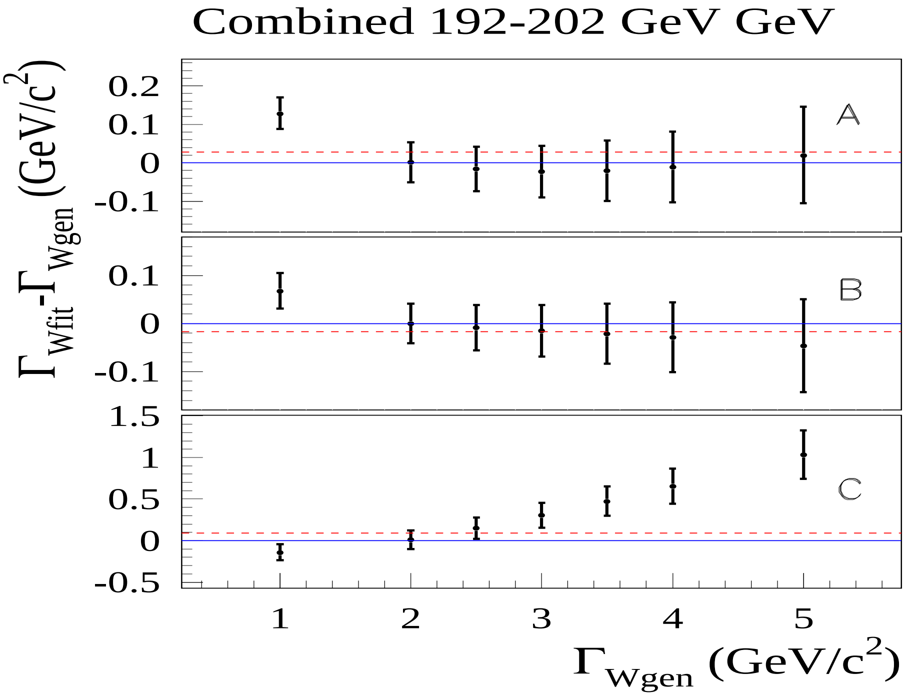

Figure 5.23: Offsets in Γ_W as a function of true W width. The plots correspond to the $e\nu q\bar{q}$ (A), $\mu\nu q\bar{q}$ (B) and $\tau\nu q\bar{q}$ (C) decay channels at a centre of mass energy of 189 GeV (top) and a combination of 192, 196, 200 and 202 GeV (bottom). The solid line marks zero offset. The dashed line indicates the offset from the linear fit to the points assuming a slope of 1. In the bottom plot the $\sqrt{s}$-dependent offset has been compensated for and so an overall offset has been corrected for. The raw individual and combined offsets can be seen in Table 5.3.

	Channel			
$\sqrt{s}$/GeV	$e\nu jj$	$\mu\nu jj$	$\tau\nu jj$	$l\nu jj$
189	26 ± 27	195 ± 22	38 ± 45	116 ± 16
192	-59 ± 42	21 ± 35	-218 ± 89	-28 ± 26
196	-30 ± 31	68 ± 25	-46 ± 62	23 ± 12
200	-30 ± 32	-17 ± 26	-1 ± 64	-20 ± 19
202	-81 ± 46	39 ± 38	-82 ± 94	-15 ± 28
192-202	-42 ± 18	25 ± 15	-54 ± 37	-6 ± 11

Table 5.2: $\mathrm{M_W}$ Offsets c in MeV for all channels and all centre of mass energies, obtained from fits to a reweighted Monte Carlo sample. The errors correspond to the statistical error on the fitted value at the original generated mass value of 80.35 GeV. The combined offsets per channel, per centre of mass energy and for all combinations are obtained by adding the likelihood curves for each individual entry after normalising each one to the corresponding data integrated luminosity.

	Channel			
$\sqrt{s}$/GeV	$e\nu jj$	$\mu\nu jj$	$\tau\nu jj$	$l\nu jj$
189	70 ± 71	270 ± 59	-186 ± 153	161 ± 44
192	-767 ± 114	-585 ± 90	-297 ± 237	-623 ± 67
196	-704 ± 86	-265 ± 70	96 ± 190	-384 ± 52
200	-338 ± 92	-17 ± 74	508 ± 204	-71 ± 56
202	-299 ± 134	159 ± 109	525 ± 291	43 ± 82
192-202	-522 ± 52	-138 ± 42	286 ± 113	-222 ± 31
189-202	-201 ± 41	59 ± 33	69 ± 90	-32 ± 25

Table 5.3: Γ_W Offsets c in MeV for all channels and all centre of mass energies, obtained from fits to a reweighted Monte Carlo sample. The errors correspond to the statistical error on the fitted value at the original generated Γ_W value of 2.09 GeV. The combined offsets per channel, per centre of mass energy and for all combinations are obtained by adding the likelihood curves for each individual entry after normalising each one to the corresponding data integrated luminosity.

bias correction is applied to the 1998 data according to the corresponding values of c seen in Tables 5.2 and 5.3. The largest effect can be seen in the $\mu\nu q\bar{q}$ channel, where a visible difference in the m_W spectra of official DELPHI and private reference `EXCALIBUR` samples results in a large bias for both the $\mathrm{M_W}$ and Γ_W measurements. The differences in the 5-constraint reconstructed mass spectra can be seen in Figure 5.21. Although there is no obvious shift to high or low masses in the peak region, where official and private samples generated at different energies are compatible with each other, the offset is very clear in the high mass tail. The effect of this discrepancy is to introduce a bias in the $\mathrm{M_W}$ fit. This was checked by perform-

	Channel			
$\sqrt{s}$/GeV	$e\nu jj$	$\mu\nu jj$	$\tau\nu jj$	$l\nu jj$
189	0.96 ± 0.05	1.00 ± 0.04	0.99 ± 0.09	0.98 ± 0.03
192	0.89	0.97	1.03	0.95
196	0.98	1.00	1.02	0.99
200	0.99 ± 0.06	0.97 ± 0.05	1.06 ± 0.12	0.98 ± 0.04
202	0.99	1.03	0.96	1.01
192-202	0.97	0.99	1.03	0.99

Table 5.4: $\mathrm{M_W}$ Slopes m for all channels and all centre of mass energies, obtained from fits to a Monte Carlo sample reweighted to different values of $\mathrm{M_W}$. A cross check calibration performed with three independent samples generated at $\mathrm{M_W} = 79.85$, 80.35 and 80.85 at centre of mass energies of 189 and 200 GeV yields compatible values of m and gives the uncertainty for that parameter quoted above. The combined results are obtained by adding the likelihood curves of individual entries in the table after normalising to their corresponding data integrated luminosity

	Channel			
$\sqrt{s}$/GeV	$e\nu jj$	$\mu\nu jj$	$\tau\nu jj$	$l\nu jj$
189	0.93	0.99	1.02	0.97
192	0.89	0.89	0.92	0.89
196	0.92	0.97	1.38	0.99
200	1.04	1.00	1.29	1.03
202	0.98	0.98	1.29	1.01
192-202	0.99	0.98	1.29	1.00
189-202	0.95	0.99	1.17	0.99

Table 5.5: Γ_W slopes m for all channels and all centre of mass energies, obtained from fits to a reweighted Monte Carlo sample. The combined results are obtained by adding the likelihood curves of individual entries in the table after normalising to their corresponding data integrated luminosity

ing a binned likelihood fit to official private and signal events only. The bias on the official sample was found to be 169 ± 23 MeV while that on the private sample was 19 ± 17 MeV, confirming the self-consistency of the reweighting method[9].

As was mentioned above, the versions of `DELANA`, `DSTANA`, and the `JETSET`/`PYTHIA` hadronisation package used for the 189 GeV private and official samples differ. The most likely causes of the discrepancies in observed spectra are the aforementioned differences in the Forward Tracking and the HCAL reconstruction code between years, which makes the privately generated 189 GeV reference samples incompatible

---

[9] These offsets should not be confused with the ones given below as the fits were performed without background events and with the cross-check *binned* likelihood method.

	M_W vs. $\sqrt{s}$ Fit Parameter		
Channel	a/GeV	b	$\chi^2/NDOF$
$e\nu q\bar{q}$	0.16 ± 1.03	$(-1.00 \pm 5.21) \times 10^{-3}$	1.31/2
$\mu\nu q\bar{q}$	0.74 ± 0.87	$(-3.58 \pm 4.40) \times 10^{-3}$	4.62/2
$\tau\nu q\bar{q}$	-3.47 ± 2.18	$(1.73 \pm 1.10) \times 10^{-2}$	2.3/2

Table 5.6: Values of the parameters in a linear χ^2 fit of M_W vs. $\sqrt{s}$. The fitted function can be seen in Figure 5.24

	Γ_W vs. $\sqrt{s}$ Fit Parameter		
Channel	a/GeV	b	$\chi^2/NDOF$
$e\nu q\bar{q}$	-12.72 ± 2.95	$(6.16 \pm 1.49) \times 10^{-2}$	1.71/2
$\mu\nu q\bar{q}$	-14.45 ± 2.36	$(7.22 \pm 1.95) \times 10^{-2}$	0.26/2
$\tau\nu q\bar{q}$	-17.94 ± 6.29	$(9.16 \pm 3.19) \times 10^{-2}$	0.70/2

Table 5.7: Values of the parameters in a linear χ^2 fit of Γ_W vs. $\sqrt{s}$. The fitted function can be seen in Figure 5.24

with the corresponding DELPHI real and simulated data. This is consistent with the fact that the problems do not occur with the samples generated at 200 GeV. It is assumed that at least the effects due to the differences in processing (Forward Tracking) will disappear when the final processing of real and Monte Carlo data is applied.

The treatment of the 1999 Monte Carlo calibration is somewhat different. There are no observed discrepancies between the private reference samples, generated at $\sqrt{s} = 200$ GeV, and the official DELPHI ones, since they are produced from exactly the same source code, albeit on different platforms. However, since the reference sample is generated at one centre of mass energy the course taken is to check the evolution of the offset as a function of $\sqrt{s}$ for each decay channel individually and apply the necessary corrections. A two-parameter linear fit of offset vs. $\sqrt{s}$ is performed to find the best a and b constants such that:

$$(\Lambda_{W fit} - \Lambda_{W true})_{fit} = a + b\sqrt{s} \tag{5.33}$$

The resulting fitted parameters and χ^2 values can be seen in Tables 5.6 and 5.7. The channel-by-channel offsets for each nominal centre of mass energy can be seen in Figure 5.24, together with the fitted correction.

	Channel			
$\sqrt{s}$ (GeV)	$e\nu jj$	$\mu\nu jj$	$\tau\nu jj$	$l\nu jj$
189	284 ± 1	227 ± 1	497 ± 2	167 ± 1
192	810 ± 4	585 ± 3	1592 ± 7	428 ± 2
196	402 ± 2	333 ± 2	971 ± 3	249 ± 1
200	399 ± 2	318 ± 2	870 ± 4	236 ± 1
202	609 ± 3	477 ± 2	1503 ± 8	359 ± 2
192-202	244 ± 1	194 ± 1	533 ± 3	145 ± 1
189-202	185 ± 1	147 ± 1	364 ± 2	110 ± 1

Table 5.8: Expected statistical error ΔM_W in MeV for all centre of mass energies and channels.

	Channel			
$\sqrt{s}$ (GeV)	$e\nu jj$	$\mu\nu jj$	$\tau\nu jj$	$l\nu jj$
189	786 ± 4	612 ± 3	1502 ± 8	456 ± 3
192	1869 ± 9	1607 ± 8	2610 ± 13	1212 ± 6
196	1267 ± 6	1006 ± 5	2103 ± 11	730 ± 3
200	1120 ± 6	933 ± 5	1641 ± 8	675 ± 3
202	1704 ± 9	1434 ± 7	1854 ± 9	1070 ± 5
192-202	709 ± 4	569 ± 3	1258 ± 6	413 ± 2
189-202	518 ± 3	414 ± 2	1006 ± 5	304 ± 2

Table 5.9: Expected statistical error $\Delta\Gamma_W$ in MeV for all centre of mass energies and channels.

Once these offset and slope corrections have been estimated, the sensitivity of the fit can be assessed. This is done by calculating the likelihood curves $L(\mathbf{\Lambda})_i$ ($\mathbf{\Lambda}$=$\mathrm{M_W}$ or Γ_W) of 20,000 samples i containing the expected number of signal plus background events for each channel and luminosity. Each of the data-sized sample's likelihood curves are corrected for the slopes and offsets shown in Tables 5.2 to 5.5 by transforming them accordingly:

$$L(\mathbf{\Lambda})_i^{'} = L(\mathbf{\Lambda}^{'})_i \tag{5.34}$$

where $\mathbf{\Lambda}^{'}$ is transformed with the slopes m and offsets c as:

$$\mathbf{\Lambda}^{'} = m(\mathbf{\Lambda} - \mathbf{\Lambda}_0) + c + \mathbf{\Lambda}_0 \tag{5.35}$$

Here, $\mathbf{\Lambda}_0$ is an arbitrary constant chosen such that the offset c is the bias at the Monte Carlo generation values of $\mathbf{\Lambda}$. Where applicable, the $\sqrt{s}$-dependent bias

		Channel			
$\sqrt{s}$ (GeV)		$e\nu jj$	$\mu\nu jj$	$\tau\nu jj$	$l\nu jj$
189	RMS	0.996 ± 0.005	1.020 ± 0.005	1.111 ± 0.005	1.019 ± 0.005
	σ_{fit}	0.995 ± 0.005	1.021 ± 0.005	1.108 ± 0.006	1.014 ± 0.005
192	RMS	1.031 ± 0.005	0.995 ± 0.005	N/A	0.997 ± 0.005
	σ_{fit}	1.012 ± 0.005	0.991 ± 0.005	N/A	0.993 ± 0.005
196	RMS	0.982 ± 0.005	0.994 ± 0.005	N/A	0.985 ± 0.005
	σ_{fit}	0.980 ± 0.005	0.992 ± 0.005	N/A	0.982 ± 0.005
200	RMS	1.008 ± 0.005	0.995 ± 0.005	N/A	0.994 ± 0.005
	σ_{fit}	1.007 ± 0.005	0.994 ± 0.005	N/A	0.990 ± 0.005
202	RMS	1.009 ± 0.005	1.032 ± 0.005	N/A	1.003 ± 0.005
	σ_{fit}	1.000 ± 0.005	1.024 ± 0.005	N/A	1.001 ± 0.005
192-202	RMS	0.991 ± 0.005	0.994 ± 0.005	1.001 ± 0.005	0.991 ± 0.005
	σ_{fit}	0.989 ± 0.005	0.992 ± 0.005	0.992 ± 0.005	0.985 ± 0.005
189-202	RMS	0.995 ± 0.005	1.007 ± 0.005	1.060 ± 0.005	1.005 ± 0.005
	σ_{fit}	0.990 ± 0.005	1.006 ± 0.005	1.055 ± 0.005	1.002 ± 0.005

Table 5.10: The RMS of the Pull distributions for $\mathrm{M_W}$ fits with the corresponding widths of a Gaussian χ^2 fits to their histograms. Due to the small statistics of the $\tau\nu q\bar{q}$ data-size samples a large number of Bootstrap experiments have upper or lower errors beyond the range of the fit. This results in an underestimation of the sample error, which gives an Pull distribution with an RMS significantly larger than unity. Furthermore, the Pull distributions are non-Gaussian, giving very large χ^2 values for the Gaussian fit and fitted widths incompatible with the RMS of the distributions. The cases where this happens are marked "N/A". The situation improves when energy points are combined as can be seen in the last column and the last two row-wise entries of the table. The corresponding Pull plots can be seen in Figures 5.25 and 5.26.

correction is included by adding an extra constant, calculated from Equation 5.33, to the RHS of Equation 5.35.

Given the magnitude of the offsets in the Γ_W fit and the low resolution of the estimator, the above procedure can shift the evaluation of the corrected likelihood curve close to or beyond the boundary of the fit, making the evaluation of one of the fit errors, or the central value itself, impossible. This problem is manifest for samples smaller than some 10^3 events and so could not be applied to the estimation of Γ_W in the Bootstrap replications. Instead, the luminosity weighted combined offsets c and slopes m seen in Table 5.3 and 5.5 were used to apply an *a posteriori* correction to all the Γ_W values fitted to the combined Bootstrap samples.

The individual and combined expected statistical errors for $\mathrm{M_W}$ and Γ_W can be seen in Tables 5.8 and 5.9 respectively. The reliability of the fit errors is tested by evaluating the Pull for the bootstrap samples using equation 5.22. The RMS values

$\sqrt{s}$ (GeV)	All Channels Combined
189	0.999 ± 0.005
192-202	1.028 ± 0.005
189-202	0.991 ± 0.005

Table 5.11: The RMS of the Pull distributions for Γ_{W} fits. Given the non-Gaussian nature of the $-2Log(\mathbf{L})$ curves of the data-sized sized samples meaningful Pull distributions are only possible after combining several sub-samples. For this reason the individual entries given in Table 5.10 are omitted here. Plots corresponding to these Pulls can be seen in Figure 5.27.

of the Pull distributions are summarised in Tables 5.10 and 5.11. In most cases for $\mathrm{M_W}$ they are compatible with unity and so the fit errors are deemed to be reliable. However, in cases where the sample statistics are small and the sample resolution poor, as is the case with the $\tau\nu q\overline{q}$ channel in the $\mathrm{M_W}$ fit and with all channels in the Γ_{W} fit, the likelihood curves can be significantly non-Gaussian, asymmetric and with long tails, and can be truncated by the boundary of the fit range before the reaching the change in likelihood necessary to evaluate the error. In these cases a parabolic error is estimated, and this is in general an underestimation of the true error, and results in a large RMS for the Pull. This is particularly true in the case of the Γ_{W} fit, where most channel by channel and energy point by energy point individual fits would yield errors that are not reliable. However, as can be seen in the combined entries in Tables 5.10 and 5.11, once samples are combined, the RMS of the Pull becomes compatible with one as the likelihood curves become more Gaussian.

Figures 5.25 and 5.26 show Pulls for 189 GeV and combined 192 to 202 GeV Bootstrap $\mathrm{M_W}$ fits for each $l\nu q\overline{q}$ channel, together with χ^2 fitted Gaussian functions. Figure 5.27 shows Pulls where channels and centre of mass energies have been combined. It is clear from the χ^2 values that the Γ_{W} Pulls are not compatible with a Gaussian, although both the RMS and the fitted Gaussian width are compatible with unity.

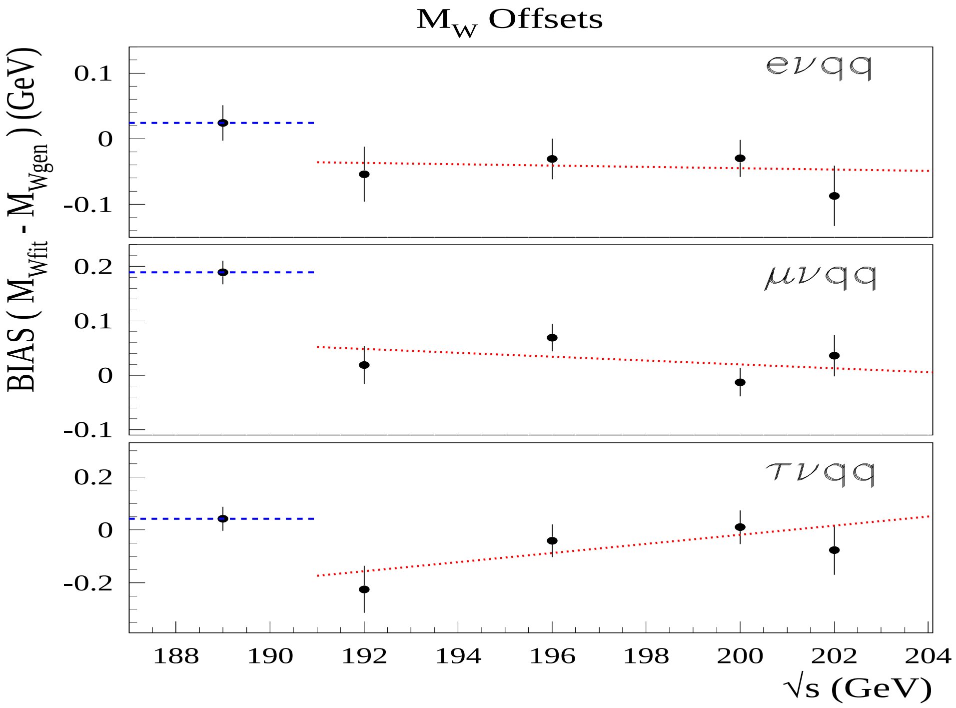

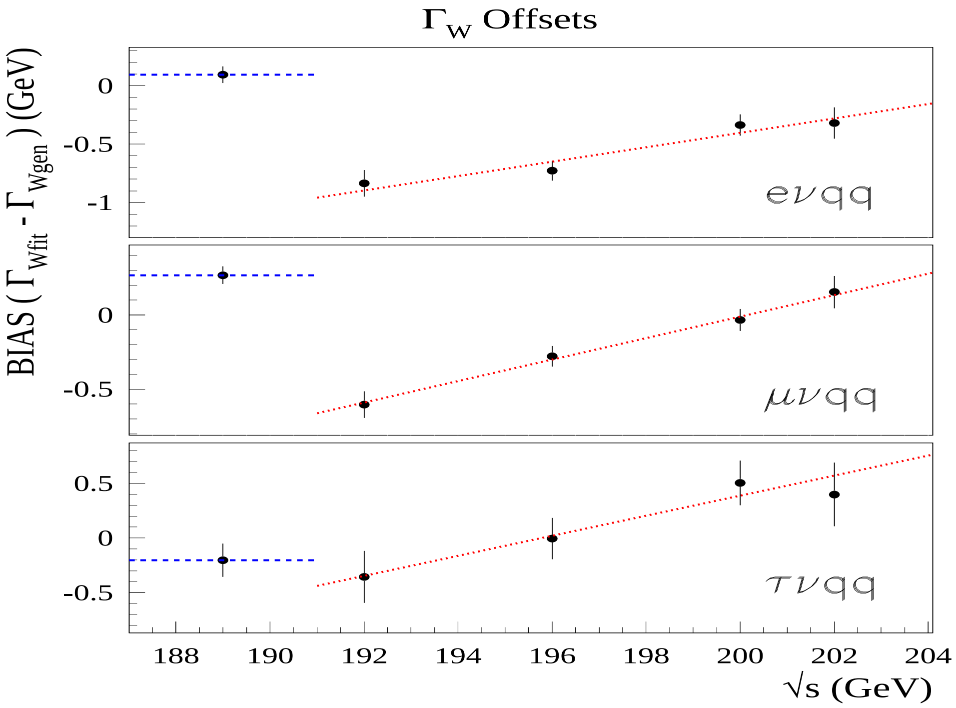

Figure 5.24: Offsets in M_W (top) and Γ_W (bottom) as a function of centre of mass energy. A mean bias correction, obtained from a two-parameter linear fit, can be seen as a dotted line in the plots and is applied to the points with centre of mass energies between 192 and 202 GeV. A single bias correction, seen as a dashed line, is applied to the 189 GeV points. The offset corrections and, where applicable, their χ^2 values, are shown in Tables 5.6 and 5.7.

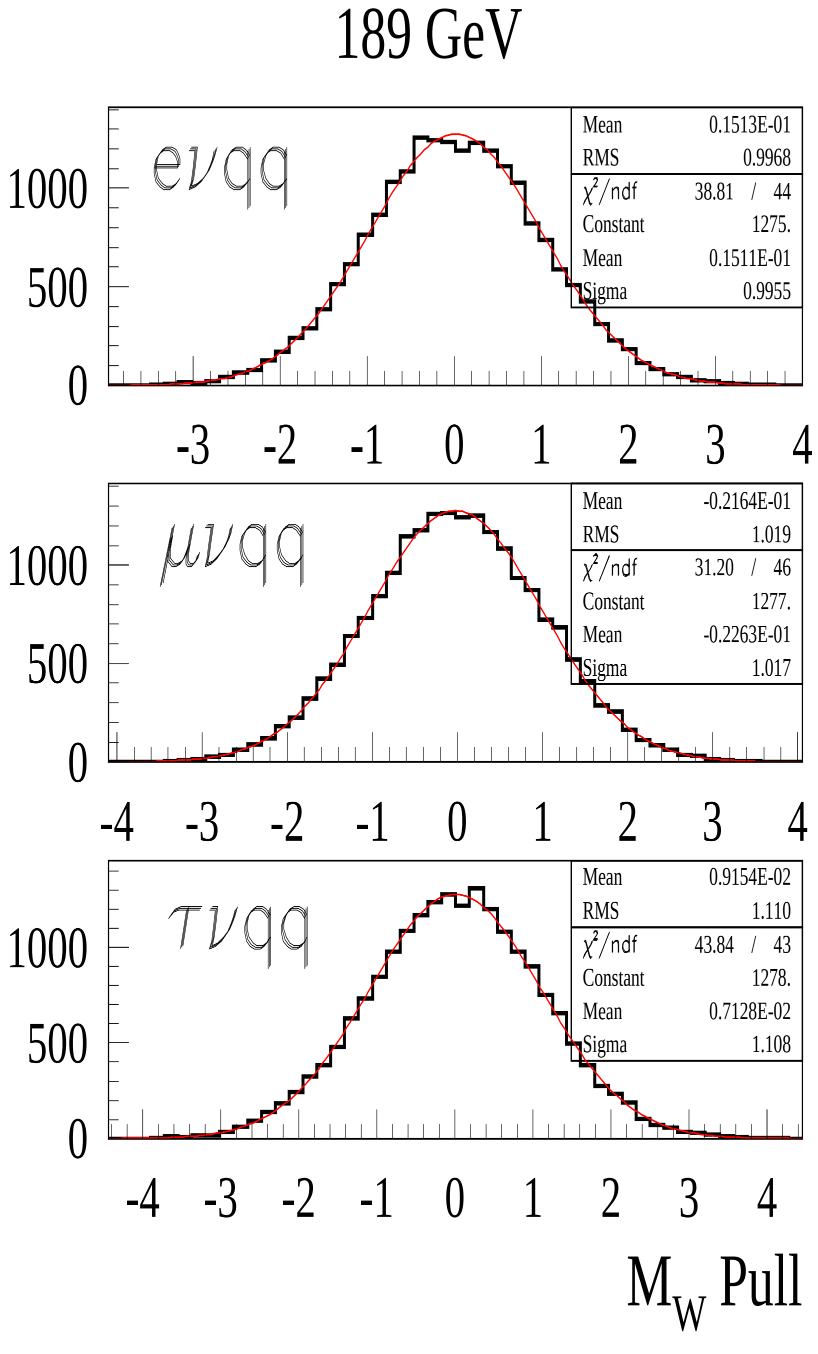

Figure 5.25: Pull distribution from 20,000 bootstrap M_W fits to data-sized samples of the three $l\nu q\overline{q}$ channels at $\sqrt{s}$ = 189 GeV .

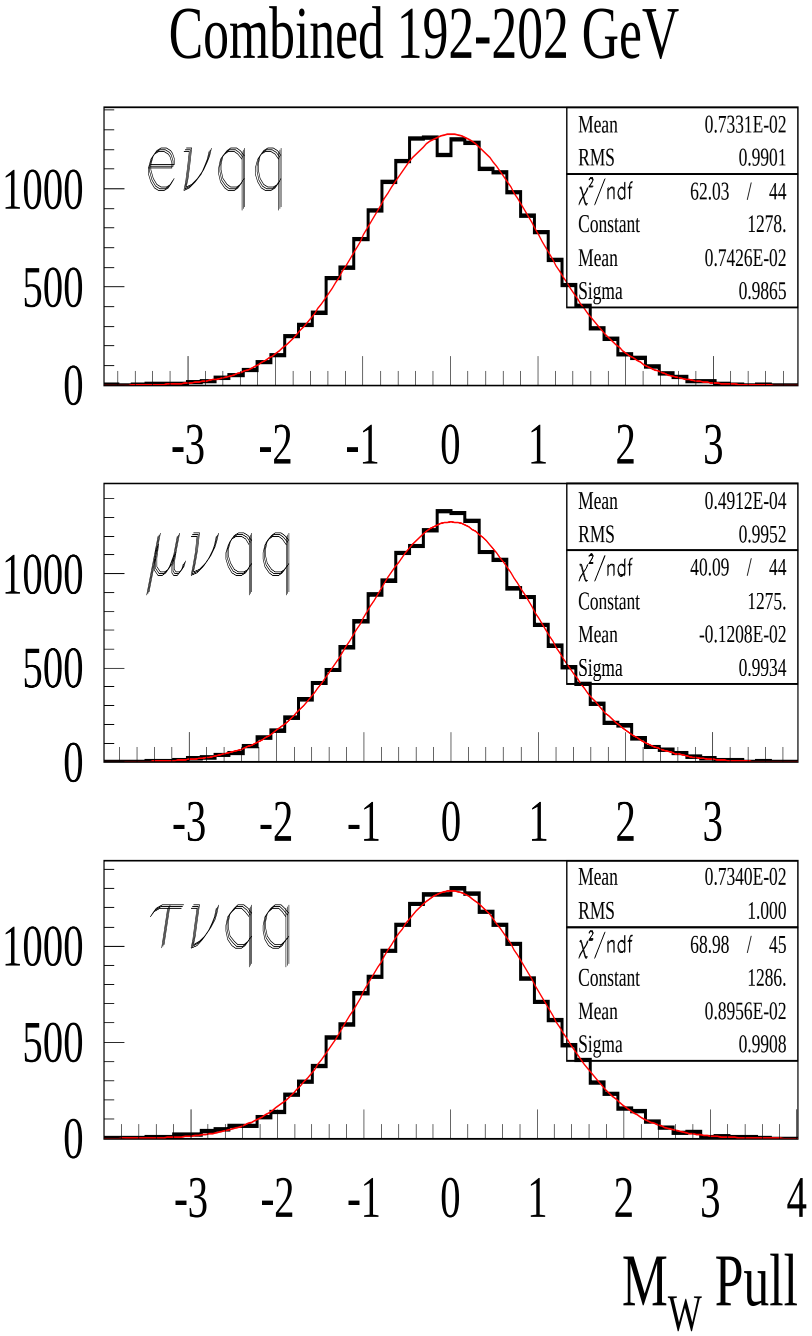

Figure 5.26: Pull distribution from 20,000 bootstrap $\mathrm{M_W}$ fits to combined data-sized samples of the three $l\nu q\bar{q}$ channels at $\sqrt{s} = 192$ to 202 GeV .

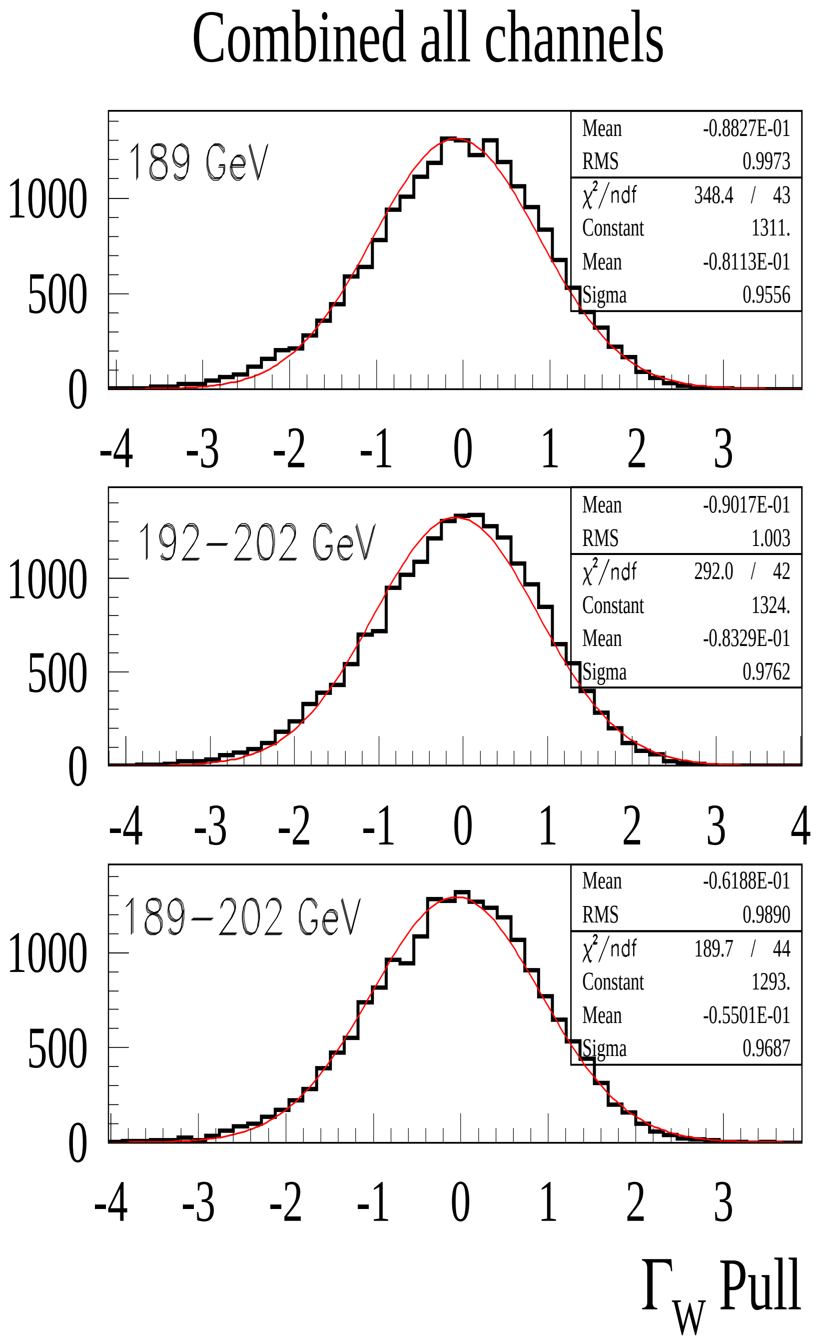

Figure 5.27: Pull distribution from 20,000 bootstrap $\mathrm{M_W}$ fits to combined data-sized samples of the three $l\nu q\bar{q}$ channels at $\sqrt{s}$ = 189 (top), $\sqrt{s}$ = 192-202 combined (middle) and for all centre of mass energies combined (bottom) .

Chapter 6

Systematic Uncertainties

6.1 Introduction

In this section the main sources of systematic uncertainties on the $\mathrm{M_W}$ and Γ_W measurements are studied and their magnitude assessed on a channel by channel basis. The systematic uncertainties are divided into six groups:

- detector effects, like lepton energy and momentum resolution, jet energy and angular resolution, and the length to width ratio of the detector
- effects due to uncertainties in the modelling of underlying physics processes, like fragmentation, ISR and higher order Electroweak corrections
- background level and description
- the uncertainty in the LEP beam energy measurement
- uncertainty due to the statistical error on the calibrations applied to likelihood curves and fitted values and of the reference Monte Carlo samples used for the reweighting method.

Each component is studied independently and its effect on each channel assessed for the 1998 analysis and for the highest luminosity data sample from the 1999 running period, which is that taken at $\sqrt{s} = 200$ GeV. This is done by applying the systematic effect to a large control Monte Carlo simulation sample. The same sample is fitted with and without the systematic effect and the difference in the result taken as the systematic error for that particular contribution. As the same samples are fitted, the correlation between the results is large and therefore the statistical uncertainty on the resulting estimate of the systematic error is minimised. The uncertainties for the other three energy points in the 1999 running period are taken to be the same as for the 200 GeV data. The combination and correlations between the different components are discussed at the end of the chapter.

6.2 Detector Effects

Any discrepancies between data and Monte Carlo simulation distributions can lead to systematic biases on the fitted parameters $\mathrm{M_W}$ and Γ_W. The raw data from the DELPHI detector undergoes calibration procedures by which quantities like charge deposits can be converted into measured energies of particles. Thus there are two possible sources of detector resolution systematic effects: an overall bias in Monte Carlo distributions when compared with real data, and an intrinsic statistical and systematic component in the calibration procedures. In general, a further layer of calibrations is performed at the level of clustered jets and selected leptons. If corrections are applied as standard to all the data and/or Monte Carlo simulation used in the analysis their statistical uncertainty is used to estimate a systematic error. In the case where these corrections are not applied as standard, the systematic error is assessed by checking the effect of the whole correction on fits to large Monte Carlo samples. A third, independent, possible effect is the uncertainty in the length to width ratio of the detector, which changes the opening angle between jets and between the lepton and the missing momentum in $l\nu q\bar{q}$ events, shifting the invariant mass of events. The electron and muon energy and momentum corrections are standard DELPHI W-team ones [81]. The jet energy and angular smearings, plus the energy scalings, together with the length to width ratio have been developed as part of this analysis. Due to the presence of one or more decay neutrinos, the τ leptons carry no information in the kinematic fit and so no systematic error is assigned to their energy scale.

6.2.1 Lepton Energy and Momentum Scale and Resolution

Muon Momentum

A comparison of the momentum scale and resolution in data and Monte Carlo simulation was performed using high purity Z^0 peak calibration $\mu^+\mu^-$ samples [57, 56] with data taken in 1998. The momentum scale was checked by comparing the peak of the $1/p$ distribution for data and Monte Carlo simulation. This was done in bins of θ and separately for positive and negative tracks. The corrections necessary to ensure agreement are applied to the candidate muon in real data events selected as $\mu\nu q\bar{q}$ in this analysis and can be seen in Figure 6.1. After the corrections were applied the width of the $1/p$ distribution was found to be smaller for Monte Carlo data. Smearings were obtained by fitting a double Gaussian function in four bins of θ. The $1/p$ distributions for real and Monte Carlo data, before and after smearing, can be seen in Figure 6.2. The smearings are applied to the Monte Carlo simulation.

Muon Momentum M_W Systematic Errors (MeV)		
Sources of systematic error	189 GeV	200 GeV
μ $1/p$ shift	7	7
μ $1/p$ smearing	1	1
Combined	7	7

Table 6.1: Systematic error on the W mass measurement due to muon momentum scale and resolution.

Muon Momentum Γ_W Systematic Errors (MeV)		
Sources of systematic error	189 GeV	200 GeV
μ $1/p$ shift	19	11
μ $1/p$ smearing	1	5
Combined	19	12

Table 6.2: Systematic error on the W width measurement due to muon momentum scale and resolution.

The systematic error due to this treatment of data was estimated by varying the corrections according to the uncertainty in their determination. Thus, the $1/p$ scale was varied by 1/2 of the total correction, while an extra 1% smearing was applied to the distribution. The individual and combined systematic shifts to the M_W and

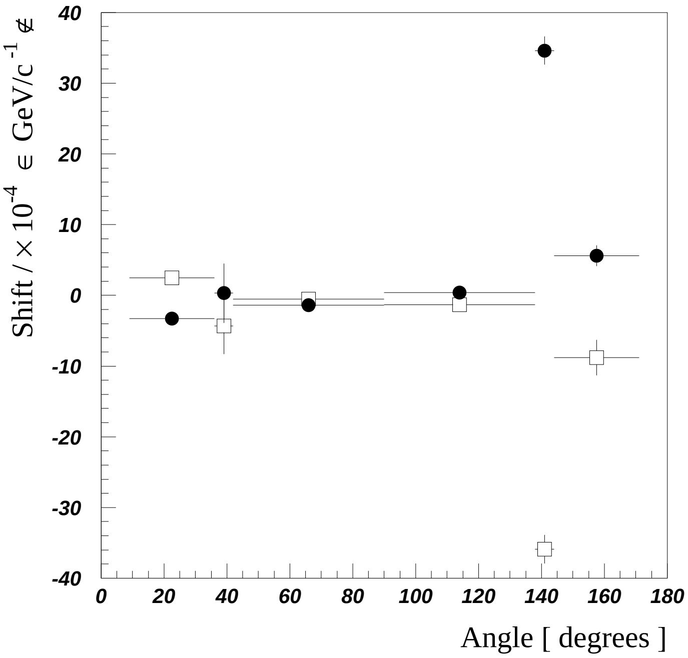

Figure 6.1: $1/p$ shifts in bins of θ. The shifts, to be applied to muons in data, ensure its agreement with Monte Carlo simulation. The open squares are for positive tracks and the solid circles for negative ones.

Γ_W fits are given in Tables 6.1 and 6.2. As no corrections and smearings are available for 1999 data and Monte Carlo simulation the 1998 ones are applied to all samples.

Electron Energy

The energy scale of electrons for real and Monte Carlo data has been compared using Bhabha events selected or simulated at the Z^0 peak [81, 82]. The study has been performed separately for 1998 and 1999. Correction factors, to be applied

Electron Energy M_W Systematic Errors (MeV)			
Sources of systematic error	189 GeV	200 GeV	Combined
Electron energy scaling	12	30	23
Electron energy smearing	32	47	41
Combined	34	56	47

Table 6.3: Systematic error on the W mass measurement due to electron energy scale and resolution.

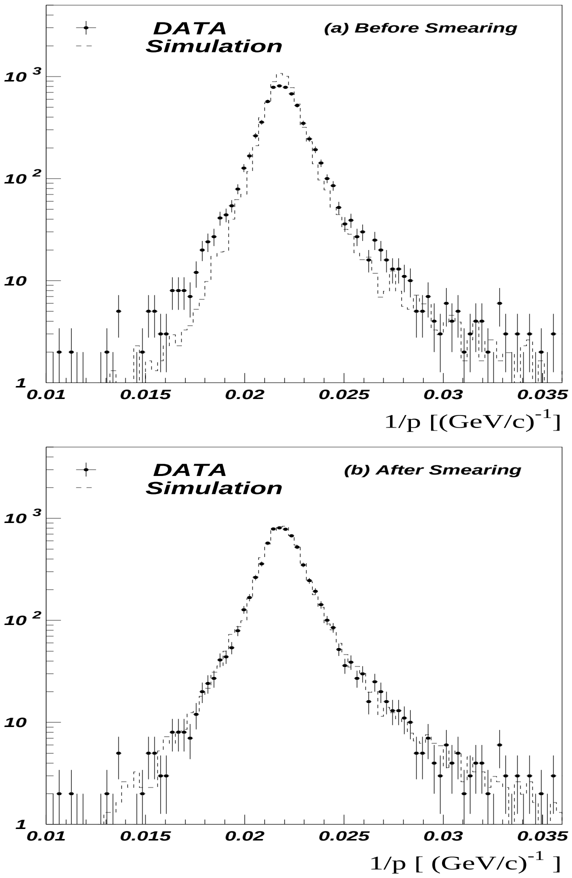

Figure 6.2: $1/p$ distributions for data and Monte Carlo simulation di-muon samples before and after Gaussian smearings are applied. The smearings are applied to the Monte Carlo simulation.

to Monte Carlo simulation, were estimated in bins of polar angle. The resolution of the Monte Carlo data was checked and found to be better than that of real data. Gaussian smearings were estimated for different polar angle regions in order to achieve agreement. Finally, the energy dependence of the corrections was checked by using low energy Compton scattering events at the Z^0 peak and high energy radiative Bhabha events. The true lepton energy was calculated from three body kinematics after assuming one unseen particle lost down the beampipe. The corrections were found to be compatible with having no energy dependence. The above energy scale and resolution corrections are not applied as standard in this analysis[1]. Therefore,

---

[1] They are applied however, in the official DELPHI 189 GeV analysis detailed in [81].

Electron Energy Γ_W Systematic Errors (MeV)		
Sources of systematic error	189 GeV	200 GeV
Electron energy scaling	38	56
Electron energy smearing	137	356
Combined	142	360

Table 6.4: Systematic error on the W width measurement due to electron energy scale and resolution.

the full corrections are used to estimate a systematic error due the disagreement in electron energy between data and Monte Carlo. The two sources of error and their combined effect can be seen in Tables 6.3 and 6.4. The corrections and smearings for 1999 are larger than those applied to the 1998 simulation [82].

6.2.2 Jet Energy and Acollinearity

A comparison between the jet energies in Z^0 peak data and Monte Carlo simulation samples from the 1998 running period was performed in bins of polar angle θ. The ratio of data to Monte Carlo mean jet energies can be seen in Figure 6.3.

The correction factors necessary to ensure agreement between data and Monte Carlo simulation were calculated and found to have an appreciable θ dependence. Nonetheless, they lie within a ±2% band over most of the angular acceptance of DELPHI. Further studies of the energy and angular spectra show that the jet energy, polar and azimuth angles of Monte Carlo data have to be smeared with a Gaussian to make them agree with the real data distributions. The smearings are of 5% in energy and 7.5 mrad in azimuth and θ. These corrections are not applied to the Monte Carlo in this analysis and so are used to estimate the full systematic

Jet M_W Systematic Errors (MeV)				
Sources of systematic error	$e\overline{\nu}_e q\bar{q}'$	$\mu\overline{\nu}_\mu q\bar{q}'$	$\tau\overline{\nu}_\tau q\bar{q}'$	$l\overline{\nu}_l q\bar{q}'$
$E_j(\theta)$ correction	5	6	4	5
E_j smearing	10	6	32	11
θ,ϕ smearing	23	14	13	17
Combined	27	17	39	21

Table 6.5: Systematic error on the W mass measurement due to modelling of jet energy and angular resolution.

Jet Γ_{W} Systematic Errors (MeV)				
Sources of systematic error	$\mathrm{e}\overline{\nu}_{\mathrm{e}}\mathrm{q}\bar{\mathrm{q}}'$	$\mu\overline{\nu}_{\mu}\mathrm{q}\bar{\mathrm{q}}'$	$\tau\overline{\nu}_{\tau}\mathrm{q}\bar{\mathrm{q}}'$	$\mathrm{l}\overline{\nu}_{\mathrm{l}}\mathrm{q}\bar{\mathrm{q}}'$
$E_j(\theta)$ correction	11	7	5	8
E_j smearing	2	33	240	38
θ,ϕ smearing	9	10	7	9
All smearing	11	43	247	47
Combined	16	44	247	49

Table 6.6: Systematic error on the W width measurement due to modelling of jet energy and angular resolution.

error, whose individual and combined components can be seen in Tables 6.5 and 6.6. The energy and acollinearity distributions can be seen in Figures 6.4 and 6.5 respectively. This study has not been applied to 1999 samples, so the systematic errors estimated from 1998 samples are applied to both running periods.

6.2.3 Aspect Ratio of DELPHI

The DELPHI detector is aligned relative to the vertex detector (VD). The largest uncertainty in the measurement of the VD is its radius, which is known with a precision of 0.05% [83][2]. The effect due to this uncertainty was studied by scaling the z-coordinate of all tracks in an event by 1 ± 0.0005 before performing the kinematic fit. The results are summarised in Tables 6.7 and 6.8. The study was performed on a $\sqrt{s} = 200$ GeV simulation sample. The resulting errors are applied to all centre of mass energy points.

Aspect Ratio M_{W} Systematic Errors (MeV)				
$\sqrt{s}$(GeV)	$\mathrm{e}\overline{\nu}_{\mathrm{e}}\mathrm{q}\bar{\mathrm{q}}'$	$\mu\overline{\nu}_{\mu}\mathrm{q}\bar{\mathrm{q}}'$	$\tau\overline{\nu}_{\tau}\mathrm{q}\bar{\mathrm{q}}'$	$\mathrm{l}\overline{\nu}_{\mathrm{l}}\mathrm{q}\bar{\mathrm{q}}'$
189	1	1	3	1
200	1	1	3	1
Combined	1	1	3	1

Table 6.7: Systematic error on the W mass measurement due to the uncertainty in the length to width ratio of the DELPHI detector.

---

[2] In fact, the error on the radius of the VD is a function of the z coordinate. 0.05% is an estimate of the uncertainty on its radius at the centre of the detector, where the effect on the measurement of tracks is minimal. The uncertainty decreases as $|z|$ increases, so the error on low θ tracks is less. Therefore the error used for the studies presented here is a conservative one. However, the effect on M_{W} and Γ_{W} is minimal.

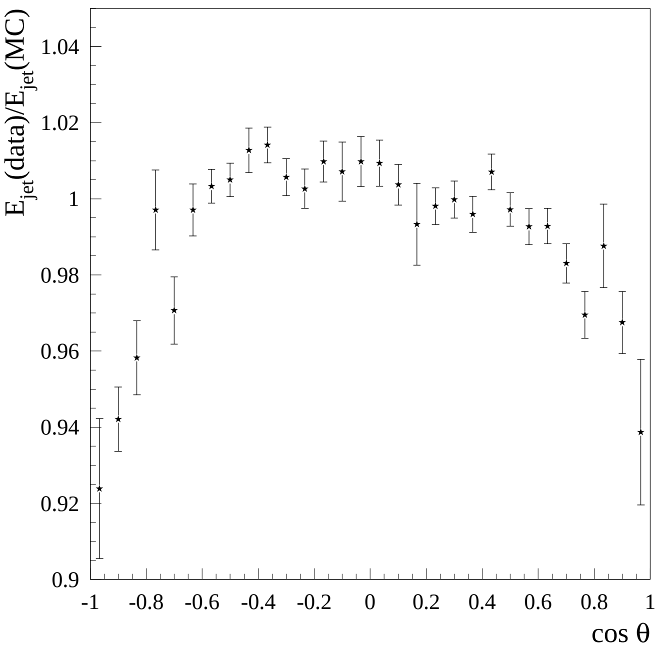

Figure 6.3: The ratio between the mean jet energies of data and Monte Carlo $e^+e^- \to q\overline{q}$ events as a function of polar angle. The disagreement is highest at low angles.

6.3 Effects due to Modelling of Physics

6.3.1 Fragmentation

The effects of event fragmentation on M_W and Γ_W were studied by performing fits to large $\sqrt{s} = 200$ GeV W^+W^- samples generated with different values of a set of four parameters affecting different aspects of the fragmentation process, as modelled by the `PYTHIA/JETSET`7.4 Parton Showers (PS) used as standard in DELPHI simulation. In each case, one parameter was varied by $\pm \sim 20\sigma$ and the others held at their standard value. The default values and their associated errors are obtained from the standard DELPHI tuning [84] of `JETSET` fragmentation parameters to hadronic Z^0 event shape variables and particle types, and are summarised, together with the values used for this systematic effect evaluation, in Table 6.9. The choice of variables is the following:

- σ_q, the width of the Gaussian transverse momentum distribution of primary hadrons.

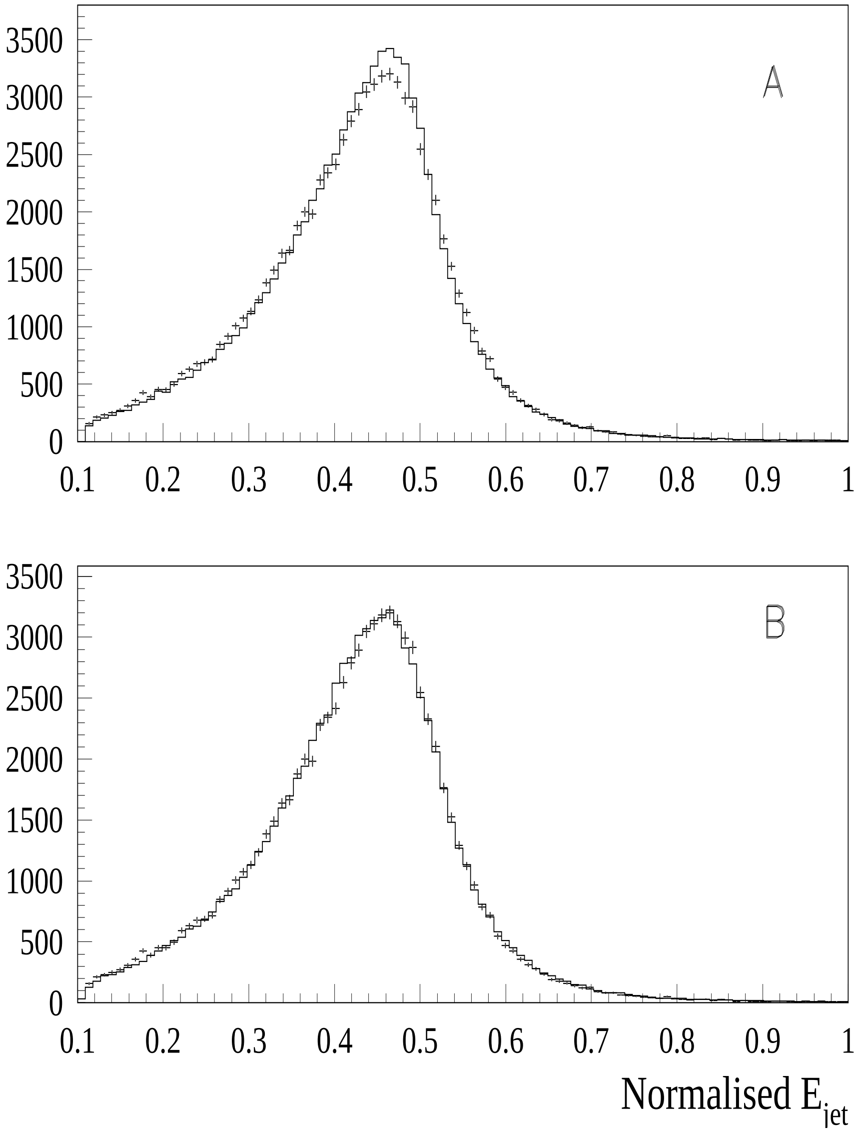

Figure 6.4: $E_{jet}/\sqrt{s}$ distributions for real and Monte Carlo data before (**A**) and after (**B**) applying a 5% Gaussian smearing. The solid histogram is the Monte Carlo and the points with error bars are the real data.

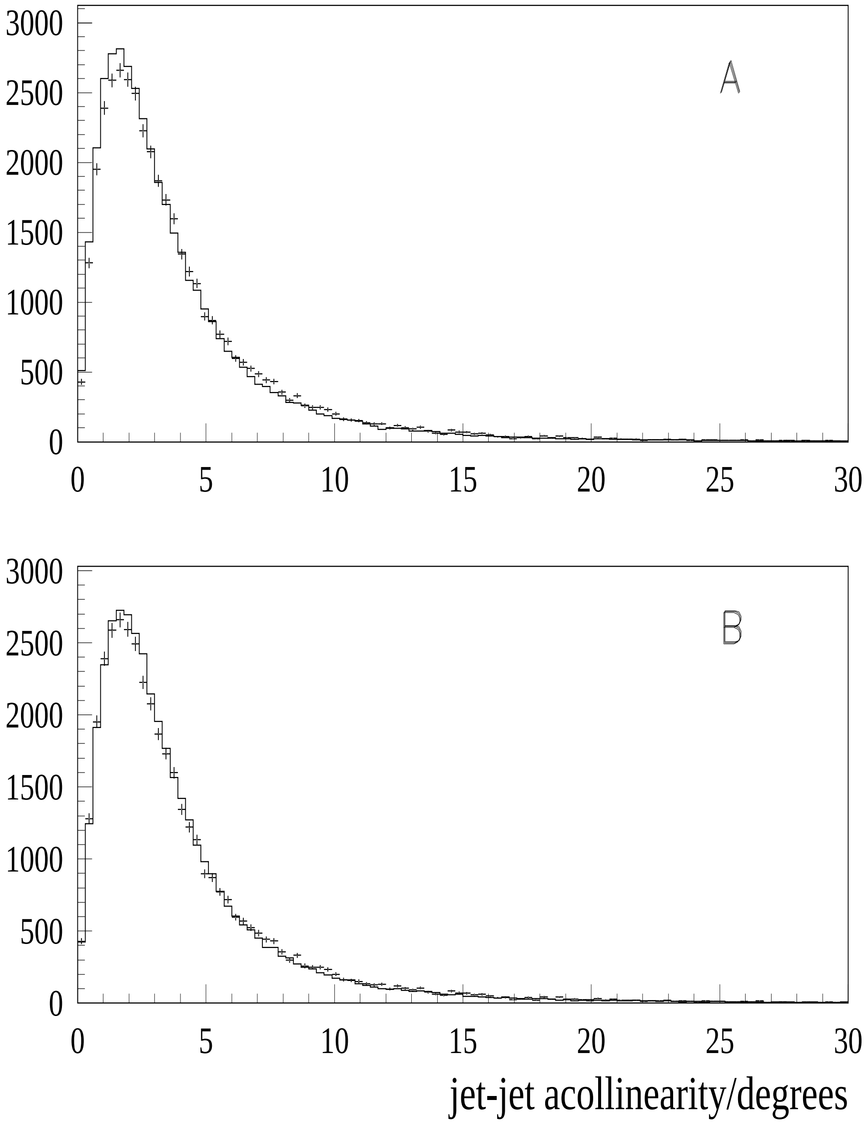

Figure 6.5: The acollinearity of two forced jets in $e^+e^- \rightarrow q\overline{q}$ data and Monte Carlo events before (**A**) and after (**B**) smearing the Monte Carlo jet direction by 7.5 mrad in θ and ϕ.

Aspect Ratio Γ_W Systematic Errors (MeV)				
$\sqrt{s}$(GeV)	$e\bar{\nu}_e q\bar{q}'$	$\mu\bar{\nu}_\mu q\bar{q}'$	$\tau\bar{\nu}_\tau q\bar{q}'$	$l\bar{\nu}_l q\bar{q}'$
189	3	3	6	4
200	3	3	6	4
Combined	3	3	6	4

Table 6.8: Systematic error on the W width measurement due to the uncertainty in the length to width ratio of the DELPHI detector.

- **Λ_{QCD}**, controls the running of the strong coupling constant, α_s.
- **Q_0**, the invariant mass cut-off for parton radiation in PS.
- Lund fragmentation parameter **a**, controlling the proportion of longitudinal momentum carried by each meson in a jet.

These variables control the transverse and longitudinal spread of jets. The results of the M_W and Γ_W fits can be seen in Figures 6.6 and 6.7. The three points on each plot are statistically uncorrelated, although the same control sample has been used for the central point on all plots. The offset at the central points has been corrected for. The dependence of the systematic shift on each of the parameters is compatible with being linear. The linearity assumption is used to interpolate the value of the shifts at $\pm 2\sigma$ for each parameter using the fitted lines seen on the plots. The systematic effects are taken to be un-correlated for each channel and are combined by adding them in quadrature. The effects between channels are taken to be correlated. The individual and combined components can be seen in Tables 6.10 and 6.11, together with their associated errors. Whereas clear trends can be observed in the bias in M_W as a function of the value of the fragmentation parameters, the study is still statistically limited and the systematic errors are compatible with zero.

This method assumes that the fragmentation and hadronisation models chosen for the DELPHI simulation give a good approximation to reality. Other methods of assesing this systematic error include the use of other fragmentation packages, and the use of mixed lorentz boosted Z^0 events. The former has the problem that all models are tuned to the same data in the same way and should, in principle, give similar results. The latter method has been tried at DELPHI in the $q\bar{q}'\bar{q}q'$ channel [70] and tested by the author for this analysis. The results hint at smaller systematic effects than those obtained by the standard methods presented here. However, in the case of this analysis, they are preliminary and thus excluded from this manuscript.

Parameter	DELPHI default	Systematic Study Values	
σ_q	$0.408^{+0.007}_{-0.014}$	0.200	0.600
Lund a	$0.417^{+0.022}_{-0.024}$	0.100	0.700
Λ_{QCD}	$0.297^{+0.013}_{-0.009}$	0.100	0.500
Q_0	$1.340^{+0.170}_{-0.120}$	0.6534	2.500

Table 6.9: The DELPHI -tuned values and errors for the four fragmentation parameters chosen for the evaluation of the systematic errors, together with the values chosen for the study.

$\mathrm{M_W}$ Fragmentation Systematic Errors (MeV)				
Parameter	$\mathrm{e\bar{\nu}_e q\bar{q}'}$	$\mu\bar{\nu}_\mu \mathrm{q\bar{q}'}$	$\tau\bar{\nu}_\tau \mathrm{q\bar{q}'}$	$lnqq$
σ_q	0 ± 2	2 ± 2	11 ± 4	2 ± 2
Lund a	5 ± 4	2 ± 3	19 ± 7	4 ± 4
Λ_{QCD}	8 ± 2	4 ± 2	24 ± 5	8 ± 2
Q_0	6 ± 7	10 ± 6	6 ± 13	8 ± 8
Combined	11 ± 9	11 ± 7	34 ± 17	12 ± 8

Table 6.10: Interpolated systematic effects on $\mathrm{M_W}$ obtained from variations in `JETSET` fragmentation parameters. The errors represent the mean variation of the fitted value for a parameter variations of $\pm 2\sigma$ from the DELPHI standard value.

6.3.2 Initial State Radiation

The standard DELPHI $\mathrm{W^+W^-}$ simulation package uses the `EXCALIBUR` four-fermion generator. Modelling of the initial state radiation is done by `QEDPS`, a parton shower algorithm wich generates photons with non-zero transverse momentum. This is in contrast to the collinear ISR treatment which is used as default in `EXCALIBUR`. A full, satisfactory assessment of the effect of ISR has not been obtained within the LEP community at the time of writing. In fact, the problem could be seen as one aspect within the whole electroweak corrections question, where effects like the interference between initial and final state radiation would have to be considered fully. Our current event generators treat ISR independently from FSR. Initial state radiation has the effect of reducing the centre of mass energy and boosting its

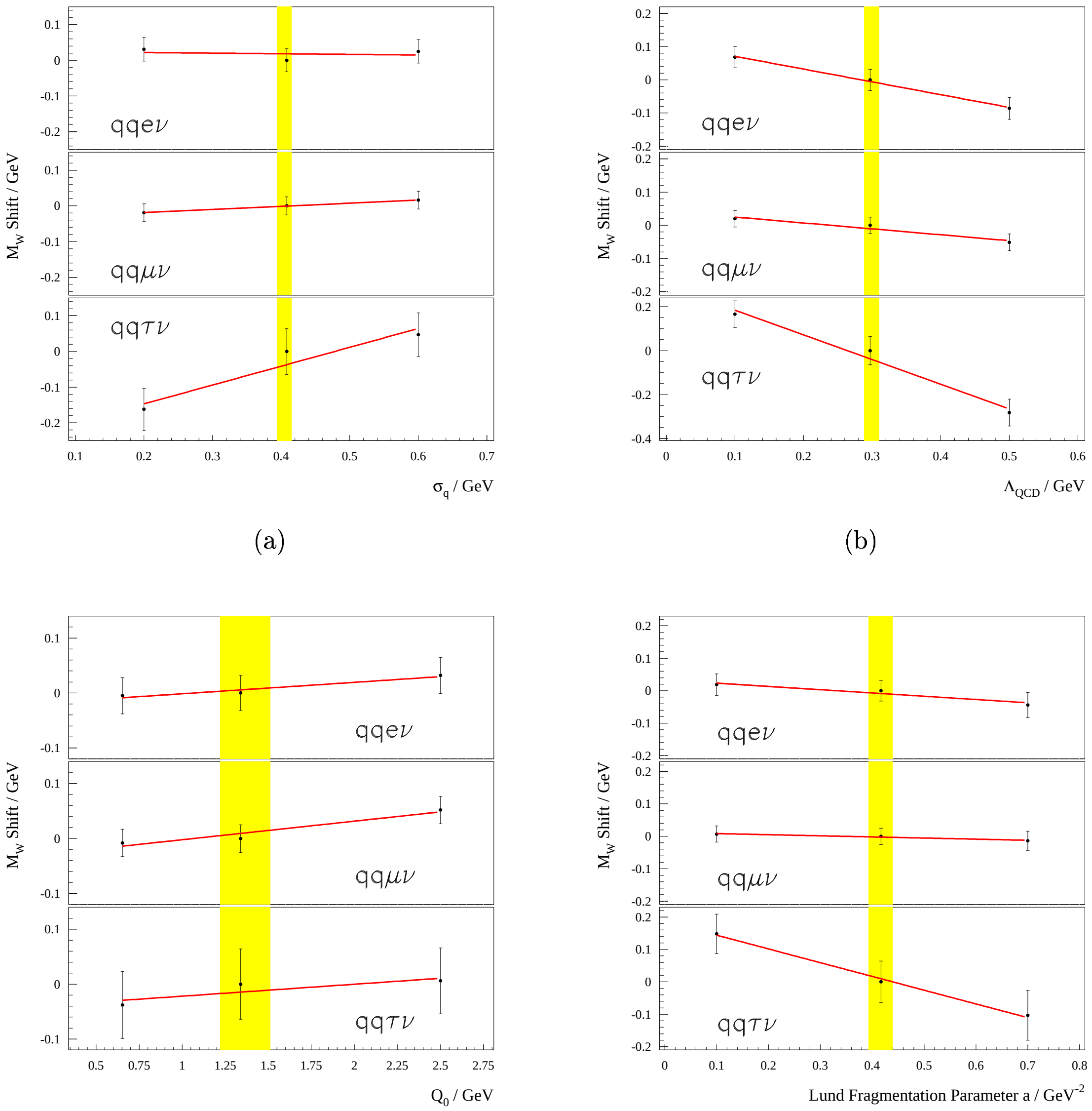

(a) (b)

(c) (d)

Figure 6.6: The effect of the M_W fit on different fragmentation parameters for all three channels. The central control point is the same for all four plots. The remaining points, generated at $\approx \pm 20\sigma$ from the DELPHI tuned values are independent and uncorrelated. The yellow bands show the uncertainty on each parameter from the tuning. The quoted errors come from a linear interpolation according to the fitted lines shown in the plots .

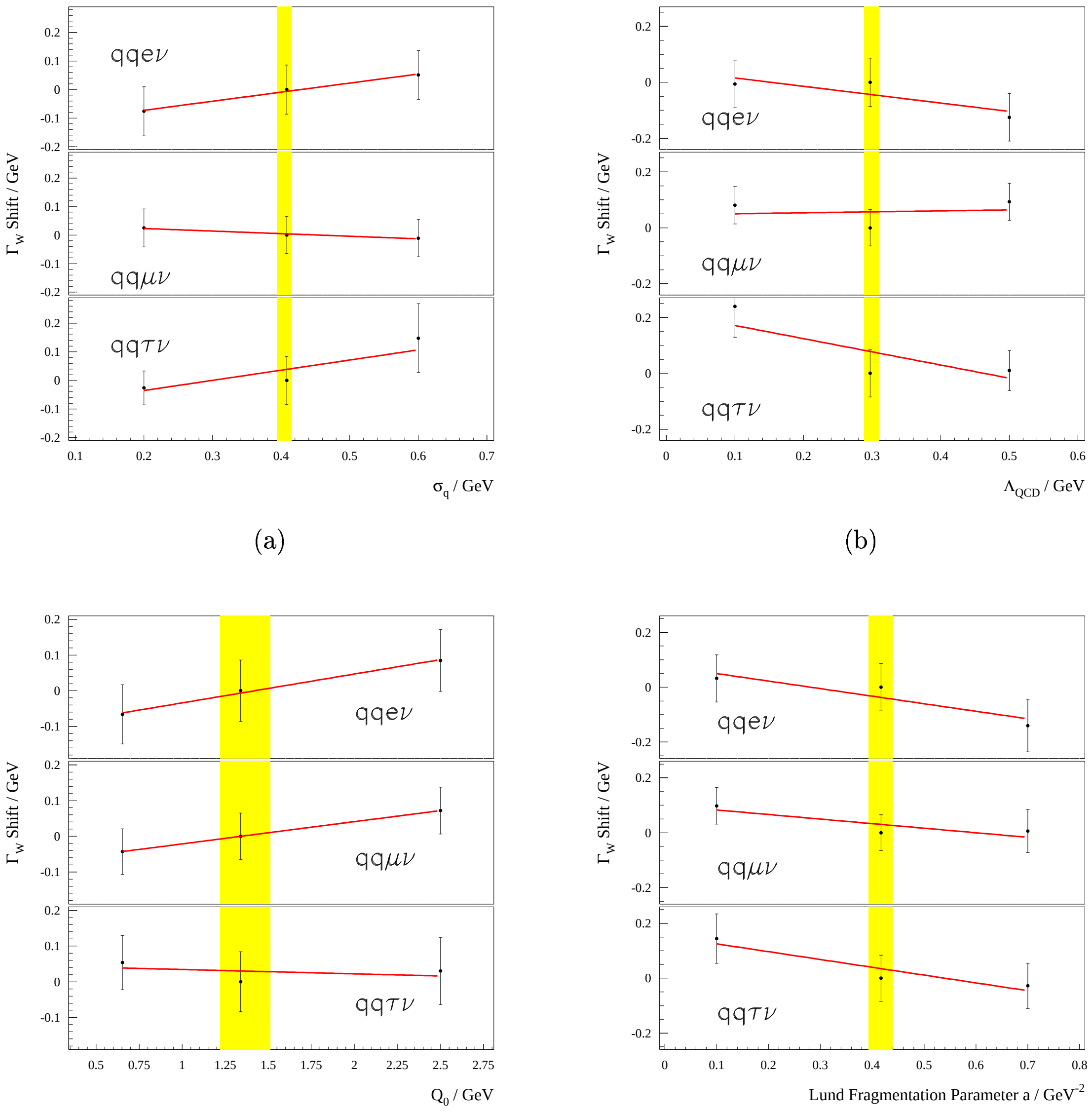

(a) (b)

(c) (d)

Figure 6.7: The effect of the Γ_W fit on different fragmentation parameters for all three channels. The central control point is the same for all four plots. The remaining points, generated at $\approx \pm 20\sigma$ from the DELPHI tuned values are independent and uncorrelated. The yellow bands show the uncertainty on each parameter from the tuning. The quoted errors come from a linear interpolation according to the fitted lines shown in the plots .

Γ_W Fragmentation Systematic Errors (MeV)				
Parameter	$e\nu q\bar{q}$	$\mu\nu q\bar{q}$	$\tau\nu q\bar{q}$	$l\nu q\bar{q}$
σ_q	7 ± 6	2 ± 5	8 ± 6	4 ± 4
Lund a	13 ± 10	8 ± 8	13 ± 9	10 ± 8
Λ_{QCD}	6 ± 6	1 ± 5	10 ± 7	2 ± 6
Q_0	12 ± 9	18 ± 14	4 ± 20	20 ± 16
Combined	24 ± 19	20 ± 18	18 ± 23	22 ± 20

Table 6.11: Interpolated systematic effects on Γ_W obtained from variations in JETSET fragmentation parameters. The errors represent the mean variation of the fitted value for a parameter variations of $\pm 2\sigma$ from the DELPHI standard value.

frame with respect to the laboratory frame. Thus the following assessment of the error due to modelling of ISR is by no means final, but has been chosen by the DELPHI collaboration [81] as a reasonable gauge of the magnitude of any effect. It is a comparison between the parton shower and YFS exponentiation methods as implemented in `QEDPS` and `KORALW` respectively. `EXCALIBUR` events are re-weighted such that the spectrum of total energy radiated as ISR matches that of `KORALW` . The resulting errors for M_W and Γ_W are quoted in Tables 6.17 and 6.18 and are treated as correlated between channels and years.

Studies of the effects of $\mathcal{O}(\alpha)$ corrections on M_W have been performed using `YFSWW`[26]. These studies point at effects below ~10 MeV [85].

6.4 Background

The shape and level of the background affect the overall shape of the distributions being fitted. The background distribution is accounted for in this analysis through the background PDF and the selection purity. Both aspects, besides being determined from finite Monte Carlo samples, have a smaller theoretical uncertainty associated to them. Studies of the effect of different hadronisation packages on the shape of the dominant $Z(\gamma)$ background have shown it to be marginal [81]. The evaluation of the background systematic error is evaluated here by varying the background level conservatively by ±10%. A scan of background level from ±50% to ±150% shows the shift to be linear both for M_W and Γ_W. The errors for the $\tau\nu q\bar{q}$ channel vary visibly between 189 GeV and 200 GeV. This is as a consequence of the difference in the background level and shape, which is due to the different selections used for for that channel in the 1998 and 1999 running periods. The 1999 $\tau\nu q\bar{q}$ background distribution is more sharply peaked and so has a larger pull on the fitted results[3]. The resulting errors are shown in Tables 6.12 and 6.13. The background level error is taken to be correlated between channels and centre of mass energy points. The effect of background parametrisation on the results was checked, where applicable, by fitting polynomials of different degrees to background histograms with different bin sizes. In all cases this effect was found to be negligible.

Background Level $\mathrm{M_W}$ Systematic Errors (MeV)				
$\sqrt{s}$(GeV)	$\mathrm{e\bar{\nu}_e q\bar{q}'}$	$\mu\bar{\nu}_\mu \mathrm{q\bar{q}'}$	$\tau\bar{\nu}_\tau \mathrm{q\bar{q}'}$	$\mathrm{l\bar{\nu}_l q\bar{q}'}$
189	3	1	7	2
200	3	1	23	3
Combined	3	1	14	2

Table 6.12: Systematic error on the W mass measurement due to the uncertainty in the background level.

Background Level Γ_W Systematic Errors (MeV)				
$\sqrt{s}$(GeV)	$\mathrm{e\bar{\nu}_e q\bar{q}'}$	$\mu\bar{\nu}_\mu \mathrm{q\bar{q}'}$	$\tau\bar{\nu}_\tau \mathrm{q\bar{q}'}$	$\mathrm{l\bar{\nu}_l q\bar{q}'}$
189	23	8	75	32
200	23	10	111	23

Table 6.13: Systematic error on the W width measurement due to the uncertainty in the background level.

6.5 LEP Beam Energy

The determination of the LEP beam energy was reviewed in section 2.6. The beam energy is measured during running every 15 minutes or each time there is a significant change in the operating energy. The measured centre of mass energy is used as one of the constraints in the kinematic fit and so the relative uncertainty on the beam energy measurement propagates directly into the $\mathrm{M_W}$ relative sensitivity:

$$\frac{\Delta \mathrm{M_W}}{\mathrm{M_W}} = \frac{\Delta E_{\mathrm{BEAM}}}{E_{\mathrm{BEAM}}} \tag{6.1}$$

---

[3] This is provided the background peak is offset with respect to the signal peak, as is the case.

The final errors for the 1998 and 1999 high energy running periods can be found in [86, 87]. This relation yields an error of 17 MeV on $\mathrm{M_W}$ for both running periods. The error is correlated between channels and between years, with the correlation coefficients for the latter being taken from the LEP energy correlation matrix.

6.6 Monte Carlo Statistics

6.6.1 Calibration Samples

The calibration corrections applied to all $\mathrm{M_W}$ and Γ_W results are derived from fits to finite Monte Carlo samples and therefore carry a statistical uncertainty. The contribution to the correction due to the linear fit parameters c (offset at $\mathrm{M_W}$=80.35 GeV), shown in Section 5.7, Tables 5.2 and 5.3, are the dominant factor in the corrections. The slope corrections, given by the parameters m in Tables 5.4 and 5.5, have influence on the statistical error of the fit but have negligible effect on the central values themselves. Therefore the calibration systematic error is given by the statistical error on the offsets c. The errors are treated as uncorrelated between channels and years and are summarised in Tables 6.17 and 6.18.

6.6.2 Reference Samples

The probability density function used to extract $\mathrm{M_W}$ and Γ_W values is constructed from finite Monte Carlo samples and so has a statistical nature of its own, which adds a component to the total systematic error. Ideally a single data sample would be fitted with N equally sized, independent reference samples, and the spread of the results taken as the systematic error. Unfortunately, splitting the reference sample is not a viable option as the instabilities arising from events with large weights in low event density regions, described in Section 5.7.6, would have the effect of increasing the scatter of the results artificially. A solution to this problem is to use the re-sampling methods described in Section 5.6.2. Each channel was fitted 50 times using 80% of the 189 GeV and 200 GeV reference samples corresponding to its centre of mass energy. The standard deviation of the results was calculated from Equation 5.18 assuming a correlation of 0.8 between results. The error on the standard deviation was calculated from Equation 5.20. Assuming a $1/\sqrt{N}$ dependence of the error due to reference Monte Carlo statistics, the errors were scaled by $\sqrt{0.8}$ to get the numbers shown in Tables 6.14 and 6.15.

ΔM_W due to Reference Monte Carlo Statistics				
$\sqrt{s}$(GeV)	$\mathrm{e}\overline{\nu}_{\mathrm{e}}\mathrm{q}\overline{\mathrm{q}}'$	$\mu\overline{\nu}_{\mu}\mathrm{q}\overline{\mathrm{q}}'$	$\tau\overline{\nu}_{\tau}\mathrm{q}\overline{\mathrm{q}}'$	$\mathrm{l}\overline{\nu}_{\mathrm{l}}\mathrm{q}\overline{\mathrm{q}}'$
189	20 ± 2	17 ± 2	29 ± 3	12 ± 1
200	28 ± 3	28 ± 3	41 ± 4	19 ± 2
Combined	19 ± 2	18 ± 2	24 ± 2	12 ± 1

Table 6.14: Systematic error on the W mass measurement due to finite statistics in the reference Monte Carlo samples.

$\Delta\Gamma_W$ due to Reference Monte Carlo Statistics				
$\sqrt{s}$(GeV)	$\mathrm{e}\overline{\nu}_{\mathrm{e}}\mathrm{q}\overline{\mathrm{q}}'$	$\mu\overline{\nu}_{\mu}\mathrm{q}\overline{\mathrm{q}}'$	$\tau\overline{\nu}_{\tau}\mathrm{q}\overline{\mathrm{q}}'$	$\mathrm{l}\overline{\nu}_{\mathrm{l}}\mathrm{q}\overline{\mathrm{q}}'$
189	55 ± 6	52 ± 5	61 ± 6	36 ± 4
200	68 ± 7	64 ± 6	120 ± 12	39 ± 4
Combined	-	-	-	27 ± 3

Table 6.15: Systematic error on the W width measurement due to finite statistics in the reference Monte Carlo samples.

6.7 Correlations and Combination

For the combination of results and errors correlations between the different systematic errors according to centre of mass energy[4] and decay channel are taken into account. The assumed correlations, which have generally been chosen conservatively, are shown on Table 6.16. The correlation between the LEP beam energy errors for samples taken at different centre of mass energies is taken from the LEP energy working group correlation matrix [87]. The treatment of the correlation between detector relolution effects is different for the $\mathrm{M_W}$ and Γ_{W} determinations. Since the resolution of lepton and jet angles, momenta and energies is better in Monte Carlo simulation than in real data, these effects have a positive bias on Γ_{W}. Therefore they are treated as correlated between channels and years for this, measurement, contrary to what is done for $\mathrm{M_W}$. Thus, the systematic effects due to the smearing

---

[4] Conventionally these are termed *year to year* correlations but the 1999 running period has multiple energy points.

of the energy, polar and azimuthal angles of jets shown in Table 6.6 are combined linearly for each channel, together with the effects due to lepton energy and momentum resolution. Then they are combined cuadratically with the corresponding errors due to jet and lepton energy scales. The resulting channel by channel errors due to combined detector resolution effects are then combined assuming 100% correlation. The results are combined using the least squares method. The covariance matrix is obtained from the correlation coefficients defined in Table 6.16 and the statistical errors in the data samples, which can be seen in Chapter 7. The errors for the 1999 running period have been estimated with fits to Monte Carlo samples generated at $\sqrt{s} = 200\text{GeV}$ and are assumed to be the same for the remaining energy points. The evaluation of individual cross-channel or cross-$\sqrt{s}$ components in all error tables has been obtained by performing the relevant combinations in the absence of all other systematic errors and considering only the statistical component of the errors. The global combination treats all errors simultaneously via the correlation matrix in the standard manner. The resulting combined errors are given in Tables 6.17 and 6.18.

Correlations between Systematic Errors		
Sources of systematic error	$\sqrt{s}$	Channels
Lepton corrections†	1	0
Jet corrections†	1	1
Aspect Ratio	1	1
Fragmentation	1	1
Background	1	0
Reference M.C. Statistics	*	0
I.S.R.	1	1
LEPBeam Energy	LEP	1

Table 6.16: Correlations between systematic errors on M_W and Γ_W . The column labeled $\sqrt{s}$ gives the assumed correlation between samples taken at different centre of mass energies for single decay channels. The column labeled *channels* gives the correlation between the different decay channels. The Reference Monte Carlo statistics errors (labeled *) are uncorrelated between 1998 and 1999 but correlated for the individual centre of mass points in 1999 as the same reference sample is used for those data sets. † The correlations for lepton and jet resolution effects have a special treatment for the case of Γ_W determination. This is discussed in the text. The LEP beam energy correlation between centre of mass energies is taken from the LEP energy working group correlation matrix.

M_W Systematic Errors (MeV)				
Sources of systematic error	$e\overline{\nu}_e q\bar{q}'$	$\mu\overline{\nu}_\mu q\bar{q}'$	$\tau\overline{\nu}_\tau q\bar{q}'$	$l\overline{\nu}_l q\bar{q}'$
Lepton corrections	47	7	0	13
Jet corrections	27	17	39	23
Aspect Ratio	1	1	3	1
Fragmentation	11	11	34	14
Background	3	1	14	2
I.S.R.	4	4	4	4
Calibration	16	13	31	10
Reference M.C. Statistics	19	18	24	12
LEP Beam Energy	17	17	17	17
Total	63	35	68	38

Table 6.17: Contributions to the systematic error on the W mass measurement.

Γ_W Systematic Errors (MeV)	
Sources of systematic error	$l\overline{\nu}_l q\bar{q}'$
Lepton corrections	96
Jet corrections	49
Combined corrections	146
Aspect Ratio	4
Fragmentation	22
Background	27
I.S.R.	11
Calibration	26
Reference M.C. Statistics	27
Total	155

Table 6.18: Contributions to the systematic error on the W width measurement.

Chapter 7

Results and Conclusions

7.1 Introduction

Values for the W boson mass and width have been obtained using the data collected by the Delphi experiment during the 1998 and 1999 running periods. The results were obtained using events selected under either of the three semi-leptonic W^+W^- decay hypotheses, excluding events selected under the single-prong τ decay mode hypothesis. The parameters M_W and Γ_W were measured by fitting event variable distributions, obtained after performing a kinematic fit, using Monte Carlo reweighting with Gaussian kernel functions. An assessment of the main systematic errors influencing the results was performed. The results quoted below take into account, unless otherwise stated, these systematic errors and their assumed correlations. The results are compared with the official Delphi ones. A comparison of the final combined results with the average of the corresponding measurements of the Aleph, L3 and Opal collaborations (**ALO**) is shown. The M_W results are interpreted in terms of higher order Electroweak corrections and the mass of the Higgs boson. The Γ_W result is compared with its standard model expectation, obtained both using the M_W result from this analysis and the current world average.

7.2 M_W Results for 1998 and 1999

The combined M_W results for the 1998 and 1999 data sets and their corresponding errors are presented below. The errors are divided into the statistical component (*stat*), the main systematic (*syst*) and the error due to the uncertainty in the

	Channel			
$\sqrt{s}$/GeV	$e\nu jj$	$\mu\nu jj$	$\tau\nu jj$	$l\nu jj$
189	79.946 ± 0.345	80.117 ± 0.224	80.310 ± 0.396	80.111 ± 0.170
192	81.296 ± 0.91	80.334 ± 0.512	80.378 ± 1.287	80.543 ± 0.418
196	80.645 ± 0.457	79.970 ± 0.350	79.681 ± 0.805	80.161 ± 0.268
200	80.958 ± 0.478	80.480 ± 0.372	80.722 ± 0.871	80.670 ± 0.276
202	80.280 ± 0.644	80.435 ± 0.363	82.945 ± 1.037	80.591 ± 0.310
192-202	80.735 ± 0.274	80.284 ± 0.194	80.754 ± 0.501	
189-202	80.435 ± 0.215	80.213 ± 0.147	80.478 ± 0.309	

Table 7.1: The individual results of M_W fits and their corresponding statistical errors. Here, the combinations between channels have been performed taking only the statistical error into account.

LEP beam energy (LEP). The total error is given in brackets. The channel-by-channel values for $\mathrm{M_W}$ at all the nominal centre of mass energies corresponding to the data sets of 1998 and 1999 and their statistical errors can be seen in Table 7.1. The combined result for 1998 data is

$$\mathrm{M_W} \;=\; 80.110 \;\pm\; 0.170\;(stat) \;\pm\; 0.036\;(syst) \;\pm\; 0.017\;(LEP)\;(\pm\;0.174)\;\mathrm{GeV}$$

The combined value for 1999 data is

$$\mathrm{M_W} \;=\; 80.468 \;\pm\; 0.151\;(stat) \;\pm\; 0.038\;(syst) \;\pm\; 0.017\;(LEP)\;(\pm\;0.157)\;\mathrm{GeV}$$

The combination of these two results yields the value

$$\mathrm{M_W} \;=\; 80.308 \;\pm\; 0.113\;(stat) \;\pm\; 0.034\;(syst) \;\pm\; 0.017\;(LEP)\;(\pm\;0.119)\;\mathrm{GeV}$$

The $-2log(\mathbf{L})$ curves for individual channels and for the two running periods, and the combined results, are shown in Figure 7.1. These curves contain information about the statistical sensitivity only. The breakdown of the sources of error is shown in Figure 7.2. It can be seen that the sensitivity of the result is statistically dominated. However, in the combined LEP values the statistical and systematic sources of error are of comparable magnitude, motivating the detailed study of the nature of the systematic errors presented here. The contribution from each of the three $\mathrm{W^+W^-}$ decay channels and each of the five centre of mass energy points considered is shown in Figure 7.3.

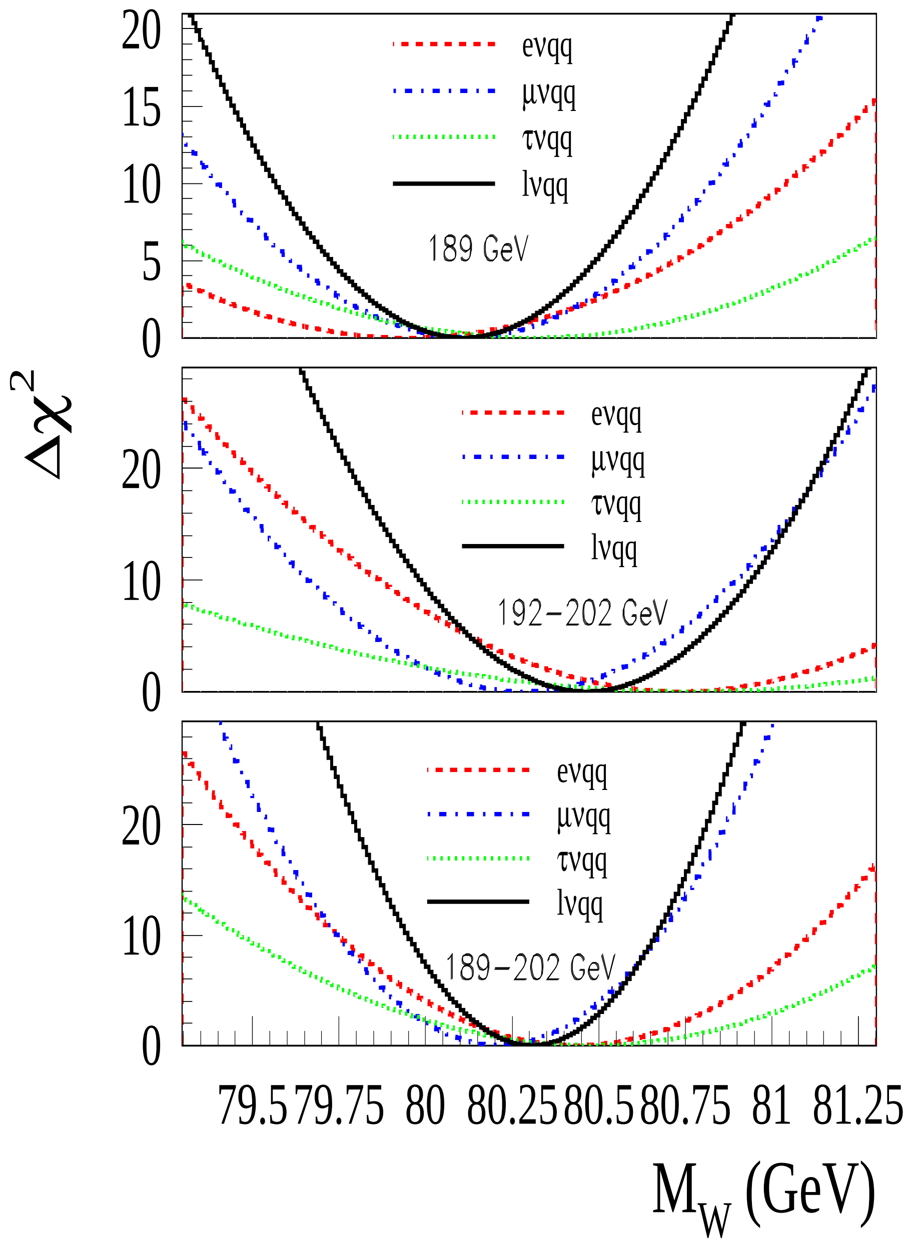

Figure 7.1: M$_{\mathrm{W}}$ $\Delta(-2log(\mathbf{L}))$ curves for individual decay channels (dotted curves) and for all channels combined (solid curve).

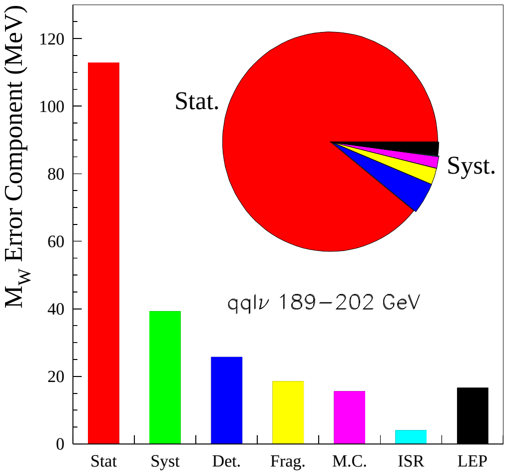

Figure 7.2: A breakdown of the sources of error in the M$_W$ measurement.

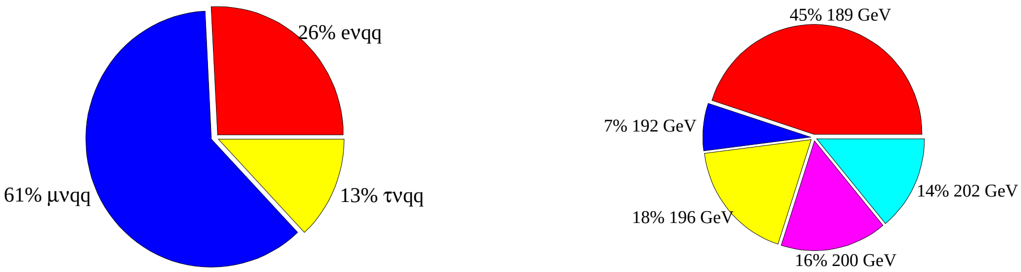

(a) **(b)**

Figure 7.3: Contributions to the final M$_W$ result from each channel **(a)**, and from each centre of mass energy point **(b)**. The higher sensitivity of the $\mu\nu q\overline{q}$ channel reflects in the weight it carries in the final result.

7.3 Γ_W Results for 1998 and 1999

The combined $\Gamma_{\rm W}$ results for the 1998 and 1999 data sets and their corresponding errors are presented below. The errors are divided into the statistical component (*stat*) and the main systematic (*syst*). The total error is given in brackets. The combined result for 1998 data is

$$\Gamma_{\rm W} \;=\; 2.137 \;\pm\; 0.451\;(stat) \;\pm\; 0.125\;(syst)\;(\pm\;0.468)\;\rm GeV$$

The combined value for 1999 data is

$$\Gamma_{\rm W} \;=\; 1.614 \;\pm\; 0.395\;(stat) \;\pm\; 0.192\;(syst)\;(\pm\;0.439)\;\rm GeV$$

The combination of these two results yields the value

$$\Gamma_{\rm W} \;=\; 1.857 \;\pm\; 0.297\;(stat) \;\pm\; 0.155\;(syst)\;(\pm\;0.336)\;\rm GeV$$

The $-2log(\mathbf{L})$ curves for individual channels and for the two running periods, and the combined results, are shown in Figure 7.4.

7.4 Comparison with DELPHI and LEP Results

The $\rm M_W$ and $\Gamma_{\rm W}$ results obtained with this analysis can be compared with the corresponding DELPHI official $\rm l\overline{\nu}_l q\bar{q}'$ values, which are,

$$\begin{aligned} M_W \;&=\; 80.253 \;\pm\; 0.151\;(stat) \;\pm\; 0.046\;(syst) \;\pm\; 0.017\;(LEP)\;GeV \\ \Gamma_W \;&=\; 2.842 \;\pm\; 0.425\;(stat) \;\pm\; 0.088\;(syst)\;GeV \end{aligned}$$

for data taken during the 1998 running period, and,

$$\begin{aligned} M_W \;&=\; 80.429 \;\pm\; 0.121\;(stat) \;\pm\; 0.045\;(syst) \;\pm\; 0.017\;(LEP)\;GeV \\ \Gamma_W \;&=\; 1.543 \;\pm\; 0.275\;(stat) \;\pm\; 0.088\;(syst)\;GeV \end{aligned}$$

for data taken during the 1999 running period. The combined DELPHI $l\nu q\overline{q}$ results are:

$$\begin{aligned} M_W \;&=\; 80.360 \;\pm\; 0.094\;(stat) \;\pm\; 0.045\;(syst) \;\pm\; 0.017\;(LEP)\;GeV \\ \Gamma_W \;&=\; 1.927 \;\pm\; 0.231\;(stat) \;\pm\; 0.086\;(syst)\;GeV \end{aligned}$$

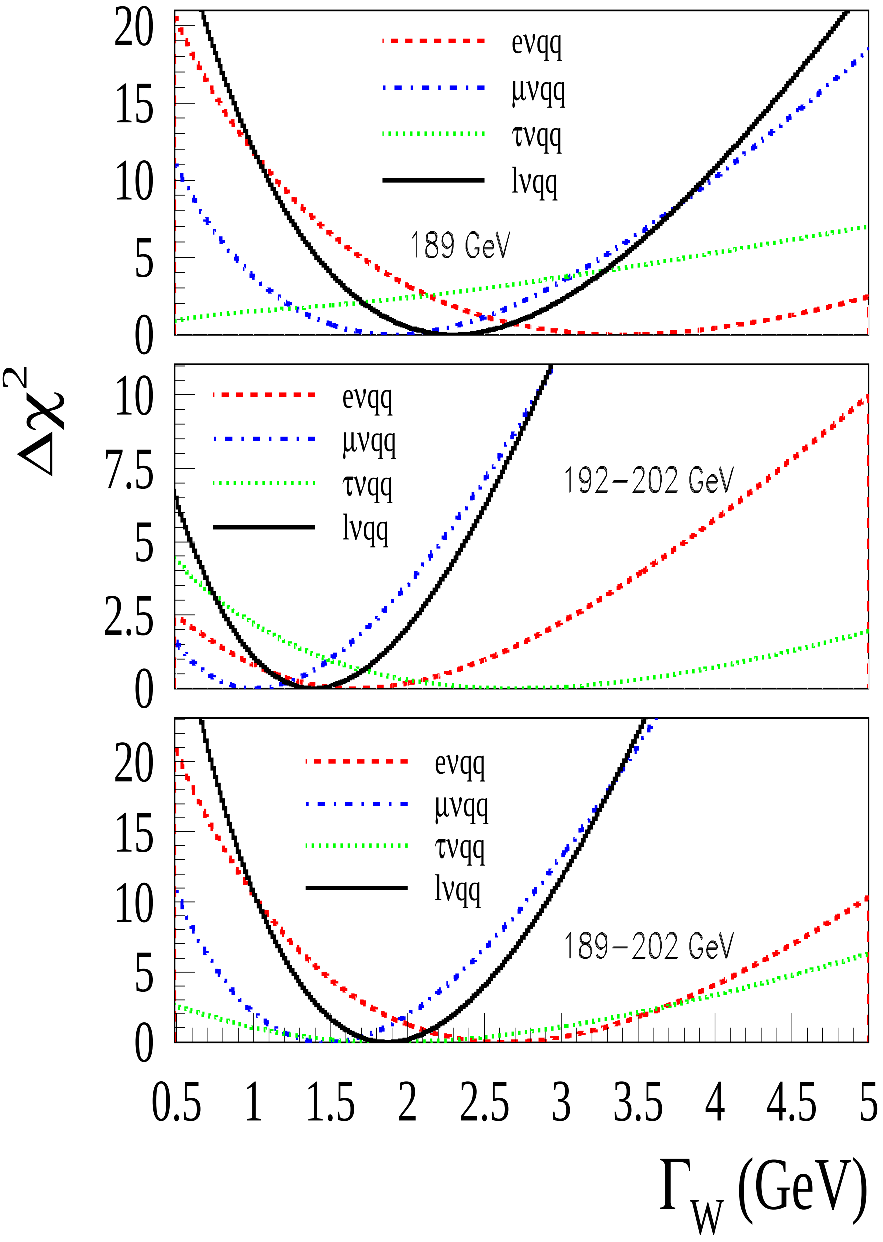

Figure 7.4: Γ_W $\Delta(-2log(\mathbf{L}))$ curves for individual decay channels (dotted curves) and for all channels combined (solid curve).

Both sets of results can be seen in Figures 7.5 and 7.6. Despite being obtained from the same overall data samples, the results between analyses differ in terms of event selection, jet clusterisation, and maximum likelihood fit method. Thus the correlation between the results is less than 100%. Concerning the $\mathrm{M_W}$ results, it can be seen that the $e\nu q\overline{q}$ channel shows some disagreement for both data sets. However, it is impossible to draw any strong conclusions from this disagreement as there is no obvious trend in the discrepancies. Besides the differences in selection and jet clusterisation, the treatment of electron energies differs between the two analyses. As can be seen in Section 6.2, the treatment of electron energies has a large impact on the result.

Channel by channel results for Γ_W are not quoted here. This is due to the fact that, for small samples, the likelihood curves for this parameter are highly asymmetric, and the errors themselves are correlated to the fitted value. The results quoted come from samples with large enough statistics as to give reasonably symmetric likelihood curves. Both the $\mathrm{M_W}$ and Γ_W results show larger error bars than the DELPHI numbers. This is entirely due to the statistical errors on the fits. One clear source of error is the fact that $\tau\nu q\overline{q}$ events selected under the hypothesis of the τ decaying in single-prong mode are excluded from this analysis. The only reason for this is that there are, at the time of writing, large data-Monte Carlo discrepancies for this channel within the common $\mathrm{W^+W^-}$ ntuple framework[62]. There is no fundamental reason why these events could not be used for this analysis in the future, increasing its sensitivity. However, the statistical sensitivity of the method presented here is lower than that of the official DELPHI method. Whether this is down to a non-optimal use of information with this method or to the differences in event selection and reconstruction is not clear. The systematic errors shown here have been evaluated independently by propagating the relevant effects through the analysis chain. The results show lower systematic uncertainties for this analysis. This is driven by the uncertainty in fragmentation effects, where a completely different method has been applied. Systematic effects due to jet and electron energy scale and resolution can be further reduced by applying corrections to the reference Monte Carlo simulation samples. A further source of systematic error that can be eliminated is that due to the limited statistics of calibration samples. The reader

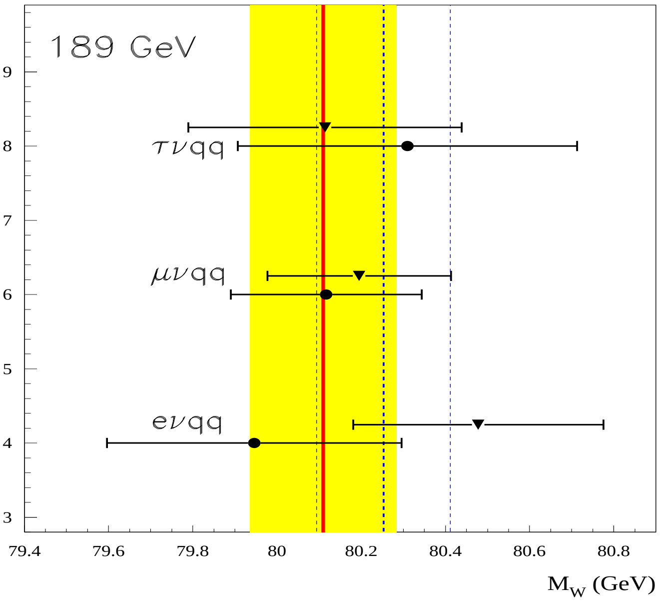

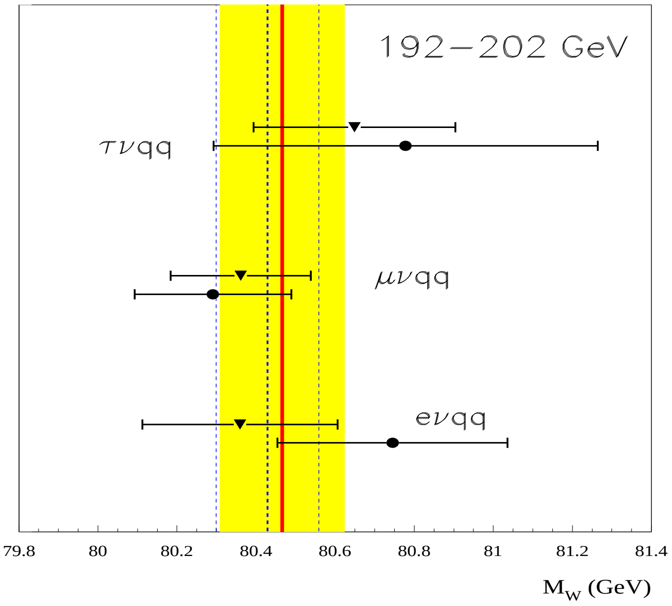

Figure 7.5: Comparison between results obtained using data from the the 1998 (top) and 1999 (bottom) running periods with this analysis (solid circles) and the official DELPHI one (solid triangles). The solid vertical line and the shaded band show the combined result and one standard deviation region for the analysis presented here. The dotted vertical lines represent the DELPHI central values and one standard deviation points.

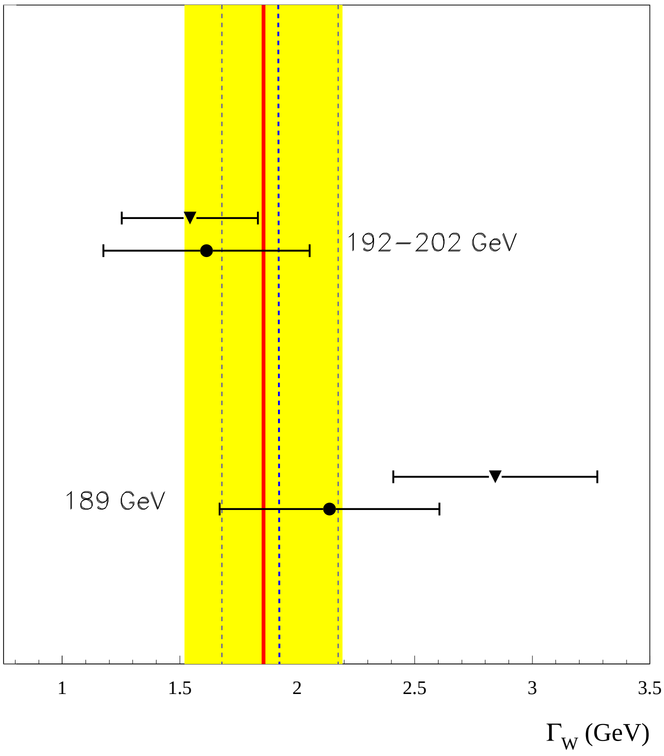

Figure 7.6: Comparison between Γ_W results obtained with this analysis (solid circles) and with the official DELPHI one (solid triangles). The solid vertical line and the shaded band show the combined result and one standard deviation region for the analysis presented here. The dotted vertical lines represent the DELPHI central values and one standard deviation points.

is reminded that this method is naturally unbiased and so, in principle, needs no calibration or bias corrections. A conservative approach has been taken here due to understood discrepancies between reference samples and the real data, and the fact that, for the 1999 data sets, the reference sample was generated at a single centre of mass energy. Therefore there is ample potential to further reduce the systematic errors shown here.

A private combination of the results of **ALO** based on the numbers given in [88] has been performed in order to compare with the results presented here. The combined 1998 and 1999 $l\nu q\bar{q}$ M_W and Γ_W results are compared to the statistically uncorrelated **ALO** results. These comparisons can be seen in Figure 7.7. The results are in agreement within $\sim 1.2\sigma$.

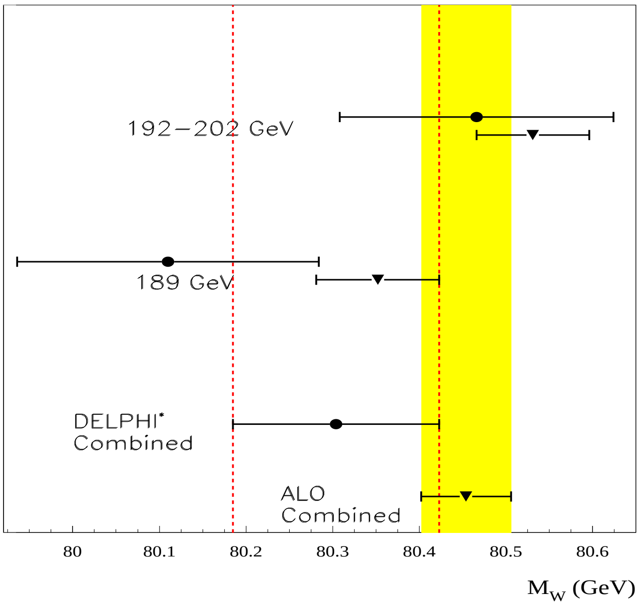

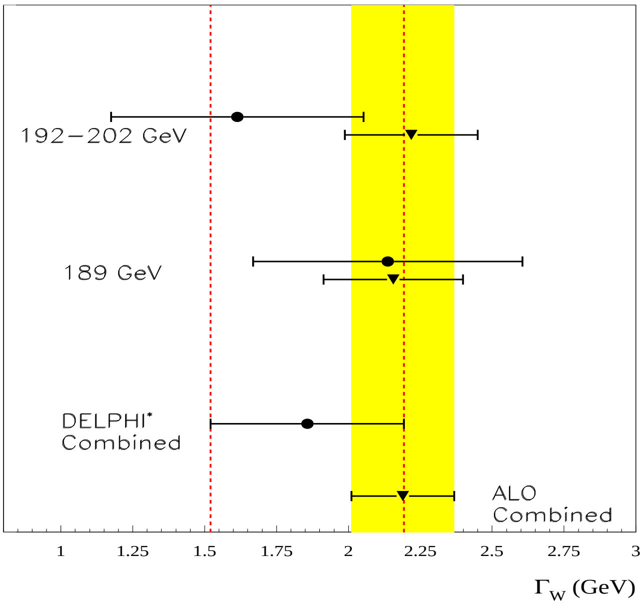

Figure 7.7: Comparison between M_W (top) and Γ_W (bottom) results obtained with this analysis (solid circles) and the average of the **ALO** ones (solid triangles). The shaded band show the combined ALO one standard deviation region. The dotted vertical lines represent the one standard deviation region for the combined result obtained using this analysis.

7.5 Interpretation of Results

The $\mathrm{M_W}$ result presented here can be used to gauge the magnitude of the Electroweak corrections Δr. Substituting the on-shell normalisation scheme relation $sin^2\theta_W = 1 - M_W^2/M_Z^2$ into Equation 1.57 and rearranging one obtains the relation

$$\Delta r \;=\; 1 \;-\; \left[\frac{\pi\alpha(M_Z^2)}{\sqrt{2}G_F}\frac{1}{M_W^2(1 \;-\; M_W^2/M_Z^2)}\right] \tag{7.1}$$

where $\alpha(M_Z)$ is the fine structure constant evaluated at the energy scale of the Z^0 boson, with value $\alpha^{-1}(M_Z^2) \;=\; 128.9 \pm 0.09$[9]. The values and errors on G_F and M_Z are taken from[89]. The evaluation gives the result

$$\Delta r \;=\; -0.0209 \;\pm\; 0.0101 \tag{7.2}$$

which is 2.1 standard deviations away from the SM born-level value and is thus compatible with the presence of higher order Electroweak corrections.

The value of $\mathrm{M_W}$ obtained with this analysis can be used to place constraints on the Higgs boson mass. However, the impact of $\mathrm{M_W}$ on the constraints depends greatly on the sensitivity $\Delta\mathrm{M_W}$. Nonetheless, the exercise of obtaining a m_H limits has been carried out for completeness [90]. Assuming the best values for SM parameters as given in [9], with a top quark mass of $m_t = 174.3 \pm 5.1$ GeV, and excluding all $\mathrm{M_W}$ results, the following result is obtained:

$$m_H \;=\; 74^{+68}_{-37}\mathrm{GeV}. \tag{7.3}$$

Including the $\mathrm{M_W}$ result from this analysis only, the following result is obtained:

$$m_H \;=\; 78^{+71}_{-39}\mathrm{GeV}. \tag{7.4}$$

Using the world average $\mathrm{M_W}$ value from [9] of 80.435 ± 0.037 GeV in the fit gives

$$m_H \;=\; 61^{+52}_{-29}\mathrm{GeV}. \tag{7.5}$$

It is clear from these results that a high sensitivity on $\mathrm{M_W}$ is required in order to have an appreciable impact on the m_H constraints. The result presented here has little impact on its own. However, including the current world average has an appreciable effect. The sensitivity on m_H is set to improve when the final LEP2 $\mathrm{M_W}$ measurement is obtained.

The Γ_W result can be compared with the SM expectation for Γ_W. Recalling Equation 1.53,

$$\Gamma_W = \frac{3G_F M_W^3}{2\pi\sqrt{2}}\left(1 + \frac{2\alpha_s(M_W^2)}{3\pi}\right) \tag{7.6}$$

and using the world average values for G_F and α_s from [89], together with the LEP $\mathrm{M_W}$ average from [91], we obtain an SM expectation of $\Gamma_W = 2.100 \pm 0.006$ GeV. Comparison with this result gives

$$\Gamma_W - \Gamma_W(SM) = -0.243 \pm 0.336 \text{ GeV} \tag{7.7}$$

showing agreement between the results obtained with this analysis and the SM value to less than 1 σ.

The compatibility between the $\mathrm{M_W}$ and Γ_W results presented in this thesis can be checked by repeating the comparison, replacing the current LEP average value of $\mathrm{M_W}$ by the number presented here. Using Equation 7.6, this yields an expected width of $\Gamma_W = 2.091 \pm 0.011$ GeV. Comparison with our Γ_W result gives

$$\Gamma_W - \Gamma_W(SM) = -0.234 \pm 0.336 \text{ GeV}, \tag{7.8}$$

showing that the results are consistent with each other, assuming the SM and the low correlation between the $\mathrm{M_W}$ and Γ_W results.

7.6 Conclusions

The LEP high energy data collected by DELPHI in 1998 and 1999, corresponding to a total integrated luminosity of 372 pb^{-1}, have been analysed in this thesis. Events conforming to the semi-leptonic $\mathrm{W^+W^-}$ decay hypotheses have been selected. Their kinematic observables have been used to obtain values for the mass and width of the W boson. The results have been found to be compatible with the current world average and with the official results published by the DELPHI collaboration, and show overall agreement with the standard model. An interpretation of these results in terms of higher order Electroweak corrections and the mass of the Higgs boson has been made. The standard model relation between M_W and Γ_W has been checked and found to be satisfied.

The LEP2 programme has finished taking data. Preliminary LEP combined results for M_W and Γ_W are available for the total collected integrated luminosity of ∼2300 pb^{-1} [88]. These experiment by experiment and combined results can be seen in Figure 7.8. The combination included all the LEP2 high energy results except those corresponding to the data taken by DELPHI and OPAL in the 2000 running period. These results are not publically available at the time of writing. The world average M_W value obtained from direct measurements at LEP2 and $p\overline{p}$ colliders is shown in Figure 7.9, together with the value obtained from indirect methods. The plot shows a disagreement between the measurements to the level of two standard deviations. Improvements in the sensitivity of the direct determination of M_W could add significance to the disagreement, stressing the importance of a precise determination of the mass of the W boson. A plot of the M_W and m_t direct and indirect measurement contours can be seen in Figure 7.10. The uncertainty on the LEP average M_W value is dominated by systematic errors. It is foreseen that these will be reduced as a better understanding of them is reached, therefore there is good reason to believe that the final LEP M_W sensitivity will improve further.

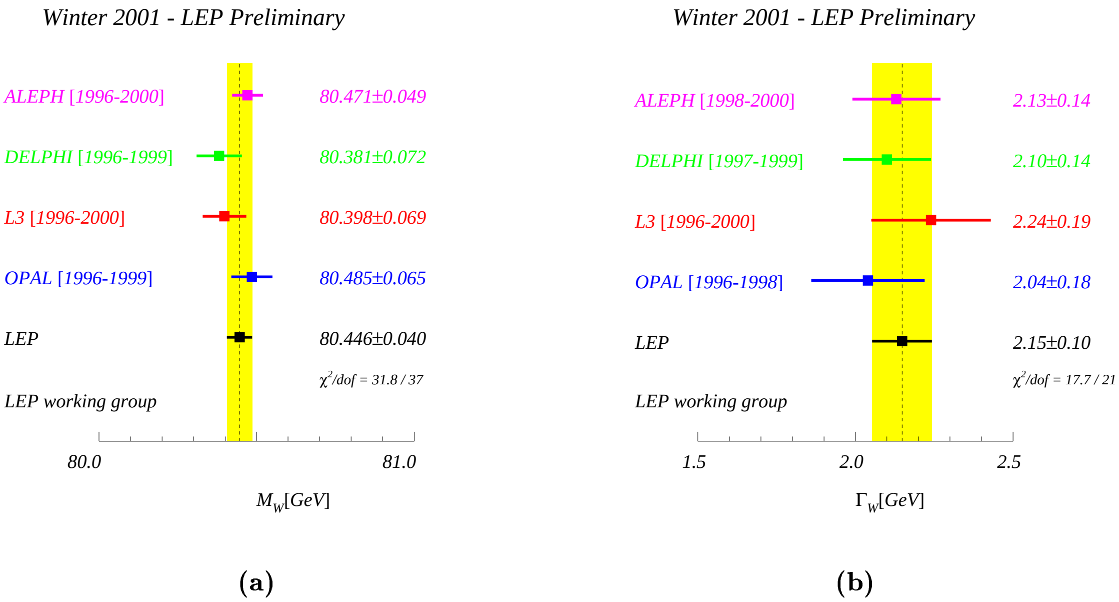

Figure 7.8: Preliminary combined results for the M_W and Γ_W measurements from the four LEP experiments [91]. The measurements of each experiment are shown.

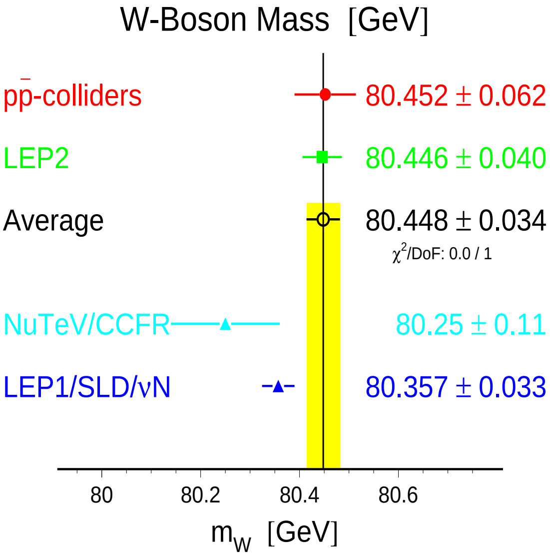

Figure 7.9: The world average W boson mass from direct measurements shown with the results from indirect estimations [91]

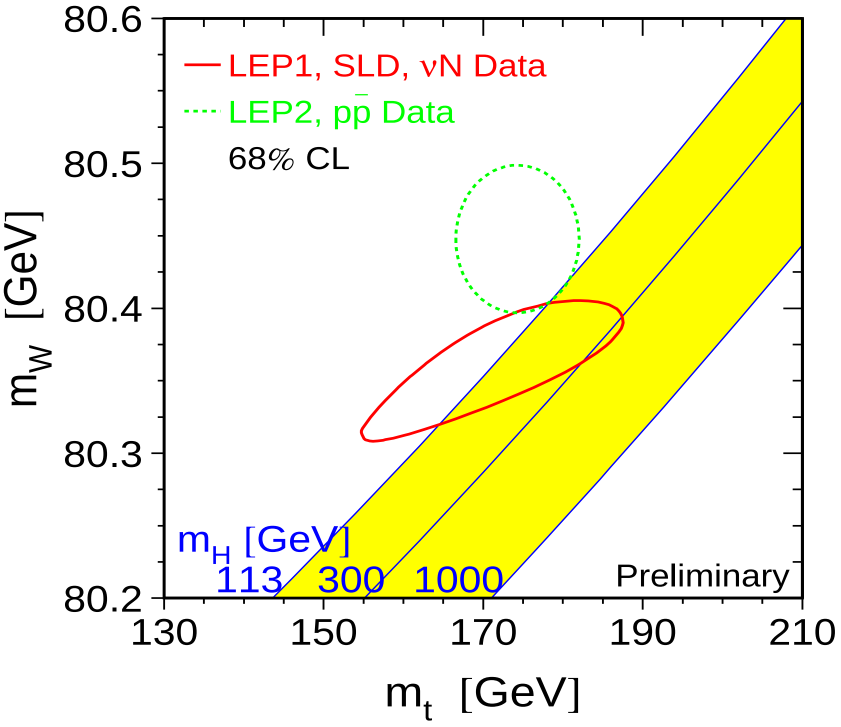

Figure 7.10: The mass of the W boson is plotted against the mass of the top quark. The contours from the direct (dotted curve) and indirect (solid curve) determination are shown. The shaded bands show the standard model predictions for M_W and m_t as a function of the Higgs mass.

Appendix A

The Equivalent Number of Reweighted Events

Defining $Y(\vec{x}, N)$ as the sum over N unweighted events in a sample:

$$Y = \sum_{i=1}^{N} x_i = N \tag{A.1}$$

and $n(\vec{x}, N)$ as the sum of weighted events in the same sample of N events:

$$n = \sum_{i=1}^{N} \mathcal{W}_i x_i = \sum_{i=1}^{N} \mathcal{W}_i \tag{A.2}$$

where $x_i = 1$, we want to find the *number of equivalent events* N_{eq} of weight unit events with the same statistical sensitivity as N weighted events. First we define the statistical error on $Y(\vec{x})$ and n. Recalling the general form for the propagation of errors on any $f(\vec{x})$ [61]:

$$\sigma_f^2 \approx \sum_{i,j=1}^{N} \left[\frac{\partial f}{\partial x_i} \frac{\partial f}{\partial x_j} \right]_{\vec{x}=\vec{\mu}} V_{ij} \tag{A.3}$$

and taking all the x_i in $\vec{x}$ to be completely uncorrelated and the errors σ_i to be equal for all i we get for A.1:

$$\sigma_Y \approx \sqrt{\sum_{i,j=1}^{N} \sigma_i^2} = \sigma\sqrt{N} \tag{A.4}$$

and for A.2:

$$\sigma_Y \approx \sqrt{\sum_{i,j=1}^{N} \mathcal{W}_i^2 \sigma_i^2} = \sigma \sqrt{N \sum_{i,j=1}^{N} \mathcal{W}_i^2} \tag{A.5}$$

We need to determine N_{eq} such that:

$$\frac{\sigma_{\tilde{Y}}}{\tilde{Y}} = \frac{\sigma_n}{n} \tag{A.6}$$

where $\tilde{Y} = Y(\vec{x}, N_{eq}) = N_{eq}$, that is, the relative error on the sum of N_{eq} *unweighted* events must be the same as that of the sum of N *weighted* ones. Condition A.6 leads to:

$$\frac{\sigma\sqrt{N_{eq}}}{N_{eq}} = \frac{\sigma\sqrt{\sum_{i=1}^{N} \mathcal{W}_i^2}}{n} = \frac{\sigma\sqrt{\sum_{i=1}^{N} \mathcal{W}_i^2}}{\sum_{i=1}^{N} \mathcal{W}_i} \tag{A.7}$$

leading to the result:

$$N_{eq} = \frac{(\sum_{i=1}^{N} \mathcal{W}_i)^2}{\sum_{i=1}^{N} \mathcal{W}_i^2} \tag{A.8}$$

Appendix B

PUFITC+: A Constrained Fitting Package

The direct reconstruction method used to measure M_W and Γ_W in this thesis makes use of the `PUFITC+` program to perform the constrained kinematic fits from which the observables used in the likelihood function are obtained. This constrained fit package is used by the official DELPHI M_W analyses [92]. The authors of `PUFITC+` are Neils Kjær and Martijn Mulders. A full description of the program can be found in [64]. A brief outline is presented here.

The constrained kinematic fit aims to improve the resolution on the observed final state objects of an event by adding extra information in the form of constraints. The constraints imposed in this analysis are are discussed in Section 4.5.

The inputs to the fit are the observed jets, charged leptons, and an ISR photon where applicable. The direction and energy of each of these is described by three parameters:

- Electrons and positrons are characterized by their `REMCLU` [6] estimated energy and angular position, $\theta\phi$. The energy errors are estimated in `REMCLU`. The errors on the angular information are determined from the track fit.

- Muons are described by their measured momenta $|p|$, and their polar and azimuthal angles $\theta\phi$. Both these quantities are obtained from the tracking and muon detectors. All the errors are obtained directly from the track fit.

- The decays of tau leptons result in the emission of at least one neutrino. Therefore their absolute momentum is undetermined, resulting in a reduction of one in the number of degrees of freedom of the constrained fit. Their treatment is similar to that of jets.

- Neutrinos escape DELPHI undetected. The three descriptive parameters are thus undetermined, resulting in a reduction in the number of degrees of freedom of the fit of three.

- The jets are collections of tracks and energy deposits clustered, in this case, using the `DURHAM` algorithm. The inputs to the fit are the clustered direction and energy of the jets. The jet errors are estimated by re-expressing the jet momentum, $\mathbf{p_i^{fit}}$, in terms of a parallel and two transverse components:

  $$\mathbf{p_i^{fit}} = exp(a_i)\mathbf{p_i^{meas}} + b_i\mathbf{p_i^b} + c_i\mathbf{p_i^c}$$

  where $\mathbf{p_i^b}$ and $\mathbf{p_i^c}$ are perpendicular to the measured jet momentum $\mathbf{p_i^{meas}}$. The parallel component includes an exponential rescaling factor while the transverse components are arbitrarily fixed to 1 GeV and their variation is described by a multiplicative parameter.

The scaling parameters can be expressed as a χ^2:

$$\chi^2 = \Sigma_i \frac{(a_i - a_0)^2}{\sigma_{a_i}^2} \ + \ \frac{b_i^2}{\sigma_{b_i}^2} \ + \ \frac{c_i^2}{\sigma_{c_i}^2}$$

The energy loss parameter, a_0, accounts for the fact that the measured jet momentum is typically lower than the true one due to undetected particles. It is parameterised, together with the expected errors on the parameters, σ_a, σ_b, and σ_c, using simulated events. The values are:

$$a_0 = 0.15 \ + \ 0.4\cos^4\theta_i$$

$$\sigma_{a_i} = 0.27 \ + \ 0.72\cos^4\theta_i$$

$$\sigma_{b_i} = 1.5$$

$$\sigma_{c_i} = 1.5$$

Thus the jet errors are parametrised to take into account their polar angle, θ_i, and their breadth.

- Photons are defined by their angular direction and by their calorimetric energy. Both are estimated using `REMCLU`. Their treatments in the fit is similar to the treatment of jets.

The conservation of energy and momentum, and equality of the two masses measured in an event, are introduced as constraints to the fit. Expressing the constraints vectorially gives:

$$\mathbf{f}(\mathbf{p_1^{fit}}, \mathbf{p_2^{fit}}, \mathbf{p_3^{fit}}, \mathbf{p_4^{fit}}) = \mathbf{0}$$

where the $\mathbf{p_i^{fit}}$ are the momentum vectors of the four fitted fermions. The method of Lagrange multipliers is used to minimise the χ^2 using an iterative procedure.

References

[1] P.B. Renton. *Electroweak Interactions.* C.U.P., *(1990).*

[2] A.D. Martin F. Halzen. *Quarks & Leptons: An Introductory Course in Modern Particle Physics.* Wiley & Sons, *(1984).*

[3] Proceedings of the School for Young High Energy Physicists. Technical Report RAL-TR-1999-024, RAL, *(1999).*

[4] C. J. Parkes. *A Determination of the W Boson Mass Near the W-Pair Production Threshold.* PhD thesis, University of Oxford *(1998).*

[5] J. F. Libby. *The Study of* $e^+e^- \rightarrow \mu^+\mu^-(\gamma)$ *and the Measurement of Trilinear Gauge Couplings at* LEP2 *using the* DELPHI *Detector.* PhD thesis, University of Oxford *(1999).*

[6] F. Cossutti, A. Tonazzo, F. Mazzucato. REMCLU: a package for the Reconstruction of ElectroMagnetic CLUsters at LEP200. *DELPHI 2000-164 PROG 242(2000).*

[7] F. Stichelbaut, G.Wilkinson. Performance of muon identification in DELPHI for the 93 and 94 data . *DELPHI 95-140 PHYS 565 (1995).*

[8] The Super-Kamiokande Collaboration. Atmospheric Neutrino Results from Super-Kamiokande. *Paper submitted to ICHEP2000.*

[9] The LEP Collaborations ALEPH, DELPHI, L3, OPAL, the LEP Electroweak Working Group and the SLD Heavy Flavour Group and Electroweak Groups. A Combination of Preliminary Electroweak Measurements and Constraints on the Standard Model. *CERN-EP/2000-016 (2000).*

[10] The LEP Working Group for Higgs Boson Searches (S. Andringa *et al*). Searches for Higgs Bosons: Preliminary combined results using the LEP data collected at energies up to 209 GeV. *ALEPH 2000-074 CONF 2000-051, DELPHI 2000-148 CONF 447, L3 Note 2600, OPAL Technical Note TN661.*

[11] G. 't Hooft. Renormalization of Massless Yang-Mills Fields. *Nucl. Phys.* **B33** *173 (1971).*

[12] G. 't Hooft. Renormalizable Lagrangians for Massive Yang-Mills Fields. *Nucl. Phys.* **B35** *167 (1971).*

[13] S.L. Glashow. Partial-Symmetries of Weak Interactions. *Nuc. Phys.* **22B** *579 (1961).*

[14] A. Salam, J.C. Ward. Electromagnetic and Weak Interactions. *Phys. Lett.* **13** *168 (1964).*

[15] S. Weinberg. A Model of Leptons. *Phys. Rev. Lett.* **19** *1264 (1967).*

[16] E. Fermi. An Attempt of a Theory of Beta Radiation. 1. *Z. Phys.* **88** *161 (1934).*

[17] UA1 Collaboration (G. Arnison *et al*). Experimental Observation of Isolated Large Transverse Energy Electrons with Associated Missing Energy at $\sqrt{s} =$ 540 GeV. *Phys. Lett.* **122B** *103 (1983).*

[18] UA2 Collaboration (M. Banner *et al*). Observation of Single Isolated Electrons of High Transverse Momentum in Events with Missing Transverse Energy at the CERN $\bar{p}p$ Collider. *Phys. Lett.* **122B** *476 (1983).*

[19] Conveners: Z. Kunst, W.J. Stirling Editors: G. Altarelli, T. Sjöstrand, F. Zwirner. Physics at LEP2 Vol. 1, Determination of the mass of the W Boson. Technical report, CERN, *(1996).*

[20] M.Consoli, A. Sirlin. Editors: J. Ellis, R. Peccei. Physics with LEP Vol. 1. Technical report, CERN, *(1986).*

[21] D. Bardin *et al* . `GENTLE`/4fan v2.0 A Program for the Semi-Analytic Calculation of Predictions for the Process $e^+e^-{\rightarrow}4f$. *DESY 96-233, HEP-PH/9612409 (1996).*

[22] F.A. Berends, R. Kleiss, R. Pittau. `EXCALIBUR`: A Monte Carlo Program to Evaluate all Four Fermion Processes at LEP-200 and Beyond. *Comput. Phys. Commun.* **85** *437-452 (1995).*

[23] Conveners: W. Beenakker, F.A. Berends Editors: G. Altarelli, T. Sjöstrand, F. Zwirner. Physics at LEP2 Vol. 1, W^+W^- Cross-Sections and Distributions. Technical report, CERN, *(1996).*

[24] A. Denner, S. Dittmaier, M. Roth and D. Wackeroth. . *BI-TP 2000/06, in preparation.*

[25] Conveners: D. Bardin, R. Kleiss Editors: G. Altarelli, T. Sjöstrand, F. Zwirner. Physics at LEP2 Vol. 2, Event generators for W^+W^- Physics. Technical report, CERN, *(1996).*

[26] Conveners: M.W. Grünewald, G. Passarino Editors: S. Jadach, G. Passarino, R. Pittau. LEP2 Monte Carlo Workshop: Report of the Working Groups on Precision Calculations for LEP2 Physics, Four-Fermion Production in Electron-Positron Collisions. Technical report, CERN, *(2000).*

[27] C.J. Parkes, P.B. Renton, H.T. Phillips. A Study of Four Fermion Final State Interference relevant to the Measurement of the W^+W^- Cross-Section and the W Mass . *DELPHI 97-96 PHYS 718 (1997).*

[28] S. Myers. Conclusions of the Ninth LEP performance Workshop. *CERN-SL-99-07.*

[29] R. Bailey *et al* . Conclusions of the Tenth LEP performance Workshop. *Available from:* `http://cern.web.cern.ch/CERN/Divisions/SL/publications/chamx2k/contents.html`.

[30] S. Myers. Conclusions of the Seventh LEP performance Workshop. *CERN SL-97-12.*

[31] S. Myers. Conclusions of the Eighth LEP performance Workshop. *CERN-SL-98-06.*

[32] LEP Energy Working Group (R. Assmann *et al*). Calibration of the centre–of–mass energies at LEP1 for precise measurements of Z properties. *Eur. Phys J.* **C6** *2 187–223 (1999).*

[33] M. Placidi and R. Rossmanith. e^+e^- Polarimetry at LEP. *Nucl. Instr. and Meth.* **A274** *79 (1989).*

[34] LEP Energy Working Group (A. Blondel *et al*). Evaluation of the LEP centre–of–mass energy above the W–pair production threshold. *Eur. Phys. J.* **C11** *4 573–585 (1999).*

[35] LEP Energy Working Group (A. Blondel *et al*). LEP energy calibration in 1996 . *The working group on* LEP *energy Note 97/01.*

[36] LEP Energy Working Group (A. Blondel *et al*). Preliminary LEP energy calibration for 1997 data. *The working group on LEP energy Note 98/01.*

[37] J. Libby, G. Morton. The Measurement of the 1997 Beam Energy using $e^+e^- \to \mu^+\mu^-\gamma$. *DELPHI 98-152 PHYS 796 (1998).*

[38] E. Graugés. LEP *Centre-of-mass energy determination from* $Z\gamma$ *events.* PhD thesis, Universitat Autònoma de Barcelona *(2000).*

[39] E. Barbero *et al* . Performance of BPM Electronics for the LEP spectrometer. In *Proc. BIW'00, MIT, Cambridge, Massachusetts, May 2000.*

[40] F. Roncarolo. *High Accuracy Magnetic Field Mapping of the* LEP *Spectrometer Magnet* . Diploma Thesis, Polytechnic of Milan *(2000).*

[41] A. S. Müller. *Precision Measurements of the* LEP *Beam Energy for the Determination of the W Boson Mass* . PhD thesis, University of Mainz *(2000).*

[42] DELPHI Collaboration (P. Aarnio *et al*). The DELPHI Detector at LEP. *Nucl. Instr. and Meth. in Phys. Res.* **A303** *233-276 (1991).*

[43] DELPHI Collaboration (P. Abreu *et al*). Performance of the DELPHI Detector. *Nucl. Instr. and Meth. in Phys. Res.* **A378** *57-100 (1996).*

[44] P. Chocula *et al* . The DELPHI Silicon Tracker At LEP2. *Nucl. Instr. and Meth.* **A412** *304-328 (1998).*

[45] DELPHI Collaboration (P. Abreu *et al*). Cross Sections and Leptonic Forward–Backward Asymmetries from the Z Running of LEP. *To be submitted to Eur. Phys. J. C. (1998).*

[46] Conveners: S. Jadach, O. Nicrosini Editors: G. Altarelli, T. Sjöstrand, F. Zwirner. Physics at LEP2 Vol. 2, Event generators for Bhabha Scattering. Technical report, CERN, *(1996)*.

[47] DELPHI STIC Collaboration (S.J. Alvsvaag *et al*). The Small Angle Tile Calorimeter in the DELPHI Experiment. *CERN-EP/98-132*.

[48] DELPHI Collaboration. DELPHI Data Analysis Program `DELANA` User's Guide. *DELPHI 89-44 PROG 137 (1989)*.

[49] V. Perevozchikov, N. Smirnov. `PHDST` Package Description V.3 VZD - Viewer of Zebra Data for DELPHI User's Manual. *DELPHI 92-118 PROG 189 (1994)*.

[50] T. Spassoff, N. Smirnov. `SKELANA`: Skeleton Analysis Program. *DELPHI note in preparation (1998)*.

[51] R. Chierici, C. Parkes, A. Tonazzo. `WWANA` A Standard Package for W Analysis. *DELPHI 96-128 PROG 218 (1996)*.

[52] F. Cossutti, C. Parkes. Improvements to `SKELANA` for Version 2.0. *DELPHI 99-175 PROG 239(1999)*.

[53] D. Jeans. Selection of $l\nu q\bar{q}$ and $q\bar{q}q\bar{q}$ WW decays using IDA. *DELPHI note in preparation (2001)*.

[54] P. Buschmann *et al* . Measurement of the W-pair Production Cross-section and W Branching Ratios at $\sqrt{s}$ = 192 - 202 GeV. *DELPHI 2000-140 ICHEP2000 CONF 439 (2000)*.

[55] S. Ask, V. Hedberg, p. Niezuravski, A. Nygren, P. Tiapkine, N. Zimin. LEP Machine Background and Noise in the DELPHI Calorimeters. *DELPHI 99-157 LEDI 12(1999)*.

[56] G.W. Wilkinson. Private Communication.

[57] G. Morton, A. Behrmann. Determination of the Muon ID and Track Reconstruction Efficiencies using Data Collected in 1998 . *DELPHI 200-02 PHYS 845 (2000)*.

[58] M. Feindt, C. Kreuter, O. Podobrin. `ELEPHANT`: Reference Manual. *DELPHI 96-82 PROG 217(1998)*.

[59] C.J. Parkes. Private Communication.

[60] T. G. M. Malmgren. An iterative nonlinear discriminant analysis program: IDA 1.0 . *Comp. Phys. Comm.* **106** *230 (1997).*

[61] G. Cowan. *Statistical Data Analysis.* Oxford University Press, *(1998).*

[62] D. Jeans. Private Communication.

[63] P. Abreu *et al* . SPRIME - A Package for Estimating the Effective s' Centre of Mass Energy in $q\bar{q}\gamma$ Events. *DELPHI 96-124 PHYS 632 (1996).*

[64] N. Kjær, R. Möller. Reconstruction of Invariant Masses in Multi-Jet Events. *DELPHI 91-17 PHYS 88 (1991).*

[65] L. Lyons. *Statistics for Nuclear and Particle Physicists.* C.U.P., *(1986).*

[66] R.J. Barlow. *Statistics - a guide to the Use of Statistical Methods in the Physical Sciences.* John Wiley and Sons, *(1989).*

[67] ALEPH Collaboration (R. Barate *et al*). Measurement of the W Mass and Width in e^+e^- Collisions at 189 GeV. *Eur. Phys. J.* **CC17** *241 (2000).*

[68] OPAL Collaboration (K. Ackerstaff *et al*). Measurement of the W Mass and Width in e^+e^-Collisions at 189 GeV. OPAL *Paper PR320. Accepted by Phys. Lett.* **B**.

[69] L3 Collaboration (M. Acciarri *et al*). Measurements of Mass and Width of the W Boson at LEP. *Phys. Lett.* **B454** *386 (1999).*

[70] DELPHI Collaboration (P. Abreu *et al*). Measurement of the Mass and Width of the W Boson in e^+e^-Collisions at $\sqrt{s} = 189$ GeV. *Accepted by Phys. Lett.* **B**.

[71] C.M. Bishop. *Neural networks for pattern recognition.* Oxford Clarendon Press, *(1994).*

[72] G.Zech. Comparing statistical data to Monte Carlo simulation: parameter fitting and unfolding . *DESY 95-113 (1995).*

[73] R.J. Barlow. Application of the Bootstrap resampling technique to Particle Physics experiments. *MAN/HEP/99/4 (2000).*

[74] A.C. Davison, D.V. Hinkley. *Bootstrap Methods and Their Application.* Cambridge University Press, *(1997).*

[75] B. Efron, R. Tibshirani. *An Introduction to the bootstrap (Monographs on Statistics and Applied Probability No. 57).* Chapman & Hall, *(1993).*

[76] A. Ouraou F. Cossutti. Reweighting of `EXCALIBUR` events for 4 fermion physics at LEP200. *DELPHI 98-39 PROG 231 (1998).*

[77] J. Allison. Multiquadratic Radial Basis Functions for Representing Multidimensional High Energy Physics Data. *Comput. Phys. Commun.* **77** *377 (1993).*

[78] C. Green, T. Bowcock. `FASTSIM` Manual, DELPHI WWW Pages.

[79] DELPHI Collaboration (P. Abreu *et al*). `DELSIM` User's Guide. DELPHI *89-67 PROG 142 (1989).*

[80] F. Cossutti. Private Communication.

[81] DELPHI collaboration (P. Abreu *et al*). Measurement of the Mass and Width of the W Boson in e^+e^- Collisions at $\sqrt{s} = 189$ GeV . *Accepted by Phys. Lett. B.*

[82] A. Ouraou. Private Communication.

[83] P. Collins. Private Communication.

[84] DELPHI Collaboration (P.Abreu *et al*). Tuning and Test of Fragmentation models Based on Identified Particles and Precision Event Shape Data. *Zeit. Phys.* **C73** *11-60 (1996).*

[85] A. Valassi. W Mass Measurement. Talk given in the LEP W Physics Jamboree, April 24, 2001.

[86] LEP Energy Working Group (R. Assmann *et al*). Evaluation of the LEP centre-of-mass energy for data taken in 1998. *The working group on LEP energy Note 99/01.*

[87] LEP Energy Working Group (R. Assmann *et al*). Evaluation of the LEP centre-of-mass energy for data taken in 1999. *The working group on LEP energy Note 00/01.*

[88] The LEP Collaborations ALEPH, DELPHI, L3, OPAL, and the LEP W Working Group. Combined Preliminary Results on the Mass and Width of the W Boson Measured by the LEP Experiments. *LEPEWWG/MASS/2001-01, ALEPH 2001-023 PHYSIC 2001-004, DELPHI 2001-007 PHYS 887, L3 Note 2642, OPAL TN-681.*

[89] The Particle Data Group (C. Caso *et al*). Review of Particle Physics . *Eur. Phys. J.* **C3** *1-794 (1998).*

[90] P.B. Renton. Private Communication.

[91] The LEP Collaborations ALEPH DELPHI, L3 OPAL, and the LEP W Working Group. Combined Preliminary Results on the Mass and Width of the W Boson Measured by the LEP Experiments. *LEPEWWG/MASS/2000-01, ALEPH 2000-086 PHYSIC 2000-032, DELPHI 2000-165 PHYS 879, L3 Note 2617, OPAL TN-667.*

[92] DELPHI Collaboration (P. Abreu *et al*). Measurement of the W-pair Cross-Section and of the W Mass in e^+e^- Interactions at 172 GeV. *CERN-PPE-97-160 (1997).*